UNIVERSITY OF THE FREE STATE
UNIVERSITEIT VAN DIE VRYSTAAT
YUNIVESITHI YA FREISTATA

UFS·UV
NATURAL AND AGRICULTURAL SCIENCES
NATUUR- EN LANDBOUWETENSKAPPE

Mathematical Modelling of Pressure Build-up Due to Geological Carbon Dioxide Storage in Deep Saline Aquifers, Using Non-local Operators: The Context of Groundwater Protection in the Climate Change Mitigation Era.

By: Hans Tah Mbah
Student Number: 2010047609

A Thesis submitted in fulfilment of degree of

Doctor of Philosophy

in the

Faculty of Natural and Agricultural Sciences
Institution For Ground Water Studies
at the
University of the Free State,
Bloemfontein campus 9300
South Africa

August 2023

Promoter: Prof Abdon Atangana

Hans Tah, MBAH

August 2023

Dedication

This thesis is dedicated to my mother, Dzekem Gladys and my son Tumisho. Above all, I dedicate this work to God in heaven, my creator, and the father of Jesus Christ my savoir.

ACKNOWLEDGEMENTS

To God in Heaven, I owe unconditional gratitude for calling me with a purpose and shaping my path for a timely attainment.

I want to express my sincere gratitude to my supervisor, Professor. Abdon Atangana, for his outstanding mentorship and patience during my post graduate studies. His technical guidance has deepened and refined my research outlook, without which this body of work would be impossible to achieve. Beyond duties of a PhD supervisory, Professor Atangana who is an excellent expert in the field of fractional calculus has shaped my thinking on memory, real world problems (geological formations) and scientific research. Working closely and travelling with him was memorable experience.

To the entire Institute for Groundwater (IGS) family, I owe a considerable amount of gratitude for always ensuring the study environments was conducive and accessible at all times. I will like to extend my special appreciation to the entire university of the Free State including the Post Graduate School and the research-funding directorate for the opportunities to register, enrol and pursue my Doctorate studies.

This milestone will not be possible without the unwavering support and unceasing prayers of my family. I would like to express my humble and deepest appreciation to my mother Mrs. Dzekem Gladys Wirngo, without whom I will not be where I am today. To my father Mr. MUSONG Fredrick Mbah, my brother Raymond-Blanch and my sister Dolly-Kelly I thank you dearly for your motivational support and spiritual intercession throughout my studies. I thank you for trusting me, and unconditionally believing in me, even when my hope was little. I will like to express my sincere gratitude to my LOVELY partner, Vuyelwa Enestina Pongwane for her highly needed support throughout our stay during my studies. Also to my colleague and friend Dr. Hangwelani Magau, and I owe profound gratitude for his assistance with result simulations, without which this thesis will not be complete.

ABSTRACT

Man-caused Green House Gas (GHG) emissions have perturbed the earth's energy balance, and the need to achieve deep emission reduction is a pressing challenge, faced by humankind. Carbon Capture and Storage (CCS) in deep geological saline aquifers is a viable option for Green House Gas (GHG) mitigation. Industrial-scale scenarios may induce large-scale reservoir pressurization and displacement of native fluids. Especially in closed systems, the pressure buildup can quickly elevate beyond the reservoir fracture threshold and potentially fracture and or reactivate existing faults in the cap rock. This can create conduits for focused leakage and mobilization of heavy metals and harmful trace elements, into capture zones of freshwater wells. Risk assessment in CCS requires that careful safety and environmental impact evaluations be considered. Through sustainable pressure management, the reservoir's hydraulic integrity is maintained. This is theoretically achievable with the help of a numerical simulation, using robust mathematical models that provide consistent and effective ways to understand and predict pressure buildup in such complex systems. This thesis focuses on modelling two aspects: (i) the pressure buildup and (ii) CO_2 saturation evolution in the two-phase flow zone, by extending the classical pressure diffusivity and the Buckley-Leverette fractional flow models to the framework of non-local differential and integral operators. The extended models describe the pressure behavior during CO_2 injection through a vertical well, open in a saline aquifer. To include in the mathematical models the effect long-range, fading memory and weak crossover from stretched exponential to power-law, several differential operators were considered. For each extended model, different numerical schemes were adapted to derive numerical solutions. The presented numerical results provide an overview of subsurface transient pressure response and are useful tools for accurate risk assessment and sustainable reservoir management and operational safety during geo-sequestration in basins with shallow freshwater capture zones.

Keyword: Pressure build-up, non-local operator, fractional flow, injectivity, mathematical modelling, diffusivity, trap mechanism

Contents

Declaration i

Dedication ii

ACKNOWLEDGEMENTS iii

ABSTRACT iv

TABLE OF CONTENT v

LIST OF FIGURES ix

CHAPTER 1: INTRODUCTION 1

1.1. Background and motivation 1

1.2. Components of a CCS system. 3

1.2.1. Flue carbon capture 3

1.2.2. Transport 4

1.2.3. Geological Storage 4

1.3. Trapping mechanisms 4

1.3.1. Physical trapping mechanisms 5

1.3.2. Chemical trapping 8

1.3.3. Physiochemical trapping 9

1.3.3. Hydrodynamic trapping 10

1.4. Problem statement 11

1.5. Aim and Objectives 12

CHAPTER TWO: GEOLOGICAL STORAGE AND CO_2 EMISSIONS MITIGATION-A LITERATURE REVIEW 14

2.1. Introduction 14

2.2. Global warming, climate change, and fossil fuels 15

2.3. Global warming mitigation and Geologic storage 19

2.4. Components of a Carbon Capture Storage system. 21

2.4.1. Capture 21

2.4.2. Transport 23

2.4.3 Geological Storage 24

2.5. Types of geological reservoirs 24

2.5.1. Unminable coal seams. 24

2.5.2. Depleted oil and gas formations 25

2.5.3. Deep Saline formations and ocean storage. 25
2.6. Phase behavior of CO_2 in Sub-surface 27
2.8. Storage capacity estimation of saline formations 28
2.9. Risk Analysis in Carbon Capture and Sequestration 30
2.10. Geomechanics of storage in saline formations 32
2.11. Pressure buildup and Geomechanical implications: In the Salah storage project case 35
2.11.1. Monitoring geomechanical changes due to pressure buildup. 35
CHAPTER THREE: MODELLING PRESSURE BUILD-UP WITH THE CLASSICAL OPERATOR (DELTA DIRAC). 39
3.1. Introduction 39
3.2. Conceptual model and mathematical framework 40
3.3. Piecewise characterization 41
3.3.1. Near well processes (Region A) 41
3.3.2. Migration processes (trapping) (Region B) 43
3.3.3. Brine flow processes (pressure diffusion) 44
3.4. Physical model and assumption 44
3.5. Governing equations. 45
3.6. Numerical analysis 48
3.6.1. Numerical solution of the classical PDE for pressure build-up with Lagrange polynomial method 49
3.6.2. Simulation results and discussion. 52
3.7. Conclusion. 54
CHAPTER FOUR: MODELLING PRESSURE BUILD-UP WITH POWER LAW – CAPUTO FRACTIONAL DERIVATIVE 56
4.1. Introduction 56
4.2. Conceptual model, assumptions, and mathematical formulation 59
4.2.1. Assumptions 59
4.4. Power law distribution 60
4.5. Fractional derivatives based on power kernel. 61
4.5.1. The Riemann Louisville Fractional Derivative 62
4.5.2. The Caputo Fractional Derivative 63
4.5.3. Derivation of numerical scheme for the Caputo derivative 65
4.6. Numerical Solution of the Pressure Diffusivity Equation based on the Caputo derivative 66

4.6.1. Numerical approximation with Lagrange polynomial 68
4.6.2. Numerical analysis 68
4.6.3. Approximation with middle point method 76
4.7. Numerical simulation 78
4.8. Discussion and conclusion 81
CHAPTER FIVE: MODELLING PRESSURE BUILDUP WITH THE EXPONENTIAL DECAY KERNEL CAPUTO FABRIZIO FRACTIONAL DERIVATIVE 83
5.1. Introduction 83
5.2. Conceptual model and assumptions. 84
5.3. Exponential decay kernel 85
5.3.1. The fractional Exponential decay kernel and fluid pressure diffusivity 85
5.4. Fractional derivative based on the exponential decay kernel 87
5.5. Numerical Solution of the Pressure Diffusivity Equation based on the Caputo-Fabrizio Derivative. 89
5.5.1. Numerical solution with the Lagrange polynomial approximation 91
5.5.2. Numerical solution with middle point approximation method 95
5.6. Simulations results 98
5.7. Discussion and conclusion 101
CHAPTER SIX: MODELLING TRANSIENT PRESSURE BUILDUP WITH CROSSOVER MITTAG-LEFFLER FUNCTION. 103
6.1. Introduction 103
6.2. Conceptual model and assumptions 104
6.2.1. Model Assumptions: 105
6.3. Mittag-Leffler function and pressure diffusivity 105
6.4. Mathematical preliminaries 105
6.5. Numerical analysis 106
6.5.1 Approximation using Trapezoidal formula 107
6.6. Simulation results 108
6.7. Discussion and Conclusion 110
CHAPTER SEVEN: TIME STOCHASTIC MODELLING OF PRESSURE BUILDUP WITH CROSS-OVER BEHAVIOR USING MITTAG-LEFFLER FUNCTION - ATANGANA BALEAUNU DERIVATIVE. 112
7.1. Introduction 112
7.2. Conceptual model 114

7.3. Application of stochastic modelling in pressure buildup due to CO_2 injection in saline reservoirs 115
7.3.1. Stochastic particle tracking 115
7.4. Types of stochastic processes 116
7.4.1. Markov process. 116
7.4.2. Weiner process 117
7.4.3. Random walk 117
7.5. Numerical analysis 117
7.5.1. Classical stochastic model for pressure buildup 117
7.5.2. Approximation with the two-step LaGrange method. 118
7.6. Numerical simulation 123
7.7. Discussion and conclusion 124
CHAPTER EIGHT: MODELLING TWO-PHASE IMMISCIBLE FLOW OF CO_2-BRINE: IMPLICATIONS FOR GEOLOGICAL CARBON STORAGE 125
8.1. Introduction and Background 125
8.2. Conceptual model and mathematical formulation 128
8.2.1. Mathematical formulation 129
8.2.2. Steady state analysis 130
8.3. Numerical analysis 131
8.4. Analysis of the Buckley-Leveret model with gravitational effect 133
8.4.1. Modelling effect of geologic heterogeneity in modelling Two-phase immiscible 134
8.5. Fractional derivatives 135
8.5.1. Application 141
8.5.2. Numerical solution of immiscible two-phase flow with gravity 145
8.6. Numerical simulation 157
8.7. Discussion and conclusion 158
CHAPTER NINE: CONCLUSION AND RECOMMENDATIONS 159
9.1. Conclusions 159
9.2. Recommendations 163
Bibliography 164

List of figures

Figure 1-1: Detailed matrix of carbon dioxide rapping mechanisms in saline aquifer. Adapted from (Al Hameli et al, 2022)..... 5
Figure 1-2: Common trapping mechanisms in deep saline aquifers and time scales in deep saline aquifers (Modified from (Metz et al., 2005)..... 7
Figure 2-1: Global CO_2 emissions per sector (Adapted from the worldwide energy outlook-2050) 16
Figure 2-2: Graph of measured mean sea level change (adapted from Invalid source specified.)..... 17
Figure 2-3: World energy supply by source (Jain and Singh, 2016) 18
Figure 2-4: Global surface temperature trend between 1970 and 2022. 20
Figure 2-5: Geological storage options for carbon dioxide (Courtesy of National Energy Technology Laboratory)..... 27
Figure 2-6: Carbon dioxide phase diagram (adapted from IEA, 2008). 27
Figure 2-7: CCS risks life cycle profile (Adopted from Benson S. 2007) 31
Figure 2-8: Schematic representation of the In-Salah injection and storage project site with monitoring (Bachu, 2009). 36
Figure 2-9: Uplift records showing the observed and modelled point displacement at In Salah from 2004 to 2010 (Adapted from (Rinaldi and Rutqvist, 2017). 37
Figure 2-10: Geomechanical processes and technical challenges associated with pressure buildup. 37
Figure 3-1: Schematic section of plume evolution and saturation profile in the sub-surface. 41
Figure 3-2: P vs. T plot of pressure dissipation over time after switching off the injection pump. 52
Figure 3-3: P vs. r plot of pressure dissipation in region 1. 53
Figure 3-4: Plot of P vs. r in region 2..... 53
Figure 3-5: Plot of P vs t - region 53
Figure 4-1: Conceptual model for anomalous pressure diffusivity (fracture flow)..... 59
Figure 4-2: Graph of Power law kernel..... 61
Figure 4-3: Plot of P vs. t for the entire reservoir domain (showing transient pressure response). 79
Figure 4-4: Plot p vs. r for region one (Near well pressure behavior). 79
Figure 4-5: plot of P vs. t for region 1 (bottom-hole transient pressure response)..... 80
Figure 4-6: Plot of P vs t for region one (Near well transient pressure response). 80
Figure 4-7: Plot of P vs. r (pressure response in region 2) two-phase flow. 81
Figure 5-1: Conceptual model of saline aquifer showing three saturation regions..... 84
Figure 5-2: Plot of e^(-ωt) vs. t for different alpha [0-1]..... 85
Figure 5-3: Plot of P vs. r showing the pressure drop in the two-phase flow region (region 2), (Alpha=0.76)..... 99
Figure 5-4: Plot of P vs. r showing the near Well pressure behavior at the near well region (Alpha=0.76)..... 99
Figure 5-5: Plot of P vs. t showing global pressure dissipation in the saline reservoir (Alpha=0.76)..... 100
Figure 5-6: Plot of P vs. t showing transient pressure response at the near well region (Alpha=0.76)..... 100

Figure 5-7: Plot of P vs. r showing the near Well pressure behavior at the near well region (Alpha=0.76)..... 101
Figure 6-1: Conceptual Model for CO_2 Injection in saline Aquifer (Crossover behavior)..... 104
Figure 6-2: plot of P vs r (cross over from region 1 to region 2). 108
Figure 6-3: Plot of P vs r showing bottom-hole transient pressure response. 109
Figure 6-4: Plot of P vs r showing bottom-hole transient pressure response at near well region. 109
Figure 6-5: Plot of P vs r showing pressure behavior in the near Well region. 110
Figure 6-6: Plot of P vs r for fractional flow region. 110
Figure 7-1: Diagram showing conceptual and interpreted seismic facies configuration for heterogeneous seismic facies configuration calibrated by gamma-ray logs. 113
Figure 7-2: Two-dimensional conceptual model showing pressure profiles and structural and reservoir heterogeneity. 114
Figure 7-3: Plot P vs r (near well region). 123
Figure 7-4: Plot P vs r (two-phase flow region). 124
Figure 8-1: Model of the reservoir saturation profile (Adapted from Azizi, 2013) 126
Figure 8-2: Schematic presentation of the two-phase flow region (Buckley-Leverette fractional flow region). (Adapted from (Adapted from (Jenkins 2019)). 128
Figure 8-3: Power law graphs for α∈[0.1-1]. 137
Figure 8-4: Exponential decay graphs for $\alpha \in [0.1 - 1]$. 137
Figure 8-5: Mittag leffler graphs for α ∈ [0.1-1]. 138
Figure 8-6: plot of CO_2 Saturation vs distance in Cartesian space. 157
Figure 8-7: Plot of Saturation vs distance in Cartesian space. 157
Figure 8-8: Plot Saturation vs distance from well 158

List of Tables

Table 1: global potentials and reservoir capacity for CO_2 storage 24
Table 2: Data used for Pressure build-up simulation analysis 160

List of symbols and units

Symbol	Parameter
Bg	$Gas\ formation\ volume\ factor, ft^3/\text{scf}.$
cg	$Gas\ compressibility, Pa^{-1}\ [M^{-1}LM^2].$
cr	$Rock\ compressibility, Pa^{-1}[M^{-1}LM^2].$
cw	$Brine\ compressibility, Pa^{-1}[M^{-1}LM^2].$
ct	$Total\ compressibility, (1 - Sg\ )cw +\ \ cr\ , Pa^{-1}\ [M^{-1}LM^2].$
ctg	$Total\ compressibility\ of\ gas\ region, cg +\ cr\ , Pa^{-1}.$
twc	$Total\ compressibility\ of\ brine\ region, cw + cr, Pa^{-1}.$
fg	$Fractional\ flow\ of\ gas -\ dimensionless.$
$F\lambda g$	$Total\ mobility, F\lambda g =\ \left(\ \lambda_g -\ \lambda_w\right)/\ \lambda_g$
$F\lambda w$	$Total\ mobility, F\lambda w =\ \left(\ \lambda_g -\ \lambda_w\right)/\ \lambda_w.$
h	$Formation\ thickness, in\ meters\ (m).$
k	$Permeability, m^{-2}.$
kh	$Horizontal\ permeability\ meters\ (m), m^{-2}.$
kv	$Vertical\ permeability,\ \ meters\ (m)m^{-2}.$
krg	$Gas\ relative\ permeability.$
krg	$Gas\ relative\ permeability\ in\ gas\ zone, (=\ 1\ krg\ Sg\ ).$
krw	$Brine\ relative\ permeability.$
P	$Formation\ pressure.$
q	$Gas\ injection\ rate\ (positive), \frac{sm^3}{s}.$
rD	$Dimensionless\ radius, r\ /rwrD\ .$
rw	$Well - bore\ radius, m.$
re	$Formation\ external\ boundary\ radius, m.$
Sg	$Gas\ saturation.$
Sg	$ave\ Average\ gas\ saturation, (SgBL +\ Sgdry\ )/2.$
$SgBL$	$Gas\ saturation\ of\ Buckley - Leverett\ front.$

$Sgdry$	$Gas\ saturation\ of\ dry\ front.$
Swr	$Residual\ water\ saturation.$
tD	$Dimensionless\ time, kkrt/\mu_g \emptyset\ r_w^2\ C_{tg}.$
ηD_3	$Diffusivity\ ratio\ \left(C_{tg}/C_{tw}\right)(\lambda w/\lambda g), dimentionless.$
λg	$Gas\ mobility, krg\ /\mu\ g\ , 1/Pa.s.$
λw	$Brine\ mobility, krw/\ \mu\ w\ , 1/Pa.s.$.
φ	$Porosity.$
μ_g	$Viscosity\ of\ brine\ \ [ML^{-1}T^{-1}].$
μ_g	$Viscosity\ of\ CO_2\ [ML^{-1}T^{-1}].$
ρ_w	$Density\ of\ brine\ [ML^{-3}].$
ρ_g	$Density\ of\ CO_2\ [ML^{-3}].$
q_{0w}	$Brine\ flux\ \ [LT^{-1}].$
q_{0g}	$CO2\ flux\ [LT^{-1}].$
P	$Fluid\ pressure\ [ML^{-1}T^{-2}].$
M_0	$Mass\ (CO_2)\ injection\ rate\ \ [MT^{-1}].$
$m\ (units)$	$metre$

List of Publications submitted from this research.

1. **Mbah, H.T and Atangana, A. (2024). Time fractional modelling of reservoir pressure build-up due to CO_2 injection in saline aquifer with fading memory: Application of the Caputo-Fabrizio derivative.**
2. **Mbah, H.T and Atangana, A. (2024). Time fractional modelling of reservoir pressure build-up due to CO_2 injection in saline aquifer with Power law Processes. Application of the Caputo-Fabrizio derivative.**
3. **Mbah, H.T and Atangana, A. (2024). Fractional stochastic modelling of reservoir pressure build-up due to CO_2 injection in saline aquifer with cross over behaviours in a disordered matrix. Application of the generalized Mittag Leffler Function.**
4. **Mbah, H.T and Atangana, A. (2024). On the Application of fractional flow theory to evaluate CO_2 injection and migration in saline aquifer.**

CHAPTER 1: INTRODUCTION

1.1. Background and motivation

The notion that artificial Green House Gas (GHG) emissions interfere with natural weather patterns is no longer fictitious content to scientific and politico-economic debates. These days, their impacts, through global warming and climatic variation is causing extreme weather conditions: floods, wildfires, droughts, and sea level rise, which threatens the survivability and adaption to life on earth (Thuiller, 2007; Change, 2017). Even though such concerns trace back to the beginning of the 20th century, practical efforts to address the issue only gained prominence in the past two decades. For example, as early as the beginning of the 20th century, an Australian news outlet- *Rodney and Otamatea,* in a July 1917 article titled ''Coal Consumption Affecting Climate,'' reported on the possible link between coal combustion for power generation and its' potential to cause changes to the earth's climate through carbon dioxide emissions. At the time, furnaces of the world were releasing 7 billion tons of CO_2 into the atmosphere per annum, sufficient to alter the in-situ climate conditions. Today, cumulative global carbon dioxide emissions from electricity generation, industry, transport, housing, and agriculture stand at 36.6 billion tons per annum, are increasing. This is sufficient to turn the air into an effective blanket. This has prompted an increase in the search for clean energy alternatives. However, given the growing litany of threats (population growth, deforestation, pollution, energy shortages, and the like.), it is safe to say there is no one fix or Holy Grail solution that will stop climate change and overturn all its causes and effects. According to new future scenario predictions, it is almost resolute that the world needs to achieve a sizable amount of harmful emissions reduction by the end of the century if global temperature increase must be limited to 1.5 ^{0}C or 2.0 ^{0}C, as delineated by the 2015 Paris Agreement (Marland et al., 1994; Mudakkar et al., 2013).

One practical approach to the problem is understanding sector-specific interventions necessary to reduce emission rates. This was popularized through the concept of forging so-called ''stabilization wedges'' (Pacala and Socolow, 2004). According to their suggestion, the emmission reduction targets could be achieved by up-scaling already available technologies to attain better energy efficiency. The geological storage of carbon, Carbon Capture, and Storage (CCS) is one viable means to achieve a significant CO_2 reduction and Green House Gas (GHG) emissions (Hendriks, 1993; IPCC 2005) through the decarbonization of hard to abate

point sources emitter, sectors such as steel, power, and fertilizer production. With the current emission trajectory, geological restoration stands out as the most viable short to mid-term approach, given the available technical and storage capacities.

Briefly, it involves the capturing and separating CO_2 from a point source and transportation through pipelines to an open well located in a suitable site where it is injected for permanent storage in the geological formation. Waste fluid injection into geological rocks for either storage or Enhanced Oil Recovery (EOR) is not a new phenomenon, giving CCS the advantage of a quicker implementation as extensive technological experience already exists from industries such as oil and gas and geohydrology. However, as in any subsurface engineering undertaking, the deployment of CCS requires robust assessments to confirm that it is both safe and environmentally friendly, but its multidisciplinary facets and the wide range of time frames can be more complicated to evaluate relative to the majority of similar problems such as mining and geohydrology.

Geological sequestration in saline aquifers involves fluid displacement, and for confined formations, the risks of reservoir pressurization can have implications on nearby sensitive environments such as shallow groundwater aquifers. Pressure buildup beyond the fracture threshold of reservoir rocks can create localized pathways along which the leakage of reservoir fluids can potentially leak outside the storage, into Underground Drinking water Sources (UDS). Significant disturbances to geological systems by natural and man-made means in the past have showcased the scale of impact on the environment and its ecological balance. For example, in 1986, the instant catastrophic release of 64 million cubic feet of CO_2 due to a limnic eruption from the tropical lake Nyos, in Cameroon killed 1746 people and over 3300 livestock (Cotel, 1999).

In the event of a leak, CCS can be analogous to Acid Rock Drainage (ARD). Being a reducing/acidic gas, large-scale vertical diffusion of CO_2 can geochemically reduce subsurface aqueous environments, increasing the potential to mobilize and transport trace elements and heavy metals under transient pressure gradients (Kling et al., 1987).

1.2. Components of a CCS system.

The CCS systems consist of a multitude of components that work together work as a bridging technology to keep point-sourced carbon dioxide from reaching the atmosphere. The main components each play a unique role:

- a capture facility to separate and compress the carbon dioxide,
- a pipeline system to transport,
- a deep borehole to inject the captured carbon dioxide into a suitable reservoir for long-term or permanent storage and a final component which is associated with monitoring the migration of carbon dioxide underground.

An exhaustive description of the different components has been reviewed in many texts (Hildebrand and Herzog, 2009; Dowd et al., 2014). The injected CO_2 is first captured from the base outlet of a power plant as flue gas, compressed, and transported through pipelines to the designated site. A borehole opened in a suitable geological formation is the means of injection.

1.2.1. Flue carbon capture

The capture mechanisms are cryogenic separation, adsorption/abstraction, and membrane separation. The approaches used significantly impact the eventual isolation process, i.e., transport and storage. The capture, separation, and compression are the more costly aspects of this value chain since it requires capital-intensive inputs to modify existing plants or redesign traditional engineering blueprints. This significantly raises the cost of energy produced; however, for CCS to make a meaningful contribution, it must be deployed at scale, which requires technological maturity to ascertain effectiveness, usability, and implementation of legal and regulatory frameworks when it is transferable to developing nations. The amount of carbon dioxide that can be permanently stored in the designated geological formations (Rubin and De Coninck, 2005), hence the reservoir's storage capacity, is evaluated in context with the quality of the CO_2 stream and the storage potential of the porous formation. The difference between the point source volumes and the final injection volumes is not only a function of the captured amounts but also dependent on the separation efficiency, transport, and integrity of the store room. The latter is essential to prevent leakage once the carbon dioxide is injected (Aydin et al., 2010).

Three technical pathways may be followed to capture CO_2 from coal power points: post-combustion capture, oxy-combustion, and pre-combustion capture. The capture methods used depends on several criteria, some of which include: The carbon dioxide concentration in the flue gas stream, the pressure gradient in the gas stream, and; the fuel type.

1.2.2. Transport

Carbon dioxide transport is achieved using existing pipelines or ships; however, regional infrastructure needs to be developed to meet future needs. The presence of impurities such as nitrogen, oxygen, and sulfides due to diverse sources of CO_2 and the different capture techniques may affect the cost of transportation (Nicot et al., 2013). Purity standards might be required for pipeline operations to avoid the cost of over-compression for dry CO_2 transport.

1.2.3. Geological Storage

In this section, we discuss three critical options (coal seams, saline aquifers, and depleted oil and gas formations) considered for the potential storage of CO_2 in subsurface formations. To keep CO_2 from reaching the atmosphere, it will require that cumulative injection rates reach 10 Gt CO_2 per year by 2050, with more than 1000 Gt in total to be safely stored by the end of this century. This anticipated ramp-up in scale will require thousands of sites to operate under total/optimal capacity, each receiving a flow rate between 1 and 5 Mt/year. The pressure magnitudes associated with such volumes are enormous, and monitoring its buildup is needed for CCS to become commercially viable (Aydin, 2010). The three options volumetrically offer the most considerable storage resource potential.

1.3. Trapping mechanisms

Different processes can trap sc CO_2 (supper critical CO_2) after it is injected into saline aquifers deep in the earth's subsurface. These processes are broadly classified as short-term physical trapping (1 year to a few decades), intermediate-time dissolution processes (0 to a thousand years), and the much longer-term mineralization processes (100 years to millions of years). These include structural trapping, residual trapping, dissolution, and mineral trapping. These mechanisms are subject to the geological and Petro-physical properties of the saline reservoir, and directly influence the injectivity of carbon dioxide, storage capacity, and its long-term confinement. Figure 1.0 displays the relationship between the different trapping mechanisms and the interdependency.

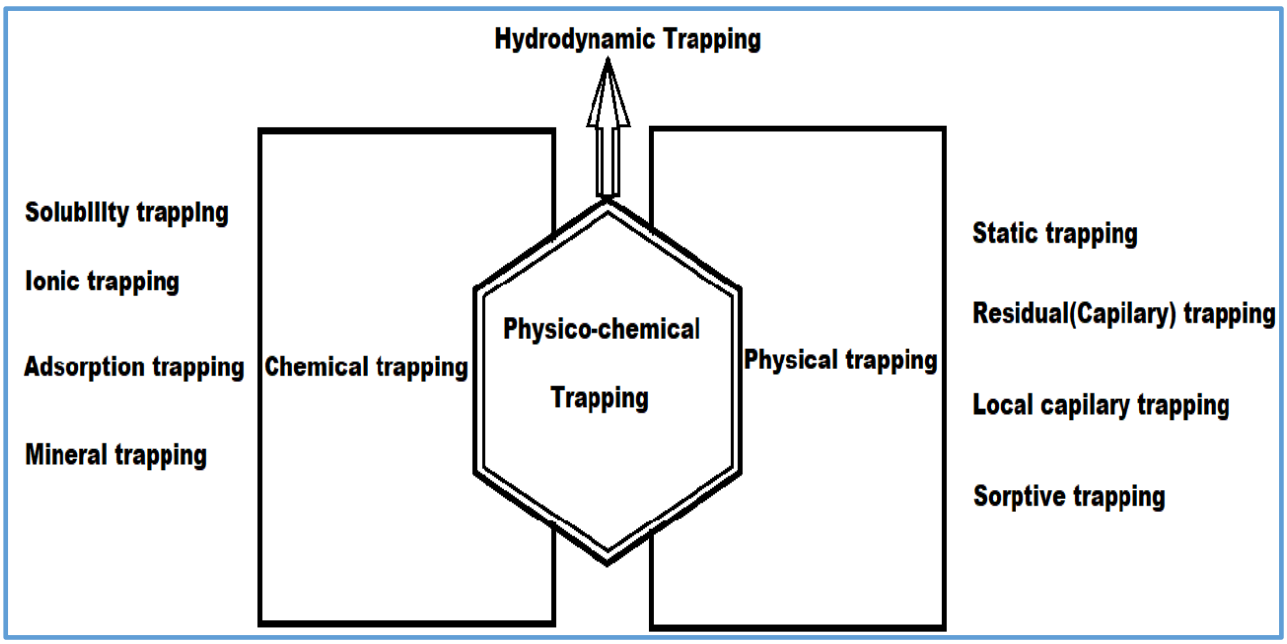

Figure 1-1: Detailed matrix of carbon dioxide rapping mechanisms in saline aquifer. Adapted from *(Al Hameli 2022)*.

1.3.1. Physical trapping mechanisms

Physical trapping involves processes whereby the carbon dioxide retains its physical properties after injection into the saline aquifer. Physical trapping can occur at two main stages: in the reservoir, during the up-dip migrations before the carbon dioxide plume reaches the cap rock, and those associated with the cap rock at the top of the reservoir. Physical trapping methods include structural or static trapping, residual or capillary trapping, local capillary trapping, and sorption.

Structural trapping

This is the most common trapping mechanism, and usually, it initiates the trapping process. It is similar to the systems that have trapped oil and gas in subsurface geological formations for millions of years until their discovery. Examples include anticlines overlain by shallow permeability cap rocks (seal units), faults, and other planar stratigraphic configuration units (figure 1-1). Buoyancy forces resulting from the difference in fluid densities drive the migration of carbon dioxide (Hesse and Woods, 2010). This requires a depth and temperature range that will maintain the supper critical state of the injected carbon dioxide, facilitating

gravity override of the less dense phase (sc CO_2) at the top of the aquifer, where it is eventually trapped under a sealing layer, e.g., mud or clay stones. Retaining supercritical state of the injected CO_2 requires ambient reservoir temperatures that are above the CO_2 critical point (31 ^{0}C and 73.8 bar) (Ringrose 2020).

Storage in this form can remain intact for thousands of years; unless the plume encounter a damaged region or fracture through which leakage can occur. Leakage can also occur along existing boreholes open in the reservoir, a phenomenon expected in basins previously explored for oil and gas resources.

Residual trapping (Capillary trapping)

Residual trapping is considered a key mechanism for trapping carbon dioxide in short terms, during the early injection phase of a sequestration project (Iglauer et al., 2016; Rahman and Iglauer, 2016). Residual trapping happens when the carbon dioxide is held in place by capillary forces due to the interaction of carbon dioxide and reservoir brine. Once injection stops, the wetting phase (brine) capillarity displaces carbon dioxide, as reservoir brines from nearby formations rocks reoccupy pores spaces where carbon dioxide had already occupied, a process called imbibition (Bachu, 2013). This causes a high carbon dioxide saturation cluster to develop, and eventually become detached, isolated, and locked in immobile phases, generally referred to in the literature as snap-off (Figure 1-2). Immobility is enhanced by the high entry pressure of the non-wetting carbon dioxide phase due to its high surface tension, which limits the further expansion of the carbon dioxide phase within the reservoir (Saadatpoor et al., 2010). This mechanism is called residual trapping.

In depleted oil and gas and saline reservoirs, new research outcomes suggest that a reservoir's storage capacity and performance are highly proportional to the residual gas concentration (Raza et al., 2018). This has to do with the wettability of the reservoir, i.e., CO_2 wet or water wet reservoir. A substantial water-wet reservoir will absorb and immobilize more CO_2 in the short term than a CO_2-wet reservoir.

Further research highlights that residual trapping can significantly limit the mobile phase displacement of injected carbon dioxide. As a result, residual trapping is vital in the capacity and security of commercial-scale geological sequestration. Non-localities in the capillary entry pressure of different reservoir rocks can also affect capillary trapping. In addition, further

research (Niu and Krevor, 2020) highlights the invariant response of the initial residual trapping curve with a range of pressure, temperature, and salinity conditions, making it a suitable consideration for the design of the much-need subsurface geoengineering CCS infrastructure.

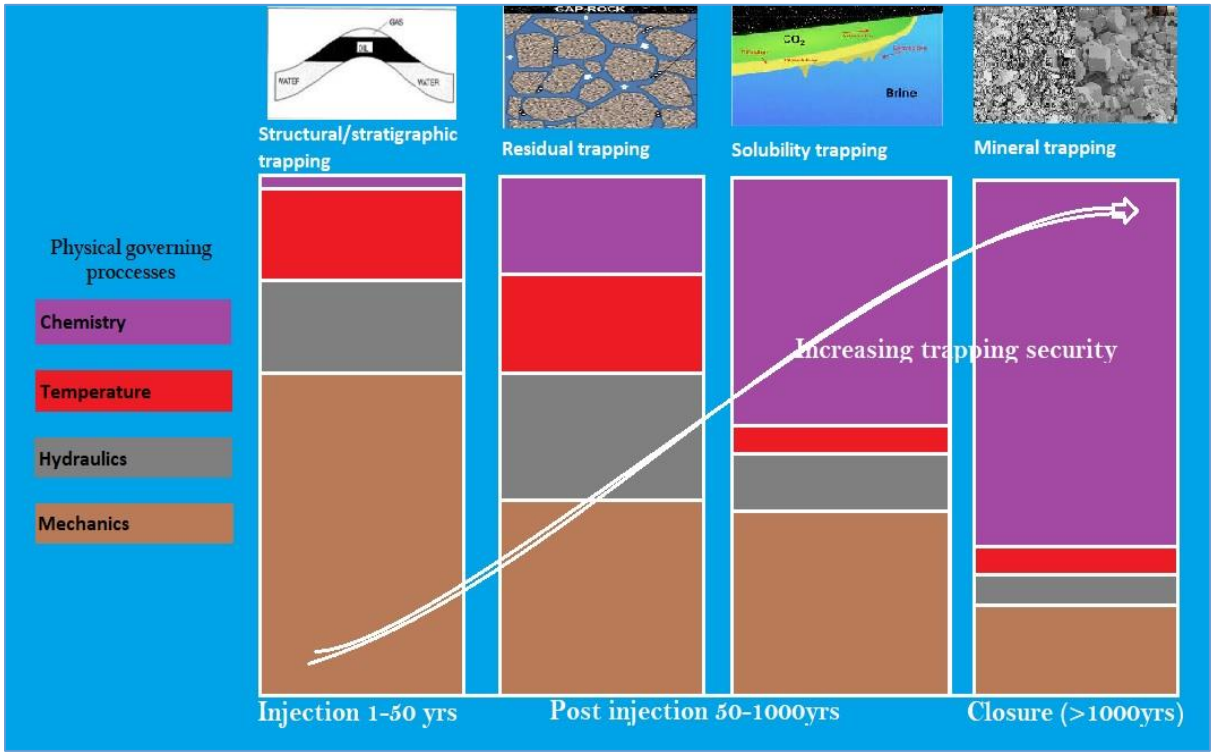

Figure 1-2: Common trapping mechanisms in deep saline aquifers and time scales in deep saline aquifers as modified from *(Metz, 2005).*

Local capillary trapping

This type of trapping is associated with pore-scale reservoir heterogeneity. It is buoyancy-driven and enabled by spatial variability in aquifer permeability and capillary entry pressure (Ren 2018). Studies show that CO_2 saturation trapped by local capillarity exceeds contributions by residual trapping, making it a viable trapping mechanism worth exploiting (Saadatpoor, 2010).

Sorptive trapping.

Unlike residual and capillary trapping, which depends on fluid saturation and reservoir permeability, sorption depends on the fluid's physical parameters, i.e., volume and density. Weak attractive forces absorb carbon dioxide into available pore space. This implies that the amount of pore space available for sorption is limited for a reservoir receiving carbon dioxide through injection. Based on gravitational mass attraction, the adsorbed phase density would

likely be greater than the free bulk phase density. As a result, only a part of the carbon dioxide, i.e., the adsorbed phase, will result in reservoir pressurization, thereby increasing the storage capacity. However, neutron diffraction spectroscopy (Rother et al., 2013) showed that a given adsorbed carbon dioxide average density would occupy more volume space than the average density of bulk carbon dioxide.

1.3.2. Chemical trapping

Chemical trapping is the outcome of permanent changes to the physical and chemical properties of the injected carbon dioxide. This happens when the carbon dioxide geochemically reacts with the brine and reservoir rock constituents. It ceases to exist as a distinct phase, neither mobile nor immobile, a well-suited requirement for long-term permanent storage in the sub-surface. Chemical trapping can result from several mechanisms: dissolution, ionic, adsorption, and mineral trapping.

Solubility trapping

Due to gravity override, carbon dioxide forms a distinct mobile phase at the top of the formation, overlain by the cap rock. Over time, there is mass exchange between the two fluids through the process of intermolecular diffusion and dissolution. This creates a less buoyant CO_2-rich brine interphase over time. Over time, the interface becomes denser than the surrounding fluids due to mass transfer until the systems attain equilibrium. Eventually, the CO_2-saturated regions eventually become detached and drop under gravity toward the bottom of the reservoir, forming cumulous sequences of securely trapped carbon dioxide. The forward reactions $(Equations\ 1.0)$ of carbon dioxide dissolution in brine is a prolonged process (millions of years) and decreases with an increase in brine salinity and temperature (Lindeberg and Wessel-Berg, 1997; Al-Khdheeawi et al., 2018).

$$CO_{2(aq)} + H_2O \leftrightarrow H^+ + HCO_3^- \quad 1.0$$

$$Ca^{2+} + CO_{2(aq)} + H_2O \leftrightarrow H^+ + CaHCO_{3(aq)} \quad 1.1$$

$$Na^+ + CO_{2(aq)} + H_2O \leftrightarrow H^+ + NaHCO_{3(aq)} \quad 1.2$$

$$Mg^{2+} + 2CO_{2(aq)} + 2H_2O \leftrightarrow 2H^+ + Mg(HCO_{3(aq)})_{2(aq)} \quad 1.3$$

Mineral trapping

Mineral trapping usually precedes solubility trapping and is considered the most permanent form of carbon dioxide storage in saline aquifers. It involves the geochemical reaction of carbon dioxide with formation mineral cations to form calcite. Depending on the mineralogical makeup of the formation, CO2 in solution forms different bicarbonate ions, which precipitate out of solution (Equation 1.4). Mineral trapping depends on the mineralogical signature of the formation, reservoir temperature and pressure, and porosity geohydrology of the sedimentary lithology. Mineral salt precipitation because of mineral trapping can significantly change the permeability and porosity of the formation (Xu and Pruess, 2003).

$$3K - feldsper + 2CO_{2(aq)} + 2H_2O \leftrightarrow Muscovite + 6Quartz + 2K^{2+} + HCO_3^- \quad 1.4$$

$$Ca^{2+} + CO_{2(aq)} + H_2O \leftrightarrow 2H^+ + calcite \quad 1.5$$

The potential of geochemical trapping during carbon capture and storage can be determined through geochemical modelling.

Ionic trapping

During ionic trapping, carbon dioxide reacts with reservoir species to form carbonate ions such as HCO_3^- and CO_3^{2-}. this process is relatively faster than solubility trapping and slower than mineral trapping and predominant is reservoirs containing abundant dolomite and calcite. The ionic species reacts with a carbonate mineral to yield calcite in aqueous form and two molecules of carbon-bearing ionic species (Raistrick et al., 2006). The total carbon consumed in the reaction is donated by both injected carbon dioxide and carbonate minerals in equal proportions.

$$H_2O + CaCO_3 + Ca^{2+} \leftrightarrow 2HCO_3^- \quad 2.6$$

1.3.3. Physiochemical trapping

Physiochemical trapping refers to the synchronous involvement of both physical and chemical trapping along the injected carbon dioxide migration route. The interaction of these processes is referred to as hydrodynamic trapping.

Hydrodynamic trapping

Hydrodynamic trapping broadly refers to all time-dependent processes involved with the migration of carbon dioxide from the near-well regions to the top of the reservoir, where it meets the sealed unit. Generally, when carbon dioxide is injected into a saline aquifer, the density difference with formation fluids results in buoyancy, which drives the plume to migrate until it meets a vertically impenetrable barrier, the seal unit. It then migrates laterally along the cap rock as a distinct phase (Bachu, 1994). Over time, one or several trapping mechanisms involve residual trapping because of capillarity or structural and stratigraphic trapping associated with the sealing layer. The time it takes for carbon dioxide to migrate to the top of the formations depends on the reservoir thickness and is typically measured in millions of years.

The process is more effective in sedimentary basins that are laterally unconfined, but characterized by large-scale flow in low-permeability media. In addition, the conductivities and location of fractures play an essential role in their effects on CO_2 migration. Sedimentary systems with limited vertical and lateral migration due to confining structures such as low permeable bounding faults and seals are less suited for carbon dioxide storage. In such geological architectures, pore pressure builds up rapidly in the near Well region, which dramatically limits the storage capacity of the saline formation (Oruganti and Bryant, 2009). Pore pressurization can significantly perturb the in-situ reservoir stress state resulting in geomechanical damage to the cap rock (reactivating existing fault) (Wang et al., 2022). This will compromise the hydraulic integrity of the reservoir with the risk of brine and carbon dioxide leakage, which could have far-reaching implications for overlying sensitive environments such as shallow groundwater aquifers (Zhou et al., 2010). Further studies suggest that permeable faults promote dissolution trapping at the expense of residual trapping. Less permeable faults will enhance dissolution for reservoirs with low gravitational potential.

Trapping mechanisms are essential in the storage capacity estimates for CCS deployment. Multiple mechanisms can simultaneously store carbon dioxide at any given point and time during its migration journey from the injection well. Their interactions can be complex, ranging across different time and length scales and affected by reservoir heterogeneities. (Figure 1-2) presents a time evolution for different trapping mechanisms in saline aquifers.

When CO_2 is captured and separated from flue gas, the geological sequestration is completed through a class VI injection well open in a saline aquifer. Class VI I ejection wells are specially designed to protect public health and protect shallow underground sources for clean water abstraction. After injection, CO_2 migrates away from the Well position, displacing formation water and resulting in reservoir pressurization, with plume fronts far beyond the size of the actual CO_2 mobile phase and has both near and far field implications.

Also by comparison, CO_2 on average is five times less dens than the formation brine, so it migrates vertically up dip due to buoyancy. This continues until the mobile plume encounters a low permeability caprock unit below which it is trapped and maintains a horizontal flow marking the unset of structural trapping. Other accompanying mechanisms throughout the storage lifetime include residual trapping, dissolution, and mineral trapping. Brine migration under transient pressure buildup can negatively affect nearby sensitive environments such as shallow freshwater aquifers. Further pressure buildup due to pore expansion and fluid compression can also compromise the reservoir's hydraulic integrity where the pressure gradient overcomes in situ stress, causing the rock's failure limits to yield. This can result in micro-seismicity and the development of localized pathways for anomalous fluid leakage from the storage room. The geo-mechanical rock properties of the storage media constrain this coupled hydromechanical problem.

1.3. Problem statement

The era for conspiracy in climate change related issues is over, today, its impacts are apparent (switch on your TV or local news channels), and not a day goes without reports or coverage of unexpected changing weather patterns, increasingly posing a serious threat to ecosystems. Implementing CCS in saline aquifers provides a window of transition from a carbon-based economy to that with a less intensive fossil dependence. Often located at least 1 km below the surface, only so much is understood about their behavior under induced stresses. Understanding and managing pressure buildup due to CO_2 injection is the main pillar on which Commercial scale deployment will depend. Delays in its implementation will only increase future mitigation cost. Therefore, against this bearing, I have answered the call, and through this thesis, I have contributed by developing a computational framework for modelling the various multi-physics, which are relevant for predicting pressure buildup due to Geological Carbon Sequestration (GCS).

1.4. Aim and Objectives

The aim of this thesis is to develop new numerical models to predict the pressure buildup in a saline aquifer during injection through a vertical well. To reach this arching goal, the following are a set of guiding objectives:

- To carry out detailed literature review of CCS and state of modelling
- Model and simulate pressure build-up using non-local and local operators.
    - Delta Dirac
    - Caputo power derivative
    - Caputo Fabrizio exponential law with weak cross over
    - ABC derivative, with strong cross over from Gaussian to non-Gaussian flow
- Model pressure build-up using fractional-stochastic operators.
    - Delta Dirac – Stochastic
    - ABC - Stochastic
- Model the two-phase fractional flow.

Chapter 2 reviews the most relevant literature on pressure buildup modelling and geomechanical implications of CO_2 injection. The literature review covers available work on resource estimation, trap mechanisms and geomechanics.

Chapter 3 presents new numerical models to predict bottom hole and reservoir pressure buildup using the classical delta Dirac differential operator. The initial and all boundary conditions used in the rest of the thesis are established and reservoir characterization in the context of CO_2 saturation is laid out.

Chapter 4 presents numerical models to predict bottom hole and reservoir pressure buildup using the Caputo fractional derivative, with power law behavior. The fractional derivative and its associated integral are used to introduce the effect of long tail dependence to the classical pressure diffusivity model.

Chapter 5 presents a new numerical solution to model pressure buildup using the Caputo-Fabrizio fractional derivative with exponential law kernel. The fractional derivative and associated numerical approximations are used to extend the PDE's that model pressure are extended to the rea of fractional calculus.

Chapter 6 models pressure build-up using the generalized Mittag-Leffler function via the Atangana Baleaunu derivative with strong crossover from Gaussian to non-Gaussian.

Chapter 7 extends the fractional deterministic pressure diffusivity model to the stochastic frame of reference by introducing random walk. Important statistical distributions are discussed and the results are reported in the context of uncertainty associated with the CO_2 injection problem.

Chapter 8 presents a numerical solution to model saturation evolution in the two-phase immiscible flow region. Models are developed based on both classical and non-local operators while numerical discretisation was complete with both finite volume and finite difference schemes.

Chapter 9 summarises the conclusion of this research and outlines recommendations for the future research.

CHAPTER TWO: GEOLOGICAL STORAGE AND CO2 EMISSIONS MITIGATION-A LITERATURE REVIEW

2.1. Introduction

The past decades are on record for soaring atmospheric CO_2 concentrations. Carbon dioxide emissions have risen since the onset of industrialization. Even though the COVID-19 pandemic in 2019 caused this trend to plummet by a five percent margin, global emissions in 2020 totaled 34.81 billion tons, up from 25.23 billion tons in the year 2000. Studies on current trends (Li et al., 2023) Confirm that emissions continue to grow exponentially, totaling 36.4 billion tons in 2022. New data suggest worsening implications over time as the effects of climate change are hitting the planet faster than predictions.

CCS in saline aquifers is contemplated as a viable means to offset the trend, and widespread research efforts affirm their potential as long-term permanent storage. While these reservoirs are globally distributed and suitable for large-scale CO_2 injection, there are plenty of risks worth addressing before the technology can be scaled. One primary concern is reservoir pressurization caused by fluid displacement, especially in closed saline aquifers (Zhou et al., 2008). CO_2 storage is a coupled poro-geo-hydro-mechanic phenomenon, an active transdisciplinary research avenue for science, engineering, and policy experts. Injection of fluids in the subsurface as means of storage or waste disposal is not new. Nuclear waste and wastewater injection for storage (Oberdorfer et al., 1985; Kim et al., 2011), geothermal energy research (Liu ey al., 2019), oil and gas recover (EOR), and artificial groundwater recharge have long benefitted from the existing technical underpinnings.

The buildup up of reservoir pressure during CO_2 injection has plenty implication on the integrity of the storage structure. Monitoring data or theoretical predictions are two ways to solve the problem. In the latter option, pressure diffusivity equations are developed on Darcy's law (Meite et al., 2022). These equations are formulated as differential equations, and solutions can be obtained for different boundary conditions and parameters. Other solutions and methodological approaches are widespread in the literature for examples artificial intelligence-based modelling (Hosseini et al., 2020), and even though solutions have been successfully used to model the flow

mechanics of a comprehensive set of porous media problems, there are some limitations. The most predominantly raised issues are the simplifying assumptions used during the model formulation.

This is subdivided into two parts. Firstly, the background issues related to global warming and climate change are discussed. This includes average emission rates, trends, and future projections, while the potential contributions through CCS deployment are presented. Further, a general overview of CCS is presented (capture, transport, and injection) in which context, types of storage formation, their respective capacities, and trapping mechanisms are discussed. The second part of the chapter is dedicated to the issue of pressure buildup within the reservoir due to CO_2 injection. Firstly, the geomechanical basis of fluid-rock interaction encompasses the concept of hydraulic pressurization, and the factors that constrain rock failure due to hydraulic action are discussed. Secondly, the idea of risks and pressure management during CCS numerical modelling and a mention of simulation codes are presented. The equations of mass balance, which underpin various numerical schemes that can be used to model CO_2 migration and pressure buildup in the subsurface, are discussed. This is followed by discussing important distributions and numerical approximation methods used to condition the modelled solutions. In the final part, the concept of reservoir disorder and heterogeneity is discussed by introducing the concept of fractional calculus.

2.2. Global warming, climate change, and fossil fuels

The systems that maintain our current global ecological balance, necessary for survival and adaptation on Earth are under increasing stresses due to climate change. This is predominantly associated to the increase in production of anthropogenic CO_2, a chemical product of fossil fuel combustion for power generation (See Figure 1). Many researchers postulate that this trend will not only continue to rise but is likely to cause irreversible consequences if business continuous as usual (Knorr et al., 2009; Yu et al., 2019; Ding et al., 2020). Changes in the atmospheric concentration of CO_2 entered a new phase since the early 1960, a well-known marker that represent the unset of Industrial Age. So far, concentrations of CO_2 in the atmosphere have steadily increased from 315 ppm when the first direct measurements were performed by Charles Keeling in 1962 to 420 ppm currently (January, 2023; Huppert & Neufeld, 2014). Today, 40 Gt of

CO_2 are emitted annually, up from 32 Gt tons in January 2013, a trend confirmed by changes in the isotopic ratios of carbon (Carbon-13) over time (Alan, 2019). Closely linked to the atmospheric CO_2 concentration trend is the global average temperature change, a key variable used to evaluate climatic variability Figure 1. The global surface temperature has ranged from approximately 9°C cooler than the current readings to 6°C warmer (Luthi et al., 2008; Nielsen-Englyst et al., 2023). The temperature graph generally shows a noisier characterestics than that of CO_2 concentration as a function of time.

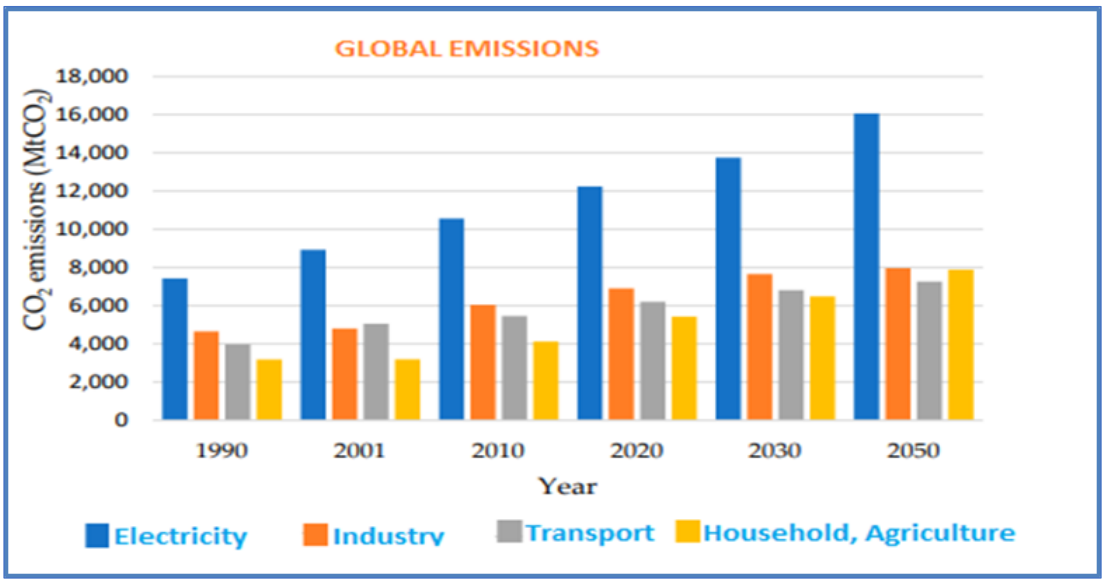

Figure 2-1: Global CO2 emissions per sector (Adapted from the worldwide energy outlook-2050)

Carbon capture and storage involves a combination of technologies that integrate the capture and compression of CO_2 from point sources such as coal fired power plants, cement factories and fertilizer production factories just to name a few, transportation along pipelines, injection, and decommissioning. Based on the fundamental concepts that underpin the injection and migration of CO_2 underground, three types of geological environments are found to be suitable for this undertaking: deep brine formations, depleted oil and gas reservoirs and un-mineable coal formations. Carbonate formations also show great potential in absorbing injected CO_2 however, both data and three principal storage/trap mechanisms identified include structural trapping, dissolution trapping, residual trapping, and chemical trapping. More scientific literature on the trapping mechanisms is available from (Koide et al., 1995, Johnson, 2004; Han et al., 2010),

(Shukla et al. 2016). The more dominant mechanisms depend of the type of geologic formation considered. For example, in saline aquifers, disolution/solubility trapping is the dominant mechanism and is responsible for the long term and permanent storage of a large volume of the sequestered CO_2 (Neufeld, 2010; Yang 2014; Soltanian, 2017). This mechanism generally occurs during the active injection phase of a project, slowing down plume migration thereby increasing storage capacity. The long term security of any injection project is important to stake holders and the public, which can be achieved thorugh understanding the multiphysics of plume scale processes, such as the mass transfer taking place between super critical CO_2 and the native brine in the formation. This is essential to assess storage capcity estimates, retention effectiveness and safety. Also needed are methods to characterize reservoirs for their suitability and to establish baselines to monitor plume migration and changing geomechanical properties.

Future predictions suggest that global sea level rise could reach 7-36 cm by 2050 and 9-69 cm by 2080.

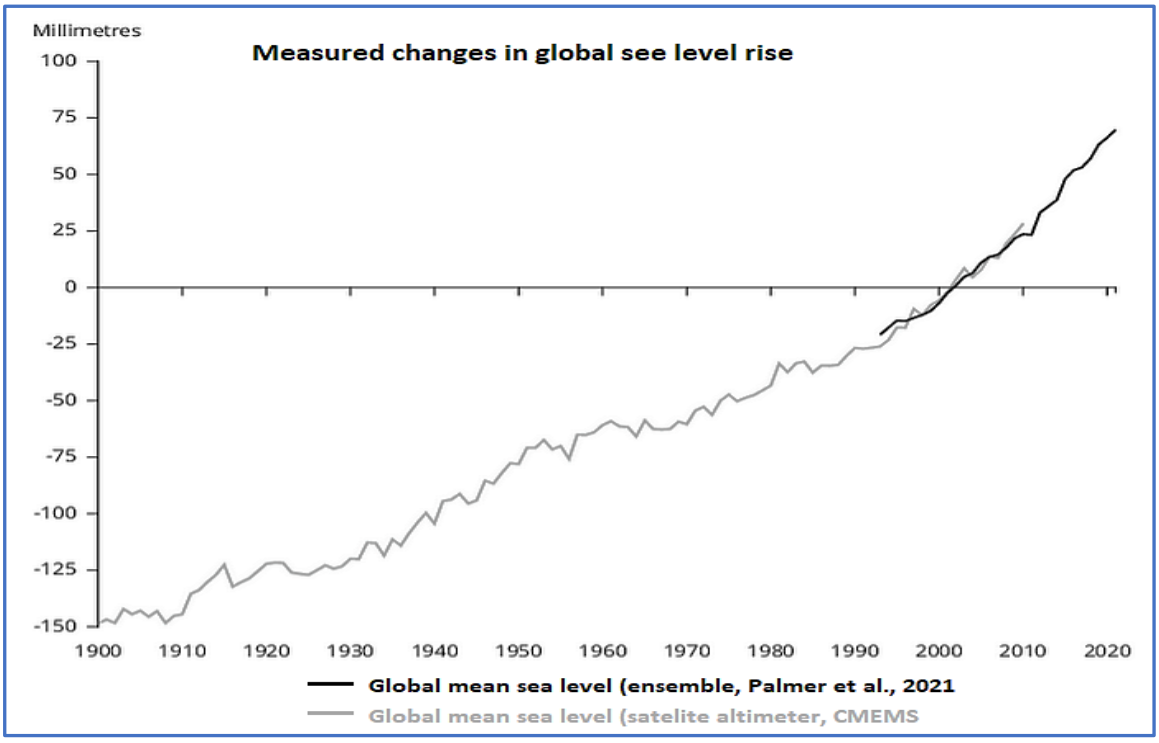

Figure 2-2: Graph of measured mean sea level change (adapted from Invalid source specified.)

Regardless of the mounting impacts of climate change, the fact remains that fossil fuels will continue to serve the coming decades as a primary source of energy. According to the International Energy Agency (IEA), fossil fuels comprise about 80% of the global energy mix while providing the fundamental energy needs of a functional society. The remaining 20% is supplied by hydropower, atomic and diverse sources of renewables such as solar, hydrothermal, wind, and biomass) (Figure 2-2). If the energy-economy paradigm continues as usual, the effects of global warming could cause irreversible impacts on the world's climate and ecological balance.

In this context, there is a need for remedial action to limit the amount of carbon dioxide sunk into the atmosphere. This aligns with the Paris Climate Accords of 2015, whose target is to bring the world closer to a safer climate trajectory by keeping the global temperature increase below 1.5 ^{0}C of pre-industrial levels (Hestres, 2018). This requires a transformed energy sector in ways the world generates and consumes energy. Carbon Capture and Storage (CCS) is the most advanced/mature innovation in this attempt to combat CO_2 emissions. It involves the isolation of carbon dioxide, captured at industrial and power plants, and its permanent storage for large time scales. Current storage approaches include injection into coal steams, depleted oil fields, and, most importantly, deep saline aquifers, which offer the most storage capacity of all repositories currently considered. They are globally widespread with well-suited permeability and residual saturation for this application suitability of saline reservoirs for CO_2 storage (Kopp and Class, 2009; Donda and Volpi, 2011).

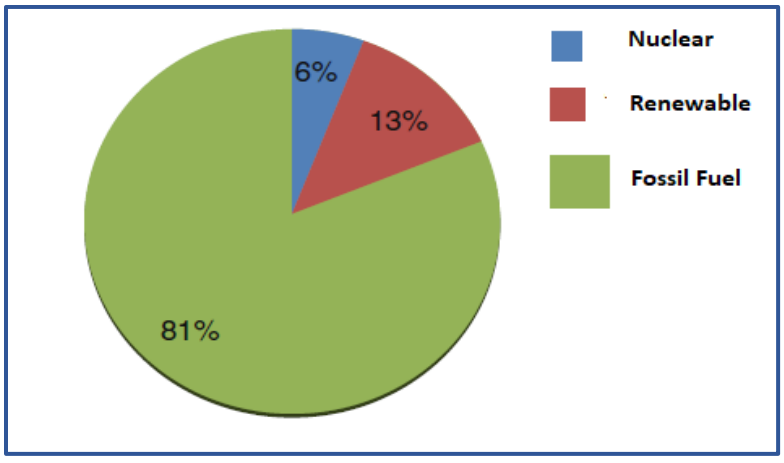

Figure 2-3: World energy supply by source (Jain and Singh, 2016)

Additionally, global trends such as natural resource depletion and geopolitical instability, including the recent Russian invasion of Ukraine, have negatively affected climate change adaptation, both locally and globally (Barchielli et al., 2022). This includes the hampering of the global economic recovery from the COVID-19 pandemic, which creates an overlap in the crisis that direly needs solutions, including food shortages and soaring energy and commodity prices. The levels of such stresses and the different fears of the 21st century have highly biased impacts on populations from other parts of the world, with long-lasting physical and psychological implications. For example, Sub-Saharan Africa, which only contributes a microscopic portion to global emissions, tends to suffer disproportionately from the impacts of climate change. This is because the leading economic growth prospects rely on agriculture, which is heavily dependent on rain. With this region accounting for over one-fifth of the global population, the consequences of climate change, such as frequent droughts, flooding, and vanishing groundwater resources, have dislocated close to 100 million people living under conditions of extreme poverty. This leads to high migration rates from rural to urban areas, which are often already crowded and must be equipped to sustain the growing population influxes (Saghir and Santoro, 2018) (Barchielli et al., 2022).

2.3. Global warming mitigation and Geologic storage

The Energy – Carbon – Economy triad is at the centre of the global marketplace. The pursuit of better living standards as a means of survival and adaptation has led to the expansion of these systems and, by so doing, caused carbon emissions to rise exponentially. According to monitored data from various sources, pre-industrial concentration was 280 parts per million (ppm), and today, the current levels are closely approximated at 420 ppm (IPCC, 2020). As of 2020, the atmosphere had a maximum CO_2 uptake budget of three hundred and thirty billion tons (330 BnT). Beyond this, the impacts of global warming would become more pervasive and irreversible. To solve this problem, a handful of models support the view that a portfolio of tested technologies already exists, which, if scaled and timely implemented, can serve as stabilization wedges to keep emissions and global warming under check (Pacala and Socolo, 2004). However, maintaining the atmospheric carbon emission concentration below the 330 BnT mark seems very unlikely without directly removing CO_2 from the atmosphere. This argument is against our

projected future fossil fuels dependence (Lipponen et al., 2017), famously reflected in the Kaya identity. This equation $(equation\ 2.0)$ relates the total carbon dioxide emission levels to the product of four factors: population, GDP per capita, energy intensity, and carbon emission intensity) (Kaya et al., 1997).

$$CO_2{}^{\uparrow} = POP \times \frac{GDP}{POP} \times \frac{BTU}{GDP} \times \frac{CO_2}{BTU} - CO_{2\downarrow} \qquad 2.0$$

In the above expression, $CO_2{}^{\uparrow}$ is the global atmospheric Carbon dioxide emissions, POP stands for the population level, BTU/GDP is gross domestic product per capita. It measure's the standard of living; BTU/GDP is a standard of energy consumption or the intensity of energy consumption CO_2/BTU is the quantity of carbon dioxide released due to unit of energy consumed (also called the carbon intensity and CO_2 is the amount of CO_2 stored or isolated from the atmosphere.

Given the current state of affairs, the world's population will not stop growing any time soon, such that decreasing energy intensity of carbon intensity levels will require a significant amount of inputs in the form of research, innovation, and a complete overhaul of the power infrastructure as they are today. Hence, the role of carbon capture and storage in states such as dissolved carbon in the ocean, subsurface rock formations, terrestrial biomass, as a fluid in deep geologic structures (traps), or as mineral carbonates. Over the past few decades, this has become less of an option and more of an urgent call to action.

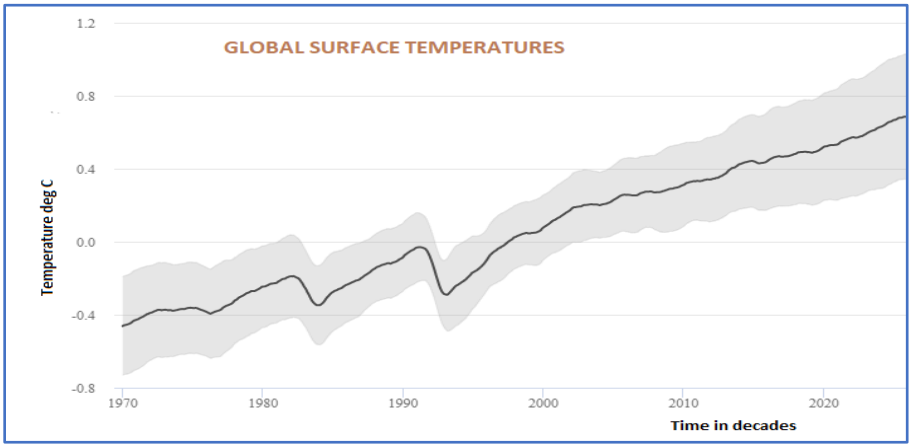

Figure 2-4: Global surface temperature trend between 1970 and 2022 averaged over 12-month periods.

Various scenario analysis seem to suggest that CCS is a critical technology, well aligned with the Paris climate agenda (Peters and Sognnaes, 2019). Commitment to its large-scale deployments remains an issue of political debates for interested nations who are still having hopes on the conventional climate policies. However, according to the IPCC special report on 1.5 degrees Celsius, the cost of emissions reduction without CCS will more than double compared to a scenario when it is fully deployed (IEA, 2017). Geologic sequestration uses direct air capture technologies capable of harvesting large volumes of CO2 for permanent storage in deep underground geological formations. This will allow the carbon-intensive industry to remain competitive and innovative, a crucial driver for the much-needed transition toward cleaner energy technologies (Huaman et al., 2014). Results from the possible future scenarios predictions suggest that CCS is an essential approach to decarbonizing heavy point source emmiters, traditionally considered hard to abate such as Ceemet, steel and power production.

2.4. Components of a Carbon Capture Storage system.

The CCS systems consist of a multitude of components that together work as a bridging technology to keep point-sourced carbon dioxide from reaching the atmosphere. The main components play a unique role: i) a capture facility to separate and compress the carbon dioxide, ii) a pipeline system to transport, iii) a deep borehole to inject the captured carbon dioxide into a suitable reservoir for long-term and permanent storage and a final component which is associated with monitoring the migration of carbon dioxide underground. An exhaustive description of the different components has been reviewed in many texts (Hildebrand & Herzog, 2009; Dowd et al., 2014; Kheshgi et al., 2018). The injected CO_2 is first captured from the base outlet of a power plant as flue gas, compressed, and transported through pipelines to the designated site. A borehole opened in a suitable geological formation is the means of injection.

2.4.1. Capture

Cryogenic separation, adsorption/abstraction, and membrane separation are the capture mechanisms. The approaches used significantly impact the eventual isolation process, i.e., transport and storage. The capture, separation, and compression are the more costly aspects of this value chain since it requires capital-intensive inputs to modify existing plants or redesign

traditional engineering blueprints. This significantly raises the cost of energy produced; however, for CO_2 to make a meaningful contribution, it must be deployed at scale, which requires technological maturity to ascertain effectiveness, usability, and implementation of legal and regulatory frameworks when it is transferable to developing nations. The amount of carbon dioxide that can be permanently stored in the designated geological formations (Rubin & De Coninck, 2005), hence the reservoir's storage capacity, is evaluated in context with the quality of the CO_2 stream and the storage potential of the porous formation. The difference between the point source volumes and the final injection volumes is not only a function of the captured amounts but also dependent on the separation efficiency, transport, and integrity of the store room. The latter is essential to prevent leakage once the carbon dioxide is injected (Aydin et al., 2010).

Three technical pathways may be followed to capture CO_2 from coal power points: post-combustion capture, oxy-combustion, and pre-combustion capture. The method used for capture depends on several criteria, some of which include: The carbon dioxide concentration in the flue gas stream, the pressure gradient in the gas stream, and; the fuel type

2.4.1.1. Post-combustion capture

This involves using a chemical absorbent, e.g., monoethanolamine, to treat the combusted flue gas. For today's coal-powered plants that use air with 80% N_2 for combustion, the technique consumes roughly ¼ of the net steam produced by the plant to generate a flue gas with a 4% to 14% CO_2 content. Thermodynamically speaking, more energy will be required to capture CO_2 at a partial pressure below 0.15 atm (Bounaceur et al., 2006). Parametric studies determine operational limits needed to obtain the required CO_2/N_2 recovery ratio. The method produces an almost pure CO_2 stream even though high input capital and large size are typical limitations encountered.

2.4.1.2. Oxy-fuel combustion

This process involves combusting the gas in an oxygen-rich environment, avoiding NO_2 formation. The gas leaving the chamber is 90% CO_2 after the SO_2 is removed (Zheng, 2011). However, further cleaning is typically required to scrub off other constituents to bring the purity to levels of the compressed gas in line with CO_2 composition.

The main setback is the low SOx requirement for the gas coming from the burner. The technique requires materials of high heat resistance. The main advantage is that no solvent is needed, and the small physical size of the module makes it easy to retrofit existing plants.

2.4.1.3. Pre-combustion capture

This process combines oxygen, air, and steam in a reaction chamber, as shown in the equation below.

$$\boldsymbol{CO + H_2O \leftrightarrow CO_2 + H_2}$$

Under the appropriate conditions of reduced temperature, CO_2 capture is possible. Calibrating to the right molar amounts of each constituent is the main challenge with this process. Despite these hurdles, pre-combustion is a relatively cheaper approach than post-combustion capture. Integrated gasification combined circles based on pre-combustion are the most efficient setups relative to pulverized coal-fired plants and hence most suited for the new systems. The discussed components are set to vary depending on the scale and purpose of the project. While each element is tasked to fulfil a specific task (capture, transport, or injection and monitoring), it is recognized that multiple wells will be used for injecting carbon dioxide into a single reservoir. In such a case, the reservoir will receive multiple carbon dioxide streams through a hub, servicing multiple point sources across a designated industrial region. In this context, the carbon dioxide loaded into pipelines should meet a minimum specification standard which usually has implications on the design of transport lines and storage efficiency in the subsurface (Harkin et al., 2017).

2.4.2. Transport

Carbon dioxide transport is achieved utilizing existing pipelines or ships. However, regional infrastructure might need to be developed to meet the scales of future needs. The presence of impurities such as nitrogen, oxygen, and sulfides due to diverse sources of CO_2 and the different capture techniques may affect the cost of transportation. To avoid the cost of over-compression for dry CO_2 transport, purity standards might be required for pipeline operations.

2.4.3 Geological Storage

In this section, we discuss three crucial options (coal seams, saline aquifers, and depleted oil and gas formations) considered for the potential storage of CO_2 in subsurface buildings. To maintain low levels of CO_2 from reaching the atmosphere, it will require that cumulative injection rates reach 10 Gt CO_2 per year by 2050, with more than 1000 Gt in total to be safely stored by the end of this century. This anticipated ramp-up in scale will require thousands of sites to operate under total/optimal capacity, each receiving a flow rate between 1 and 5 Mt/year. The pressure magnitudes associated with such volumes are enormous, and monitoring its buildup is needed for CCS to become commercially viable. Table 1 presents categories of geological formations identified as suitable options that volumetrically offer the most considerable storage resources potential.

table 1: global potentials and reservoir capacity for co2 storage

Geological sequestration options	Storage Capacity	Experimental location
Ocean	1000-10,000 +GtC	Isle of man, Hawaii
Depleted oil and gas reservoirs	100-1000 GtC	USA, Canada, Australia
CO2-EOR	61-123 GtC	China-Jilin reserve
Coal seams	10-1000 GtC	USA-Pennsylvania
Organic rich shales	2.5-25 GtC	

2.5. Types of geological reservoirs

2.5.1. Unminable coal seams.

This reference is used for waste coal formations, typically of high sulfur content and too thin or deep to develop for extraction. Coal beds are generally dual porous, consisting of microporosity and macro porosity, associated with pore matrix and cleat networks. These formations are endowed with significant natural gas resources where almost 90% of the gas is trapped and adsorbed in the microporous domain while the rest exists as free gas in the cleat networks. Carbon dioxide sequestration in coal beds makes use of the fact that coal has a lesser chemical affinity for methane than carbon dioxide.

When injected, carbon dioxide migrates by laminar flow along the cleats until it is finally adsorbed at the microspores. During this process, methane gas is displaced and reverses the same route

toward a production well. Carbon dioxide storage in coal seams can be beneficial by increasing the recovery of coal bed methane (CBM) (Li and Fang, 2014). With global CBM reserves estimated at over 2 trillion scm (standard cubic meter)., sequestration in unmineable coal seams can potentially offset the injection cost of carbon dioxide. During this process, changes in the structure of the coal result from the interaction of the coal and the injected fluid, which result in geochemical and physical-thermodynamic changes within the coal formation. Primarily, due to adsorption and desorption, the coal matrix undergoes shrinkage and swell, which directly affects the formation's permeability and, of course, implications to consider on the physical integrity of the reservoir (Zheng et al., 2021).

Permeability variation during the process of Enhanced Coal Bed Methane (ECBM) can play a significant role in the recovery of methane, and different studies have investigated this phenomenon widely. Firstly, the composition of the injected fluid plays an important role; for example, when CO_2 is combined with Nitrogen, the formation permeability is greatly enhanced, leading to higher recovery rates than during the injection of pure CO_2 (Talapatra, 2020).

2.5.2. Depleted oil and gas formations

Carbon dioxide disposal in depleted oil and gas reservoirs is a new concept in the fight against climate. However, the approach has gained tremendous popularity owing to its successful history of containing disposed bi-products of oil and gas exploitation and processing, such as sulfur and acid gas. The approach is motivated by the assumption that disposal in depleted reservoirs is less harmful to the environment than schemes involving treatment and disposal of waste, in which carbon dioxide will make up 90% of the total. Experience with this approach has proven depleted oil and gas reservoirs to be effective and reliable storage rooms for permanently containing carbon dioxide, hydrocarbons, and acid gasses.

2.5.3. Deep Saline formations and ocean storage.

Saline aquifers are geological reservoirs of highly permeable rocks fully saturated with salt-rich water called brines. Compared to the other listed storage modes, saline aquifers are a more significant storage reserve and the most feasible prospectively, with a global storage capacity of up to 10,000 Gt of storage potential. Due to the high difference in density between CO_2 and brine, the transmission currents help to foster the storage dynamics. Several trapping mechanisms are

responsible for the long-term containment of carbon dioxide in saline aquifers: hydrodynamic trapping, residual trapping, and mineral and solubility trapping for their detailed description.

The migration of carbon dioxide in saline aquifers from the near Well region away into the reservoir domain results in a two-phase immiscible flow region. Many factors, including flow behavior, constrain the fate of each developed fluid system, the geomechanical traits of the formations rocks and fluid interaction, geochemical interaction, formation porosity, fluid relative permeabilities, and capillary forces, among others. Saline aquifers became of interest for waste disposal purposes following similar needs in the case of depleted oil and gas reservoirs, i.e., for disposal of sulfur and acid gas in the form of H_2S, both of which are byproducts of oil and gas processing. They will eventually lead to pilot test projects to assess their suitability for storing anthropogenic carbon dioxide. However, the first saline aquifer commercial scale project was set up in 1996: The Sleipner and Snøhvit in Norwegian offshore regions and the In-Salah in Algeria. In total, 15 Mt of captured anthropogenic carbon dioxide were successfully injected between 1996 and 2007. Similar projects included the Gorgon and Nagaoka in Australia and Japan, respectively.

Oceans are currently the most prominent natural sinks, already harboring an estimated 40000 GtC compared to the 750 GtC and 2200 GtC in the atmosphere and terrestrial biosphere. However, any plans to actively inject carbon dioxide into the ocean must first establish a basic understanding of patterning to the interaction of CO2 and seawater. Changes in seawater pH. values due to such attempts are sensitive and require careful consideration.

Storage in saline aquifers requires that CO_2 be compressed to liquid form before transport to injection sites. The recommended injection depth should be greater than 1 km to ensure sufficient cover with multiple trap systems to prevent leakage that would eventually recirculate the captured carbon dioxide back into the atmosphere.

For geological storage to become a full-scale option with the potential to offset emission concentrations, all the discussed storage modes should be deployed commercially**.** Figure 2-5 demonstrate the different geological settings associated with each set.

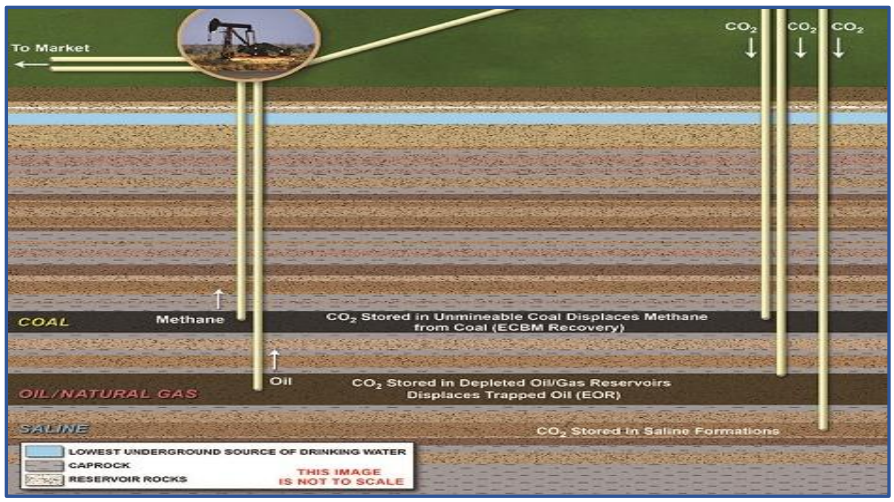

Figure 2-5: Geological storage options for carbon dioxide (Courtesy of National Energy Technology Laboratory)

2.6. Phase behavior of CO2 in Sub-surface

One of the critical goals of geological sequestration in saline aquifers is to optimize the storage reserve in a saline aquifer. A denser and less viscous carbon dioxide means more fluid will be stored in the available pore spaces. This is possible if carbon dioxide is in a supercritical state at the injection time. Therefore, it is preferred that carbon dioxide is first compressed and converted to a supercritical state than its natural gaseous form (Bachu, 2003). According to the tertiary phase model, carbon dioxide is supper critical at the critical point; 30.1 ^{o}C and 7.38 MPa, see (Figure 2.6).

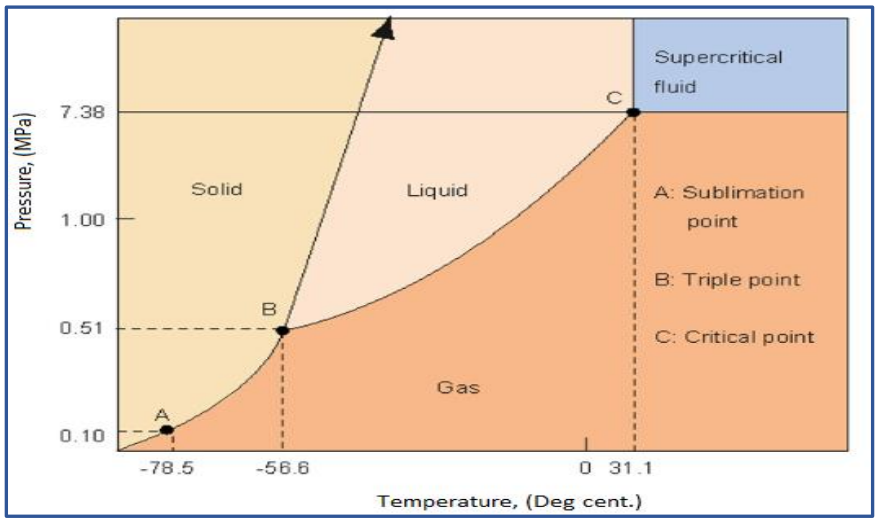

Figure 2-6: Carbon dioxide phase diagram (adapted from IEA, 2008).

Under these conditions, more carbon dioxide is stored in the available pore spaces due to lower viscosity and a corresponding increase in relative permeability with the formation rock matrix (Holloway and van der Straaten, 1995) See (Figure 2-6). Secondly, injecting supercritical carbon dioxide prevents it from separating into liquid and gas phases, promoting a longer resident time. These attributes are essential for storage safety and cost-related issues of the project.

According to the average global geothermal gradient and hydrostatic pressures, supper critical CO_2 forms approximately 800m below the surface, hence the minimum preferred injection depths of 1 km (1000m). At the supper critical state, carbon dioxide is generally less dense than the reservoir brine by an average 70% difference (Bachu and Gunter, 2004), causing a gravity override in which buoyancy forces resolve vertical segregation with carbon dioxide occupying the top and denser brine staying at the bottom. This state is maintained throughout the migration of the plume until the different trapping mechanisms begin to take effect.

2.8. Storage capacity estimation of saline formations

Depending on the needs of an estimate, the storage capacity of a reservoir can be classified into three hierarchies: Theoretical, realistic, and viable (Bachu et al., 2007) The theoretical storage can be seen as a total storage volume that captures the total amount of CO_2 injected into underground formation as a function of the pore volume provided by the pore spaces. On the other hand, realistic storage or specific storage refers to the amount of pore volume used up for CO_2 storage and is only a fraction of the total storage. However, CO_2 injection involves the displacement of reservoir water, hence pressure buildup, which has impacts beyond the plume's confines. The displaced fluid must be accommodated in some form of storage, which many simulation scenarios naively failed to account for, even though pressure buildup a key limiting factors of storage potential. Realistic storage considers reservoir parameters such as permeability, porosity, sealing capacity, hydraulic integrity, and the type of boundary conditions present. In this context, the storage potential of a site should include the total target pore space, the threshold average pressure allowable, and the rock compressibility (van der Meer et al., 2009). The viable storage and realistic and theoretical capacities will include legal, regulatory, social, and environmental constraints.

Storage capacity estimates for CO_2 injection in saline formations are complex. Many research models attempt to develop standardized global and regional assessments have resulted in vastly conflicting results. Geological heterogeneities vary in scale between different formations, such that applying a general technique could result in very unreliable estimates for a specific region.

An essential parameter for storage capacity estimates is storage efficiency: the amount of theoretical storage volume that would effectively accommodate injected CO_2. An accurate procedure to calculate storage estimates will first involve constructing a geological model populated with reservoir parameters and using this data to simulate the potential storage (Kopp and helmig, 2009). Using the residual water saturation of a reservoir and a wide range of reservoir petrophysical parameters, (Bradshaw et al., 2007) presented a formula to calculate the theoretical storage capacity of structural and stratigraphic traps in saline aquifers.

$$V_{CO2t} = V_{trap}.\emptyset(1 - S_{wirr}) = A.h.\emptyset(1 - S_{wirr}) \qquad 2.2$$

Where $V_{CO2t}$the theoretical storage volume (m^3) is, V_{trap} is the volume accounted for by the specific trap (m^3), $\emptyset$ is the reservoir porosity (dimensionless), A is the total surface area of the trap (m^2), S_{wirr} is the irreducible water saturation, and h is the average trap high.

A wide range of methods have been suggested for evaluating the CO_2 storage capacity of saline aquifers, including analytical and numerical techniques. Analytical techniques have received greater attention in this pursuit due to their ease of use, time, and cost-saving attributes. In most cases, rapid storage capacity estimation is required to screen and rank target sites for their suitability for CO_2 storage.

Most of the analytical techniques are based on the mass balance of displaced fluids; (Mathias et al., 2009). Later, other researchers modified these methods to account for reservoir pressurization and local geological heterogeneities (Ganjdanesh et al., 2015). The process by (Zhou and Bihrkoltzi, 2008; Spanos and De La Cruz, 1986) was based on pore expansion due to reservoir pressurization. It predicted storage estimates at the early injection stages, used for quick assessments and screening of sites for their suitability as tags.

Several studies have estimated storage capacities based on numerical models (Obdam, 2003) (Bachu et al., 2007; Bradshaw et al., 2007; Wei and Saaf, 2009; Alcalde et al., 2018). Many of these considered the storage security factor by quantifying the amount of CO_2 immobilized and the leakage potential to arrive at specific and viable storage estimates. To accommodate the effects of scale and geological heterogeneity, (Obdam and Van Der Meer, 2003) used the streamlined approach to model the storage potential of the North Sea formations. Their models also included the effects on salt precipitation and CO_2 dissolution rates. Their study concluded that reservoirs generally have a low storage efficiency, mainly influenced by formation heterogeneity.(Alcalde et al., 2018), Emphasized the need to include any limitations of the results, e.g., limited data, time, and knowledge of the exhaustive scale and effectiveness of trapping mechanisms.

2.9. Risk Analysis in Carbon Capture and Sequestration

Carbon capture and storage is a reliable approach to mitigate the rising CO_2 concentrations in the atmosphere. However, large-scale deployment means handling an overwhelming volume of gas. The CCS system value chain can be broken into two components: the pre-injection and post-injection phases, which are analogous to the upstream and downstream segments of the oil and gas industry. The setup is characterized by intense design and operational complexities with potential health, safety, and environmental risks associated with the release of captured CO_2 back into the atmosphere. The risk assessment process is generally performed concerning each handling stage, i.e., separation at plants, along the transportation pipelines, injection, and migration in the subsurface. Once injected, the CO_2 migrates laterally and vertically away from the injection well in a radial fashion. The difference in density between the CO_2 and brine constrains the brine at the bottom of the formation while the CO_2 is displaced up dip and laterally forwards.

The technological applications of Carbon Capture and Storage have been around for over half a century since when they were utilized to enhance the recovery of depleting oil field production. Significant advances in its development have enabled a deep understanding of the processes involved, especially the systemic identification, characterization, and quantification of risks. Lessons learned from pilot-scales projects and simulation results have shed light on the potential

of CCS to retain the injected CO_2. Sound analysis into site selection and appropriately managed injection reservoirs is likely to achieve 99% containment of the injected CO_2 over long-time spans (1000 yrs.), with risks decreasing over time (Figure 2-7).

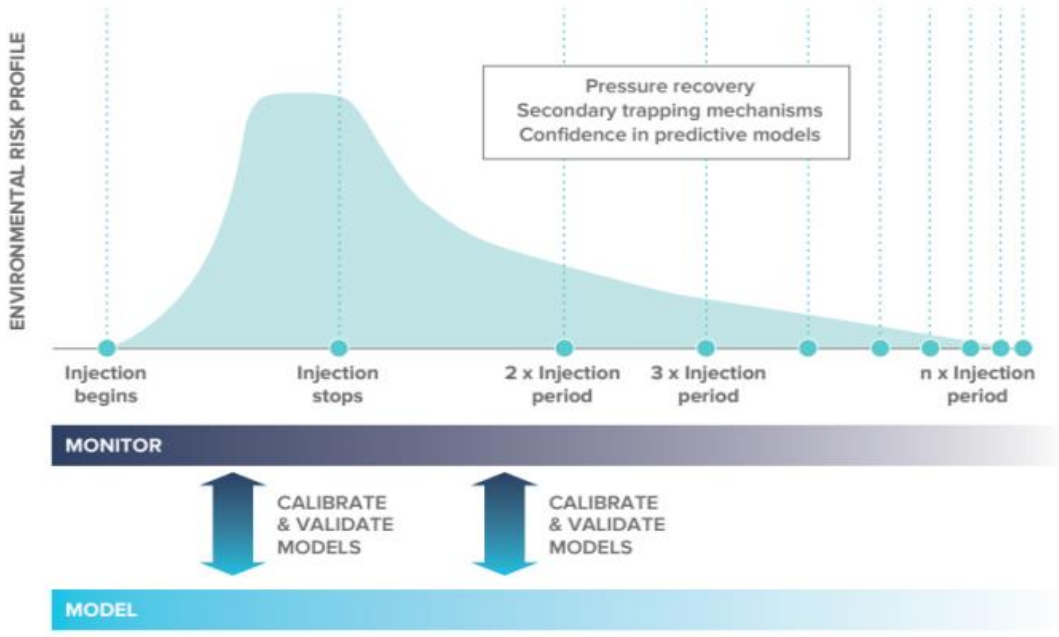

Figure 2-7: CCS risks life cycle profile (Adopted from Benson, 2007)

Monitoring and reservoir performance assessment suggest that the onset of injection is characterized by rapid risk growth. This peaks when the injection stops and gradually drops with a doubling factor over time. The entire risk spectrum is characterized by the change in pressure profile within the reservoir over time.

The pressure buildup in reservoirs is a function of the captured CO_2 emissions intended for injection into saline reservoirs. They are transforming saline aquifers into CO2 reservoirs by injecting large volumes of CO_2 resulting in reservoir pressurization due to brine displacement and rock compression. Keeping the process under control requires that sustainable injection rates are first calculated for each site to avoid excessive perturbation of in-situ stress conditions within the reservoir. Excessive stress perturbation can impact the reservoir's hydraulic and mechanical properties, a hydro-mechanical coupled process with the potential to cause instability due to rock failure. Rock failure can lead to fault reactivation creating preferentially localized flow paths

through which CO_2 and brine can leak out of the storeroom into overlying formations. Also, the far-field effect of the transient pressure gradient can displace brine, mostly up dip across open reservoir boundaries into nearby sensitive formations such as usable groundwater aquifers. The impact of pressure build is far-reaching, and its implications are a central component in the entire risk assessment life cycle of the injection and migration phase of a CCS injection program.

Even though injecting CO_2 underground is not entirely new, doing so as a storage mechanism to lessen CO_2 emissions is yet to be deployed commercially. There is still much to be learned, and even though a handful of pilot projects are operational, there still exist some knowledge gaps related to the coupled hydro-mechanical responses of deep injection due to scarcity of data. Pilot plants such as In-Sala in Algeria have provided significant insight into some processes associated with stress changes and rock behaviours. The following section presents a recap of reservoir geomechanics and fluid-rock relations. Finally, we mention the In-Sala injection project before reviewing the mathematical formulations for pressure and the numerical approaches used in this thesis.

2.10. Geomechanics of storage in saline formations

An injection site geomechanical model deals with stress and strain rate-related issues and rock failure under compressional, shear, and or tensional forces induced by pore pressure changes due to CO_2 injection (Ahmed and Al-Jawad, 2020). Rocks and their fracture systems tend to be very mechanically complex; geomechanically, their analysis relies heavily on disciplines outside of the earth sciences, e.g., mathematics, physics, and computer sciences, to answer most of its questions. Rocks are anisotropic, highly polycomponential, and have rheological properties that vary with stress states, pressure, and temperature conditions.

Most of the critical scientific basis needed to advance our technical understanding of CCS development at scale has already been established through the theoretical evolution of other sciences and their associated applications. Examples include oil and gas, petroleum Engineering, Geology, and Mining. In the oil and gas example, cap rocks help to the retard the upwards migration of hydrocarbons, which is dependent on the column high between the fluid surface and cap rock or during EOR for production and pore pressure evolution, which is analogous to the carbon capture scenario, the only difference being the reactivity of CO_2 with a cap rock. To

ensure the hydraulic integrity of impermeable boundaries such as cap rocks and faults, a geomechanical study is required to understand and monitor induced defects and seismic reactivations (Han, 2012; Serra De Souza, 2012).

However, a careful measure of the in-situ stresses across a reservoir and external stress sources surrounding the wellbore area, combined with the geomechanical properties of the rocks in the identified storage site, can help to address a wide range of decision-making issues relevant to CCS success, its operational safety and overall storage integrity. In the context of this study, we will focus on the mechanical response of the reservoir rocks to pressure buildup due to CO_2 injection. Naturally occurring faults tend to show a characteristic brittle deformation higher in the earth's crust, which transitions into a more ductile deformation with depth (Ramsay and Lisle, 2000) Fault traces are often identified based on their topographic expressions, and it will be essential to understand the long-term impacts of hydraulic fracturing, both below and above the impact position.

This section presents a general recap of the main principles governing fault reactivation and faulting. The critical theoretical concepts associated with the geomechanical modelling of rocks under different stress and strain states due to CO_2 injection are reviewed. This takes us into a discussion of the underpinning concepts of poro-elasticity.

The geomechanical response of formation rocks under pressurization from CO_2 injection continues to attract the interest of many researchers, including mathematicians, reservoir engineers, and geoscientists. Various connections to reservoir pressurization have been explored in literature. The role of trapping mechanisms, e.g., CO_2 dissolution and capillary trapping, on the rate of pressure buildup (Trevisan et al., 2015) is a good example. Other studies in a similar direction have the impact on good processes, including salt precipitation, change in CO_2 saturation of the wetting phase, and drying out on the rate of reservoir pressure buildup (Falcon-Suarez et al., 2020), while (Mathias et al., 2011) investigated the role of partial miscibility on the pressure evolution trend. Their study also considered the part of reservoir boundary conditions on pressure buildup. In a separate analysis based on the Laplace transform, (Cihan et al., 2013) presented solutions for three boundary conditions: closed boundary, infinite acting, and constant

pressure boundary. Much recently (Khan et al., 2020) used an experimental approach to investigate the effect of reservoir size and boundary conditions on pore pressure buildup. By coupling their results with the Mohr stability criteria, they concluded that large reservoirs were more stable and better suited for CO_2 storage than small reservoirs. Their modelling results with the COSMOL package predicted a higher degree of deformation and surface uplift in the small reservoirs than in large reservoirs. In another study, hypothetical injection case studies were used to investigate the impact of multi-layered/stratified reservoir architecture on diffuse brine leakage due to far-field pressure buildup (Cihan et al., 2013; Birkholzer., 2009). Their results suggest a low probability of pressure-driven diffuse leakage reaching shallow groundwater resources. If it happened, it would be unlikely to have any measurable quality changes. However, physical changes such as hydraulic gradient and the discharge rate of baseflow will most likely be impacted. However, (Zheng et al., 2015), in a separate study based on reactive transport models of large data sets, showed that a hydraulic connection between storage formation and shallow aquifer could result in the mobilization of hazardous chemical constituents, e.g., arsenic and lead from deep in the storage. (Liu et al., 2014) looked at the effect of temperature and injectivity plume migration in between the layers of a stratified reservoir. Their numerical experiments highlight the significant roles of injection rate and temperature plume extend, laterally and vertically. It appears that, including pressure buildup magnitude that drives leakage, the impact of CCS on shallow groundwater can depend on the reservoir mineralogy, given that geochemical equilibria determine the mineral dissolution pathways for the release and remobilization of trace elements. Secondly, the travel distance from the store room to the shallow aquifer and, finally, the rate of baseflow runoff also play a role. This can be fast enough to either wash away and dilute the metal concentration or slow sufficiently to cause accumulation of the metals in the aqueous face. These studies were helpful for uncertainty quantification, parameter estimates, and the calibration of pressure management schemes. At full-scale deployment, a given reservoir will receive CO_2 injected through more than one borehole at a given time in a last study considered. In this accord, (Zakrisson et al., 2008) evaluated the interference between multiple wells and their impact on the reservoir pressure buildup and injectivity. To calculate the number of wells for a given parameter, their model, Their model, estimated modelled this case in a study

aimed to determine the injection rate and the maximum number of wells suitable for a given reservoir parameter and The interference of the pore pressure buildups between multiple wells.

2.11. Pressure buildup and Geomechanical implications: In the Salah storage project case

The In Salah CCS project located in the Krechba oil field in Algeria was Africa's first and only carbon Storage project. The Carbon Storage Project was commissioned as a pilot scale project. The operation ran between 2004 and till 2011, when it was decommissioned, and injection halted after a series of devasting micro seismic events and significant surface uplift associated with reservoir pressurization and eventual loss of good integrity (Ringrose et al., 2013). The onshore In Salah project served multiple natural gas fields. The gas produced from the numerous fields with a high CO_2 content had to be stripped off to meet the required export specifications of < 0.3% CO2. On average, 5 - 10% carbon dioxide was recovered after the gas was purified and treated with the MEA Amine process before being compressed and transported to the storage site. The facility, a joint venture between BP and Stat Oil Hydro, was injecting, on average, one million tons of CO_2 annually, with a cumulative injection totaling 3.8 metric tons stored in the subsurface by the end of its life cycle. Storage performance at the site used various existing and newly developed tools, including geophysical and geochemical methods, time-lapse seismic, micro seismic, downhole logging and wellhead sampling, groundwater monitoring, and satellite InSAR (section 2.11.1.1) data.

As a world-pioneering onshore storage project, industry partners and research institutions, including the US Energy Department, have since seized the opportunity to use the project as a natural real-world laboratory to demonstrate geological sequestration.

The injection formation consisted of a 20-m thick Carboniferous sandstone located 1.9 km below the surface with low porosity and permeability, 15% and ten mD, respectively. The injection was completed through horizontal wells-drilled perpendicular to the flat stress fields.

2.11.1. Monitoring geomechanical changes due to pressure buildup.

As listed above, CO_2 migration and containment within the target storage room were monitored by various methods. InSAR and seismic are the two essential methods that shed light on the

geomechanical changes necessary to assess storage performance and the hydraulic integrity of the storeroom.

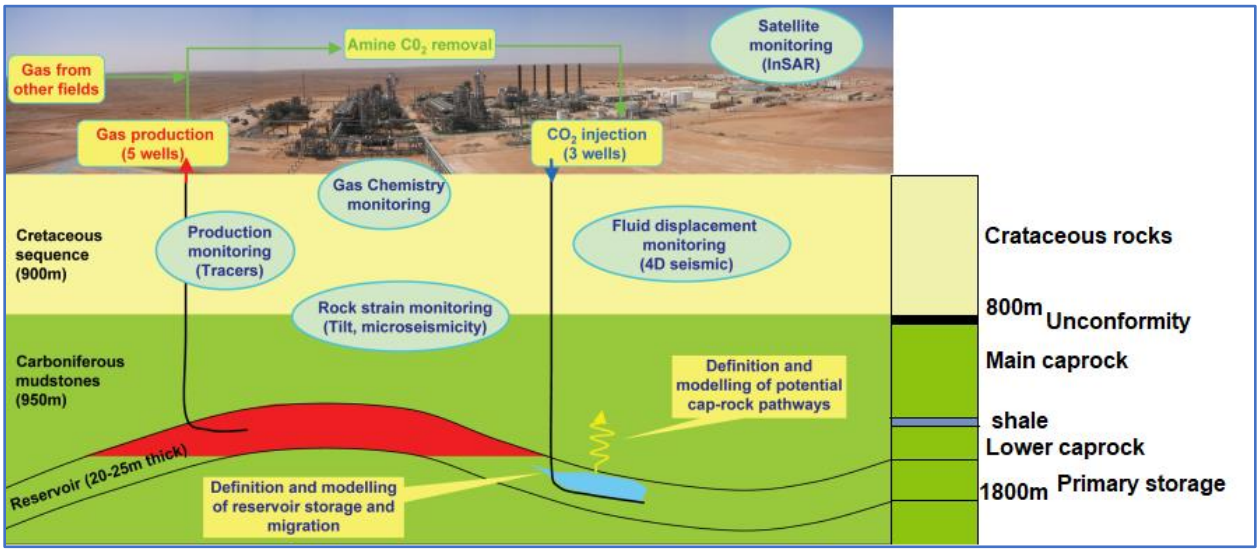

Figure 2-8: Schematic representation of the In-Salah injection and storage project site with monitoring (Bachu et al., 2009).

This case study attracted significance research interest spanning the different Multiphysics involved. For example, in (White et al., 2014), the pressure plumes and CO_2 had migrated vertically upwards; however, there was no direction confirmation that the entire storage system (store unit and 950 m thick interlayered cap rock systems) had been compromised. Integrating data from monitoring efforts and earlier gas exploration reservoir characterizations reproduces a detailed geological representation of the reservoir. Processing this data provided a thorough understanding of the main geological controls on CO_2 dispersion, forming the basis for storage site performance assurance.

2.11.1.1. Satellite airborne radar interferometry (InSAR)

Data analysis based on satellite airborne radar interferometry (InSAR) provided a valuable understanding of the coupled hydro-mechanical changes associated with such vertical flow (Rinaldi and Rutgvist, 2017). By connecting the satellite data with rock deformation models, the InSAR method captured geomechanical changes resulting from subsurface pressure buildup, a

critical pillar whose mastery and management have implications for the safe large-scale deployment of CCS (Mathieson et al., 2009), (Figure 2.9).

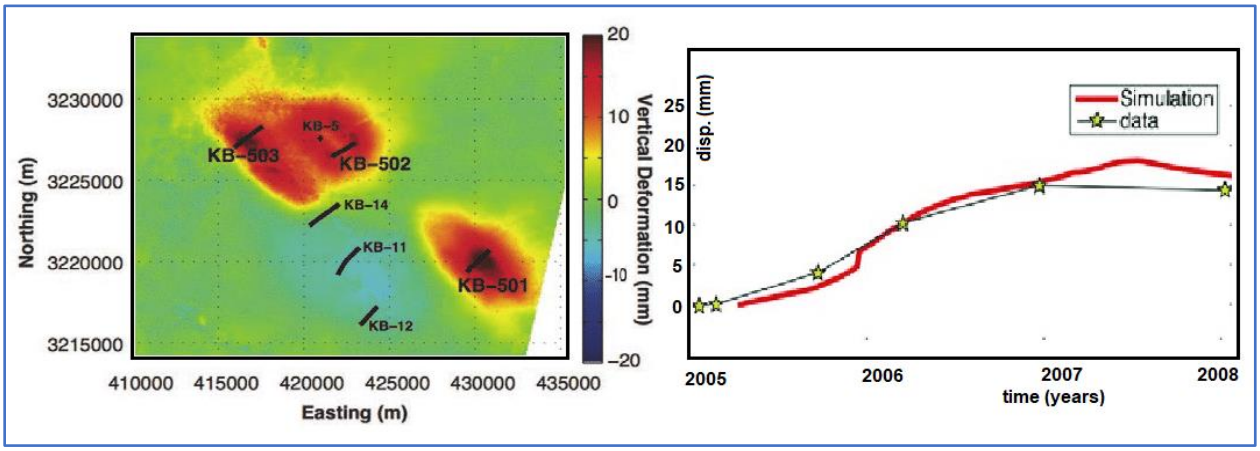

Figure 2-9: Uplift records showing the observed and modelled point displacement at In Salah from 2004 to 2010 (Adapted from (Rinaldi and Rutqvist, 2017).

The geomechanical changes observed in the figure above result from coupled hydraulic action and mechanical response of the rocks due to underground reservoir pressurization (figure 2-10). Although there are no indications of complete damage to the overall storage system, the observations have opened avenues for research into the mechanisms governing the observed geomechanical responses. In a study (White et al., 2014), the authors affirmed no pressure leakage out of the reservoir. This was concluded through a bleed-off test that showed no escape of pressure, shallow soil, and water chemistry analysis, whose results confirmed that the concentration of CO_2 was still within baseline values.

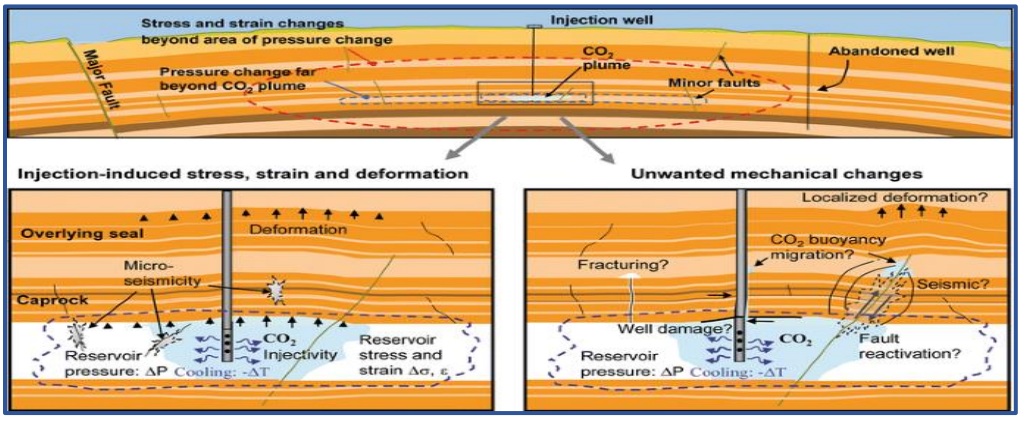

Figure 2-10: Geomechanical processes and technical challenges associated with pressure buildup. Adapted from (Vilarrasa et al., 2010).

In conclusion, reservoir pressurisation is a multicoupled process that is heavily impacted by reservoir disorder such as the effect of heterogeneity. To capture subgrid variation, the classical approach to prediction which is based on the Darcy and Newtonian definition of the derivative shows some limitations. The following chapters discuss the the extension of pressure diffusivity model to the fractional real. The purpuse of applying a fractional derivative is to benefit from the memory defination, which allows the effect of different reservoir processes, i.e., local and non-local to be examined in the context of pressure buildup.

CHAPTER THREE: MODELLING PRESSURE BUILD-UP WITH THE CLASSICAL OPERATOR (DELTA DIRAC).

3.1. Introduction

Geological Carbon Storage (GCS) has become recognized as an indispensable technology for achieving deep emission cuts necessary to mitigate the effect of climate change. Storage in unmineable coal seams depleted oil and gas reservoirs, carbonate reservoirs, and, more importantly, deep saline formations offer substantial storage capacity and are abundant in many parts of the world. During CCS, CO_2 is captured and injected underground until permanent Storage. Carbon capture and Storage is to be accessed and quantified with all available technological and scientific means. Numerical models are required to monitor reservoir operations and predict their performance over time. Mathematical models that can account for the relevant processes that constrain the fate of CO_2 migration within the subsurface. These may include flow and migration, pressure buildup transport of multi-phase systems, geochemical reactions, and geomechanical effects.

CO_2 injection is a multi-coupled process, and mathematical formulations can lead to a very complex system of non-linear equations. Formulation of a model concept that accounts for a CO_2-rich phase, the two-phase flow and brine flow regions are considered. Numerical simulations give insight into principal processes during CO_2 storage in a geological formation. Simulation runs over extended periods can assess plume scale, pore scale, and reservoir scale processes, affecting plume migration and pressure diffusivity within the reservoir (Bielinski, 2007). The complex coupled thermo-mechanic problem always results in very complex mathematical systems, which are difficult to handle analytically. Carbon dioxide storage has been assessed analytically and semi-analytically. Solutions are predominantly dedicated to evaluating pressure gradients and fluid flow (Kivi et al., 2022; Vilarrasa et al., 2010). In the same pressure and flow response context, (Vasco et al., 2008) investigated the surface uplift due to reservoir pressurization, and (Li et al., 2015) developed a solution for the coupled hydromechanical processes of cap rock and surface deformation. These models are generally based on traditional mass and energy balance equations through Darcy's equation which relates flux to the pressure gradient. In cases where analytical solutions have been obtained, the approach was based on assumptions and oversimplifications such as homogeneity, isotropic, constant thickness, and even parameter distribution. These are far from real-world

problems and can render the results erroneous. However, semi-analytical and analytical solutions remain valuable for our continuous understanding of the coupled processes. Furthermore, these models can be used as standards for verifying numerical models.

Numerical models are increasingly developed to handle the diverse spectrum of hydromechanical processes associated with CO_2 injection and Storage. In a pioneering study, Rutqvist (Rutqvist et al., 2010) showed that uplift due to CO_2 injection is a function of pore pressurization and elastic expansion and a function of pressure evolution on the cap rock. Additionally, several numerical models have been dedicated to understanding the effects of pore pressure evolution, CO_2 quality, CO_2 dissolution on pressure buildup and geomechanical rock stability. In one such study (Jiang, 2011) the author conclude that multi scale grid based modelling as oppose to analytical modelling proofs to be more reliable in modelling the long term fate of CO_2 injection. The study further suggest that high resolution rubost numerical models would be better off reserved for simulating short term high energy local dispersion. this study, the authors suggest that the effect of geomechanics can be ignored if the pore pressure changes are minor but can be supported for large-scale commercial applications.

The primary purpose of this chapter is to understand the transient pressure behaviour by modelling the hydromechanically coupled pressure diffusivity model as it applies to geological Carbon sequestration. A focus is on reservoir characterization based on the partitioned regions. The primary model assumptions are stated, and the physical process of buoyancy-driven CO_2 migration is considered. A finite difference numerical scheme is used to solve the equations describing pressure built in each saturation region.

3.2. Conceptual model and mathematical framework

The aquifer is considered to be initially filled with saline water. After injecting CO_2, the reservoir is transformed into a partially saturated domain of three sub-regions: dry out (region 1), two-phase (region 2) flow, and brine flow (region 3). Given the suggested framework in Figure 3.1, the study can take into account the effect of some significant hydromechanical processes associated with CO_2 injection:

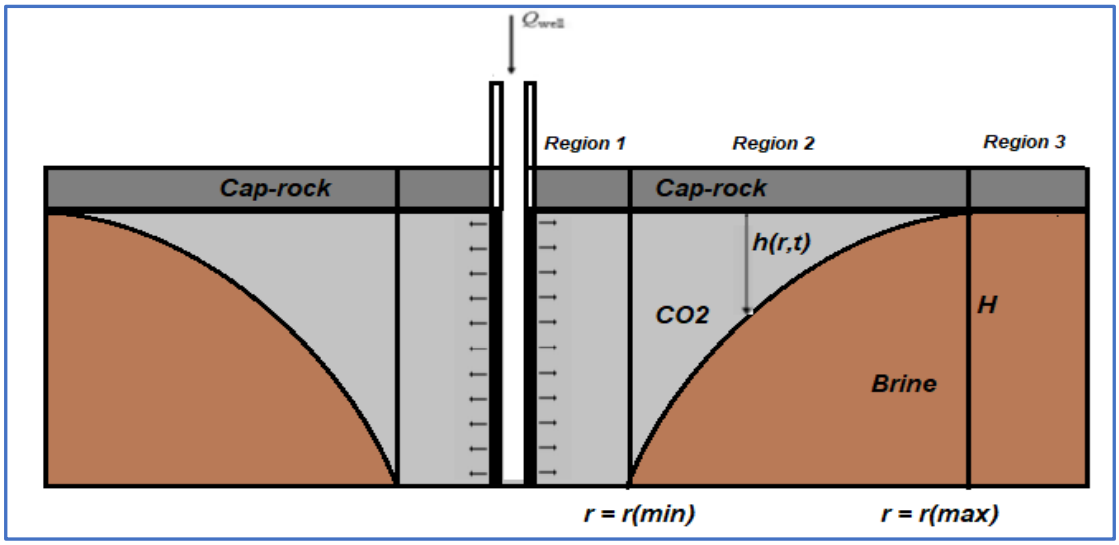

Figure 3-1: Conceptual schematic section of plume evolution and saturation profile in the sub surface. Adapted from (Azizi, 2013).

3.3. Piecewise characterization

3.3.1. Near well processes (Region A)

Near-well processes are generally classified into two groups. Those occurring near the wellbore, characterized by high flow rates of injected CO_2 with short time flow powered processes, and those just outside the wellbore region with a more sustained high flow rate (see Figure. 3-1). In both cases, the perturbation of formations equilibrium due to feedback response between formation and wellbore results in changing injectivity. Critical processes responsible for these observations include local formation damage, halite precipitation, and forming a drying out front with injection. These processes have essential flow implications through their potential to alter formation permeability and influence pressure build; for example, the local reservoir damage and the forming of a drying out front enhance formation permeability while simultaneously facilitating halite (salt) precipitation that, on the other reduces permeability (Pruess and Garcia, 2002).

In addition, the difference in temperature between the saline formation and well fluid (CO_2) adds to the dynamics of the injection of CO_2. When CO_2 leaves the Well at a significantly high pressure, it expands as it enters the porous formation leading to cooling due to decompression. This process is called the Joule-Thompson cooling effect.

Modelling approaches and insight into near-well processes

Early attempts at modelling the injection phenomena used a constant pressure boundary to account for a source term of specific mass for good inflow. While this approach simplified the

problem and allowed certain aspects of the process to be investigated, it came short of representing the coupled well (turbulent)-formation (porous media) flow system. In (Pan et al., 2011) the first numerical model encompassing drift flux for viscous flow coupled with the 2-phase porous media flow was presented. This study identified that injection into the reservoir causes a rapid increase in the reservoir pressure in the near well vicinity. Both well-bore-only, wellbore-formation coupled models and formation-only models continue to provide insight into different aspects of the problem (Lu and Cornell, 2008; White et al., 2014).

Numerical models have not only shed light on the processes before the unknown, but they are also tools to investigate possible solutions to inherent reservoir limitations. These include the issue of non-linearity imposed by geological matrix and varying scales of heterogeneity. In one such example, (Mijic et al., 2014) showed that non-Darcy model formulations to investigate factors that control imbibition efficiency and halite precipitation yielded informative results. In their study, the use of non-Darcy flow conditions made it possible to the partitioning of pressure and saturation. However, natural processes can be site-specific, and halite precipitation is no exception. Other models were used to investigate mitigation options, such as the use of water to flush away and dissolve salts from the Well region area (Pruess and Muller, 2009) as well as placing high permeability material between the Well and formation (Kim et al., 2012), a technique already in use for groundwater extraction Well construction. In another study, involving CO_2 injection into low permeability non-Darcy reservoir flows (Song et al., 2015), numerical modelling is used to assess the implications of a capping pressure gradient, which is used in accurate assessments carried out to evaluate the storage efficiency.

Different studies aimed at understanding the impact of decompression cooling due to CO_2 injection into saline formation reveal that its role can be undermined. This has to do with the fact that reservoir material already possesses a heat content, and together with a continuous supply of a thermal gradient due to injection render, the Joule-Thompson (decompression cooling) becomes less pronounced (Singh and Georke, 2011). Also, (Han *et al*., 2012) used numerical models and sensitivity studies to show that near wellbore temperature-driven processes such as drying front, halite precipitation, and decompression cooling were thermodynamically coupled with formation material properties and injection rates (R. a. Wang 2009). Other vital studies also considered specific near-well processes' effects on the

thermal gradient. For example, (Han *et al.,* 2012) showed that the most influence on temperature emanated from expansion processes such as drying front, an observation made through monitoring field scale injection projects. While the global impact of JT cooling, drying front, and precipitation due to temperature changes are generally low, near-well formation temperature tends to be decreased by low enthalpy inflow of the fluid from the Well due to heat loss along the Well flow path (Singh and Chaudhuri, 2023; Goodarzi, 2010; Jiang et al., 2014; Roy, 2018). However, the imperative to measure and understand fault reactivation propensity as a safety requirement for injection site suitability requires a geomechanical analysis and appropriate stress regime (type of faulting) calculations. This is to evaluate and avoid brittle deformation that could lead to unwarranted movement of fluids out of the storage complex (Roy *et al*., 2018).

3.3.2. Migration processes (trapping) (Region B)

The formation of a funnel-shaped plume results in prolonged injection of CO_2 in a single-layer Saline Unit. This is due to buoyancy, the main driving force of the CO_2 plume in the two-phase flow (CO_2-Brine) region and denotes the pressure front propagation. With time, the plume develops vertically downwards and horizontally sloping upwards until trapping occurs under a large cap-rock formation.

Due to its implication on pressure build-up distribution, the plume shape and its propagation front have been an essential area of modelling interest. Comprehensive analytical and numerical modelling studies exist in the literature (Dentz and Tartakovsky, 2009; Zhoua et al., 2010; de Coninck and Benson, 2014) that address this need. Accurate modelling in the two-phase region requires a careful understanding of the driving forces and how these interrelate with one another. Pressure build-up related to CO_2 compressibility is controlled by the fluid's density, which, in turn, is controlled by the fluid pressure build-up and other reservoir process parameters.

Further, important insights from modelling two-phase flow problems in geological formations can be correlated for CO_2 storage in saline aquifers. In the two-phase area (region B), a vertical hydrostatic equilibrium is maintained by the density difference between the two fluids described by the sharp interface (so-called sharp interphase model or assumption), which controls the behavior and resulting propagation front of the CO_2 plume in contact with the formation brine. This sharp interphase is generally controlled by capillary pressure, capillary

trapping, and gravity currents (Juanes et al., 2010; Nordbotten and Dahle, 2011), and (Hesse, 2008) advanced the research by including the effect of compressibility. Taking cognizance of most near-well processes, including CO_2 compressibility, has allowed radial flow around an injection well to be resolved in one dimension. These calculations have allowed the saturation profile for the different regions to be predicted by considering two sharp fronts separating the three regions of different fluid saturation. This example did not account for the effect of gravity currents, not capillary pressure, and uses the Buckley Leverette fractional flow concept (1947), which mainly takes account of the relative fluid permeability's.

The vertically integrated models use vertical separation due to buoyancy, for which the pressure field driving the flow and migration of CO_2 is two-dimensional in the horizontal direction (Gasda et al., 2009). This approach analyzes plume mixing and vertical saturation based on hydrostatic equilibrium. Numerical models advanced the modelling capabilities to include all possible phase combinations and leakage mechanisms (Vialle et al., 2016). Numerical models can be used to test the validity of analytical models, simulate the injection complexities, and simulate high-resolution grids with considerations of heterogeneities applied in the context of uncertainty analysis. As shown in (Figure 3-5), trapping mechanisms are associated with different time scales; as such, a numerical model has been used to predict the approximate storage budgets for each mechanism. Numerical models can give insight into new trapping mechanisms, as in the case of capillary trapping (Saadatpoor and Sepehrnoori, 2010) as well as constrain essential processes that affect trapping, such as the role of hysteresis in immobilizing through the process of combined drainage (Jin et al., 2018).

3.3.3. Brine flow processes (pressure diffusion)

Modelling results reveal that flow in this region is mainly controlled by the nature of the flow boundaries. For example, for a semi-open reservoir, when the brine displacement reaches the boundary, there is a drop in pressure at the near Well region, and the leakage, as expected for both semi-closed and closed reservoirs, will be lesser (Villarassa, 2013).

3.4. Physical model and assumption

Several assumptions are made to simplify the problem for analytical solutions. One-dimensional radial flow from a CO_2 injection well into a saline formation is modelled. The saline formation is assumed to be homogeneous, isotropic, horizontal, isothermal, and uniform in thickness. A fully penetrating vertical well injects pure CO_2 at a constant rate. The

fluids' compressibility's and viscosities are constant. For simplicity, the effects of gravity and capillary forces are neglected.

In principle, CO_2 injection creates three saturation regions in the formation, as schematically depicted in Figure 3.1. Region 1 represents a dry gas region where brine is displaced to region 2 or evaporated into CO_2. Region 2 shows a two-phase region where water-saturated CO_2 displaces brine. Region 3 shows the region beyond the CO_2 front, fully saturated with brine. As a result, the problem has two saturation fronts. Different outer boundaries of the formation are modelled. These include infinite-acting, closed, or constant pressure. Because CO_2 injection is planned to take a long (current projections suggest a range of 20-40 years), the pressure response is expected to reach formation outer boundaries or at least flow boundaries within the formation during the injection period. Given that saline formation is initially filled fully with brine, a slightly compressible fluid, any pressure created at an injection well should be quickly transmitted into a large area. In contrast, the CO_2 plume created should be around the injection area.

3.5. Governing equations.

Based on the existing conceptual and analytical models, the 1D governing equations in radial coordinates for pressures ($P_1,\ P_2, and\ P_3$) in the three regions of an infinite-acting saline formation are given as:

The 1D governing equations in radial coordinates for pressures ($P_1,\ P_2\ \ and\ P_3$) in the three regions of an infinite-acting saline formation can be written as,

$$\frac{1}{r}\frac{\partial}{\partial r}\left(r\frac{\partial P_1}{\partial r}\right)=\frac{\emptyset C_{tg}}{k\overline{\lambda_g}}\frac{\partial P_1}{\partial t}, \qquad r_W < r < r_{dry} \qquad 3.1.1$$

$$\frac{1}{r}\frac{\partial}{\partial r}\left(r\frac{\partial P_2}{\partial r}\right)=\frac{\emptyset C_{tw}}{k\lambda_t}\frac{\partial P_2}{\partial t}, \qquad r_{dry} < r < r_{BL} \qquad 3.1.2$$

$$\frac{1}{r}\frac{\partial}{\partial r}\left(r\frac{\partial P_3}{\partial r}\right)=\frac{\emptyset C_t}{k\lambda_w}\frac{\partial P_3}{\partial t}, \qquad r_{BL} < r < r_{\infty} \qquad 3.1.3$$

Where

$$\overline{\lambda_g} = \frac{\overline{k_{rg}}}{\mu_g}$$

$$\overline{\lambda_w} = \frac{1}{\mu_W}$$

$$\bar{\lambda_t} = \frac{\overline{k_{rg}}}{\mu_g} + \frac{\overline{k_{rw}}}{\mu_w}$$

Substituting the and simplifying, we obtain the systems of equation as

$$\frac{1}{r_D}\frac{\partial}{\partial r_D}\left(r_D \frac{\partial P_{D1}}{\partial r_D}\right) = \frac{\partial P_{D1}}{\partial t_D}, \quad 0 < r_D < r_{Ddry}$$

$$\frac{1}{r_D}\frac{\partial}{\partial r_D}\left(r_D \frac{\partial P_{D2}}{\partial r_D}\right) = \frac{1}{F_{\lambda g}\eta_{D2}}\frac{\partial P_{D2}}{\partial t_D}, \quad r_{Ddry} < r_D < r_{DBL}$$

$$\frac{1}{r_D}\frac{\partial}{\partial r_D}\left(r_D \frac{\partial P_{D3}}{\partial r_D}\right) = \frac{1}{\eta_{D3}}\frac{\partial P_{D3}}{\partial t_D}, \quad r_{DBL} < r_D < \infty$$

Where $\eta_{D2},\ \eta_{D3}, and\ F_{\lambda g}$ are the compressibility ratios and the ratio of total mobility to gas mobility.

$$\eta_{D2}, = \frac{c_{tg}}{c_t}$$

$$\eta_{D3} = \frac{c_{tg}}{c_{tw}}\frac{\overline{\lambda}_w}{\overline{\lambda}_g}$$

$$F_{\lambda g} = \frac{\overline{\lambda}_t}{\overline{\lambda}_g}$$

We also consider a reservoir at rest, with initial equilibrium pressure P_i

$$P(total) = P_i \ \ t = o \qquad 3.1.4$$

At the well bore $r = r_w$, CO_2 is injected at a constant rate approximated as

$$q = -\frac{2\pi rhk\bar{k}_{rg}B_{g(P_n - P_i)}}{q\mu}, \ r = r_W \quad 3.1.5$$

Where q is the total injection rate at surface conditions, B_g is the gas formation volume factor, and h is the formation thickness. The formulation is defined as a piecewise problem with the final output of each region being input as the initial conditions of the proceeding region. The Well is assumed to be a line source, i.e., for an infinitesimally small well bore (r-Well = 0), the dimensionless initial and boundary conditions as

$$P_1 = P_2, \ r = r_{dry} \quad 3.1.6a$$

$$\overline{\lambda_g}\frac{\partial P_1}{\partial r} = \bar{\lambda_t}\frac{\partial P_2}{\partial r}, \quad r = r_{dry} \quad 3.1.6b$$

The same formulation can be done for the outer boundary region, $P_2, and\ P_3$, and the flux across the two phases is given as

$$P_2 = P_3, r = r_{BL} \quad 3.1.7a$$

$$\overline{\lambda_g}\frac{\partial P_3}{\partial r} = \bar{\lambda_t}\frac{\partial P_2}{\partial r}, \ r = r_{BL} \quad 3.1.7b$$

At the boundary of the drying-out region, $P_1\ and\ P_2$ and the flux are equal.

At the outer boundary of the formation, the pressure is always equal to the initial formation pressure (condition for an infinite-acting reservoir)

$$P_3 = P_i, r \to \alpha \quad 3.1.8$$

The final set of equations simplified with the product rule into the following forms.

$$\frac{\partial^2 p_{D1}}{\partial^2 r_D} + \frac{1}{r}\frac{\partial p_{D1}}{\partial r_D} = \frac{\partial P_{D1}}{\partial t_D}, \quad 0 < r_D < r_{Ddry} \quad 3.2.1$$

$$\frac{\partial^2 p_{D2}}{\partial^2 r_D} + \frac{1}{r}\frac{\partial p_{D2}}{\partial r_D} = \frac{1}{F_{\lambda g}\eta_{D2}}\frac{\partial P_{D2}}{\partial t_D}, \ r_{Ddry} < r_D < r_{DBL} \quad 3.2.2$$

$$\frac{\partial^2 p_{D3}}{\partial^2 r_D}+\frac{1}{r}\frac{\partial p_{D3}}{\partial r_D}=\frac{1}{\eta_{D3}}\frac{\partial P_{D3}}{\partial t_D},\ \ r_{DBL}<r_D<\infty \tag{3.2.3}$$

3.6. Numerical analysis

$$H_1\left(t,r_D,p_{D1}(t,r_D)\right)=\frac{\partial^2 p_{D1}}{\partial^2 r_D}+\frac{1}{r}\frac{\partial p_{D1}}{\partial r_D} \tag{3.3a}$$

$$H_2\left(t,r_D,p_{D2}(t,r_D)\right)=\left(F_{\lambda g}\eta_{D2}\right)\left[\frac{\partial^2 p_{D2}}{\partial^2 r_D}+\frac{1}{r}\frac{\partial p_{D2}}{\partial r_D}\right] \tag{3.3b}$$

$$H_3\left(t,r_D,p_{D3}(t,r_D)\right)=\left(\eta_{D3}\right)\left[\frac{\partial^2 p_{D3}}{\partial^2 r_D}+\frac{1}{r}\frac{\partial p_{D3}}{\partial r_D}\right] \tag{3.3c}$$

Which are then expressed as

The above systems can be expressed as a Cauchy problem, given as in Cauchy form as

$$\begin{cases} p_{D1}^{\alpha}(t,r_D)=H_1\left(t,r_D,p_{D1}(t,r_D)\right),t>0 \\ p_{D2}^{\alpha}(t,r_D)=H_2\left(t,r_D,p_{D2}(t,r_D)\right),t>0 \\ p_{D3}^{\alpha}(t,r_D)=H_3\left(t,r_D,p_{D3}(t,r_D)\right),t>0 \\ p_{(D1,D2,D3)}(r_D,0)=0,t=0 \end{cases} \tag{3.4}$$

The functions $P_{D1},\ P_{D2}, and\ P_{D3}$ are the fractional differential equations associated with pressure build-up region 1, region 2, and region 3, as labeled in the conceptual model. For simplicity, we will present one equation for which the index n can take the values of $1,2,3$ as follows.

$$\begin{cases} p_{Dn}^{\alpha}(t,r_D)=H_n\left(t,r_D,p_{Dn}(t,r_D)\right),t>0 \\ p_{(Dn)}(r_D,0)=0,t=0 \end{cases} \tag{3.5}$$

Following the fundamental theorem of calculus along with the initial condition, we can reformulate the set of equations into integral form given as

$$p_{Dn}(t,r_D)-p_{Dn}(0,r_D)=\int_0^t H_n\left(\tau,r_D,p_{Dn}(\tau,r_D)\right)d\tau \tag{3.6}$$

Substituting $t=t_{k+1}=(k+1)\Delta t,\ \forall\ k\in[0,1,2\ldots]$

$$p_{Dn}(t_{k+1},r_D)=p_{Dn}(0,r_D)+\int_0^{t_{k+1}} H_n\left(\tau,r_D,p_{Dn}(\tau,r_D)\right)d\tau \tag{3.7.1}$$

And at $t=t_k$

$$p_{Dn}(t_k, r_D) = p_{Dn}(0, r_D) + \int_0^{t_k} H_n\big(\tau, r_D, p_{Dn}(\tau, r_D)\big)d\tau \qquad 3.7.2$$

Taking the difference between $equ.\ 3.7.1\ and\ 3.7.2$

$$p_{Dn}(t_{k+1}, r_D) = p_{Dn}(t_k, r_D) + \int_{t_k}^{t_{k+1}} f(\tau, p_{D1}(\tau, r)d\tau \qquad 3.8$$

3.6.1. Numerical solution of the classical PDE for pressure build-up with Lagrange polynomial method.

This section analyses the system of equations for their numerical solution with the two-step LaGrange polynomial method. Given as

$$p_k(\tau) = \frac{\tau - t_k}{\Delta t} H_n\big(t_k, r_D, p_{Dn}(t_k, r_D)\big) - \frac{\tau - t_{k-1}}{\Delta t} H_n\big(t_{k-1}, r_D, p_{Dn}(t_{k-1}, r_D)\big) \qquad 3.9$$

Substitute the scheme to approximate within$[t_{n+1}, t_n]$,

$$\begin{aligned} p_{Dn}(t_{k+1}, r_D) - p_{Dn}(t_k, r_D) \\ &= \int_{t_k}^{t_{k+1}} \frac{\tau - t_k}{\Delta t} H_n\big(t_k, r_D, p_{Dn}(t_k, r_D)\big)d\tau \\ &- \int_{t_k}^{t_{k+1}} \frac{\tau - t_{k-1}}{\Delta t} H_n\big(t_{k-1}, r_D, p_{Dn}(t_{k-1}, r_D)\big)\, d\tau \end{aligned}$$

$$\begin{aligned} p_{Dn}(t_{k+1}, r_D) - p_{Dn}(t_k, r_D) \qquad 3.10 \\ &= \frac{H_n\big(t_k, r_D, p_{Dn}(t_k, r_D)\big)}{\Delta t} \int_{t_k}^{t_{k+1}} (\tau - t_k)d\tau \\ &- \frac{H_n\big(t_{k-1}, r_D, p_{Dn}(t_{k-1}, r_D)\big)}{\Delta t} \int_{t_k}^{t_{k+1}} (\tau - t_{k-1})\, d\tau \end{aligned}$$

$$\int_{t_k}^{t_{k+1}} (\tau - t_k)d\tau = \frac{3}{2}(\Delta t)^2,$$

$$\int_{t_k}^{t_{k+1}} (\tau - t_{k-1})\, d\tau = \frac{1}{2}(\Delta t)^2.$$

Replacing we get

$$p_{Dn}(t_{k+1}, r_D) = p_{Dn}(t_k, r_D) + \frac{3}{2}\frac{H_n\left(t_k, r_D, p_{Dn}(t_k, r_D)\right)}{\Delta t}(\Delta t)^2 - \frac{1}{2}\frac{H_n\left(t_{k-1}, r_D, p_{Dn}(t_{k-1}, r_D)\right)}{\Delta t}(\Delta t)^2 \quad 3.10$$

Which can be simplified as

$$p_{Dn}{}_{r_D}^{k+1} = p_{Dn}{}_{r_D}^{t_k} + \frac{3}{2}H_n\left(t_k, r_D, p_{Dn}{}_{r_D}^{t_k}\right) - \frac{1}{2}H_n\left(t_{k-1}, r_D, p_{Dn}{}_{r_D}^{t_{k-1}}\right)(\Delta t) \quad 3.11$$

where

$$H_1\left(t, r_D, p_{D1}(t, r_D)\right) = \frac{\partial^2 p_{D1}}{\partial^2 r_D} + \frac{1}{r}\frac{\partial p_{D1}}{\partial r_D}$$

$$H_2\left(t, r_D, p_{D2}(t, r_D)\right) = \left(F_{\lambda g}\eta_{D2}\right)\left[\frac{\partial^2 p_{D2}}{\partial^2 r_D} + \frac{1}{r}\frac{\partial p_{D2}}{\partial r_D}\right]$$

$$H_3\left(t, r_D, p_{D3}(t, r_D)\right) = \left(\eta_{D3}\right)\left[\frac{\partial^2 p_{D3}}{\partial^2 r_D} + \frac{1}{r}\frac{\partial p_{D3}}{\partial r_D}\right]$$

Discretized at $(r_{Di},\ t_k)$ and $(r_{Di},\ \ t_{k-1})$, we obtain the following expressions, which are then substituted into $3.11, 3.12, and\ 3.13$.

<u>Region A:</u>

$$H_1\left(t, r_D, p_{D1}(t, r_D)\right) = \frac{\partial^2 p_{D1}}{\partial^2 r_D} + \frac{1}{r}\frac{\partial p_{D1}}{\partial r_D}$$

$$H_1\left(r_{D,i}, t_k, p_{D1}(t_k, r_{D,i})\right)\Big|_{(t_k,\ r_{D,i})} = \left[\frac{1}{r_{D,i}}\left(\frac{p_{D1}(r_{Di+1}, t_k) - p_{D1}(r_{Di-1}, t_k)}{2\Delta r}\right) + \frac{p_{D1}(r_{Di+1}, t_k) - 2p_{D1}(r_{Di}, t_k) + p_{D1}(r_{Di-1}, t_k)}{\Delta r^2}\right] \quad 3.12a$$

$$H_1(r_{Di}, t_{k-1}, p_{D1}(r_{Di}, t_{k-1}))\big|_{(t_{k-1},\ r_{Di})} \qquad 3.12b$$

$$= \left[\left(\frac{p_{D1}(r_{Di+1}, t_{k-1}) - 2p_{D1}(r_{Di}, t_{k-1}) + p_{D1}(r_{Di-1}, t_{k-1})}{\Delta r^2}\right)\right.$$

$$\left. + \frac{1}{r_{D,i}}\left(\frac{p_{D1}(r_{Di+1}, t_{k-1}) - p_{D1}(r_{Di-1}, t_{k-1})}{2\Delta r}\right)\right]$$

Let

$$H_1\left(r_{D,i}, t_k, p_{D1}(t_k, r_{D,i})\right)\Big|_{(t_k,\ r_{D,i})} = W_{k,i} \text{ and}$$

$$H_1(r_{Di}, t_{k-1}, p_{D1}(r_{Di}, t_{k-1}))\big|_{(t_{k-1},\ r_{Di})} = \bar{W}_{k,i}$$

Therefore, the pressure diffusivity model for region A can be written as

$$p_{D1}{}_{r_{Di}}^{k+1} = p_{D1}{}_{r_{Di}}^{t_k} + \frac{3}{2}W(\Delta t) - \frac{1}{2}\bar{W}(\Delta t) \qquad 3.13a$$

Region B:

$$p_{D2}{}_{r_{Di}}^{k+1} = p_{D2}{}_{r_{Di}}^{t_k} + \frac{3}{2}H_2\left(t_k, r_{Di}, p_{D2}{}_{r_{Di}}^{t_k}\right)(\Delta t) - \frac{1}{2}H_2\left(t_{k-1}, r_{Di}, p_{D2}{}_{r_{Di}}^{t_{k-1}}\right)(\Delta t) \qquad 3.12$$

Where,

$$H_2\left(r_{D,i}, t_k, p_{D2}(t_k, r_{D,i})\right)\Big|_{(t_k,\ r_{D,i})} = \left(F_{\lambda g}\eta_{D2}\right)W_{i,k}$$

and

$$H_2(r_{Di}, t_{k-1}, p_{D2}(r_{Di}, t_{k-1}))\big|_{(t_{k-1},\ r_{Di})} = \left(F_{\lambda g}\eta_{D2}\right)\bar{W}_{i,k}$$

$$p_{D2}{}_{r_{Di}}^{k+1} = p_{D2}{}_{r_{Di}}^{t_k} + \frac{3}{2}\left(F_{\lambda g}\eta_{D2}\right)W_{i,k}(\Delta t) - \frac{1}{2}\left(F_{\lambda g}\eta_{D2}\right)\bar{W}_{i,k}(\Delta t) \qquad 3.13b$$

Region C:

$$p_{D3}{}_{r_{Di}}^{k+1} = p_{D3}{}_{r_{Di}}^{t_k} + \frac{3}{2}H_3\left(t_k, r_{Di}, p_{D3}{}_{r_{Di}}^{t_k}\right)(\Delta t) - \frac{1}{2}H_3\left(t_{k-1}, r_{Di}, p_{D3}{}_{r_{Di}}^{t_{k-1}}\right)(\Delta t) \qquad 3.13$$

$$H_3\left(r_{D,i}, t_k, p_{D3}(t_k, r_{D,i})\right)\Big|_{(t_k,\ r_{D,i})} = (\eta_{D3})W_{i,k}$$

and

$$H_3(r_{Di}, t_{k-1}, p_{D3}(r_{Di}, t_{k-1}))\Big|_{(t_{k-1},\ r_{Di})} = (\eta_{D3})\bar{W}_{i,k}$$

$$p_{D3}{}_{r_{Di}}^{k+1} = p_{D3}{}_{r_{Di}}^{t_k} + \frac{3}{2}(\eta_{D3})W_{i,k}(\Delta t) - \frac{1}{2}(\eta_{D3})\bar{W}_{i,k}(\Delta t) \qquad 3.13c$$

3.6.2. Simulation results and discussion.

In this section, the simulation results are presented for pressure build-up due to CO_2 injection in a saline aquifer. To obtain these figures, the following table with input parameters where used.

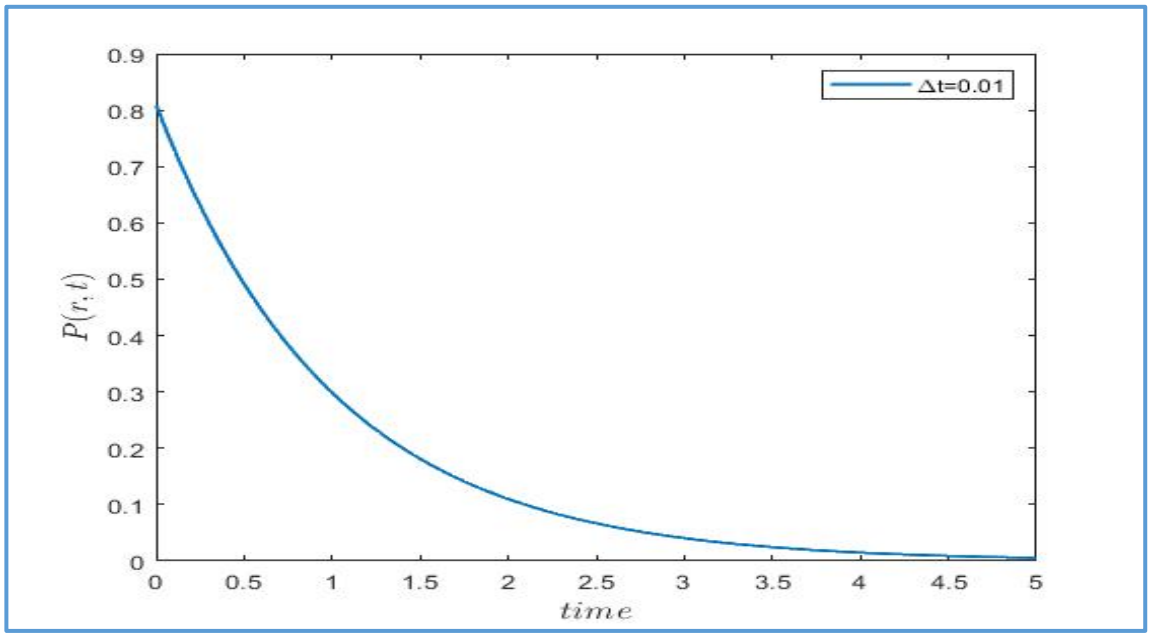

Figure 3-2: P vs. T plot of pressure dissipation over time after switching off the injection pump.

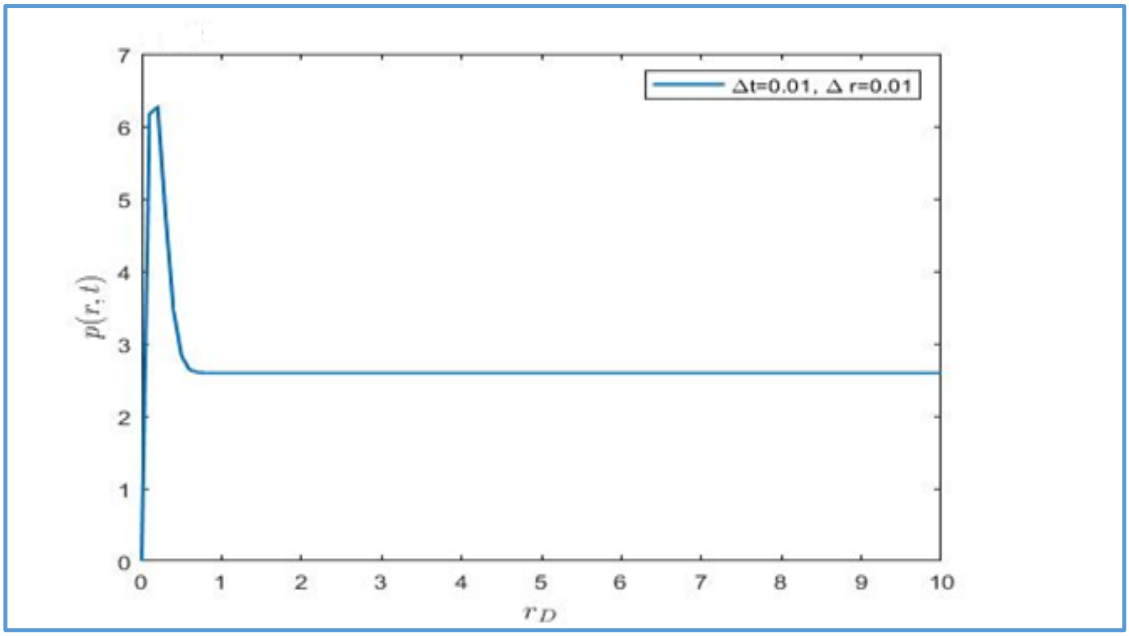

Figure 3-3: P vs. r plot of pressure dissipation in region 1.

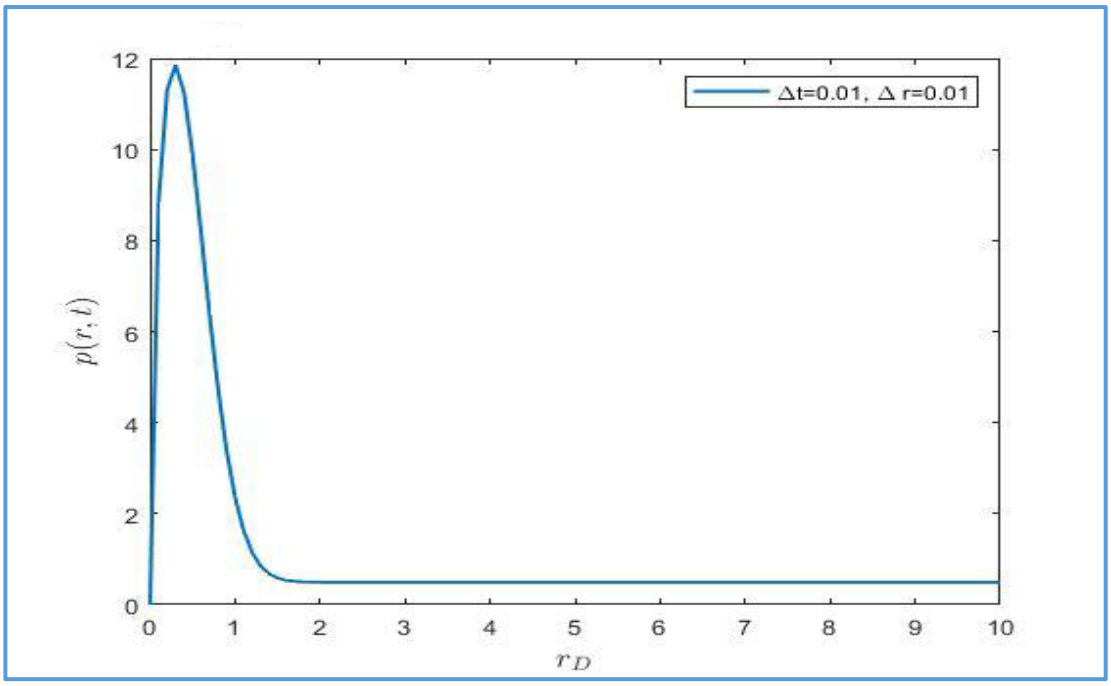

Figure 3-4: Plot of p vs. r in region 2 (two phase B-L flow)

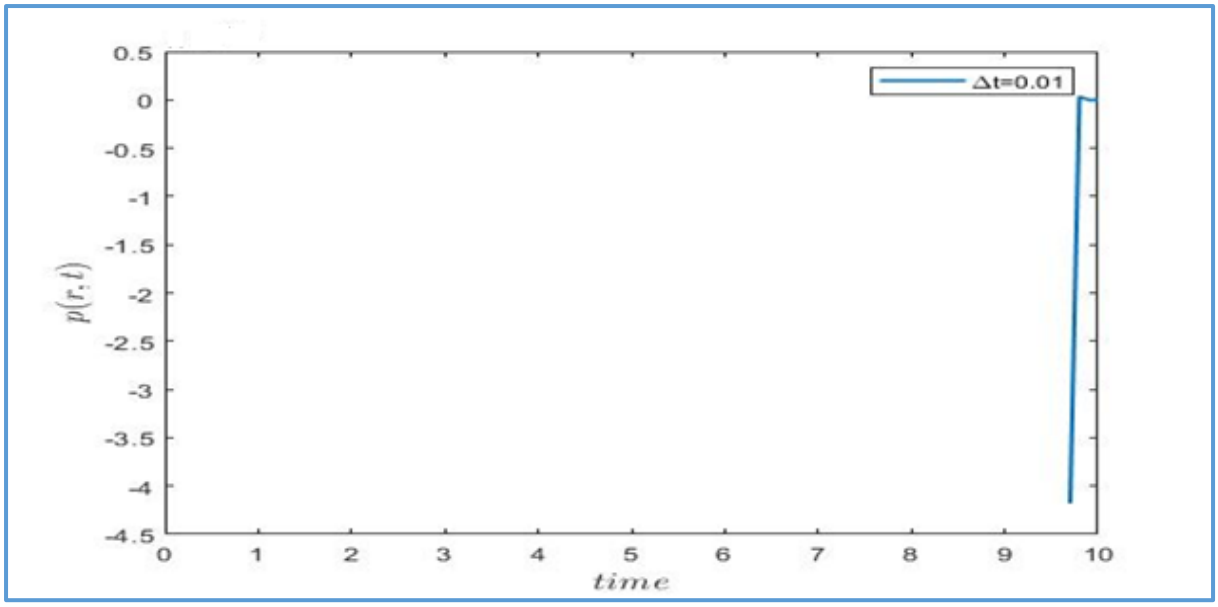

Figure 3-5: Plot of p vs t – region 3 (Late pulse).

3.7. Conclusion.

In this chapter, we considered a highly simplified model for CO_2 injectivity to evaluate and predict spatial behavior and transient pressure responses. We have assessed the impact of different saturation regions to obtain logical approximations of the pressure build-up solutions. The primary attention here is the interplay between pressure and space over time.

The model results agree with the hypothesis that fluid injectivity causes pressure build-up in a saline reservoir. The build-up pressure is highest at the near Well region, encompassing region one of the conceptual models, consistent with the stress propagation theory under hydraulic loading (Horner, 1951). Secondly, the model results suggest a considerable drop in pressure beyond the immediate region of the injection flux's area of influence (Pickup et al., 2012). This is evident in the disappearing pressure pulse (Figure 3-5) for region three (far field) due to injection.

The following can be summed:

- CO_2 injection causes displacement of reservoir fluids and expansion of pores which results in pressure build-up.
- The pressure build-up is affected by the saturation profile for each region. In region A, the CO_2 saturation is taken as one responsible for the highest magnitude of pressurization. The initial value of the pressure is decreased by a factor of 0.5 at the

saturation front of region A. This means that region B at this time would already be pressurized by an equivalent factor (0.5 of original injection pressure).

- The pressure shock generated at the inlet of the injection well creates a pulse that can be instantaneously picked up at the reservoir boundaries. This is due to wave propagation through the fluid-filled reservoir, which decreases in magnitude through space (Figure 3-5).

CHAPTER FOUR: MODELLING PRESSURE BUILD-UP WITH POWER LAW – CAPUTO FRACTIONAL DERIVATIVE.

4.1. Introduction

The impacts of climate change continue to threaten the future of our ecology and adaptation to life on Earth. Avoiding irreversible and potentially devastating consequences requires urgent and profound offsetting of the current CO_2 emissions trend. Power generated through burning fossil fuels accounts for 26% of annual emissions, and decarbonizing this sector requires declining coal and petroleum demand. Unfortunately, fossil fuels are projected to still provide 50% of our total energy demand by 2030. The release of CO_2 from heavy point source emitters can be captured and sequestered to meet the net zero 2050 target, and Carbon Capture and Storage (CCS) in geological formations is considered a suitable approach (Cook and Cook, 2005). However, rigorous, and accurate monitoring, founded on advanced sciences, is necessary to guarantee the safety of CCS, given the long-time spans and volumes anticipated.

Our knowledge of geological sequestration in saline aquifers has steadily advanced over the past decade (Ringrose, 2020). Furthermore, there is a growing scientific, industrial, and legislative consensus to deploy CCS commercially. Techno-economic analysis suggests that there are more reservoir assessment and validation solutions than it is with capture and transport. Even though most innovation and predictions heavily depend on simulation (McCoy, 2005), lessons learned in pilot plants (Michael et al., 2009; Eiken et al., 2011) suggest that accurate prediction of pressure dissipation due to CO_2 injectivity, combined with detailed site characterization and monitoring is necessary to prove storage capacity and containment. One of the objectives is to determine safe reservoir injectivity. In reservoir risk assessment, an important goal is to identify, evaluate and mitigate the effects of a high reservoir pressure. These effects include leakage, fault reactivation, caprock damage, and microseismicity.

Qualified saline reservoirs become scheduled for injection planning after in-depth characterization. The build-up of pore pressure during CO_2 injection calls for assessing the geomechanical response of the formation rocks in the context of triggering damage on the cap rock and reactivating existing rocks. This requires developing powerful assessment tools that can fully describe the fate of CO_2 injection in a saline formation and numerical simulations. Some of these tools are used for: screening candidates' sites (Bachu, 2003)

(Wendt et al., 2022) and predictive modelling for assessing long-term storage performances (CQUESTRA, 2008; Middleton et al., 2020; Roussanaly et al., 2020). As a result, there is an increase in the demand and development of numerical models that accurately represent real-world reservoir conditions (Pruess et al., 2007, Langhi et al., 2019, Postma et al., 2021). Numerical models have become invaluable in simulating the solutions of master Partial Differential Equations (PDEs) is commonly used to describe flow and pressure diffusivity in saline aquifers and porous mediums. In CCS simulation research, numerical experiments have significantly contributed to our understanding of the constraints to the fate of CO_2 underground, and this includes; two-phase immiscible flow (Hoteit and Firoozabadi, 2008), reservoir heterogeneity (Shao et al., 2022), salt precipitation (Kim and Sinton, 2013). Geomechanical response to reservoir pressurization (Rutqvist and Myer, 2020) and well-bore heat transfer (Li et al., 2017). Even though these models can incorporate detailed rock relationships, they require intense computing, which makes them hard to apply directly. Secondly, the PDEs that describe flow and pressure build-up are idealized models based on the classical mechanics of mass, momentum, and energy conservation. The permeability distribution governs CO_2 migration; heterogeneity imposes unique properties on the fluid's behaviour, e.g., viscosity. When the fluid, the reservoir material, and memory are considered, the resulting stress-strain relationship due to pressure build-up is non-linear (Zimmerman, 1986). This variation which can be lateral or vertical, is contextualized as memory.

Reservoir parameters are sensitive to geological heterogeneity, and the efforts constitute an active area of research on reservoir processes. This includes CO_2 injection-induced stress perturbation and pressure diffusivity, which is equally dependent on the history of the fluid in the formation. For example, injecting CO_2 into tight sand reservoirs results in a non-Darcy flow for which the classical derivative will yield erroneous results. To model and predict the fate of such systems required researchers to reformulate Darcy's law, using, for example, fractional formalism, which captures the memory effect imposed by most complex real-world systems. The shortcomings of the classical derivatives have exposed the versatility of memory formalism as a powerful modelling approach (Atangana and Zakia, 2019).

A range of parameters controls pressure build-up and injectivity during CO_2 storage. The classical mass balance models that obey homogenous diffusion consider the key governing parameters to capture and constrain flow and pressure estimates. Increasing the number of

parameters is used in the classical setting to capture the complexities. For example, (Roeloffs 1988) showed that ignoring rock and fluid compressibilities would underestimate the pore pressure build-up in early times. It is also noted that the injection of CO_2 into a saline reservoir is characterized by processes such as partial miscibility (Mathias et al., 2011) a drying out front (Sokama-Neuyam, 2023), with a corresponding reduction in absolute permeability within the well vicinity. As a result, research efforts have led to the developing of some pressure diffusivity solutions. For example, Burton et al. 2008 identified three flow regions that evolve due to CO_2 injection. These results followed their Buckley-Laverrete-based solution in which constant pressure boundaries were assumed. (Mathias et al., 2009) Assumed a sharp interphase model to improve the Buckley Laverrete solution by including the effect of rock and fluid compressibilities. (Mathias, 2011) further extended the pressure build-up equation to account for partial miscibility in formations of finite arial extend.

The greatest strength of fractional calculus over integer order calculus is its ability to describe the memory of the fluid through a reservoir. Firstly, the memory formalism of the Caputo derivative needs to be better posed as it faces a problem of non-locality, singularity, non-uniqueness, and stability. In this chapter, we will focus on applying the Caputo derivative, as in chapter three, to approximate the bottom hole pressure build-up due to CO_2 injection. The Caputo derivative can describe complex processes with memory effects. The long-range dependence of the power law has been used to model systems exhibiting self-similarity and anomalous diffusion (Mohebbi et al., 2019; Almeida et al., 2018). Memory formalism filters out the spectral properties of the fluid flow. While it handles boundary conditions and external impacts with ease, it also uses traditional sciences to describe anomalous flow in complex systems.

While the Caputo derivative has successfully modelled some complex problems, limitations exist. For example, the derivative depends on the entire history of the function being differentiated and not on the time behaviour of the function. Secondly, to apply the Caputo derivative, knowledge of the initial conditions must be explicitly stated. This dependence can be restricted in some practical applications where initial conditions are hard to establish (Atangana and Goufo, 2020). In terms of singularity and stability, the presence of a Caputo derivative in FDE can introduce singularities that affect the numerical method's convergence and stability. Given these limitations, the Caputo derivative has been successfully applied in

modelling complex problems, such as flow in fracture media that obey power law distributions (Bogdanov, 2007; Morakaladi and Atangana, 2023). Researchers in fractional calculus actively address some limitations, and new derivatives have since been suggested, for example, the Caputo-Fabrizio derivative.

This chapter uses the Caputo fractional derivative to develop new numerical models for pressure diffusivity in a saline aquifer during CO_2 injection. As a layout for the work, this chapter proceeds with subsections; conceptual model, power law distribution, numerical analysis, simulations, and discussion.

4.2. Conceptual model, assumptions, and mathematical formulation

This section describes the concept of CO_2 injection through a vertical well open in a saline aquifer. The model in question describes the flow through a fractured aquifer.

4.2.1. Assumptions

The formation is assumed to be uniform in thickness, isothermal, isotropic, and under constant rate injection. In addition, the approach ignores the effects of gravity and capillary forces, while the fluid and rock compressibilities are given as constants. After injections, the difference in density gives rise to a buoyancy-driven flow of the less dense CO_2 up dip until the mobile plume encounters the cap rock.

Lastly and more importantly, this model assumes a flow from matrix into the fractures.

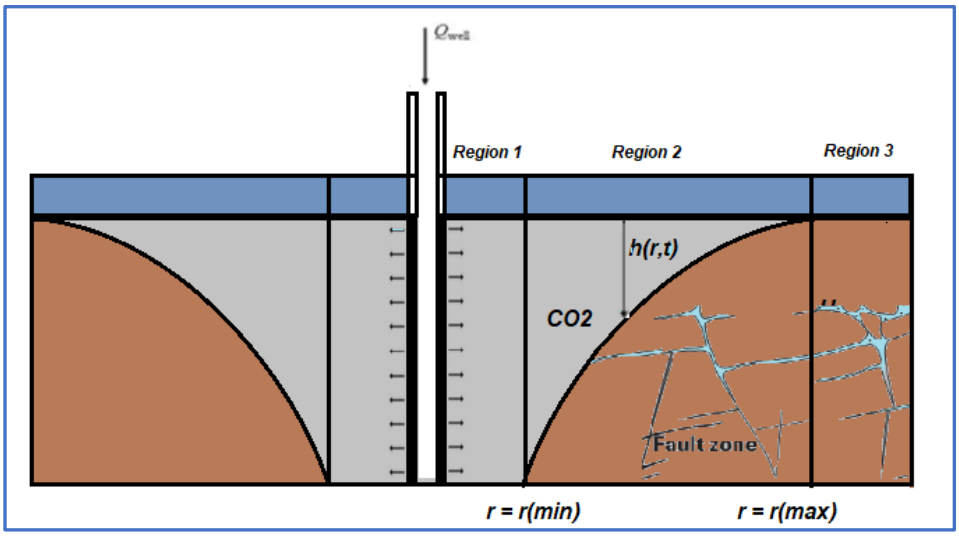

Figure 4-1: Conceptual model for anomalous pressure diffusivity (fracture flow)

Power laws describe relationships where a change in one-quantity results in a proportional change in another quantity, irrespective of the starting amounts. The applications of powers laws in scholarly research is diverse (Bar-Yam, 2010, Bauke, 2007), and their occurrence in data sets of a diverse range of systems, e.g., biological, planetary, and fluid transport, all point to the success achieved in exploring the capabilities of power laws in predictive modelling. Furthermore, the space dimensions of the power law can be damaging, fractional, or optimistic, to which effect is a limitless possibility for numerical experimentation, mainly as applied in fractional (Figure 4.1), fractal, and fractal-fractional power-law memory formulations (Giuseppe and caputo, 2010; Gomez-Aguilar and Atangana, 2018; Atangana and Zakia, 2019). Power laws have a long tail dependency that can help to reveal underlying regularities in complex systems, such as fracture networks in typical saline (Zeighami et al., 2022).

4.4. Power law distribution

The power law Kernel also known as the Pareto kernel, is generally characterized by the high volume of data mobilized for extreme values due to its heavy tail distribution. The power law kernel is limited in that it has a non-locality that cannot be directly inferred and is scale-invariant (Atangana and Sonal, 2018). However, it has found use and success in many traditional and fractional calculus applications, such as network analysis, where affinities are prioritized for a select data grouping at specific times. Fractional calculus has opened many research avenues involving complex systems with non-local and memory-dependent interplays. For example, in geologic reservoirs, capillary pressure controls the saturation distribution of fluids through an inverse proportionality relationship with the pore throat radius, $equation\ 4.1.0$ The graph of fluid volumes in pores against pore throat radius exhibits a long tail dependence, suggesting less entrapment for large values of pore throat radius (Raeini et al., 2015).

$$P_c = 2\sigma \cos\theta R \qquad 4.1.0$$

The implications of this dependence are of practical application in hydrocarbon exploitation and carbon dioxide injection problems.

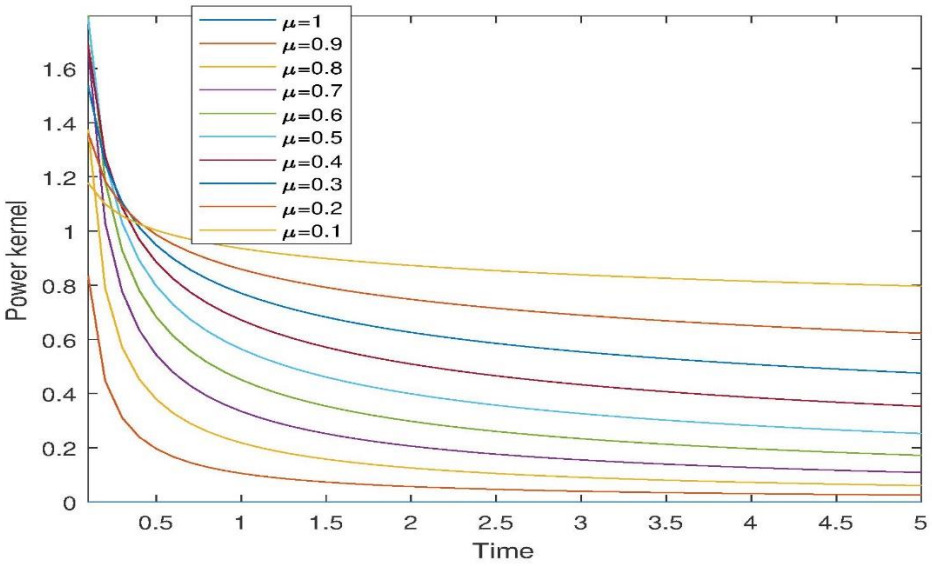

Figure 4-2: Graph of Power law kernel

4.3. Power law and pressure diffusivity in CO2 storage

Understanding and succinct representation of scaling properties can unveil underlying relationships between system structure and response functions, improve the parameterization of natural variability and heterogeneity, and help us address societal needs by effectively merging knowledge acquired at different scales.

4.5. Fractional derivatives based on power kernel.

This section provides a systemic method used to compute the fractional differential operator based on the power law kernel. Two prominent examples are stated in literature: the Riemann Lowville fractional operator and Caputo fractional operator. Both models take their bases in the convolution theory, which can be verified via the Laplace transform. While both models vary only by changing the position of the first derivative$p^{'}$, the practical implications are not to be undermined. Below stated are the two fractional derivatives based on power law, Riemann-Liouville and Caputo derivative.

$$ {}^{RL}_{0}D^{\alpha}_{t}p(t) = \frac{1}{\Gamma(1-\alpha)}\frac{d}{d\tau}\int_{0}^{t} p(\tau)(t-\tau)^{-\alpha}\,d\tau, \qquad t>0, 0<\alpha\leq 1 \tag{4.1.1}$$

$$ {}^{C}_{0}D^{\alpha}_{t}p(t) = \frac{1}{\Gamma(1-\alpha)}\int_{0}^{t}\frac{d}{d\tau}p(\tau)(t-\tau)^{-\alpha}d\tau, \qquad t>0, 0<\alpha\leq 1 \tag{4.1.2}$$

$$\Psi(t) * p(t) = \int_0^x \Psi(t).\, p(t-\tau)\, d\tau, \qquad 4.1.3$$

As a convolution, $(Eq.\, 3.1\ and\ 3.2)$, can be written as

$$\frac{d}{dt}\left(\Psi(t) * \frac{t^{-\alpha}}{1-\alpha}\right), t > 0, 0 < \alpha \leq 1 \qquad 4.1.4$$

$$\frac{d}{dt}\Psi(t) * \frac{t^{-\alpha}}{(1-\alpha)}, t > 0, 0 < \alpha \leq 1$$

Generally, the derivative $d\Psi/dt$ approximates the function $\Psi(t)$ within an interval. The first derivative Ψ' can be viewed as a blurring operation whereby the inverse process known as integration recovers the original function. This process is one of two fundamental theorems of calculus. A simple but practical analogy of the two fractional operators is described:

- In the Riemann Lowville case, first, apply a filter (power law kernel) to function $\Psi(t)$, then blur the outcome. With the Caputo derivative, we observe a different sequence of the same processes, i.e.,
- Firstly, blur the function, and then apply a filter to the blurred outcome.

On this accord, one can see that the Caputo formulation preserves memory better than the Riemann Louisville power derivative.

4.5.1. The Riemann Louisville Fractional Derivative

The Riemann Louisville derivative is one of the most popular non-integer derivatives, extensively applied in modelling real-world problems (Loverro et al., 2004; Sun, 2018) used a space-time fractional Darcy law based on the Riemann Louisville derivative to capture the impact of various flow regimes on pressure gradients produced by heterogeneous and fractured porous reservoirs. However, the Riemann Louisville derivative embodies several properties that limit its success in modelling real-world problems (Sousa and Oliviera, 2020); and review notes (Almeida et al., 2018): firstly, it notably does not require a function to be differentiable nor continuous at the origin. The Riemann Louisville fractional derivative of a constant is not zero, which does not fit practically. This is because, at the origin, some functions, e.g., exponential and the Mittag-Leffler functions, are constant, meaning their fractional derivative with Riemann is non-zero, creating a state of singularity (Atangana and Secer, 2013). We can state the example of pressure build-up due to CO2 storage in a saline

aquifer. The origin (well) is defined by a constant pressure boundary, where pressure build-up is constant, implying the rate of change of the pressure gradient is zero, which the Riemann Louisville derivative will not describe.

This derivative is a classical derivative as can be shown below.

$$Y(t) = \int_0^t \Psi(t) \frac{(t-\tau)^{-\alpha}}{\Gamma(1-\alpha)} d\tau, \tag{4.1.5}$$

Taking the Riemann Louisville derivation, we have that,

$${}^{RL}_{0}D_t^{\alpha}\Psi(t) = \frac{d}{dt}Y(t). \tag{4.1.6}$$

In this form, the derivative can be analyzed by the first principle, such that at the origin when $t = t_0$

$${}^{RL}_{0}D_t^{\alpha}\Psi(t_0) = \lim_{t \to t_0} \frac{\Psi(t) - \Psi(t_0)}{t - t_0}. \tag{4.1.7}$$

This defines the local character bestowed upon the Riemann Louisville (RL) fractional derivative.

4.5.2. The Caputo Fractional Derivative

On the other hand, the Caputo fractional derivative possesses properties more suitable for modelling real-world problems. From its formulation, one can appreciate the requirement of the function's differentiability, which will always be valid for as long as continuity exists (Atangana and Secer, 2013). Caputo first formulated his derivative in 1965, guided by experimental results on elastic media research, which has applications in a wide range of fields, including problems in poor mechanics, engineering, and biological sciences where many of the processes are based on the continuum principle. Often than not, real-world scenarios and problem modelling involve plotting field data and using a suitable mathematical model to describe and solve for parameters. Often, the graphs are continuous, and the function is differentiable for the time of interest to the investigator. According to its definition, the Caputo derivative is an integral, and from traditional calculus, the following can be stated.

$$\int_0^t \Psi'(\tau) d\tau = \Psi(t) - \Psi(0), \tag{4.1.8}$$

Whereas Riemann formulation in a classical sense would produce

$$\frac{d}{dt}\int_0^t \Psi(\tau)d\tau = \Psi(t) \qquad 4.1.9$$

Which always recovers the original function.

Preserving the initial condition in the Caputo formulation highlights the strength of an integral over a derivative. Any process should have a starting point and an end. The ability to capture the accumulated history has practical implications in modelling real-world problems where the issue of determining an inverse is required to complete most solutions.

The Caputo derivative better handles the issue of the initial condition, which appears clearly in the CO_2 injection problem described below in the conceptual model and procedure we will employ. In this chapter, we therefore, will use the Caputo definition to investigate the pressure diffusivity model, which predicts the pressure build-up in a saline aquifer due to CO_2 storage. Before presenting the numerical scheme of the associated Cauchy problem, we present the integral of the Caputo fractional derivative.

Firstly, we recall the Caputo derivative as given by eq. 3.2.

$${}_0^C D_t^\alpha P(t) = \frac{1}{\Gamma(1-\alpha)}\int_0^t \frac{d}{d\tau}P(\tau)(t-\tau)^{-\alpha}d\tau, \qquad t > 0, 0 < \alpha \leq 1$$

Where $P \in]0,1]$

We assume the solution given by the right-hand side to be given by the function H as

$$H\big(t, x, P(t,x)\big),$$

So that we have

$${}_0^C D_t^\alpha P(t) = H\big(t, x, P(t,x)\big)$$

Where the function $H\big(t, x, P(t,x)\big)$ is two times differentiable.

$$\frac{1}{\Gamma(1-\alpha)}\int_0^t \frac{d}{d\tau}P(\tau)(t-\tau)^{-\alpha}d\tau = H\big(t, x, P(t,x)\big) \qquad 4.2.0$$

We apply the Laplace transform on both sides.

$$\mathcal{L}\left(\frac{1}{\Gamma(1-\alpha)}\int_0^t \frac{d}{d\tau}p(\tau)(t-\tau)^{-\alpha}d\tau\right) = \mathcal{L}\left(H\big(t, x, p(t,x)\big)\right) \qquad 4.2.1$$

Which yields

$$s^{\alpha}\tilde{p}(s) - p^{\alpha-1}p(0) = \mathcal{L}\left(H\big(t,x,p(t,x)\big)\right)(s), \tag{4.2.2}$$

Where s is the Laplace variable and simplifying gives,

$$\tilde{p}(s) = \frac{1}{s}p(0) + \frac{1}{s^{\alpha}}\mathcal{L}\left(H\big(t,x,p(t,x)\big)\right)(s). \tag{4.2.3}$$

Using the convolution theory, we obtain

$$\frac{1}{\Gamma(\alpha)}\int_0^t H\big(t,x,p(t,x)\big)(t-\tau)^{\alpha-1}\,d\tau = p(t) - p(0), \tag{4.2.4}$$

And then finally, the space-time fractional integral associated with the Caputo fractional derivative is

$${}_0^C I_t^{\alpha} f(x) = \frac{1}{\Gamma(1-\alpha)}\int_0^t \frac{d}{d\tau}P(\tau)(t-\tau)^{-\alpha}d\tau \tag{4.2.5}$$

4.5.3. Derivation of numerical scheme for the Caputo derivative

In this section, we derived and present a numerical approximation for the Caputo derivative. Firstly, we recall the derivative $(Eq.4.1.2)$ and consider the time step:$t = t_{k+1} = (k+1)\Delta t$, $\forall\, k \in [0,1,2\ldots]$

$${}_0^C D_t^{\alpha} f(x)|_{t_{n+1}} = \frac{1}{\Gamma(1-\alpha)}\int_0^t f'(\tau)(t_{n+1}-\tau)^{-\alpha}d\tau \tag{4.2.6}$$

$${}_0^C D_t^{\alpha} f(x)|_{t_{n+1}} = \frac{1}{\Gamma(1-\alpha)}\sum_{j=0}^{k}\int_{t_j}^{t_{j+1}} \frac{f\big(t_{j+1}\big) - f\big(t_j\big)}{\Delta t}(t_{n+1}-\tau)^{-\alpha}d\tau \tag{4.2.7}$$

$${}_0^C D_t^{\alpha} f(x)|_{t_{n+1}} = \frac{1}{\Gamma(1-\alpha)}\sum_{j=0}^{k}\frac{f\big(t_{j+1}\big) - f\big(t_j\big)}{\Delta t}\int_{t_j}^{t_{j+1}}(t_{n+1}-\tau)^{-\alpha}d\tau \tag{4.2.8}$$

Integrating and simplifying further, we obtain the final numerical approximation as

$${}_0^C D_t^{\alpha} f(x)|_{t_{n+1}} = \frac{\Delta t^{-\alpha}}{\Gamma(2-\alpha)}\sum_{j=0}^{k} f\big(t_{j+1}\big) - f\big(t_j\big)\{(n-j+1)^{1-\alpha} - (n-j)^{1-\alpha}\} \tag{4.2.9}$$

Which is the numerical approximation scheme associating the Caputo derivative.

4.6. Numerical Solution of the Pressure Diffusivity Equation based on the Caputo derivative.

This section will demonstrate and present the numerical procedure and solution for pressure build-up modelled by the Caputo derivative. The functional approximation will be completed using the two-step LaGrange polynomial, as demonstrated by Atangana and Toufik.

We recall the Caputo derivative.

$$ {}_0^C D_t^\alpha f(x)|_{t_{n+1}} = \frac{1}{\Gamma(1-\alpha)} \int_0^t f'(\tau)(t_{n+1}-\tau)^{-\alpha} d\tau, \text{t>0} $$

As in the previous chapter, the set of pressure diffusivity equations in the three saturations will be considered in the Caputo sense as follows. A numerical analysis for the pressure build-up model using the two-step Lagrange polynomial method is presented below as

$$ {}_0^C D_t^\alpha P_{D1}(x) = H\big(t, r, P_{D1}(t,r)\big). \qquad 4.3.0a $$

$$ {}_0^C D_t^\alpha P_{D2}(x) = H\big(t, r, P_{D2}(t,r)\big) \qquad 4.3.0b $$

$$ {}_0^C D_t^\alpha P_{D3}(x) = H\big(t, r, P_{D3}(t,r)\big) \qquad 4.3.0c $$

Considering the associated Cauchy problem, we can write the system as follows

$$ \begin{cases} {}_0^C \mathcal{D}_t^\alpha P_{D1}(t, r_D) = H_1\big(t, r_D, P_{D1}(t, r_D)\big), t > 0 \\ {}_0^C \mathcal{D}_t^\alpha P_{D2}(t, r_D) = H_2\big(t, r_D, P_{D2}(t, r_D)\big), t > 0 \\ {}_0^C \mathcal{D}_t^\alpha P_{D3}(t, r_D) = H_3\big(t, r_D, P_{D3}(t, r_D)\big), t > 0 \\ P_{(D1,D2,D3)}(r_D, 0) = 0, t = 0 \end{cases} \qquad 4.3.1 $$

The functions P_{D1}, P_{D2}, $and\ P_{D3}$ are the fractional differential equations associated with pressure build-up for region 1, region 2, and region 3, as labeled in the conceptual model.

Following the fundamental theorem of calculus with the stated initial condition, we can convert the set of equations using the Caputo integral as follows into integral equations.

$$ P_{D1}(t, r_D) - P_{D1}(0, r_D) = \frac{1}{\Gamma(\alpha)} \int_0^t H_1\big(\tau, r, P_{D1}(t, r_D)\big)(t-\tau)^{\alpha-1} d\tau \qquad 4.3.2a $$

$$P_{D2}(t,r_D) - P_{D2}(0,r_D) = \frac{1}{\Gamma(\alpha)}\int_0^t H_2\big(\tau, r, P_{D2}(t,r_D)\big)(t-\tau)^{\alpha-1}d\tau \quad 4.3.2b$$

$$P_{D3}(t,r_D) - P_{D3}(0,r_D) = \frac{1}{\Gamma(\alpha)}\int_0^t H_3\big(\tau, r, P_{D3}(t,r_D)\big)(t-\tau)^{\alpha-1}d\tau \quad 4.3.2c$$

Substituting$t = t_{k+1} = (k+1)\Delta t, \forall\, k \in [0,1,2\ldots]$

$$P_{D1}(t_{k+1},r_D) - P_{D1}(0,r_D) = \frac{1}{\Gamma(\alpha)}\int_0^{t_{k+1}} H_1\big(\tau, r, P_{D1}(t,r_D)\big)(t_{k+1}-\tau)^{\alpha-1}d\tau \quad 4.3.3a$$

$$P_{D2}(t_{k+1},r_D) - P_{D2}(0,r_D) = \frac{1}{\Gamma(\alpha)}\int_0^{t_{k+1}} H_2\big(t, r, P_{D2}(t,r_D)\big)(t_{k+1}-\tau)^{\alpha-1}d\tau \quad 4.3.3b$$

$$P_{D3}(t_{k+1}) - P_{D3}(0,r_D) = \frac{1}{\Gamma(\alpha)}\int_0^{t_{k+1}} H_3\big(\tau, r, P_{D3}(t,r_D)\big)(t_{k+1}-\tau)^{\alpha-1}d\tau \quad 4.3.3c$$

Substituting $t = t_k = (k)\Delta t, \forall\, k \in [0,1,2\ldots]$

$$P_{D1}(t_k,r_D) - P_{D1}(0,r_D) = \frac{1}{\Gamma(\alpha)}\int_0^{t_k} H_1\big(\tau, r, P_{D1}(t,r_D)\big)(t_{k+1}-\tau)^{\alpha-1}d\tau \quad 4.3.4a$$

$$P_{D2}(t_k,r_D) - P_{D2}(0,r_D) = \frac{1}{\Gamma(\alpha)}\int_0^{t_k} H_2\big(\tau, r, P_{D2}(t,r_D)\big)(t_{k+1}-\tau)^{\alpha-1}d\tau \quad 4.3.4b$$

$$P_{D3}(t_k,r_D) - P_{D3}(0,r_D) = \frac{1}{\Gamma(\alpha)}\int_0^{t_k} H_3\big(\tau, r, P_{D3}(t,r_D)\big)(t_{k+1}-\tau)^{\alpha-1}d\tau \quad 4.3.4c$$

Before making use of a polynomial approximation, we first apply the Caputo integral as follows

$${P_{D1}}^{k+1} = P_{D1}(0,r_D) + \frac{1}{\Gamma(\alpha)}\sum_{m=0}^{k}\int_{t_m}^{t_{m+1}} H_1\big(\tau, r_{Di}, P_{D1}(\tau,r_{Di})\big)(t_{k+1}-\tau)^{\alpha-1}d\tau \quad 4.3.5a$$

$$P_{D2}{}^{k+1} = P_{D2}(0, r_D) + \frac{1}{\Gamma(\alpha)} \sum_{m=0}^{k} \int_{t_m}^{t_{m+1}} H_2\big(\tau, r_{Di}, P_{D2}(t, r_{Di})\big)(t_{k+1} - \tau)^{\alpha-1} d\tau \quad \text{4.3.5b}$$

$$P_{D3}{}^{k+1} = P_{D3}(0, r_D) + \frac{1}{\Gamma(\alpha)} \sum_{m=0}^{k} \int_{t_m}^{t_{m+1}} H_3\big(\tau, r_{Di}, P_{D3}(t, r_{Di})\big)(t_{k+1} - \tau)^{\alpha-1} d\tau \quad \text{4.3.5c}$$

4.6.1. Numerical approximation with Lagrange polynomial

In this section, we will use the LaGrange polynomial method within the interval $[t_m, t_{m+1}]$ to approximate the function. For the problem, the scheme is given as follows:

$$\begin{aligned} &H\big(t, r_{Di}, P_D(t, r_{Di})\big) \\ &\quad \approx \frac{H\big(r_{Di}, t_m, P_D(r_{Di}, t_m)\big)}{h}(\tau - t_{m-1}) \\ &\quad - \frac{H\big(r_{Di}, t_{m-1}, P_D(r_{Di}, t_{m-1})\big)}{h}(\tau - t_m) \end{aligned}$$

Which can be simply written as

$$H\left(t, r_{Di}, P_{D}{}_{r_{Di}}^{t}\right) \approx H\left(\frac{r_{Di}, t_m, P_{D_i}{}^{t_m}}{h}(\tau - t_{m-1}) - \frac{r_{Di}, t_{m-1}, P_{D_i}{}^{t_{m-1}}}{h}(\tau - t_m)\right) \quad \text{4.3.6}$$

Where h is the time step.

4.6.2. Numerical analysis

Recalling the original systems of equation, we can substitute the approximation as follows

$$\begin{aligned} P_{D1}{}^{k+1} &= P_{D1}(0, r_D) \\ &\quad + \frac{1}{\Gamma(\alpha)} \sum_{m=0}^{k} \int_{m_k}^{t_{m+1}} \left\{ \frac{H_1\big(r_{Di}, t_m, P_{D1_i}{}^{t_m}\big)}{h}(\tau - t_{m-1}) \right. \\ &\quad \left. - \frac{H_1\big(r_{Di}, t_{m-1}, P_{D1_i}{}^{t_{m-1}}\big)}{h}(\tau - t_m) \right\} (t_{k+1} - \tau)^{\alpha-1} d\tau \end{aligned} \quad \text{4.3.7a}$$

$$P_{D2}{}^{k+1} = P_{D2}(0, r_D) \qquad \text{4.3.7b}$$
$$+ \frac{1}{\Gamma(\alpha)} \sum_{m=0}^{k} \int_{t_m}^{t_{m+1}} \left\{ \frac{H_2\left(r_{Di}, t_m, P_{D2}{}_i^{t_m}\right)}{h} (\tau - t_{m-1}) \right.$$
$$\left. - \frac{H_2\left(r_{Di}, t_{m-1}, P_{D2}{}_i^{t_{m-1}}\right)}{h} (\tau - t_m) \right\} (t_{k+1} - \tau)^{\alpha-1} d\tau$$

$$P_{D3}{}^{k+1} = P_{D3}(0, r_D) \qquad \text{4.3.7c}$$
$$+ \frac{1}{\Gamma(\alpha)} \sum_{m=0}^{k} \int_{t_m}^{t_{m+1}} \left\{ \frac{H_3\left(r_{Di}, t_m, P_{D3}{}_i^{t_m}\right)}{h} (\tau - t_{m-1}) \right.$$
$$\left. - \frac{H_3\left(r_{Di}, t_{m-1}, P_{D3}{}_i^{t_{m-1}}\right)}{h} (\tau - t_m) \right\} (t_{k+1} - \tau)^{\alpha-1} d\tau$$

The equations can further be rearranged as

$$P_{D1}{}^{k+1} = P_{D1}(0, r_D) \qquad \text{4.3.8a}$$
$$+ \frac{1}{\Gamma(\alpha)} \sum_{m=0}^{k} \frac{H_1\left(r_{Di}, t_m, P_{D1}{}_i^{t_m}\right)}{h} \int_{t_m}^{t_{m+1}} (\tau - t_{m-1})(t_{k+1} - \tau)^{\alpha-1} d\tau$$
$$- \frac{1}{\Gamma(\alpha)} \sum_{m=0}^{k} \frac{H_1\left(r_{Di}, t_{m-1}, P_{D1}{}_i^{t_{m-1}}\right)}{h} \int_{t_m}^{t_{m+1}} (\tau - t_m)\,(t_{k+1} - \tau)^{\alpha-1} d\tau$$

$$P_{D2}{}^{k+1} = P_{D2}(0, r_D) \qquad \text{4.3.8b}$$
$$+ \frac{1}{\Gamma(\alpha)} \sum_{m=0}^{k} \frac{H_2\left(r_{Di}, t_m, P_{D2}{}_i^{t_m}\right)}{h} \int_{t_m}^{t_{m+1}} (\tau - t_{m-1})(t_{k+1} - \tau)^{\alpha-1} d\tau$$
$$- \frac{1}{\Gamma(\alpha)} \sum_{m=0}^{k} \frac{H_2\left(r_{Di}, t_{m-1}, P_{D2}{}_i^{t_{m-1}}\right)}{h} \int_{t_m}^{t_{m+1}} (\tau - t_m)\,(t_{k+1} - \tau)^{\alpha-1} d\tau$$

$$P_{D3}{}^{k+1} = P_{D3}(0, r_D) \qquad \text{4.3.8c}$$
$$+ \frac{1}{\Gamma(\alpha)} \sum_{m=0}^{k} \frac{H_3\left(r_{Di}, t_m, P_{D3}{}_i^{t_m}\right)}{h} \int_{t_m}^{t_{m+1}} (\tau - t_{m-1})(t_{k+1} - \tau)^{\alpha-1} d\tau$$
$$- \frac{1}{\Gamma(\alpha)} \sum_{m=0}^{k} \frac{H_3\left(r_{Di}, t_{m-1}, P_{D3}{}_i^{t_{m-1}}\right)}{h} \int_{t_m}^{t_{m+1}} (\tau - t_m)\,(t_{k+1} - \tau)^{\alpha-1} d\tau$$

At this stage, the integrals are simplified and can be evaluated by one of the suitable integration methods. Therefore, the system's integration's part is considered, and the following calculations apply.

Integration

$$\int_{t_k}^{t_{m+1}} (\tau - t_{m-1})(t_{k+1} - \tau)^{\alpha-1} d\tau \qquad 4.3.9a$$

And

$$\int_{t_k}^{t_{m+1}} (\tau - t_m)\,(t_{k+1} - \tau)^{\alpha-1} d\tau \qquad 4.3.9b$$

Expanding the terms, we get

We have two separate terms, and the integrals can be computed by change of variables as follows

$$\int_{t_m}^{t_{m+1}} (\tau - t_{m-1})(t_{k+1} - \tau)^{\alpha-1} d\tau = \int_{t_m}^{t_{m+1}} \tau(t_{k+1} - \tau)^{\alpha-1} d\tau - t_{m-1} \int_{t_m}^{t_{m+1}} (t_{k+1} - \tau)^{\alpha-1}\, d\tau \qquad 4.4.0$$

Firstly, we consider the integral

$$t_{m-1} \int_{t_m}^{t_{m+1}} (t_{k+1} - \tau)^{\alpha-1}\, d\tau$$

And say, let $u = t_{k+1} - \tau$

$$du = dt_{k+1} - d\tau$$

$$du = -d\tau$$

Change of boundaries gives

$u = t_{k+1} - t_m, when\ \tau = t_m$ And $u = t_{k+1} - t_{m+1} = 0, when\ \tau = t_{m+1}$

$$Such\ that$$

$$= \int_{t_{k+m}}^{0} -u^{\alpha-1}\, du = \int_{0}^{t_{k+1}-t_k} u^{\alpha-1}\, du$$

$$= \frac{1}{\alpha} u^{\alpha}]_0^{t_{k+1}-t_k}$$

$$= \frac{t_{m-1}}{\alpha}(t_{k+1} - t_k)^{\alpha} = \frac{h(m-1)}{\alpha}\{h(m+1) - hm\}^{\alpha}$$

Finally, we have that

$$t_{m-1}\int_{m}^{t_{m+1}} (t_{k+1} - \tau)^{\alpha-1}\, d\tau = \frac{h}{\alpha}(m-1)h^{\alpha} = \frac{h^{\alpha}}{\alpha}(m-1)$$

Now, we evaluate the second integral, given as

$$\int_{t_k}^{t_{k+1}} \tau(t_{k+1} - \tau)^{\alpha-1} d\tau$$

The above integral requires the application of a special function, and the solution can be stated by definition as

$$\int_{t_j}^{t_{j+1}} \tau(t_{k+1} - \tau)^{\alpha-1} = t_{j-1}^{\alpha+1}\left\{B(2,\alpha) - B\left(\frac{t_j}{t_{j+1}}, 2, \alpha\right)\right\}$$

Where the solution set is defined for

$$(Complete\ Beta) \qquad B(a,b) = \int_0^1 z^{a-1}\,(1-z)^{b-1} dz$$

and

$$(Incomplete\ Beta) \quad B(z,a,b) = \int_0^z u^{a-1}\,(1-u)^{b-1} du$$

$$\int_{t_j}^{t_{j+1}} (\tau - t_{m-1})(t_{k+1} - \tau)^{\alpha-1} d\tau = t_{j-1}^{\alpha+1}\left\{B(2,\alpha) - B\left(\frac{t_j}{t_{j+1}}, 2, \alpha\right)\right\} - \left(\frac{h^{\alpha+1}}{\alpha}(m-1)\right) \quad 4.4.1$$

Similarly, the procedure evaluates the integral given by $Eq.$ 4.3.9b.

$$\int_{t_k}^{t_{k+1}} (\tau - t_m)\,(t_{k+1} - \tau)^{\alpha-1} d\tau \quad 4.4.2$$

Expanding and rearranging the functions yields

$$\int_{t_j}^{t_{j+1}} (\tau - t_m)(t_{k+1} - \tau)^{\alpha-1} d\tau = \int_{t_j}^{t_{j+1}} \tau(t_{k+1} - \tau)^{\alpha-1} d\tau - t_m \int_{t_j}^{t_{j+1}} (t_{k+1} - \tau)^{\alpha-1}\, d\tau \quad 4.4.3$$

$$\int_{t_j}^{t_{j+1}} (\tau - t_m)(t_{k+1} - \tau)^{\alpha-1} d\tau = t_{j-1}^{\alpha+1}\left\{B(2,\alpha) - B\left(\frac{t_j}{t_j}, 2, \alpha\right)\right\} \quad 4.4.4$$

For simplicity,

$$\int_{t_j}^{t_{j+1}}(\tau - t_m)(t_{k+1} - \tau)^{\alpha-1}d\tau = A_{\alpha,k+1,j} \text{ and}$$

$$\int_{t_j}^{t_{j+1}}(\tau - t_m)(t_{k+1} - \tau)^{\alpha-1}d\tau = B_{\alpha,k+1,j}$$

A numerically computed representation of the solutions are given below

$$A_{\alpha,k+1,j} = \int_{t_j}^{t_{j+1}}(\tau - t_m)(t_{k+1} - \tau)^{\alpha-1}d\tau \qquad 4.4.5a$$

$$= \frac{(h)^{\alpha+1}}{\alpha(\alpha+1)}[(k-m+1)^{\alpha}(k-m+2+\alpha) - (k-m)^{\alpha}(k-m+2 + 2\alpha)]$$

And

$$B_{\alpha,m,j} = \int_{t_j}^{t_{j+1}}(\tau - t_m)(t_{k+1} - \tau)^{\alpha-1}d\tau \qquad 4.4.5b$$

$$= \frac{(h)^{\alpha+1}}{\alpha(\alpha+1)}(k-m+1)^{\alpha+1} - (k-m)^{\alpha}(k-m+1+\alpha)$$

Before discretizing each of the functions $H_1, H_2, \ and \ H_3$, we record the integrals by the simple notation of $A_{\alpha,k+1,j}$ and $B_{\alpha,k+1,j}$ as below.

$$P_{D1,i}{}^{k+1} = P_{D1}(0, r_D) + \frac{1}{\Gamma(\alpha)}\sum_{m=0}^{k}\frac{H_1\left(r_{D,i}, t_m, P_{D1_i}{}^{t_m}\right)}{h}A_{\alpha,k+1,j} - \frac{1}{\Gamma(\alpha)}\sum_{m=0}^{k}\frac{H_1\left(r_{D,i}, t_{m-1}, P_{D1_i}{}^{t_{m-1}}\right)}{h}B_{\alpha,m,j}$$

$$P_{D2,i}{}^{k+1} = P_{D2}(0, r_D) + \frac{1}{\Gamma(\alpha)}\sum_{m=0}^{k}\frac{H_2\left(r_{D,i}, t_m, P_{D2,i}{}^{t_m}\right)}{h}A_{\alpha,k+1,j} - \frac{1}{\Gamma(\alpha)}\sum_{m=0}^{k}\frac{H_2\left(r_{D,i}, t_{m-1}, P_{D2,i}{}^{t_{m-1}}\right)}{h}B_{\alpha,k+1,j}$$

$$P_{D3,i}{}^{k+1} = P_{D3}(0, r_D) + \frac{1}{\Gamma(\alpha)} \sum_{m=0}^{k} \frac{H_3\left(r_{D,i}, t_m, P_{D3,i}{}^{t_m}\right)}{h} A_{\alpha,k+1,j} - \frac{1}{\Gamma(\alpha)} \sum_{m=0}^{k} \frac{H_3\left(r_{D,i}, t_{m-1}, P_{D3,i}{}^{t_{m-1}}\right)}{h} B_{\alpha,k+1,j}$$

Below, the three sets of equations that characterize pressure build-up for each saturation regions are recalled.

$$\frac{\partial^2 P_{D1}}{\partial^2 r} + \frac{1}{r}\frac{\partial P_{D1}}{\partial r_D} = \frac{\partial P_{D1}}{\partial t_D}, 0 < r_D < r_{Ddry}$$

$$\frac{\partial^2 P_{D2}}{\partial^2 r} + \frac{1}{r}\frac{\partial P_{D2}}{\partial r_D} = \frac{1}{F_{\lambda g}\eta_{D2}}\frac{\partial P_{D2}}{\partial t_D}, r_{Ddry} < r_D < r_{DBL}$$

$$\frac{\partial^2 P_{D3}}{\partial^2 r} + \frac{1}{r}\frac{\partial P_{D3}}{\partial r_D} = \frac{1}{\eta_{D3}}\frac{\partial P_{D3}}{\partial t_D}, r_{DBL} < r_D < \infty$$

Recalling$Equ.\ 4.3.1a$, we write

$$H_1\big(t, r_D, P_{D1}(t, r_D)\big) = \frac{\partial^2 P_{D1}}{\partial^2 r} + \frac{1}{r}\frac{\partial P_{D1}}{\partial r_D}$$

$$H_2\big(t, r_D, P_{D2}(t, r_D)\big) = \big(F_{\lambda g}\eta_{D2}\big)\left[\frac{\partial^2 P_{D2}}{\partial^2 r} + \frac{1}{r}\frac{\partial P_{D2}}{\partial r_D}\right]$$

$$H_3\big(t, r_D, P_{D3}(t, r_D)\big) = (\eta_{D3})\left[\frac{\partial^2 P_{D3}}{\partial^2 r} + \frac{1}{r}\frac{\partial P_{D3}}{\partial r_D}\right]$$

At this stage, the central difference scheme discretizes the second-order part. In contrast, the forward Euler scheme is used to discretize the first-order component of the partial differential equation as follows.

$$\big(t, r_D, P_{D1}(t, r_D)\big) = H_1\big(r_{Di}, t_m, P_{D1}{}_i^{t_m}\big)$$

$$P_{D1,i}{}^{k+1} = P_{D1}(0, r_D) + \frac{1}{\Gamma(\alpha)} \sum_{m=0}^{k} \frac{H_1\left(r_{Di}, t_m, P_{D1_i}{}^{t_m}\right)}{h} A_{\alpha,k+1,j} - \frac{1}{\Gamma(\alpha)} \sum_{m=0}^{k} \frac{H_1\left(r_{Di}, t_{m-1}, P_{D1_i}{}^{t_{m-1}}\right)}{h} B_{\alpha,k+1,j}$$

$$p_{D1,i}{}^{k+1} = p_{D1}(0, r_D) + \frac{1}{\Gamma(\alpha)} \sum_{m=0}^{k} \frac{1}{h} \left[\frac{\left(p_{D1,}{}_{i+1}^{m} - 2p_{D1_i}{}^{m} + p_{D1,}{}_{i-1}^{m}\right)}{(\Delta r)^2} + \frac{1}{r} \frac{\left(p_{D1,}{}_{i+1}^{m} - p_{D1,}{}_{i-1}^{m}\right)}{2\Delta r} \right] A_{\alpha,k+1,j} - \frac{1}{\Gamma(\alpha)} \sum_{m=0}^{k} \frac{1}{h} \left[\frac{\left(p_{D1,}{}_{i+1}^{m-1} - 2p_{D1,}{}_{i}^{m-1} + p_{D1,}{}_{i-1}^{m-1}\right)}{(\Delta r)^2} + \frac{1}{r} \frac{\left(p_{D1,}{}_{i+1}^{m-1} - p_{D1,}{}_{i-1}^{m-1}\right)}{2\Delta r} \right] B_{\alpha,k+1,j} \quad \text{4.4.6b}$$

Substituting the integral solutions as given by $Equation.\ 4.4.5a$ and $Equation.\ 4.4.5b$ given as

$$P_{D1,i}{}^{k+1} = P_{D1}(0, r_D) + \frac{(h)^{\alpha+1}}{\Gamma(\alpha+2)} \sum_{m=0}^{k} \left[\frac{\left(P_{D1,}{}_{i+1}^{m} - 2P_{D1_i}{}^{m} + P_{D1,}{}_{i-1}^{m}\right)}{(\Delta r)^2} + \frac{1}{r} \frac{\left(P_{D1,}{}_{i+1}^{m} - P_{D1,}{}_{i-1}^{m}\right)}{2\Delta r} \right] \times [(k-m+1)^{\alpha}(k-m+2+\alpha) - (k-m)^{\alpha}(k-m+2+2\alpha)] - \frac{(h)^{\alpha+1}}{\Gamma(\alpha+2)} \sum_{m=0}^{k} \left[\frac{\left(P_{D1,}{}_{i+1}^{m-1} - 2P_{D1,}{}_{i}^{m-1} + P_{D1,}{}_{i-1}^{m-1}\right)}{(\Delta r)^2} + \frac{1}{r} \frac{\left(P_{D1,}{}_{i+1}^{m-1} - P_{D1,}{}_{i-1}^{m-1}\right)}{2\Delta r} \right] \times [(k-m+1)^{\alpha+1} - (k-m)^{\alpha}(k-m+1+\alpha)] \quad \text{4.4.6}$$

Which is the final numerical solver for pressure build-up in the region one region.

Following the same steps, the equivalent solutions for the second and third saturation regions are obtained.

Region two

$$ {}_0^C\mathcal{D}_t^{\alpha} P_{D2}(t, r_D) = H_2\big(t, r_D, P_{D2}(t, r_D)\big) = \big(F_{\lambda g}\eta_{D2}\big)\left[\frac{\partial^2 P_{D2}}{\partial^2 r} + \frac{1}{r}\frac{\partial P_{D2}}{\partial r_D}\right] $$

$$ {P_{D2,i}}^{k+1} = P_{D2}(0, r_{D,i}) $$
$$ + \frac{1}{\Gamma(\alpha)}\sum_{m=0}^{k}\frac{1}{h}\left\{\big(F_{\lambda g}\eta_{D2}\big)\left[\frac{\left({P_{D2,}}_{i+1}^{m} - 2{P_{D2}}_{i}^{m} + {P_{D2,}}_{i-1}^{m}\right)}{(\Delta r)^2}\right.\right. $$
$$ \left.\left. + \frac{1}{r}\frac{\left({P_{D2,}}_{i+1}^{m} - {P_{D2,}}_{i-1}^{m}\right)}{2\Delta r}\right]\right\}.\int_{t_k}^{t_{k+1}}(\tau - t_{m-1})(t_{k+1} - \tau)^{\alpha-1}d\tau $$
$$ - \frac{1}{\Gamma(\alpha)}\sum_{m=0}^{k}\frac{1}{h}\left\{\big(F_{\lambda g}\eta_{D2}\big)\left[\frac{\left({P_{D2,}}_{i+1}^{m-1} - 2{P_{D2,}}_{i}^{m-1} + {P_{D2,}}_{i-1}^{m-1}\right)}{(\Delta r)^2}\right.\right. $$
$$ \left.\left. + \frac{1}{r}\frac{\left({P_{D2,}}_{i+1}^{m-1} - {P_{D2,}}_{i-1}^{m-1}\right)}{2\Delta r}\right]\right\}\int_{t_k}^{t_{k+1}}(\tau - t_m)\,(t_{k+1} - \tau)^{\alpha-1}d\tau $$

$$ P_{D2,}i^{k+1} = P_{D2}(0, r_{D,i}) \qquad \text{4.4.6b} $$
$$ + \frac{(h)^{\alpha+1}}{\Gamma(\alpha+2)}\sum_{m=0}^{k}\left\{\big(F_{\lambda g}\eta_{D2}\big)\left[\frac{\left({P_{D2,}}_{i+1}^{m} - 2{P_{D2}}_{i}^{m} + {P_{D2,}}_{i-1}^{m}\right)}{(\Delta r)^2}\right.\right. $$
$$ \left.\left. + \frac{1}{r}\frac{\left({P_{D2,}}_{i+1}^{m} - {P_{D2,}}_{i-1}^{m}\right)}{2\Delta r}\right]\right\}[(k-m+1)^{\alpha}(k-m+2+\alpha) - (k-m)^{\alpha}(k $$
$$ - m + 2 + 2\alpha)] $$
$$ - \frac{(h)^{\alpha+1}}{\Gamma(\alpha+2)}\sum_{m=0}^{k}\left\{\big(F_{\lambda g}\eta_{D2}\big)\left[\frac{\left({P_{D2,}}_{i+1}^{m-1} - 2{P_{D2,}}_{i}^{m-1} + {P_{D2,}}_{i-1}^{m-1}\right)}{(\Delta r)^2}\right.\right. $$
$$ \left.\left. + \frac{1}{r}\frac{\left({P_{D2,}}_{i+1}^{m-1} - {P_{D2,}}_{i-1}^{m-1}\right)}{2\Delta r}\right]\right\}.[(k-m+1)^{\alpha+1} - (k-m)^{\alpha}(k-m+1 $$
$$ + \alpha)] $$

Which is the final numerical solution for pressure build-up in region two.

Finally, for region three, we have

$$ {}_0^C\mathcal{D}_t^{\alpha} P_{D3}(t, r_D) = H_3\big(t, r_D, P_{D3}(t, r_D)\big) $$

Where

$$H_3\left(t, r_D, P_{D3}(t, r_D)\right) = (\eta_{D3})\left[\frac{\partial^2 P_{D3}}{\partial^2 r} + \frac{1}{r}\frac{\partial P_{D3}}{\partial r_D}\right]$$

And the numerical solution can be expressed as

$$P_{D3,i}{}^{k+1} = P_{D3}(0, r_{D,i}) \qquad \text{4.4.6c}$$
$$+ \frac{(h)^{\alpha+1}}{\Gamma(\alpha+2)} \sum_{m=0}^{k} \left\{ (\eta_{D3}) \left[\frac{\left(P_{D3,i+1}{}^{m} - 2P_{D3}{}_{i}^{m} + P_{D3,i-1}{}^{m} \right)}{(\Delta r)^2} \right.\right.$$
$$\left.\left. + \frac{1}{r} \frac{\left(P_{D3,i+1}{}^{m} - P_{D3,i-1}{}^{m} \right)}{2\Delta r} \right] \right\} [(k-m+1)^{\alpha}(k-m+2+\alpha) - (k-m)^{\alpha}(k$$
$$- m + 2 + 2\alpha)]$$
$$- \frac{(h)^{\alpha+1}}{\Gamma(\alpha+2)} \sum_{m=0}^{k} \left\{ (\eta_{D3}) \left[\frac{\left(P_{D3,i+1}{}^{m-1} - 2P_{D3,i}{}^{m-1} + P_{D3,i-1}{}^{m-1} \right)}{(\Delta r)^2} \right.\right.$$
$$\left.\left. + \frac{1}{r} \frac{\left(P_{D3,i+1}{}^{m-1} - P_{D3,i-1}{}^{m-1} \right)}{2\Delta r} \right] \right\}.) [(k-m+1)^{\alpha+1} - (k-m)^{\alpha}(k-m+1$$
$$+ \alpha]$$

Which is the final approximate numerical solution for region 3.

Equations $3.3.3, 3.3.4, and\ 3.3.6$ are fractional Caputo pressure build-up numerical solvers for regions 1,2 and 3 based on the LaGrange polynomial approximation method.

4.6.3. Approximation with middle point method

The middle point method is one of several existing methods to evaluate the definite integrals of functions whose antiderivatives cannot be expressed in closed form. Given a line section, the point that divides it into two halves is geometrically referred to as the midpoint. The middle point considers the centroid of the line segment and the edges of each halve and can be mathematically represented below as:

$$\left(\frac{t_j + t_{j+1}}{2}, \frac{y_j + y_{j+1}}{2}\right).$$

Recalling equations $Equ.\ 4.3.1$, within $[t_n, t_{n+1}]$, we apply the middle point method to approximate the function.

$$\text{For } H\left(t, r_D, P_{D1}(t, r_D)\right) = H_1\left(r_{Di}, t_m, P_{D1}{}_{i}^{t_m}\right)$$

The middle point method can be stated as follows:

$$H\big(t, r_D, P_{D1}(t, r_D)\big) = H\left(r_{D,i}, \frac{t_m + t_{m+1}}{2}, P\left(\frac{r_{D,i}, t_{m+1} + P(r_{D,i}, t_m)}{2}\right)\right).$$

$$H\big(t, r_D, P_{D1}(t, r_D)\big) = H\left(r_{D,i}, \frac{t_m + t_{m+1}}{2}, \frac{P_i^{m+1} + P_i^m}{2}\right) \quad 4.4.7$$

$$H\big(t, r_D, P_{D1}(t, r_D)\big) = H\left(r_{D,i}, \frac{h}{2}, \frac{P_i^{m+1} + P_i^m}{2}\right) \quad 4.4.8$$

Within $[t_n, t_{n+1}]$ we approximate the function H for each zone,

Before making use of a polynomial approximation, we first apply the Caputo integral as follows:

For region one, we have

$${P_{D1,i}}^{k+1} = P_{D1}(0, r_{D,i}) + \frac{1}{\Gamma(\alpha)} \sum_{m=0}^{k} \int_{t_m}^{t_{m+1}} H_1\big(, r_{Di}, P_{D1}(t, r_{Di})\big)(t_{k+1} - \tau)^{\alpha-1} d\tau$$

Substituting, we have

$${P_{D1,i}}^{k+1} = P_{D1}(0, r_{D,i}) + \frac{1}{\Gamma(\alpha)} \sum_{m=0}^{k} \int_{t_m}^{t_{m+1}} H_1\left(r_{D,i}, \frac{t_m + t_{m+1}}{2}, \frac{P_{1,i}^{m+1} + P_{1,i}^m}{2}\right)(t_{k+1} - \tau)^{\alpha-1} d\tau$$

$${P_{D1,i}}^{k+1} = P_{D1}(0, r_{D,i}) + \frac{1}{\Gamma(\alpha)} \sum_{m=0}^{k} H_1\left(r_{D,i}, \frac{t_m + t_{m+1}}{2}, \frac{P_{1,i}^{m+1} + P_{1,i}^m}{2}\right) \int_{t_m}^{t_{m+1}} (t_{k+1} - \tau)^{\alpha-1} d\tau \quad 4.4.9a$$

Where we note that by the method of substitution,

$$\int_{t_m}^{t_{m+1}} (t_{k+1} - \tau)^{\alpha-1} d\tau = \frac{(t_{m+1} + t_m)^{\alpha}}{\alpha} = \frac{h^{\alpha}}{\alpha}\left((k + 1 - m)^{\alpha} - (k + m)^{\alpha}\right)$$

Therefore,

$${P_{D1,i}}^{k+1} = P_{D1}(0, r_{D,i}) + \frac{1}{\Gamma(\alpha)} \sum_{m=0}^{k} H_1\left(r_{D,i}, \frac{t_m + t_{m+1}}{2}, \frac{\bar{P}_{1,i}^{m+1} + P_{1,i}^m}{2}\right) \frac{h^{\alpha}}{\alpha}\left((k + 1 - m)^{\alpha} - (k + m)^{\alpha}\right)$$

The Heun method can be used to fix the implicit form of the results by introducing a corrector by defining $\bar{P}_{1,i}^{m+1}$ as

$$\bar{P}_{D1,i}^{m+1} = P_{D1}(t_m) + \frac{1}{\Gamma(\alpha)}\int_0^{t_k} H_1\big(t, r, P_{D1}(t, r_D)\big)(t_{k+1} - \tau)^{\alpha-1} d\tau$$

For region two,

$$P_{D2}{}^{k+1} = P_{D2}(0, r_{D,i}) + \frac{1}{\Gamma(\alpha)}\sum_{m=0}^{k}\int_{t_m}^{t_{m+1}} H_2\big(t, r_{Di}, P_{D2}(t, r_{Di})\big)(t_{k+1} - \tau)^{\alpha-1} d\tau$$

$$H_2\big(t, r_D, P_{D2}(t, r_D)\big) = \big(F_{\lambda g}\eta_{D2}\big)\left[\frac{\partial^2 P_{D2}}{\partial^2 r} + \frac{1}{r}\frac{\partial P_{D2}}{\partial r_D}\right]$$

Substituting, we have

$$P_{D2,i}{}^{k+1} = P_{D2}(0, r_{D,i}) + \frac{1}{\Gamma(\alpha)}\sum_{m=0}^{k}\int_{t_m}^{t_{m+1}} H_2\left(r_{D,i}, \frac{t_m + t_{m+1}}{2}, \frac{P_{2,i}^{m+1} + P_{2,i}^{m}}{2}\right)(t_{k+1} - \tau)^{\alpha-1} d\tau \quad \text{4.4.9b}$$

For region three

$$P_{D3,i}{}^{k+1} = P_{D3}(0, r_{D,i}) + \frac{1}{\Gamma(\alpha)}\sum_{m=0}^{k}\int_{t_m}^{t_{m+1}} H_3\big(t, r_{Di}, P_{D3}(t, r_{Di})\big)(t_{k+1} - \tau)^{\alpha-1} d\tau$$

And substituting, we have

$$P_{D3,i}{}^{k+1} = P_{D3}(0, r_{D,i}) + \frac{1}{\Gamma(\alpha)}\sum_{m=0}^{k}\int_{t_m}^{t_{m+1}} H_3\left(r_{D,i}, \frac{t_m + t_{m+1}}{2}, \frac{P_{3,i}^{m+1} + P_{3,i}^{m}}{2}\right)(t_{k+1} - \tau)^{\alpha-1} d\tau \quad \text{4.4.9c}$$

4.7. Numerical simulation

This section covers the relevant numerical simulation results. The simulations presented results from the one-dimensional radially defined reservoir into which CO_2 is injected at a constant rate. The mathematical models that describe pressure diffusivity in saline aquifers during injection of CO_2 are modified with the Caputo fractional derivative, and the discretized solutions are obtained using Crank Nicolson second-order discretization's numerical discretization completed. The model input parameters are generated from existing literature, and the data set is representative of a realistic reservoir makeup.

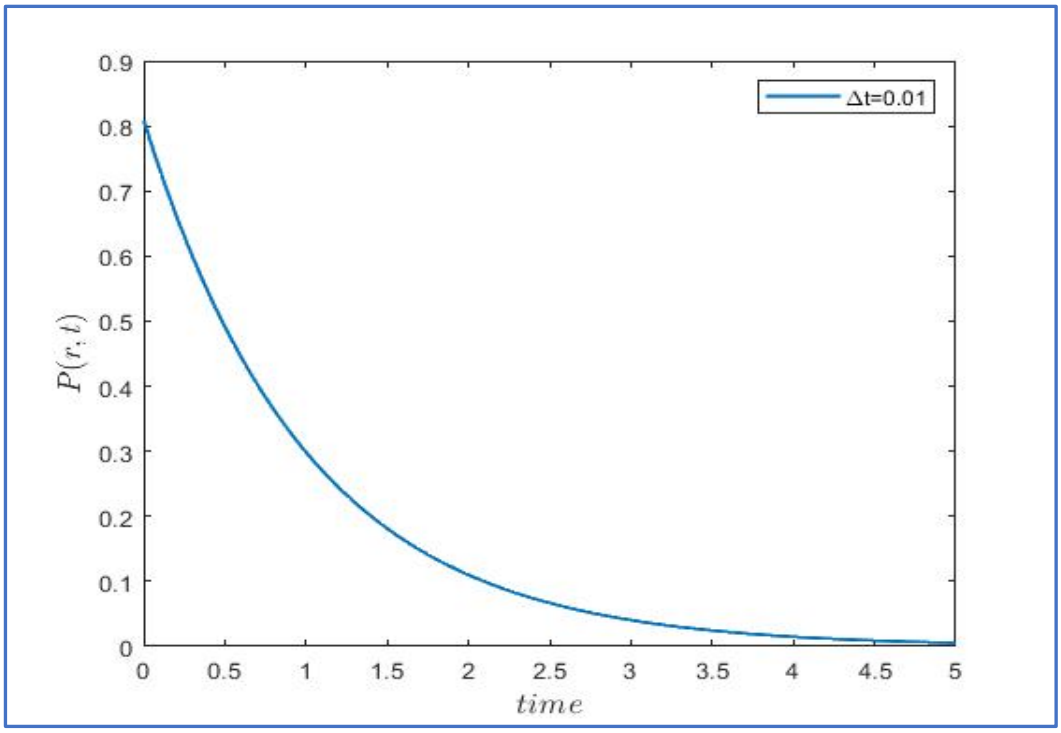

Figure 4-3: Plot of P vs. t for the entire reservoir domain (showing transient pressure response).

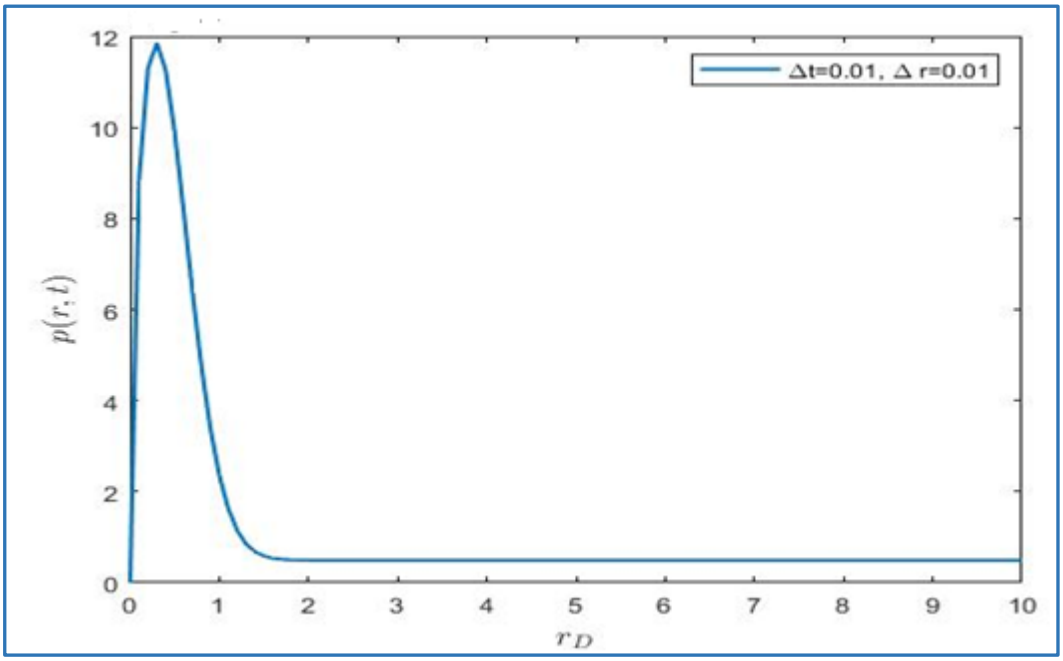

Figure 4-4: Plot p vs. r for region one (Near well pressure behavior).

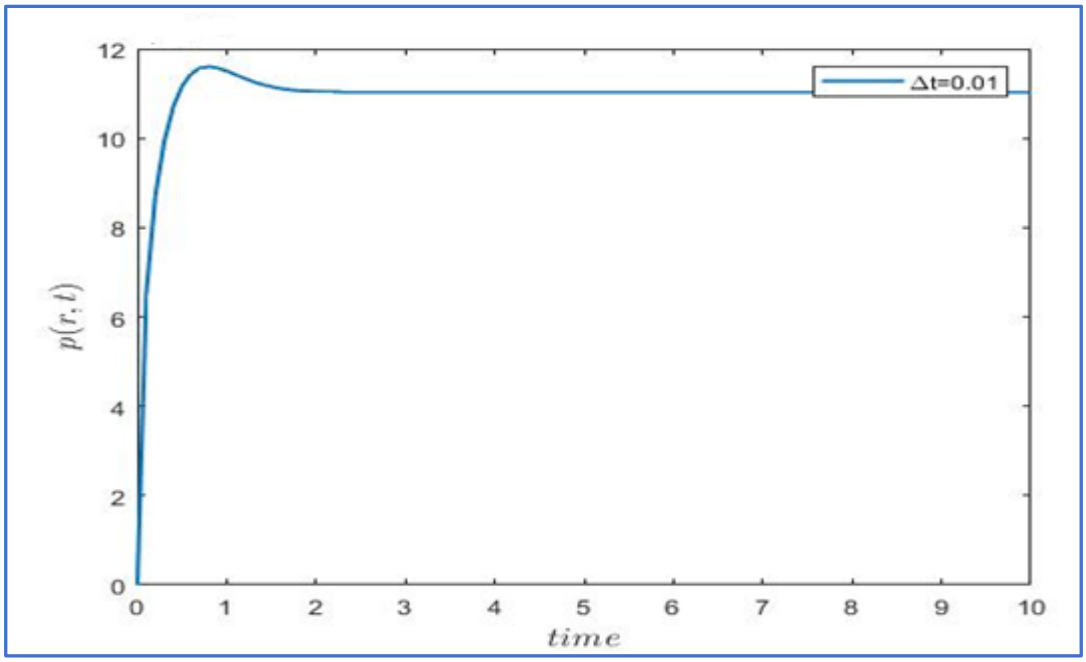

Figure 4-5: plot of P vs. t for region 1 (bottom-hole transient pressure response).

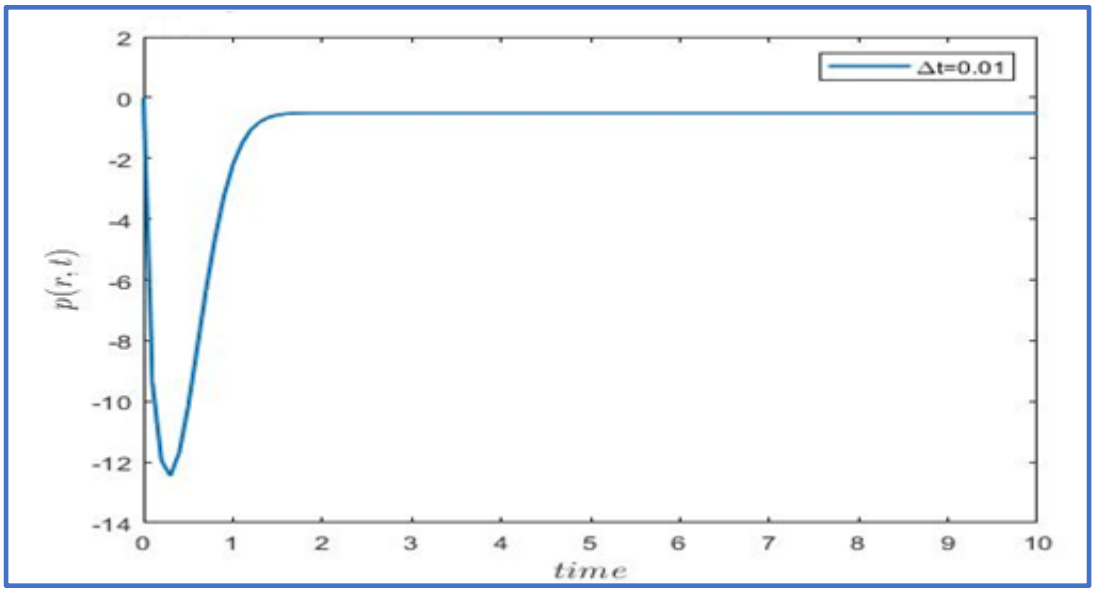

Figure 4-6: Plot of P vs t for region 1 (Near well transient pressure response).

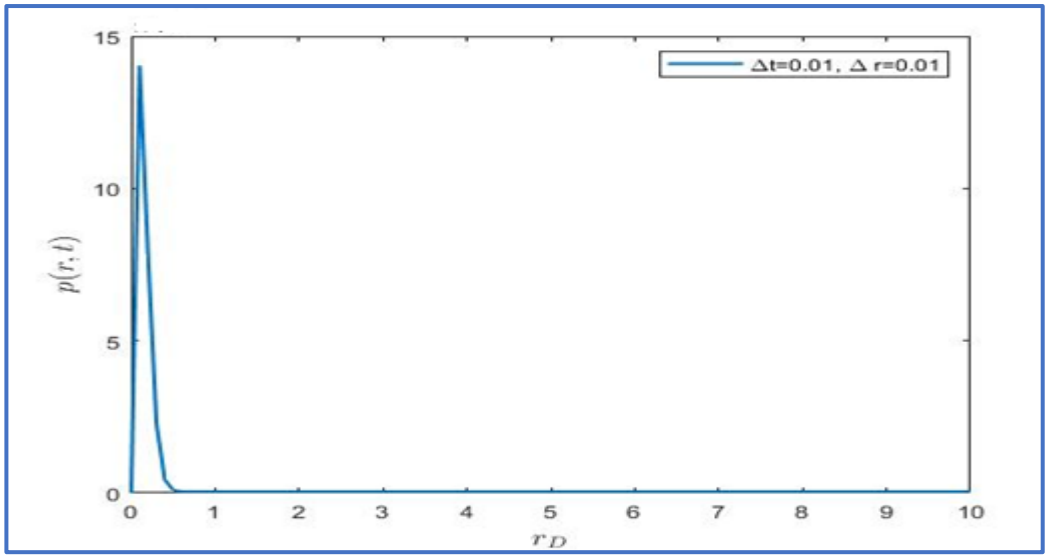

Figure 4-7: Plot of P vs. r (pressure response in region 2) two-phase flow.

4.8. Discussion and conclusion

This section presents a concluding remark on the model results obtained. Power laws have been helpful in characterizing non-Darcian flows and the resulting pressure fronts in porous media. This is common in inertia-conditioned and anomalous flow systems, such as fractures in rock matrix with long-term dependence.

Using the Caputo derivative, the diffusivity model has been extended to describe non-Darcian fluid processes. This assumes the case where the transition from anomalous to un-anomalous flow is the dominant transport mechanism described. Studies in literature (Isah et al., 2022) show that fractal-fractional power law models can model the memory dependence of stresses in coupled hydro-mechanic processes. Theoretically, the Caputo derivative provides various possible solutions for pressure response, reducing complexity and computation time (Atangana and Zakia, 2019).

The numerical solutions used for simulation could accurately predict the pressure evolution in a reservoir during a constant rate of CO_2 injection. The experiments investigated the effect of permeability, viscosity, fractional flow, and compressibility on pressure build-up. The simulation results were obtained for an infinitely acting aquifer such that the overall fluid pressure decreases throughout the injection period. Modelling with the Caputo derivative showed that fluid injection causes a pressure drop at the bottom of the well, amounting to a negative reading, before leveling up. This means that an early-time drop in reservoir pressure accommodates the injection of CO_2 into a saline formation, as further injection is made

possible by the global decline in formation. The Caputo derivative is an effective tool for modelling CO_2 injection pressure build-up. While the Caputo derivative has successfully modelled many real-world problems dealing with similarity solutions and heavy tail dependence, its scale invariance and lack of accurate memory limit its application in many other complex problems.

CHAPTER FIVE: MODELLING PRESSURE BUILDUP WITH THE EXPONENTIAL DECAY KERNEL CAPUTO FABRIZIO FRACTIONAL DERIVATIVE

5.1. Introduction

Geologic Carbon Sequestration can achieve a profound reduction in existing atmospheric CO_2 emissions. Hence, many of the future scenario predictions see CCS as a strategic partner toward a short-term de-carbonization agenda (Zahasky and Krevor, 2020). If CCS is to fulfil its role, on average, 5000 Mt of CO_2 will need to be injected annually by 2050, up from 80 Mt per year in 2018. Annually, between 500 and 1200 new injection wells will be commissioned at a capacity estimated at 5 to 10 Mt of CO_2 per year (Kearns and Consoli, 2021). At this scale, volumetric implications present a risky challenge for pressure management. Significant changes to in-situ stresses are expected, and predicting the pressure buildup in the subsurface is necessary to ensure safe and long-term containment. This is achieved by carefully limiting the reservoir pressure buildup below the fracture limits of the formation rocks. The role and sensitivity of reservoir heterogeneity on parameter estimates have inspired researchers to introduce different memory formalisms for capturing certain observed complex behaviours. The Caputo-Fabrizio derivative is used in this chapter to capture higher-order complexity and predict the pressure buildup due to CO_2 injection in a saline aquifer.

Carbon dioxide is highly compressible in the critical state and the pressure buildup increases with density, which is difficult to estimate due to non-linear relationships and the effect of temperature (Nooner et al., 2007). The buildup of pressure is also controlled by factors such as the type of boundary conditions (Birkholzer et al, 2009) and the cap rock sealing capacity (permeability) (Gasda, 2017). An unbounded reservoir system will experience lesser flow resistance and pressure buildup in the lateral dimension, even though the escaped brine could salinize nearby sensitive environments. On the other hand, a low permeability boundary will increase compressibility and pressurization, which limits storage capacity. To ensure safe long-term storage, it is necessary that the pressure buildup remains below the reservoir fracture point and capillary entry pressure of the shaley cap rock. Localized pathways from fault slip or fracture reactivation can compromise the hydro-chemical integrity of nearby shallow groundwater resources. In

addition, pressurization provides the driving force to mobilize trace elements, cause micro seismicity and alter the natural hydraulic equilibrium gradient of shallow groundwater aquifers, which may increase the aquifer's base flow towards outlets like lakes and streams (Nicot, 2008).

In chapter four, the Caputo derivative was used to accurately simulate pressure diffusivity in a saline reservoir during CO_2 injection for storage. While the obtained results align with analytical solutions due to their contribution to the fractional calculus and it's abilities to model complex problems, there are some limitations to be considered. Firstly, the memory formalism of the Caputo derivative needs to be better posed as it faces a problem of non-locality, singularity, non-uniqueness, and stability. It depends on the entire history of the function being differentiated and not the current state of the process as defined by the function. Knowledge of the initial conditions must be explicitly presented to apply the Caputo derivative. This dependence on initial conditions can be restricted in some practical applications where initial conditions are hard to establish. In terms of singularity and stability, the presence of a Caputo derivative in FDE can introduce singularities that affect the numerical method's convergence and stability.

5.2. Conceptual model and assumptions.

Our conceptual model (Figure 5-1) assumes isothermal, 1-dimensional system. The effect of gravity, capillarity and temperature are not considered in modelling.

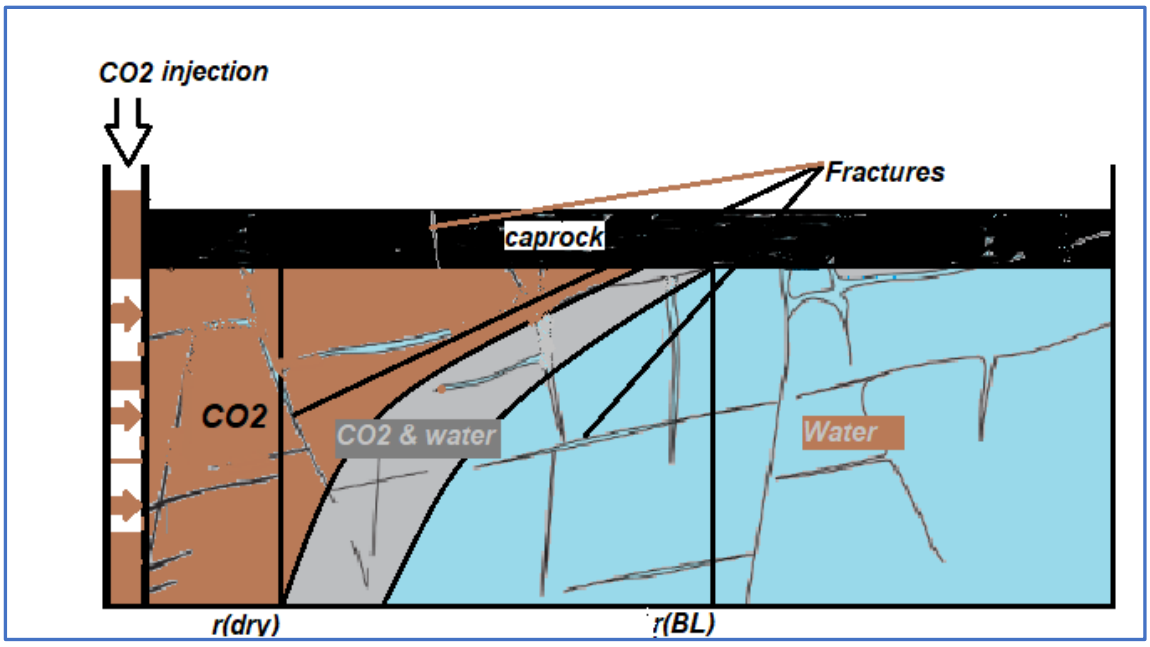

Figure 5-1: Conceptual model of saline aquifer showing three saturation regions.

Formation is assumed to be bounded at the top and bottom by an impermeable layer representing a no flow boundary.

The injection well is infinitesimally small $(r \to 0)$.

5.3. Exponential decay kernel

The exponential decay law is a mathematical function used to describe many real-world complex processes, where the rate of change of the decaying quantity is in proportion to its current value (Figure 5.2.) This kernel is represented below,

$$K(t) = Ae^{-\omega t} \qquad 5.1$$

$K(t)$ is the initial amount of the changing quantity, and ω is the decay constant.

Strong fluid-rock interactions

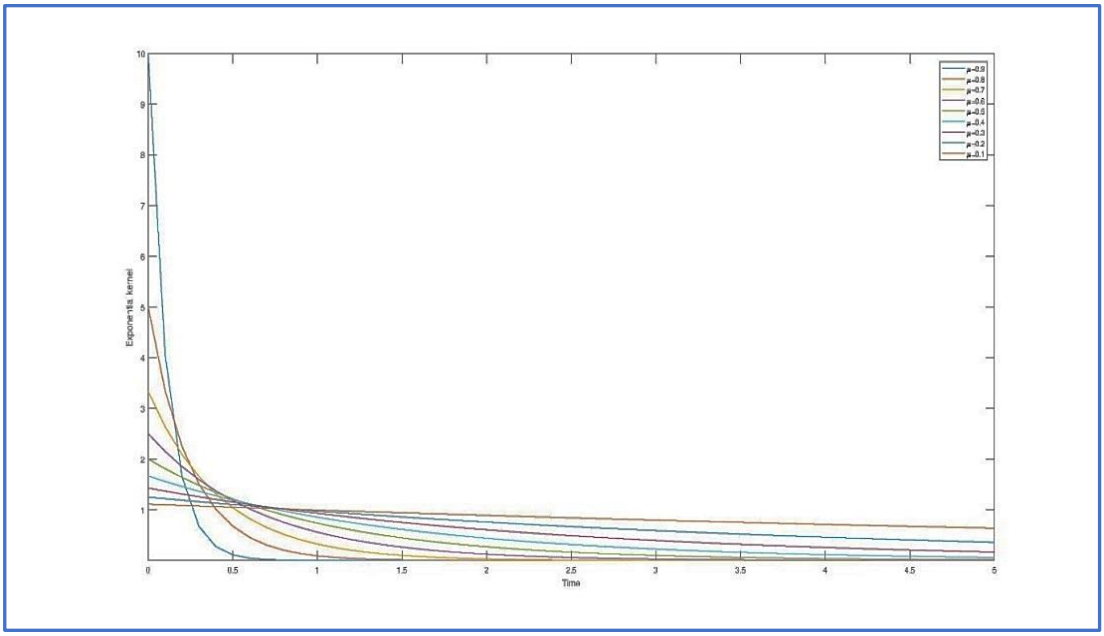

Figure 5-2: Plot of e^(-ωt) vs. t for different alpha [0-1]

5.3.1. The fractional Exponential decay kernel and fluid pressure diffusivity

Non-Darcian flows are a typical observation in tight sediments with low permeability. This is a result of rock matrix interaction with water, which impose a memory effect on the fluid (Caputo and Plastino, 2004). To model this phenomenon, researchers have investigated the role of non-linear functions such as power law (chapter four), exponential function (Swartzendruber, 1962), and Mittag-Leffler function (Atangana and Gomez, 2018). The non-local properties of fractional operators are one meaningful way to consider memory and path non-gaussian processes. The application of fractional

calculus in porous media fluid flow has increased over the past two decades due to advances in the field. In this context, clot and Botha transformed the traditional Darcy flow model that relates flux and pressure gradient into a fractional differential equation. In another study, Ochoa-Tapia described sheer stress variation in a reservoir using a modified fractional Darcy model. Also, within the framework diffusivity, the true reservoir architechture controls the flow fields and reservoir responses to changes mass, momentum and energy. The concept of fractional calculus is generally to modelle real world problems however, the idea of a general fractional kernel is impractical as real world systems tend to be unique and site specific. For media with non-integral fractal dimensions, most well known pysics such as Darcy and Ficks law's, all based on Euclidean geometry show great limitations. While measuring fractal dimensions comes as a big challenge especially for a field as reservoir mechanics, it is well known that self similar fracture systems and the porous architecture of the formation media are highly fractal (Atangana, 2017).

Literature surveys suggest that Rieman Liouville and Caputo are the two most used formalisms of a fractional derivative. As already noted, the Caputo derivative has some limitations that limit its applicability in some complex settings. On the other hand, the Riemann Liouville and Caputo have singularity issues with the kernel, while the Riemann derivative of a constant is not zero. These issues are related to these derivatives' memory and physical meaning. The Caputo-Fabrizio derivative has been introduced in the past decade to capture fluid memory in a porous medium accurately. It extends from the initial caputo derivative by tackling some of its fundamental weaknesses including the problem of non-singulairty at the origin. The derivative has been extensively applied in many real world context with great success in matching experimental data with numerical approximation. In one such poineering studies intudies (Atangana and Baleaunu, 2017) presented new analitical solutions based on method of integral transform, to describe groundwater flow behaviour in a geological formation. In another study, the author described the pile-up of slime mold by extending the chemotaxis model using the Caputo-Fabrizio fractional operator. Ofther studies have not only advanced the reach of fractional calculus, but also contribute to the theoritical bases. (Agarwal et al., 2020) presented the uniqueness and convergence of solutions of immiscible flow

through porous media using the Caputo-Fabrizio derivative while (Saqib and Khan, 2018) amongt others reseachers investigated the heat transfer of nanofluids under specific boundary conditions using a porous medium.

In another connection, the Caputo derivative has been extended to describe the concept of fractional random walks. In fractional formulations, the accumulation of random steps can be expressed as fractional integrals using the Caputo derivative. In continuous random walks, fractional derivatives describe the long-range dependence of particle movement. This technique has been used to describe the processes of subdiffusion and supper diffusion.

5.4. Fractional derivative based on the exponential decay kernel.

Before we present the numerical analysis for pressure diffusivity in each saturation region, we first present the derivation of the integral associated with the Caputo-Fabrizio fractional derivative. For a function $P(r) \in W_2^1(0,l), \alpha \in]0,1]$, the time fractional Caputo derivative is given as

$$ {}^{CF}_{0}D_t^{\alpha} P(t) = \frac{M(\alpha)}{1-\alpha}\int_0^t P'(\tau) exp\left[-\frac{\alpha}{1-\alpha}(t-\tau)\right] d\tau, \text{ t > 0} \qquad 5.1.0 $$

where

$$ {}^{CF}_{0}D_t^{\alpha} p(t) = \lim_{\alpha\to 1}\frac{M(\alpha)}{1-\alpha}\int_0^t p'(\tau) exp\left[-\frac{\alpha}{1-\alpha}(t-\tau)\right] d\tau, \text{ t > 0} \qquad 5.1.1 $$

If $\gamma = 1-\alpha$, then we can rewrite.

$$ {}^{CF}_{0}D_t^{\alpha} p(t) = \lim_{\gamma\to 1}\frac{M(1-\gamma)}{1-\alpha}\int_0^t p'(\tau) exp\left[-\frac{\alpha}{1-\alpha}(t-\tau)\right] d\tau, \text{ t > 0} \qquad 5.1.2 $$

Such that

$$ \lim_{\gamma\to 0} M(1-\gamma) = M(1) = 1 \qquad 5.1.2.1 $$

And

$$ \lim_{\gamma\to 0}\frac{1}{\gamma} exp\left[-\frac{1}{\gamma}(t-\tau)\right] = \delta(t-\tau). $$

Therefore

$$\lim_{\gamma\to 0}\frac{M(1-\gamma)}{\gamma}\int_0^t p'(\tau)exp\left[-\frac{1-\gamma}{\gamma}\right](t-\tau)d\tau=\int_0^t p'(\tau)\delta(t-\tau)d\tau=p'(\tau) \quad 5.1.3$$

Which recovers the first derivative.

The integral associated with the Caputo Fabrizio fractional derivative, along with the derivation via the Laplace transform, is presented.

Recalling the Caputo Fabrizio (Equation 5.1.0) derivative, we apply Laplace as follows

We can write.

$$^{CF}_{0}D^{\alpha}_{t}p(t)=\ H(t,p(t)) \quad 5.1.4$$

Such that

$$\frac{M(\alpha)}{1-\alpha}\int_0^t p'(\tau)exp\left[-\frac{\alpha}{1-\alpha}(t-\tau)\right]d\tau=H(t,p(t)) \quad 5.1.5$$

Applying the Laplace transform, we obtain the next expressions.

$$\mathcal{L}\left(\frac{M(\alpha)}{1-\alpha}\int_0^t p'(\tau)exp\left[-\frac{\alpha}{1-\alpha}(t-\tau)\right]d\tau\right)=\mathcal{L}\big(H(t,p(t))\big) \quad 5.1.6$$

$$\frac{M(\alpha)}{1-\alpha}\{s\tilde{p}(s)-u(0)\}\ \frac{1}{s+\frac{\alpha}{1-\alpha}}=\mathcal{L}\big(H(t,p(t))\big) \quad 5.1.7$$

$$\tilde{p}(s)=\frac{p(0)}{s}+\frac{1-\alpha}{M(\alpha)}L\left((H\big(t,p(t)\big)\right)+\frac{\alpha}{M(\alpha)}\int_0^t H(\tau,p(\tau))d\tau \quad 5.1.8$$

Finally, from $equation$ 5.1.3, the fractional integral with the exponential kernel is given as

$$^{CF}_{0}I^{\alpha}_{t}(p(t))=\frac{1-\alpha}{M(\alpha)}p(t)+\frac{\alpha}{M(\alpha)}\int_0^t p(\tau)d\tau \quad 5.1.9$$

5.5. Numerical Solution of the Pressure Diffusivity Equation based on the Caputo-Fabrizio Derivative.

This section will demonstrate and present the numerical procedure and solution for pressure buildup modelled by the Caputo derivative. The functional approximation will be completed using the two-step LaGrange polynomial.

We recall the Caputo-Fabrizio derivative.

$$ {}^{CF}_{0}D^{\alpha}_{t}p(x) = \frac{1}{\mathrm{M}(\alpha)}\int_{0}^{t} p'(\tau)exp\left[-\frac{\alpha}{1-\alpha}(t-\tau)\right]d\tau, t > 0 \qquad 5.2.0$$

As in the previous chapter, the set of pressure diffusivity equations in the three saturations will be considered in the Caputo sense as follows.

Where the associated PDEs are given as

$$ H_1\left(t, r_D, p_{D1}(t, r_D)\right) = \frac{\partial^2 p_{D1}}{\partial^2 r_D} + \frac{1}{r}\frac{\partial p_{D1}}{\partial r_D} \qquad 5.2.1$$

$$ H_2\left(t, r_D, p_{D2}(t, r_D)\right) = \left(F_{\lambda g}\eta_{D2}\right)\left[\frac{\partial^2 p_{D2}}{\partial^2 r_D} + \frac{1}{r}\frac{\partial p_{D2}}{\partial r_D}\right] \qquad 5.2.2$$

$$ H_3\left(t, r_D, p_{D3}(t, r_D)\right) = \left(\eta_{D3}\right)\left[\frac{\partial^2 p_{D3}}{\partial^2 r_D} + \frac{1}{r}\frac{\partial p_{D3}}{\partial r_D}\right] \qquad 5.2.3$$

Which are then expressed as

$$ {}^{CF}_{0}D^{\alpha}_{t}p_{D1}(x) = H_1\left(t, r, p_{D1}(t, r)\right) \qquad 5.2.4a$$

$$ {}^{CF}_{0}D^{\alpha}_{t}p_{D2}(x) = H_2\left(t, r, p_{D2}(t, r)\right) \qquad 5.2.4b$$

$$ {}^{CF}_{0}D^{\alpha}_{t}p_{D3}(x) = H_3\left(t, r, p_{D3}(t, r)\right) \qquad 5.2.4c$$

Considering the associated Cauchy problem, we can write the system as follows

$$\begin{cases} {}_0^{CF}\mathcal{D}_t^{\alpha} p_{D1}(t, r_D) = H_1\big(t, r_D, p_{D1}(t, r_D)\big), t > 0 \\ {}_0^{CF}\mathcal{D}_t^{\alpha} p_{D2}(t, r_D) = H_2\big(t, r_D, p_{D2}(t, r_D)\big), t > 0 \\ {}_0^{CF}\mathcal{D}_t^{\alpha} p_{D3}(t, r_D) = H_3\big(t, r_D, p_{D3}(t, r_D)\big), t > 0 \\ p_{(D1,D2,D3)}(r_D, 0) = 0, t = 0 \end{cases} \quad 5.2.5$$

The functions P_{D1}, P_{D2}, $and\ P_{D3}$ are the fractional differential equations associated with pressure buildup for region 1, region 2, and region 3, as labeled in the conceptual model.

Following the fundamental theorem of calculus and the initial condition, we can reformulate the set of equations into an integral form using the Caputo integral as defined.

Substituting $t = t_{k+1} = (k+1)\Delta t$, $\forall\ k \in [0,1,2 \dots]$,

$$p_{D1}(r_{D,i}, t_{k+1}) - p_{D1}(0) = \frac{1-\alpha}{M(\alpha)} H_1\big(t_{k+1}, r_D, p_{D1}(t_{k+1}, r_D)\big) + \frac{\alpha}{M(\alpha)} \int_0^{t+1} H_1\big(\tau, r_D, p_{D1}(\tau, r_D)\big) d\tau \quad 5.2.6$$

Substituting $t = t_k = (k)\Delta t$, $\forall\ k \in [0,1,2 \dots]$

$$p_{D1}(r_{D,i}, t_k) - p_{D1}(0) = \frac{1-\alpha}{M(\alpha)} H_1\big(t_k, r_D, p_{D1}(t_k, r_D)\big) + \frac{\alpha}{M(\alpha)} \int_0^{t+1} H_1\big(\tau, r_D, p_{D1}(\tau, r_D)\big) d\tau \quad 5.2.7$$

Taking the difference, we have

$$\begin{aligned} p_{D1}(r_{D,i}, t_{k+1}) = p_{D1}(r_{D,i}, t_k) &+ \frac{1-\alpha}{M(\alpha)} \big[H_1\big(r_D, t_{k+1}, p_{D1}(r_D, t_{k+1})\big) - H_1\big(r_D, t_k, p_{D1}(r_D, t_k)\big)\big] \\ &+ \frac{\alpha}{M(\alpha)} \int_{t_k}^{t_{k+1}} H_1\big(r_D, r_D, \tau, p_{D1}(\tau, r_D)\big) d\tau \end{aligned} \quad 5.2.8$$

Following the similar procedure for region two and region three, we get

$$\begin{aligned} p_{D2}(r_{D,i}, t_{k+1}) = p_{D2}(r_{D,i}, t_k) &+ \frac{1-\alpha}{M(\alpha)} \big[H_2\big(r_D, t_{k+1}, p_{D2}(r_D, t_{k+1})\big) - H_2\big(r_D, t_k, p_{D2}(r_D, t_k)\big)\big] \\ &+ \frac{\alpha}{M(\alpha)} \int_{t_k}^{t_{k+1}} H_2\big(r_D, \tau, p_{D2}(\tau, r_D)\big) d\tau \end{aligned} \quad 5.2.9$$

$$p_{D3}(r_{D,i},t_{k+1}) = p_{D3}(r_{D,i},t_k) + \frac{1-\alpha}{M(\alpha)}\left[H_3(r_D,t_{k+1},p_{D3}(t_{k+1},r_D)) - H_3(r_D,t_k,p_{D3}(t_k))\right] + \frac{\alpha}{M(\alpha)}\int_{t_k}^{t_{k+1}} H_3(r_D,\tau,p_{D3}(\tau,r_D))d\tau \quad 5.3.0$$

5.5.1. Numerical solution with the Lagrange polynomial approximation

In the following section, the Lagrange approximation within$[t_n, t_{n+1}]$ is presented.

$$H_n\left(t,r_{Di},p_{D_{r_{Di}}}^{t}\right) \approx \frac{3}{2}\Delta t H_n\left(r_{D,i},t_k,p_{D1}(r_{D,i},t_k)\right) - \frac{\Delta t}{2}H_n\left(r_{D,i},t_{k-1},p_{D1}(r_{D,i},t_{k-1})\right) \quad 5.3.1$$

H_n is the unknown function for the pressure diffusivity model, given as $H_1, H_2, and\ H_3$.

Substituting 5.13, we get

$$\begin{aligned} p_{Dn}(r_{D,i},t_{k+1}) - p_{Dn}(r_{D,i},t_k) &= (1-\alpha)\left[H_n\left(t_{k+1},r_D,p_{Dn}(t_{k+1,r_D})\right) - H_n(t_k,r_D,p_{Dn}(t_k,r_D))\right] \\ &+ \alpha h\left\{\frac{3\Delta t}{2}H_n\left(r_{D,i},t_k,p_{Dn}(r_{D,i},t_k)\right)\right. \\ &\left. - \frac{\Delta t}{2}H_n\left(r_{D,i},t_{k-1},p_{Dn}(r_{D,i},t_{k-1})\right)\right\}\int_{t_k}^{t_{k+1}} d\tau \end{aligned} \quad 5.3.2$$

Therefore, we can express the pressure buildup numerical scheme in all three regions as follows:

<u>Region 1</u>

$$\begin{aligned} p_{D1}(r_{Di},t_{k+1}) - p_{D1}(r_{Di},t_k) &= (1-\alpha)\left[H_1(t_{k+1},r_{Di},\tilde{p}_{D1}(t_{k+1},r_{Di})) - H_1(t_k,r_{Di},p_{D1}(t_k,r_{Di}))\right] \\ &+ \alpha h\left\{\frac{3\Delta t}{2}H_1(r_{Di},t_k,p_{D1}(r_{Di},t_k)) - \frac{\Delta t}{2}H_1(r_{Di},t_{k-1},p_{D1}(r_{Di},t_{k-1}))\right\} \end{aligned} \quad 5.3.3$$

Where

For the functionH_1, the discretization is completed at the $r_{D,i}$ such that.

$$H_1\left(r_{D,i}, t_k, p_{D1}(r_{D,i}, t_k)\right)\Big|_{(r_{Di},\, t_k)} \qquad 5.3.4$$
$$= \left[\left(\frac{p_{D1}(r_{Di+1}, t_k) - 2p_{D1}(r_{Di}, t_k) + p_{D1}(r_{Di-1}, t_k)}{\Delta r^2}\right)\right.$$
$$\left. + \frac{1}{r_{D,i}}\left(\frac{p_{D1}(r_{Di+1}, t_k) - p_{D1}(r_{Di-1}, t_k)}{2\Delta r}\right)\right]$$

And likewise

$$H_1\left(r_{Di}, t_{k-1}, p_{D1}(r_{Di}, t_{k-1})\right)\Big|_{(r_{Di},\ t_{k-1})} \qquad 5.3.5$$
$$= \left[\left(\frac{p_{D1}(r_{Di+1}, t_{k-1}) - 2p_{D1}(r_{Di}, t_{k-1}) + p_{D1}(r_{Di-1}, t_{k-1})}{\Delta r^2}\right)\right.$$
$$\left. + \frac{1}{r_{D,i}}\left(\frac{p_{D1}(r_{Di+1}, t_{k-1}) - p_{D1}(r_{Di-1}, t_{k-1})}{2\Delta r}\right)\right]$$

The full scheme can thus be expressed as

$$p_{D1}(r_{Di}, t_{k+1}) - p_{D1}(r_{Di}, t_k)$$
$$= (1-\alpha)\left\{H_1\left(t_{k+1}, r_{Di}, \tilde{p}_{D1}(t_{k+1}, r_{Di})\right) - H_1\left(t_k, r_{Di}, p_{D1}(t_k, r_{Di})\right)\right\}$$
$$+ \alpha h\left\{\frac{3\Delta t}{2} H_1\left(r_{Di}, t_k, p_{D1}(r_{Di}, t_k)\right) - \frac{\Delta t}{2} H_1\left(r_{Di}, t_{k-1}, p_{D1}(r_{Di}, t_{k-1})\right)\right\}$$

Substituting and simplifying, we get to

$$p_{D1}(r_{Di}, t_{k+1}) - p_{D1}(r_{Di}, t_k) \qquad 5.3.6a$$
$$= (1-\alpha)\left\{H_1\left(t_{k+1}, r_{Di}, \tilde{p}_{D1}(t_{k+1}, r_{Di})\right)\right.$$
$$- \left[\left(\frac{p_{D1}(r_{Di+1}, t_k) - 2p_{D1}(r_{Di}, t_k) + p_{D1}(r_{Di-1}, t_k)}{\Delta r^2}\right)\right.$$
$$\left.\left. + \frac{1}{r_{D,i}}\left(\frac{p_{D1}(r_{Di+1}, t_k) - p_{D1}(r_{Di-1}, t_k)}{2\Delta r}\right)\right]\right\}$$
$$+ \alpha h\left\{\frac{3\Delta t}{2}\left[\left(\frac{p_{D1}(r_{Di+1}, t_k) - 2p_{D1}(r_{Di}, t_k) + p_{D1}(r_{Di-1}, t_k)}{\Delta r^2}\right)\right.\right.$$
$$\left. + \frac{1}{r_{D,i}}\left(\frac{p_{D1}(r_{Di+1}, t_k) - p_{D1}(r_{Di-1}, t_k)}{2\Delta r}\right)\right]$$
$$- \frac{\Delta t}{2}\left[\left(\frac{p_{D1}(r_{Di+1}, t_{k-1}) - 2p_{D1}(r_{Di}, t_{k-1}) + p_{D1}(r_{Di-1}, t_{k-1})}{\Delta r^2}\right)\right.$$
$$\left.\left.\left. + \frac{1}{r_{D,i}}\left(\frac{p_{D1}(r_{Di+1}, t_{k-1}) - p_{D1}(r_{Di-1}, t_{k-1})}{2\Delta r}\right)\right]\right\}$$

where

$$\tilde{p}_{D1}(r_{Di}, t_{k+1}) = p_{D1}(r_{Di}, t_k) + (1-\alpha)\left[H_1\left(r_{Di}, t_k, p_{D1}(t_k)\right) - H_1\left(r_{Di}, t_{k-1}, p_{D1}(t_{k-1})\right)\right] \qquad 5.3.5b$$
$$+ hH_1\left(t_k, r_{Di}, p_{D1}(t_k, r_{Di})\right)$$

Similarly, we obtain the numerical solvers for the region two and zone three.

Region two

$$p_{D2}(r_{Di},t_{k+1})-p_{D2}(r_{Di},t_k)$$
$$=(1-\alpha)\{H_2(t_{k+1},r_{Di},\tilde{p}_{D1}(t_{k+1},r_{Di}))-H_2(t_k,r_{Di},p_{D2}(t_k,r_{Di}))\}$$
$$+\alpha h\left\{\frac{3\Delta t}{2}H_2(r_{Di},t_k,p_{D2}(r_{Di},t_k))-\frac{\Delta t}{2}H_2(r_{Di},t_{k-1},p_{D2}(r_{Di},t_{k-1}))\right\}$$

where

$$H_2\left(r_{D,i},t_k,p_{D1}(r_{D,i},t_k)\right)\Big|_{(r_{Di},\ t_k)}$$
$$=(F_{\lambda g}\eta_{D2})\left[\left(\frac{p_{D2}(r_{Di+1},t_k)-2p_{D2}(r_{Di},t_k)+p_{D2}(r_{Di-1},t_k)}{\Delta r^2}\right)\right.$$
$$\left.+\frac{1}{r_{D,i}}\left(\frac{p_{D1}(r_{Di+1},t_k)-p_{D2}(r_{Di-1},t_k)}{2\Delta r}\right)\right]$$

and

$$H_2(r_{Di},t_{k-1},p_{D1}(r_{Di},t_{k-1}))\Big|_{(r_{Di},\ t_{k-1})}$$
$$=(F_{\lambda g}\eta_{D2})\left[\left(\frac{p_{D2}(r_{Di+1},t_k)-2p_{D2}(r_{Di},t_k)+p_{D2}(r_{Di-1},t_k)}{\Delta r^2}\right)\right.$$
$$\left.+\frac{1}{r_{D,i}}\left(\frac{p_{D2}(r_{Di+1},t_{k-1})-p_{D2}(r_{Di-1},t_{k-1})}{2\Delta r}\right)\right]$$

Substituting we get

$$p_{D2}(r_{Di},t_{k+1})-p_{D2}(r_{Di},t_k) \qquad \text{5.3.6b}$$
$$=(1-\alpha)\left\{H_2(t_{k+1},r_{Di},\tilde{p}_{D1}(t_{k+1},r_{Di}))\right.$$
$$-(F_{\lambda g}\eta_{D2})\left[\left(\frac{p_{D2}(r_{Di+1},t_k)-2p_{D2}(r_{Di},t_k)+p_{D2}(r_{Di-1},t_k)}{\Delta r^2}\right)\right.$$
$$\left.\left.+\frac{1}{r_{D,i}}\left(\frac{p_{D1}(r_{Di+1},t_k)-p_{D2}(r_{Di-1},t_k)}{2\Delta r}\right)\right]\right\}$$
$$+\alpha h\left\{\frac{3\Delta t}{2}(F_{\lambda g}\eta_{D2})\left[\left(\frac{p_{D2}(r_{Di+1},t_k)-2p_{D2}(r_{Di},t_k)+p_{D2}(r_{Di-1},t_k)}{\Delta r^2}\right)\right.\right.$$
$$\left.+\frac{1}{r_{D,i}}\left(\frac{p_{D1}(r_{Di+1},t_k)-p_{D2}(r_{Di-1},t_k)}{2\Delta r}\right)\right]$$
$$-\frac{\Delta t}{2}(F_{\lambda g}\eta_{D2})\left[\left(\frac{p_{D2}(r_{Di+1},t_k)-2p_{D2}(r_{Di},t_k)+p_{D2}(r_{Di-1},t_k)}{\Delta r^2}\right)\right.$$
$$\left.\left.\left.+\frac{1}{r_{D,i}}\left(\frac{p_{D2}(r_{Di+1},t_{k-1})-p_{D2}(r_{Di-1},t_{k-1})}{2\Delta r}\right)\right]\right\}$$

Where

$$\tilde{p}_{D2}(r_{Di}, t_{k+1}) = p_{D2}(r_{Di}, t_k) + (1 - \alpha)\left[H_2\left(r_{Di}, t_k, p_{D2}(t_k)\right) - H_2\left(r_{Di}, t_{k-1}, p_{D2}(t_{k-1})\right)\right] + hH_2\left(t_k, r_{Di}, p_{D2}(t_k, r_{Di})\right)$$

Region three

$$p_{D3}\left(r_{D,i}, t_{k+1}\right) - p_{D3}(r_{D,i}, t_k) = (1-\alpha)\left[H_3\left(t_{k+1}, r_D, p_{D3}\left(t_{k+1,r_D}\right)\right) - H_3\left(t_k, r_D, p_{D3}(t_k, r_D)\right)\right] + \alpha h\left\{\begin{array}{c} \frac{3\Delta t}{2} H_3\left(r_{D,i}, t_k, p_{D3}\left(r_{D,i}, t_k\right)\right) \\ -\frac{\Delta t}{2} H_3\left(r_{D,i}, t_{k-1}, p_{D3}\left(r_{D,i}, t_{k-1}\right)\right) \end{array}\right\}$$

where

$$H_3\left(r_{D,i}, t_k, p_{D1}\left(r_{D,i}, t_k\right)\right)\Big|_{(r_{Di},\ t_k)} = (\eta_{D3})\left[\left(\frac{p_{D2}(r_{Di+1}, t_k) - 2p_{D2}(r_{Di}, t_k) + p_{D2}(r_{Di-1}, t_k)}{\Delta r^2}\right) + \frac{1}{r_{D,i}}\left(\frac{p_{D1}(r_{Di+1}, t_k) - p_{D2}(r_{Di-1}, t_k)}{2\Delta r}\right)\right]$$

and

$$H_3\left(r_{Di}, t_{k-1}, p_{D1}(r_{Di}, t_{k-1})\right)\Big|_{(r_{Di},\ t_{k-1})} = (\eta_{D3})\left[\frac{1}{r_{D,i}}\left(\frac{p_{D2}(r_{Di+1}, t_{k-1}) - p_{D2}(r_{Di-1}, t_{k-1})}{2\Delta r}\right) + \left(\frac{p_{D2}(r_{Di+1}, t_k) - 2p_{D2}(r_{Di}, t_k) + p_{D2}(r_{Di-1}, t_k)}{\Delta r^2}\right)\right]$$

Substituting we get

$$p_{D3}(r_{D,i},t_{k+1}) = p_{D3}(r_{D,i},t_k) + (1 \qquad 5.3.6c$$
$$- \alpha)\left[H_3\left(t_{k+1},r_D,p_{D3}(t_{k+1,r_D})\right)\right.$$
$$- (\eta_{D3})\left[\left(\frac{p_{D2}(r_{Di+1},t_k) - 2p_{D2}(r_{Di},t_k) + p_{D2}(r_{Di-1},t_k)}{\Delta r^2}\right)\right.$$
$$\left.\left. + \frac{1}{r_{D,i}}\left(\frac{p_{D1}(r_{Di+1},t_k) - p_{D2}(r_{Di-1},t_k)}{2\Delta r}\right)\right]\right]$$
$$+ \alpha h\left\{\frac{3\Delta t}{2}(\eta_{D3})\left[\frac{1}{r_{D,i}}\left(\frac{p_{D1}(r_{Di+1},t_k) - p_{D2}(r_{Di-1},t_k)}{2\Delta r}\right)\right.\right.$$
$$\left. + \left(\frac{p_{D2}(r_{Di+1},t_k) - 2p_{D2}(r_{Di},t_k) + p_{D2}(r_{Di-1},t_k)}{\Delta r^2}\right)\right]$$
$$- \frac{\Delta t}{2}(\eta_{D3})\left[\frac{1}{r_{D,i}}\left(\frac{p_{D1}(r_{Di+1},t_k) - p_{D2}(r_{Di-1},t_k)}{2\Delta r}\right)\right.$$
$$\left.\left. + \left(\frac{p_{D2}(r_{Di+1},t_k) - 2p_{D2}(r_{Di},t_k) + p_{D2}(r_{Di-1},t_k)}{\Delta r^2}\right)\right]\right\}$$

$$\tilde{p}_{D3}(r_{D,i},t_{k+1}) = p_{D3}(r_{D,i},t_k) + (1-\alpha)\left[H_3\left(r_{D,i},t_k,p_{D3}(t_k)\right) - H_3\left(r_{D,i},t_{k-1},p_{D3}(t_{k-1})\right)\right]$$
$$+ h(\eta_{D3}).H_3\left(t_k,r_{D,i},p_{D3}(t_k,r_{D,i})\right)$$

Which represents the final numerical solver for zone three, approximated with the La-Grange polynomial.

5.5.2. Numerical solution with middle point approximation method

Equations 5.28, 5.2.9, and 5.30 are recalled, and the solutions for pressure build are completed with the middle point method within $[t_n, t_{n+1}]$.

$$p_{D1}{}^{k+1}_{r_{D,i}} = p_{D1}{}^{k}_{r_{D,i}} + (1-\alpha)\left[H_1\left(r_{D,i},t_{k+1},p_{D1}{}^{k+1}_{r_D,i}\right) - H_1\left(r_{D,i},t_k,p_{D1}{}^{k}_{r_D}\right)\right] \qquad 5.3.7$$
$$+ \alpha\int_{t_m}^{t_{m+1}} H_1\left(r_{D,i},\tau,p_{D1}{}^{k}_{r_{D,i}}\right)d\tau$$

Following a similar procedure for regions two and three, we get

$$p_{D2}{}^{k+1}_{r_{D,i}} = p_{D2}{}^{k}_{r_{D,i}} + (1-\alpha)\left[H_2\left(r_{D,i},t_{k+1},p_{D1}{}^{k+1}_{r_D,i}\right) - H_2\left(r_{D,i},t_k,p_{D2}{}^{k}_{r_D}\right)\right] \qquad 5.3.8$$
$$+ \alpha\int_{t_m}^{t_{m+1}} H_2\left(r_D,\tau,p_{D2}{}^{k}_{r_{D,i}}\right)d\tau$$

$$p_{D3}{}_{k+1}^{r_D} = p_{D3}{}_{r_{D,i}}^{k} + (1-\alpha)\left[H_3\left(r_{D,i}, t_{k+1}, p_{D3}{}_{r_{D,i}}^{k+1}\right) - H_2\left(r_{D,i}, t_k, p_{D3}{}_{r_D}^{k}\right)\right] + \alpha H_3\left(r_{D,i}, \tau, p_{D3}{}_{r_{D,i}}^{k}\right)\int_{t_m}^{t_{m+1}} d\tau \quad 5.3.9$$

Applying the middle point method between $[t_n, t_{n+1}]$, we approximate the integral as follows.

$$H_n\left(r_{D,i}, \tau, p_n(r_{D,m}, \tau)\right) \approx H_n\left(r_{D,i}, \frac{t_{m+1}+t_m}{2}, \frac{p_{n,i}{}^{m+1} + p_{n,i}{}^{m}}{2}\right)$$

Substituting, we get

$$p_{Dn}{}_{r_{D,i}}^{k+1} = p_{Dn}{}_{r_{D,i}}^{k} + (1-\alpha)\left[H_n\left(r_{D,i}, t_{k+1}, p_{Dn}{}_{r_{D,i}}^{k+1}\right) - H_n\left(r_{D,i}, t_k, p_{Dn}{}_{r_D}^{k}\right)\right] + \alpha\int_{t_m}^{t_{m+1}} H_1\left(r_{D,i}, \frac{t_{m+1}+t_m}{2}, \frac{p_{n,i}^{m+1}+p_i^m}{2}\right)dt \quad 5.4.0$$

$$p_{Dn}{}_{r_{D,i}}^{k+1} = p_{Dn}{}_{r_{D,i}}^{k} + (1-\alpha)\left[H_n\left(r_{D,i}, t_{k+1}, p_{Dn}{}_{r_{D,i}}^{k+1}\right) - H_n\left(r_{D,i}, t_k, p_{Dn}{}_{r_D}^{k}\right)\right] + \alpha H_n\left(r_{D,i}, \frac{t_{m+1}+t_m}{2}, \frac{p_{n,i}^{m+1}+p_{n,i}^{m}}{2}\right)\int_{t_m}^{t_{m+1}} dt$$

$$p_{Dn}{}_{r_{D,i}}^{k+1} = p_{Dn}{}_{r_{D,i}}^{k} + (1-\alpha)\left[H_n\left(r_{D,i}, t_{k+1}, p_{Dn}{}_{r_{D,i}}^{k+1}\right) - H_n\left(r_{D,i}, t_k, p_{Dn}{}_{r_D}^{k}\right)\right] + \alpha h H_n\left(r_{D,i}, \frac{t_{m+1}+t_m}{2}, \frac{p_{n,i}^{m+1}+p_{n,i}^{m}}{2}\right)$$

<u>For region 1</u>

Where H_n is H_1, we can rewrite the scheme as

$$p_{D1}{}_{r_{D,i}}^{k+1} = p_{D1}{}_{r_{D,i}}^{k} + (1-\alpha)\left[H_1\left(r_{D,i}, t_{k+1}, \tilde{p}_{D1}{}_{r_{D,i}}^{k+1}\right) - H_1\left(r_{Di}, t_k, p_{D1}{}_{r_D}^{k}\right)\right] + \alpha h H_1\left(r_{D,i}, \frac{t_{m+1}+t_m}{2}, \frac{\tilde{p}_{D1}{}_i^{m+1}+p_i^m}{2}\right) \quad 5.4.1$$

If $t_{m+1} = h + t_m$, we have that

$$p_{D1}{}_{r_{D,i}}^{k+1} = p_{D1}{}_{r_{D,i}}^{k} + (1-\alpha)\left[H_1\left(r_{D,i}, t_{k+1}, \tilde{p}_{D1}{}_{r_{D,i}}^{k+1}\right) - H_1\left(r_{D,i}, t_k, p_{D1}{}_{r_D}^{k}\right)\right] + \alpha h H_1\left(r_{D,i}, \frac{h}{2}+t_m, \frac{\tilde{p}_{D1}{}_i^{m+1}+p_i^m}{2}\right) \quad 5.4.2$$

Where

For the function H_1, the discretization is completed at the $r_{D,i}$ such that.

$$H_1\left(r_{D,i},t_k,p_{D1}(r_{D,i},t_k)\right)\Big|_{(r_{Di},\,t_k)} = \left[\frac{1}{r_{D,i}}\left(\frac{p_{D1}(r_{Di+1},t_k)-p_{D1}(r_{Di-1},t_k)}{2\Delta r}\right) + \frac{p_{D1}(r_{Di+1},t_k)-2p_{D1}(r_{Di},t_k)+p_{D1}(r_{Di-1},t_k)}{\Delta r^2}\right]$$

And likewise

$$H_1(r_{Di},t_{k-1},p_{D1}(r_{Di},t_{k-1}))\Big|_{(r_{Di},\;t_{k-1})} = \left[\left(\frac{p_{D1}(r_{Di+1},t_{k-1})-2p_{D1}(r_{Di},t_{k-1})+p_{D1}(r_{Di-1},t_{k-1})}{\Delta r^2}\right) + \frac{1}{r_{D,i}}\left(\frac{p_{D1}(r_{Di+1},t_{k-1})-p_{D1}(r_{Di-1},t_{k-1})}{2\Delta r}\right)\right]$$

Moreover, from the Heinz approach, we can obtain the implicit solution by introducing a predictor-corrector.

$$\tilde{p}_{D1}{}_{r_{D,i}}^{k+1} = p_{D1}{}_{k}^{r_D} + (1-\alpha)\left[H_1(r_D,t_k,p_{D1}{}_{k}^{r_D}) - H_1(r_D,t_{k-1},p_{D1}{}_{k-1}^{r_D})\right] + hH_1(r_D,t_k,p_{D1}{}_{k}^{r_D})$$

Similarly, we obtain the solutions for region 2 and region 3 as

<u>Region 2</u>

$$p_{D2}{}_{r_{D,i}}^{k+1} = p_{D2}{}_{r_{D,i}}^{k} + (1-\alpha)\left[H_2\left(r_{D,i},t_{k+1},\tilde{p}_{D2}{}_{r_{D,i}}^{k+1}\right) - H_2\left(r_{D,i},t_k,p_{D2}{}_{r_D}^{k}\right)\right] + \alpha hH_2\left(r_{D,i},\frac{h}{2}+t_m,\frac{\tilde{p}_{D2}{}_{i}^{m+1}+p_{D2}{}_{i}^{m}}{2}\right) \qquad 5.4.5$$

where

$$\tilde{p}_{D2}{}_{r_{D,i}}^{k+1} = p_{D2}{}_{k}^{r_D} + (1-\alpha)\left[H_2(r_D,t_k,p_{D1}{}_{k}^{r_D}) - H_2(r_D,t_{k-1},p_{D2}{}_{k-1}^{r_D})\right] + hH_2(r_D,t_k,p_{D2}{}_{k}^{r_D})$$

And the functions discretized at $r_{D,i}$ are given as

$$H_2\left(r_{D,i},t_k,p_{D1}(r_{D,i},t_k)\right)\Big|_{(r_{Di},\;t_k)} = (F_{\lambda g}\eta_{D2})\left[\frac{1}{r_{D,i}}\left(\frac{p_{D1}(r_{Di+1},t_k)-p_{D2}(r_{Di-1},t_k)}{2\Delta r}\right) + \left(\frac{p_{D2}(r_{Di+1},t_k)-2p_{D2}(r_{Di},t_k)+p_{D2}(r_{Di-1},t_k)}{\Delta r^2}\right)\right]$$

and

$$H_2\left(r_{Di}, t_{k-1}, p_{D1}(r_{Di}, t_{k-1})\right)\Big|_{(r_{Di},\ t_{k-1})} = \left(F_{\lambda g}\eta_{D2}\right)\left[\left(\frac{p_{D2}(r_{Di+1}, t_k) - 2p_{D2}(r_{Di}, t_k) + p_{D2}(r_{Di-1}, t_k)}{\Delta r^2}\right) + \frac{1}{r_{D,i}}\left(\frac{p_{D2}(r_{Di+1}, t_{k-1}) - p_{D2}(r_{Di-1}, t_{k-1})}{2\Delta r}\right)\right]$$

Region 3

$$p_{D3}{}_{r_{D,i}}^{k+1} = p_{D3}{}_{r_{D,i}}^{k} + (1-\alpha)\left[H_3\left(r_{D,i}, t_{k+1}, \tilde{p}_{D3}{}_{r_{D,i}}^{k+1}\right) - H_3\left(r_D, t_k, p_{D3}{}_{r_D}^{k}\right)\right] + \alpha h H_3\left(r_{D,i}, \frac{h}{2} + t_m, \frac{\tilde{p}_{D3}{}_i^{m+1} + p_{D3}{}_i^{m}}{2}\right) \quad 5.4.6$$

$$\tilde{p}_{D3}{}_{r_{D,i}}^{k+1} = p_{D3}{}_{k}^{r_D} + (1-\alpha)\left[H_3\left(r_D, t_k, p_{D3}{}_{k}^{r_D}\right) - H_3\left(r_D, t_{k-1}, p_{D3}{}_{k-1}^{r_D}\right)\right] + hH_3\left(r_D, t_k, p_{D3}{}_{k}^{r_D}\right)$$

$$H_3\left(r_{D,i}, t_k, p_{D1}(r_{D,i}, t_k)\right)\Big|_{(r_{Di},\ t_k)} = (\eta_{D3})\left[\left(\frac{p_{D2}(r_{Di+1}, t_k) - 2p_{D2}(r_{Di}, t_k) + p_{D2}(r_{Di-1}, t_k)}{\Delta r^2}\right) + \frac{1}{r_{D,i}}\left(\frac{p_{D1}(r_{Di+1}, t_k) - p_{D2}(r_{Di-1}, t_k)}{2\Delta r}\right)\right]$$

and

$$H_3\left(r_{Di}, t_{k-1}, p_{D1}(r_{Di}, t_{k-1})\right)\Big|_{(r_{Di},\ t_{k-1})} = (\eta_{D3})\left[+\left(\frac{p_{D2}(r_{Di+1}, t_k) - 2p_{D2}(r_{Di}, t_k) + p_{D2}(r_{Di-1}, t_k)}{\Delta r^2}\right) + \frac{1}{r_{D,i}}\left(\frac{p_{D2}(r_{Di+1}, t_{k-1}) - p_{D2}(r_{Di-1}, t_{k-1})}{2\Delta r}\right)\right]$$

5.6. Simulations results

This section presents graphical solutions of the numerical model based on Caputo-Fabrizio derivative.

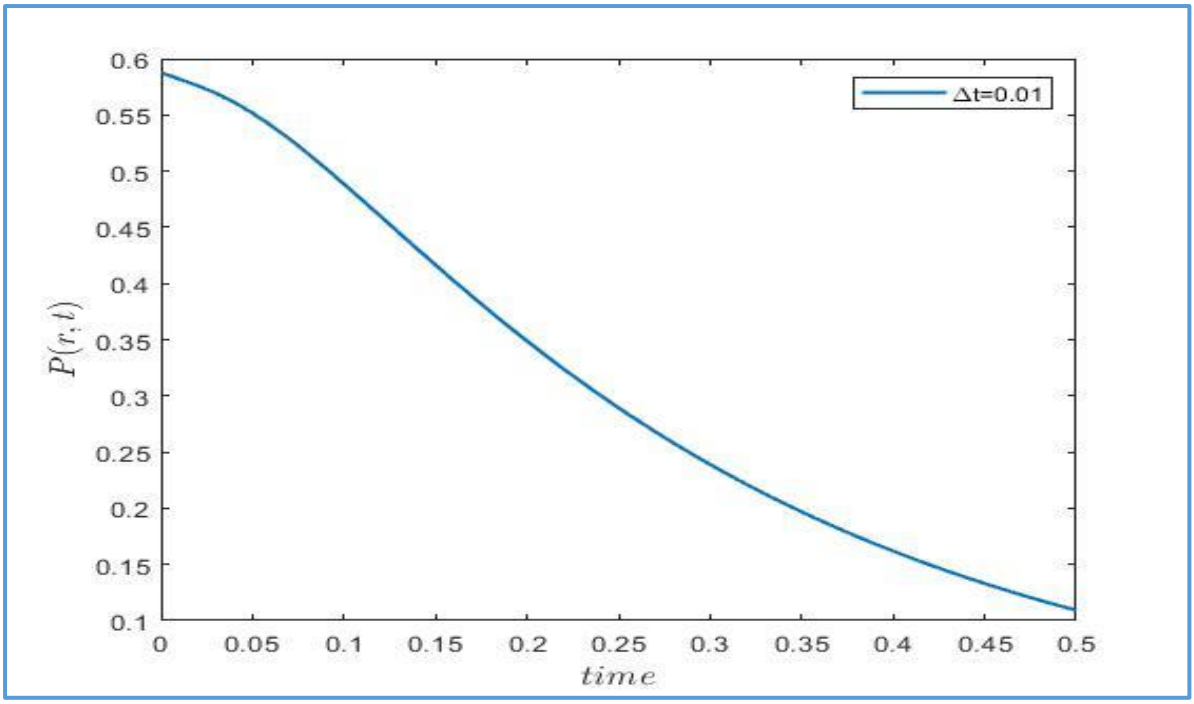

Figure 5-3: Plot of P vs. r showing the pressure drop in the two-phase flow region (region 2), (Alpha=0.76)

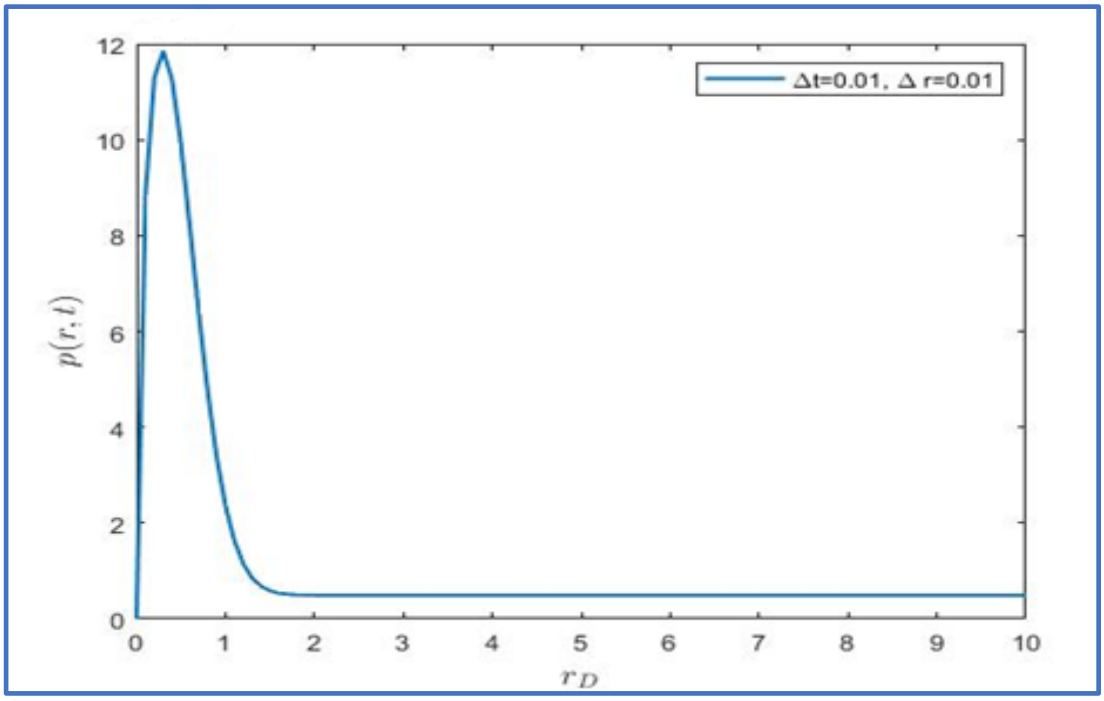

Figure 5-4: Plot of P vs. r showing the near Well pressure behavior at the near well region (Alpha=0.76).

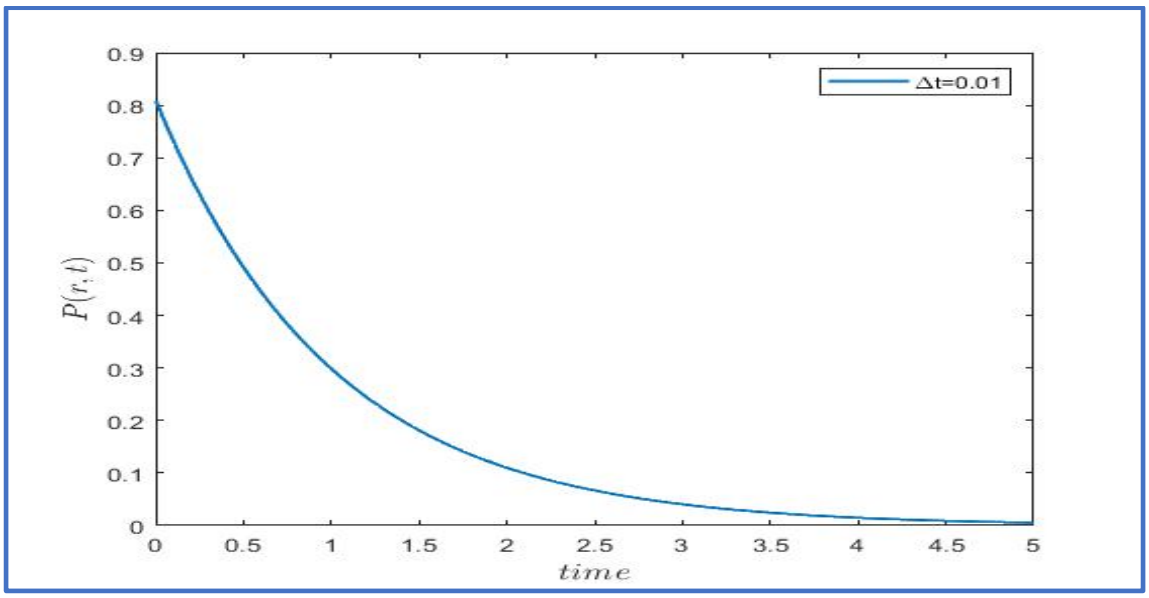

Figure 5-5: Plot of P vs. t showing global pressure dissipation in the saline reservoir (Alpha=0.76).

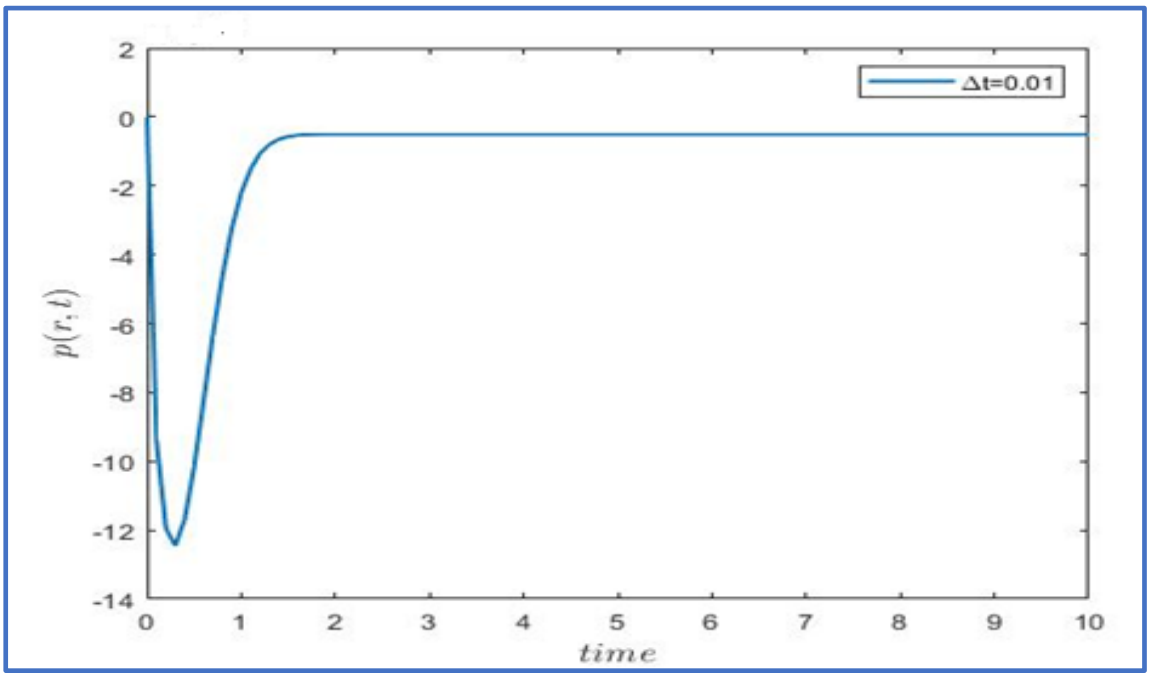

Figure 5-6: Plot of P vs. t showing transient pressure response at the near well region (Alpha=0.76).

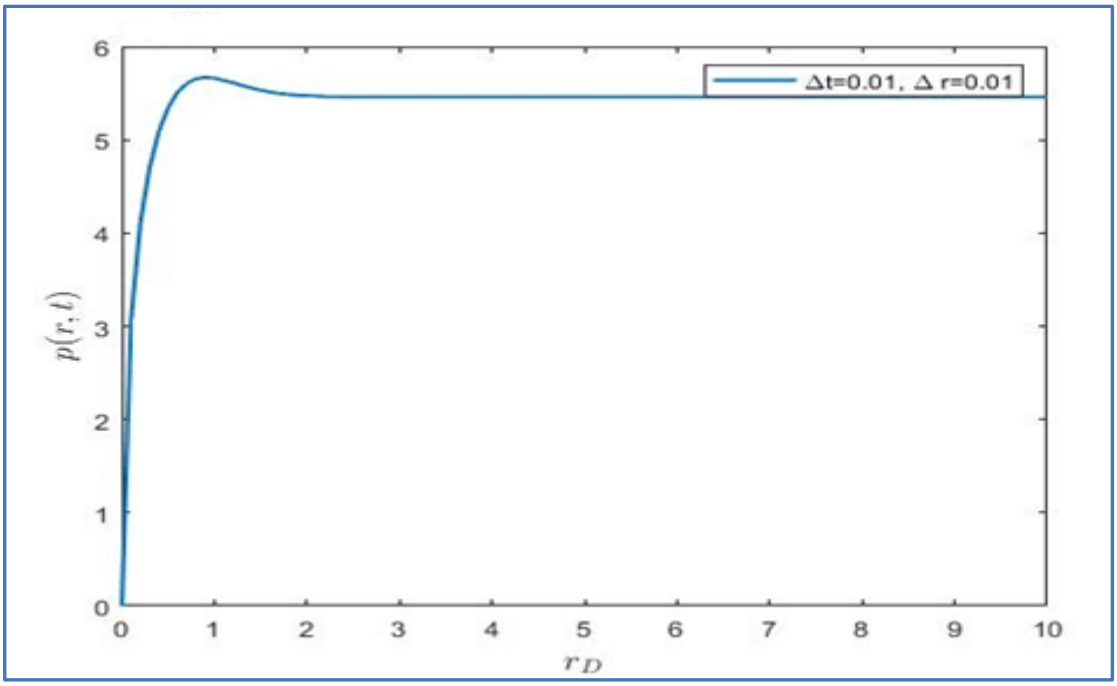

Figure 5-7: Plot of P vs. r showing the near Well pressure behavior at the near well region (Alpha=0.76)

5.7. Discussion and conclusion

This section is dedicated to the simulation results obtained. The Caputo Fabrizio fractional derivative is a convolution of the first derivative and the memory kernel, in this case, the fractional exponential memory function. Unlike the Gaussian distribution, the exponential kernel determines the value of a function by considering the history of the studied process. For the value of alpha taken as one, the non-local kernel decomposes into a classical Delta Dirac function $\delta(t)$. To demonstrate the memory effect of the Caputo Fabrizio derivative, (Figures 5-3 – 5-7) illustrate the results obtained for pressure buildup. It should be noted that all simulations presented were performed using the same alpha for the sake of comparison.

The chapter aimed to approximate pressure buildup in a non-homogenous saline aquifer using the Caputo Fabrizio fractional derivative. The numerical schemes simulated in this chapter were completed using a two-step Lagrange polynomial, and the results were plotted with MATLAB software.

Figure 5-4 shows the global pressure response throughout the reservoir. At early injection time, the pressure is highest close to the well and gradually dissipates further away from the injection well. During injection, the supper critical Formation is assumed

to be bounded at the top and bottom by an impermeable layer representing a no flow boundary.

The injection well is infinitesimally small $(r \to 0)$.

upon entry causes saline fluids to evaporate around the well vicinity, which creates regions of negative pressure (Figure 5-6) at early times and a corresponding buildup in pressure within the reservoir. Carbon dioxide injection invokes a two-phase immiscible flow problem described by fractional flow, a function of saturation, phase mobilities, and relative permeability (Figure 5-3). The following conclusions can be drawn:

- The Caputo Fabrizio derivative was able to model the pressure buildup due to injection through a vertical well, taking cognizance of the entire memory effect. Notably, the threshold pressure in the near weal region is an essential parameter. For example, the peak pressure starts to drop after the maximum capillary fringe has been overcome. The maximum pressure shock seems important for assessing rock stability under fluid pressurization.
- The theoretical predictions presented in this chapter agree with experimental data regarding bottom-hole pressure buildup, making a powerful modelling tool for the diffusive movement of fluids through porous media.
- Simulation results suggest that the method and approach used in this problem could capture the effect of fractional flow as it appeals to region two Figure 5-3.

CHAPTER SIX: MODELLING TRANSIENT PRESSURE BUILDUP WITH CROSSOVER MITTAG-LEFFLER FUNCTION.

6.1. Introduction

Global warming and the worsening impacts of climate change have long underpinned the efforts to capture carbon dioxide out of the atmosphere. Several successful demonstrations have proven that geological storage is viable for achieving short-term deep emission reductions. However, the magnitude of subsurface stress perturbation due to industrial-scale injection has far-ranging impacts, such as brine displacement and pressure buildup (J. T. Birkholzer 2009). Fluid pressurization can drive diffuse migration of fluids through cap rock if the capillary entry pressure is overcome (Mosaheb and Zeidoun, 2017; Birkholzer and Oldenburg, 2015) and enhance focused leakage through high permeability pathways such as old abandoned leaky wells (Nordbotten et al., 2004), reactivated or newly developed fractures (Lucier, 2006). The goal is to understand the spatial transient pressure behavior and predict its response in the event of a leakage from storage and into sensitive environments such as shallow capture regions for fresh groundwater abstraction. Groundwater is critical for sustaining the world's depleting water resources, and understanding the effects of pressure buildup due to sub-surface CO_2 injection is of concern.

The three previous chapters in this thesis have successfully developed numerical solutions for the pressure buildup based on local and non-local derivatives. The purpose of using a fractional derivative is to capture the effect of fluid memory on the pressure buildup during migration and dispersing through porous media and extend the model to the concept of fractional calculus. While the classical delta Dirac derivative can replicate the pressure response from CO_2 injection, its limitation to capture complex real-world problems continues to be widely recognized. This is predominantly the result of Darcy-based formalism, which is strictly associative and commutative and obeys the semigroup theory, underpinning the traditional laws of mass, momentum, and energy conservation. The Caputo and Caputo-Fabrizio fractional derivatives applied in chapters four and five are fractional derivatives introduced to capture complexities that were invisible to the traditional delta Dirac. The Caputo-Fabrizio derivative, the most popular fractional derivative, was introduced after the

Riemann Lowville derivative and before the Caputo-Fabrizio derivatives. The goal of the Caputo-Fabrizio derivative was to overcome some of the limitations highlighted in the Caputo formalisms, including issues such as scale invariance and singularity at the origin. The Caputo derivative lacks a well-defined average value for $\alpha < 1$. For a detailed account of these limitations, (Atangana and Gomez, 2018) is recommended. The Caputo-Fabrizio derivative appears naturally in nature through the decay law, and even though it is classically posed, it is integral. All past information is captured in the initial condition (Caputo & Fabrizio, 2021). It is a convolution of the fractional exponential function and the first derivative$(f't)$. The exponential decay kernel occurs naturally in many processes, and as opposed to the local character of the Caputo derivative, physical processes can be non-locally described using the generalized Mittag-Leffler function.

This chapter focuses on modelling pressure buildup with crossover behavior using the Mittag-Leffler function to describe pressure diffusivity in the saline reservoirs due to CO_2 injection. Firstly, we present some mathematical preliminaries of the Mittag-Leffler function, the conceptual model, numerical analysis, and some simulations.

6.2. Conceptual model and assumptions

CO2 injection into the subsurface generates three saturation regions described in (Figure 6.1): Region A, B, and C.

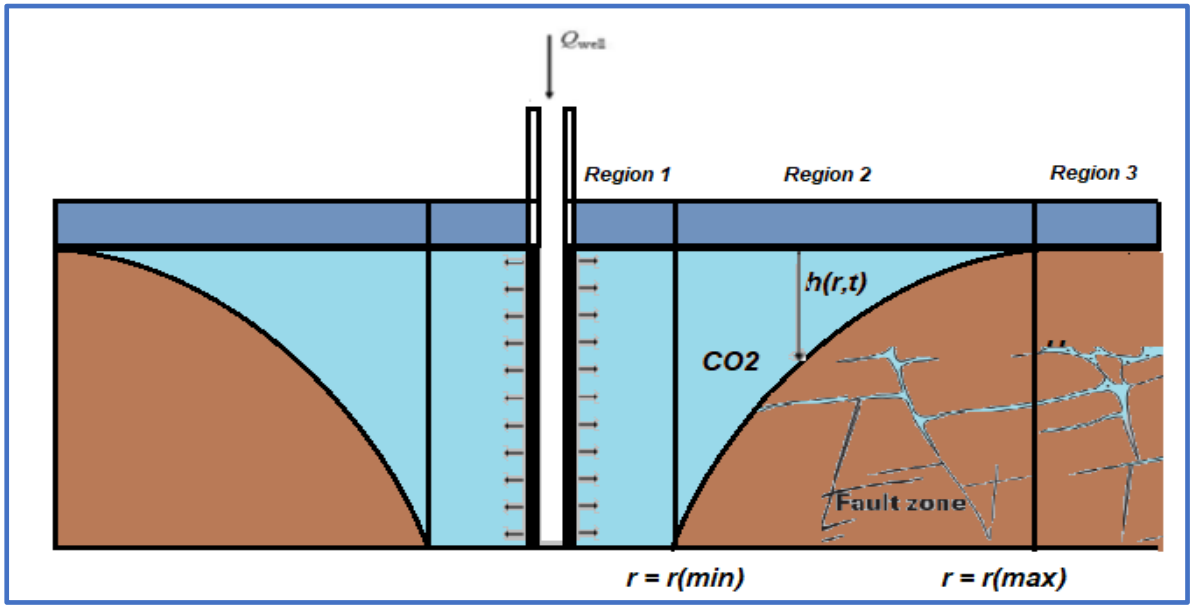

Figure 6-1: Conceptual Model for CO2 Injection in saline Aquifer (Crossover behavior). Adapted from (Azizi, 2013).

6.2.1. Model Assumptions:

- Flow is dominated by crossover from Gaussian to the non-Gaussian flow characteristic from matric to fracture.
- See Figure 6.2
- Constant rate injection,
- Finite acting boundaries.

6.3. Mittag-Leffler function and pressure diffusivity

While some derivatives, such as the Caputo derivative, can conveniently capture the effect of low-order heterogeneity, such as anomalous diffusion in rock fractures, other memory kernels can capture higher-order complexity. This includes cross behavior from Gaussian to non-Gaussian, with a steady state waiting for distribution, e.g., Caputo-Fabrizio, or crossover from Gaussian to non-Guassian with crossover waiting for time distribution showing the crossover from Gaussian to non-Guassian with the Atangana Baleaunu derivative (Atangana & Gomez, 2018). The Mittag-Leffler function captures mean square displacement as a crossover from usual to sub-diffusion.

Sedimentary basins can be uniformly fractured or may display strain localization. In some reservoirs, incredibly tight sands with low permeability, flow primarily depends on the fractures' interconnectivity. The Atangana-Baleanu derivative is invoked for the case of the pressure front due to fluid flow from the matrix (Gaussian) to fracture (non-Guassian) flow. This process is memory dependent and can only be modelled with fractional derivatives with a well-defined.

6.4. Mathematical preliminaries.

This section presents the popular formalisms for the fractional Mittag-Leffler function as defined by the Atangana-Baleanu derivative. The Atangana-Baleanu fractional derivative is expressed in both Caputo and Riemann-Liouville senses.

Firstly, for a function $u(t)$, the Atangana Baleanu derivative in the sense of Caputo is defined as

$$ {}^{ABC}_{a}D_{t}^{\alpha}u(t) = \frac{AB(\alpha)}{1-\alpha}\int_{a}^{t}\frac{d}{d\tau}u(\tau)E_{\alpha}\left[-\frac{\alpha}{1-\alpha}(t-\tau)^{\alpha}\right]d\tau \qquad (6.1) $$

Likewise, the Atangana-Baleanu derivation in Riemann Liouville sense is defined as

$$ {}^{ABC}_{a}D^{\alpha}_{t}u(t) = \frac{AB(\alpha)}{1-\alpha}\frac{d}{dx}\int_a^t u(\tau)E_\alpha\left[-\frac{\alpha}{1-\alpha}(t-\tau)^\alpha\right]d\tau \tag{6.2} $$

The following can be defined for the above equations: the function $u(t) \in Z_2^1(0,l), \alpha \in [0,1]\ and\ AB(\alpha) = 1-\alpha+\frac{\alpha}{\Gamma(\alpha)}$.

In addition, the approximation for the fractional integral states

$$ {}^{ABC}_{a}I^{\alpha}_{t}u(t) = \frac{1-\alpha}{AB(\alpha)}u(t) + \frac{\alpha}{AB(\alpha)\Gamma(\alpha)}\int_a^t u(\tau)(t-\tau)^{\alpha-1}d\tau \tag{6.3} $$

6.5. Numerical analysis

We consider the following system of equations for the given initial and boundary conditions.

$$ \begin{cases} {}^{ABC}_{t}D^{\alpha}_{0}P_{D1}(t,r_D) = \mathcal{H}_1(t,r_D,p_1(t,r) \\ {}^{ABC}_{t}D^{\alpha}_{0}P_{D2}(t,r_D) = \mathcal{H}_2(t,r_D,p_1(t,r) \\ {}^{ABC}_{t}D^{\alpha}_{0}P_{D3}(t,r_D) = \mathcal{H}_3(t,r_D,p_1(t,r) \\ P_{D1},P_{D2},P_{D3}(r,0) = P_0 = 0 \end{cases} \tag{6.4} $$

From the fundamental theorem of calculus, we have that.

$$ \begin{aligned} p_n(t,r_{D,i}) - p_n(0,r_{D,i}) &= (1-\alpha) + \mathcal{H}_n(t,r_D,p_n(t,r)) \\ &+ \frac{\alpha}{\Gamma(\alpha)}\int_0^t \mathcal{H}_n(t,r_D,p_1(t,r_D)(t-\tau)^{\alpha-1}d\tau \end{aligned} \tag{6.5} $$

Were $n = 1,2,3,\ such\ that\ p_n = p_1,p_2,p_3\ and\ \mathcal{H}_n = \mathcal{H}_1,\mathcal{H}_2,\mathcal{H}_3$

We consider the point $t_{k+1} = (k+1)\Delta t$ giving.

$$ \begin{aligned} p_n(t_{k+1,}r_{D,i}) &= p_n(r_{D,i},0) + (1-\alpha)\mathcal{H}_n(t_{k+1},r_D,p_n(r_{D,i},t_{k+1})) \\ &+ \frac{\alpha}{\Gamma(\alpha)}\sum_{m=0}^{k}\int_{t_k}^{t_{k+1}}\mathcal{H}_n(r_{D,t_m},\tau,p_n(t_m,r_D)(t_{k+1}-\tau)^{\alpha-1}d\tau \end{aligned} \tag{6.6} $$

$$ \begin{aligned} p_n(t_{k+1,}r_{D,i}) &\approx p_{n_{k+1}}^{r_{D,i}} \\ &= p_{n_{r_{D}i}}^{0} + (1-\alpha)\mathcal{H}_n(r_D,t_{k+1},p_{n_{k+1}}^{r_D}) \\ &+ \frac{\alpha}{\Gamma(\alpha)}\sum_{m=0}^{k}\int_{t_m}^{t_{m+1}}\mathcal{H}_n(r_{D,i},t_m,p_{n_m}^{r_Di}(t_{k+1}-\tau)^{\alpha-1}d\tau \end{aligned} \tag{6.7} $$

$$p_{n_{r_{D,i}}}^{k+1} = p_{n_{r_{D}i}}^{0} + (1-\alpha)\mathcal{H}_n\left(r_D, t_{k+1}, p_{n_{r_D}}^{k+1}\right) + \frac{\alpha}{\Gamma(\alpha)}\sum_{m=0}^{k}\mathcal{H}_n(r_{D,i}, t_m, p_{n_m}^{r_D i})\int_{t_m}^{t_{m+1}}(t_{k+1}-\tau)^{\alpha-1}d\tau \quad 6.8$$

Computing the integral, we have that.

$$\int_{t_m}^{t_{m+1}}(t_{k+1}-\tau)^{\alpha-1}d\tau = \frac{(t_{k+1}-\tau)^{\alpha}}{\alpha}\Big|_{t_m}^{t_{m+1}} = \frac{(t_{k+1}-t_m)^{\alpha}}{\alpha} - \frac{(t_{k+1}-t_{m+1})^{\alpha}}{\alpha}$$

$$\approx \frac{(h(k+1)-hm)^{\alpha}}{\alpha} - \frac{h(k+1)-h(m+1)^{\alpha}}{\alpha} = \frac{h^{\alpha}}{\alpha}\{(k-m+1)^{\alpha}-(k-m)^{\alpha}\}$$

Substituting gives

$$p_{n_{r_{D,i}}}^{k+1} = p_{n_{r_{D}i}}^{0} + (1-\alpha)\mathcal{H}_n\left(r_D, t_{k+1}, p_{n_{r_D}}^{k+1}\right) + \frac{\alpha}{\Gamma(\alpha)}\sum_{m=0}^{k}\mathcal{H}_n\left(r_{D,i}, t_m, p_{n_m}^{r_D i}\right)\left[\frac{h^{\alpha}}{\alpha}\{(k-m+1)^{\alpha}-(k-m)^{\alpha}\}\right] \quad 6.9$$

6.5.1 Approximation using Trapezoidal formula.

$$p\left(r_{Di,}t_{k+1}\right) = p\left(r_{D,i},0\right) + (1-\alpha)\mathcal{H}_n\left(r_{Di}, t_{k+1}, p(r_{Di}, t_{k+1})\right) + \frac{\alpha}{\Gamma(\alpha)}\sum_{m=0}^{k}\frac{\mathcal{H}_n(r_{Di}, t_m, p_{n_{r_{Di}}}^{m}) + \mathcal{H}_n(r_{Di}, t_{m+1}, p_{n_{r_{Di}}}^{m+1})}{2}\delta_{k,m}^{\alpha} + \frac{h^{\alpha}}{\alpha}\mathcal{H}_n(r_{Di}, t_m, p_{n_{r_{Di}}}^{m}) \quad 6.10$$

where

$$\delta_{k,m}^{\alpha} = \frac{h^{\alpha}}{\alpha}\{(k-m+1)^{\alpha}-(k-m)^{\alpha}\}. \quad 6.11$$

For

$$\mathcal{H}_n(r_D, t, P_n(t, r_D) = {}^{ABC}_{t}D_0^{\alpha}P_n(t, r_D) \quad 6.12$$

<u>Region one:</u>

$$\mathcal{H}_1(r_{Di}, t_m, p_1(t_m, r_{Di}) = \left[\frac{\left(P_{D1,i+1}^{m} - 2P_{D1}{}_i^{m} + P_{D1,i-1}^{m}\right)}{(\Delta r)^2} + \frac{1}{r_i}\frac{\left(P_{D1,i+1}^{m} - P_{D1,i-1}^{m}\right)}{2\Delta r}\right] \quad 6.13$$

<u>Region two:</u>

$$\mathcal{H}_2(r_{Di}, t_m, p_2(t_m, r_{Di}) = \left(F_{\lambda g}\eta_{D2}\right)\left[\frac{\partial^2 P_{D2}}{\partial^2 r} + \frac{1}{r_i}\frac{\partial P_{D2}}{\partial r_D}\right] \qquad 6.14$$

$$= \left(F_{\lambda g}\eta_{D2}\right)\frac{\left(P_{D1,i+1}{}^{m} - 2P_{D1}{}_{i}^{m} + P_{D1,i-1}{}^{m}\right)}{(\Delta r)^2} + \frac{1}{r_i}\frac{\left(P_{D1,i+1}{}^{m} - P_{D1,i-1}{}^{m}\right)}{2\Delta r}$$

Region three:

$$\mathcal{H}_3(r_{Di}, t_m, p_3(t_m, r_{Di}) = \frac{\left(P_{D1,i+1}{}^{m} - 2P_{D1}{}_{i}^{m} + P_{D1,i-1}{}^{m}\right)}{(\Delta r)^2} + \frac{1}{r_i}\frac{\left(P_{D1,i+1}{}^{m} - P_{D1,i-1}{}^{m}\right)}{2\Delta r} \qquad 6.15$$

6.6. Simulation results

This section is dedicated to simulation results obtained with the trapeze integral approximation method.

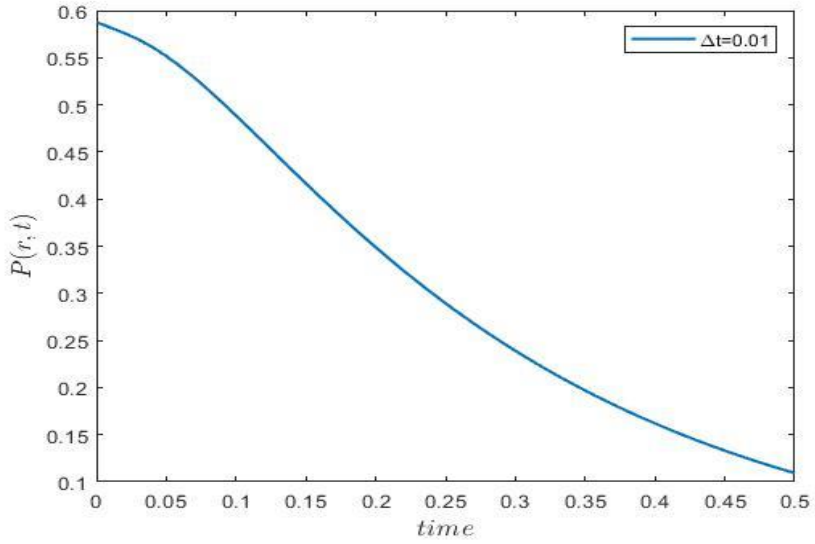

Figure 6-2: plot of P vs r (cross over from region 1 to region 2).

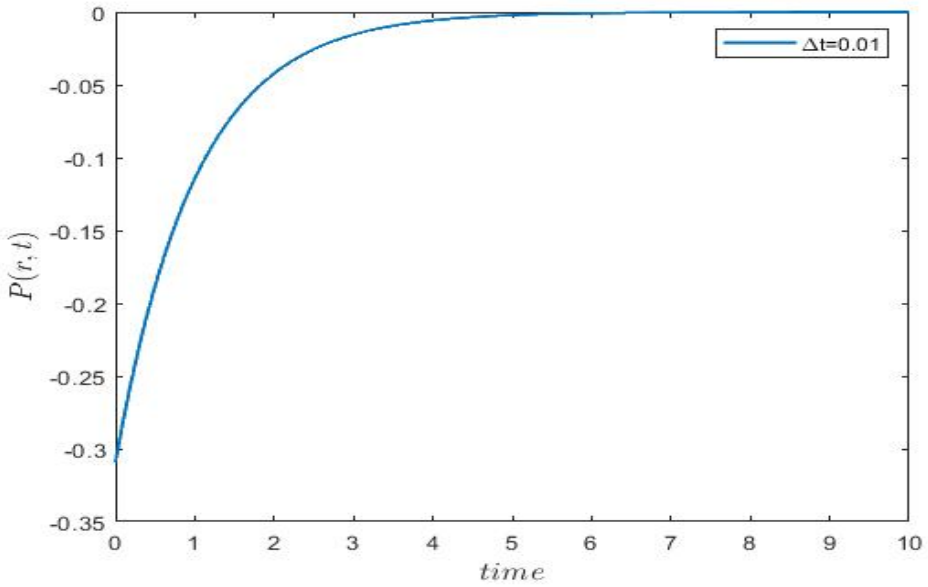

Figure 6-3: Plot of P vs r showing bottom-hole transient pressure response.

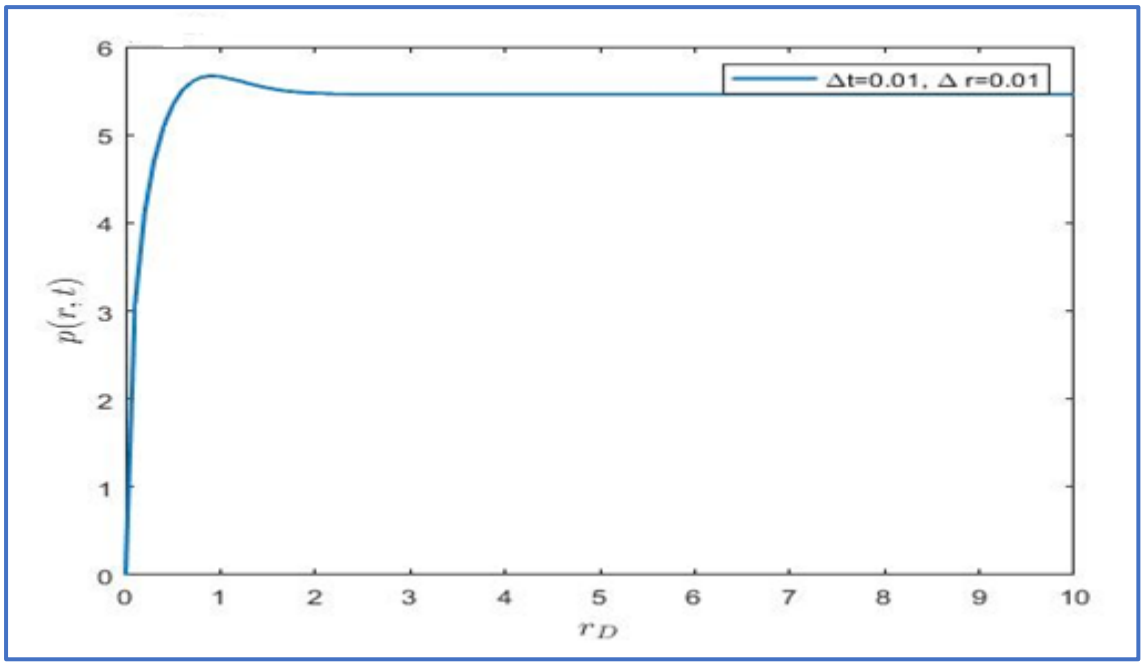

Figure 6-4: Plot of P vs r showing bottom-hole transient pressure response at near well region.

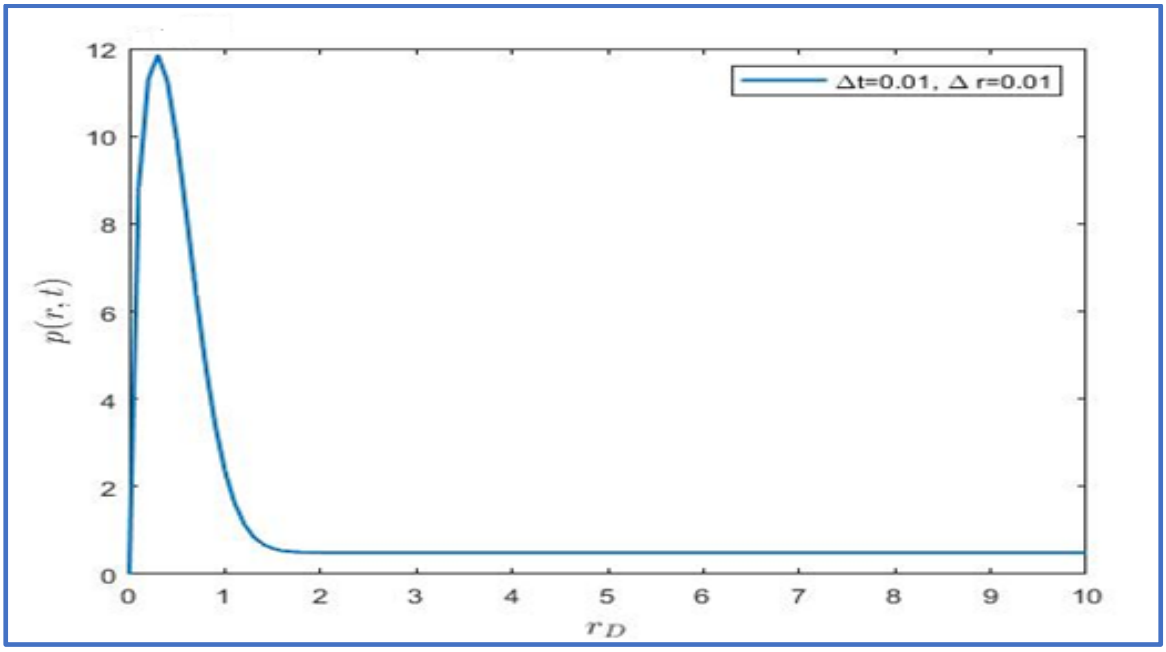

Figure 6-5: Plot of P vs r showing pressure behavior in the near Well region.

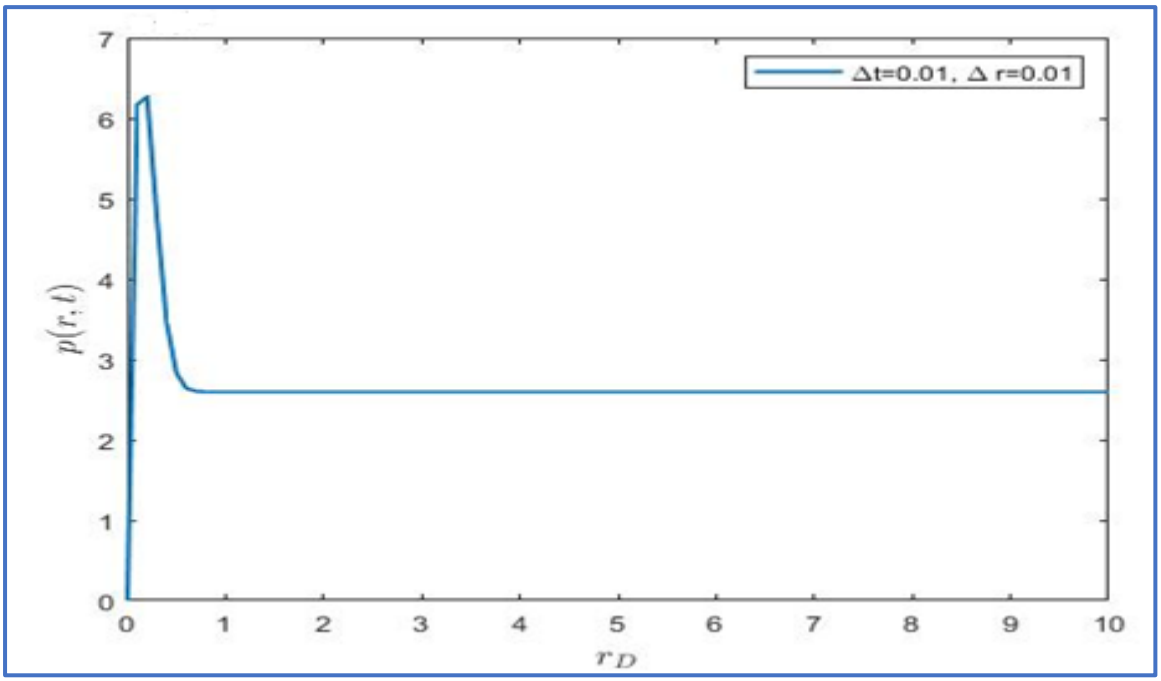

Figure 6-6: Plot of P vs r for fractional flow region.

6.7. Discussion and Conclusion

This section covers the concluding remarks on the model results obtained for pressure diffusivity simulations using the ABC derivative.

First, power laws have been valuable for characterizing non-Darcian flows and the resulting pressure fronts in porous media. This is common in inertia-conditioned and anomalous flow systems, such as fractures in rock matrix with long-term dependence.

Using the Caputo derivative, the diffusivity model has been extended to describe non-Darcian fluid processes. This assumes the case where the transition from anomalous to un-anomalous flow is the dominant transport mechanism described. Studies in literature (Arif et al., 2021) show that fractal-fractional power law models can model the memory dependence of stresses in coupled hydro-mechanic processes. Theoretically, the Caputo derivative provides various possible solutions for pressure response, reducing complexity and computation time (Atangana and Zakia, 2019).

CHAPTER SEVEN: TIME STOCHASTIC MODELLING OF PRESSURE BUILDUP WITH CROSS-OVER BEHAVIOR USING MITTAG-LEFFLER FUNCTION - ATANGANA BALEAUNU DERIVATIVE.

7.1. Introduction

The relentless increase of atmospheric CO_2 and other Green House Gas (GHG) concentrations is responsible for rising global surface temperatures. At the current accumulation rates, the potential to cause apocalyptic (severe and non-reversible) climate conditions continues to threaten the quality of life on Earth. Most remarkably, the year 2022 saw extreme weather scenarios across large portions of the northern hemisphere: most notably, severe heatwaves across Western Europe and Central and Eastern China, followed by floods that left some major European cities and most of Pakistan submerged (Vacek and Cukor, 2023). Against these odds, the call to curb atmospheric CO_2 concentration has become urgent, and geological CO_2 sequestration is a leading paradigm in this pursuit. However, the CO_2 injection problem is complex, with many coupled processes, which give rise to uncertainties at varying scales.

Limiting the risk uncertainties and increasing the safety confidence for large-scale deployment remains a significant challenge. In a heterogeneous reservoir, monitoring pressure buildup is particularly important for the integrity of the storage complex. Heterogeneity impacts plume migration, which reflects the pressure distribution within the reservoir. Injection and flow in a heterogeneous formation is a multi-coupled thermo-hydro-geomech-geochem process. The aim is to obtain accurate predictions of the performance of the reservoir by simulating predicted outcomes from fluid and pressure diffusivity equations. CO_2 ingress and the advance of the pressure front are described as a function of the CO_2 saturation profile, and the set of differential equations that model and predict pressure behavior assume injection in a homogenous, isotropic, isothermal condition, a consideration that grossly undermines the true complexity of a saline reservoir. Obtaining reliable results requires detailed reservoir characterization by integrating all geophysical properties of the rocks. Fluvial systems are generally heterogeneous (Figure 7-1) in various scales, and understanding the various scales of heterogeneity is needed to characterize the reservoir, reliably analyze, and predict pressure buildup (Keogh et al., 2007). While heterogeneities can be grouped into structural and stratigraphic, this chapter employs stochastic modelling to understand better the role of stochastic facies variation on the pressure diffusivity model.

By definition, a stochastic process is a family of random variables which are defined on a standard probability space. In reservoir modelling, two coupled steps involved are the sequential Gaussian simulation (SGS) which predicts the standard deviation of the mean of a variable at a position of calculation, where the random variable is defined by a standard Gaussian distribution (Bohling, 2005). In chapters 4, 5, and 6, heterogeneity was captured by applying time fractional derivatives to describe and quantify non-localities' effect on fluid-induced pressure buildup.

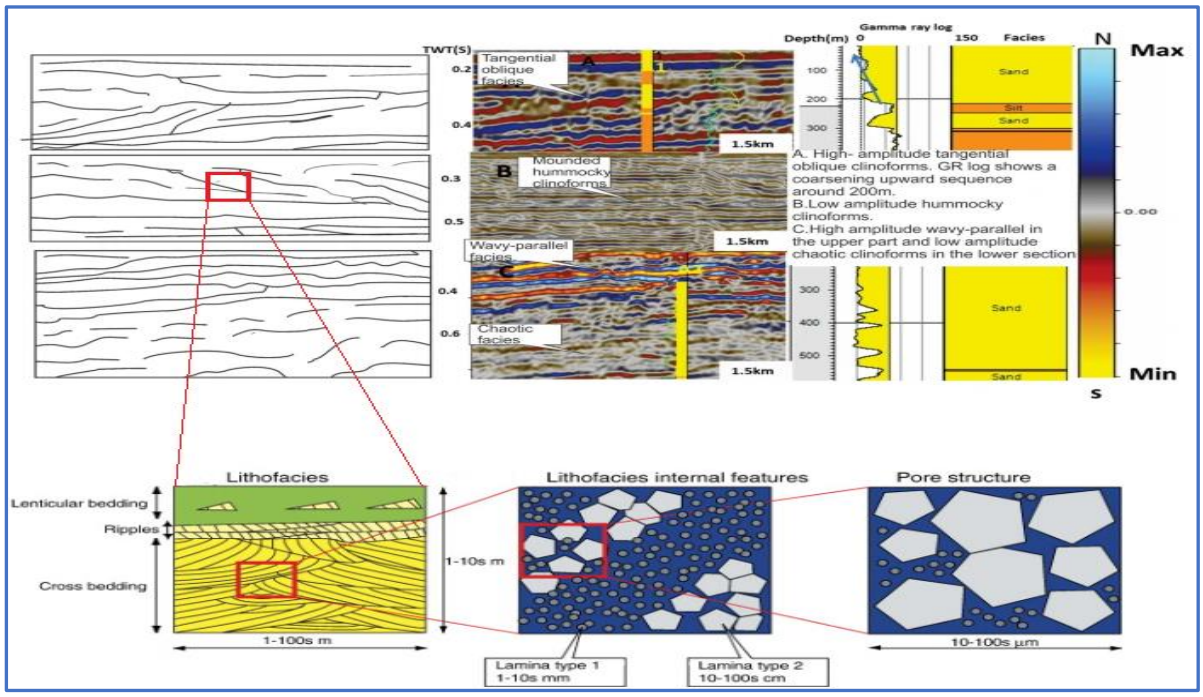

Figure 7-1: Diagram showing conceptual and interpreted seismic facies configuration for heterogeneous seismic facies configuration calibrated by gamma-ray logs. Adapted from (Roussanaly, 2020).

These derivatives (Caputo Fabrizio, Caputo, and the ABC derivatives) introduce memory formulation to capture the history of the fluid through the geological formation. This chapter extends the classical model in Chapter 3 and the fractional model of the ABC derivative by introducing a stochastic term. Going forward, we present the conceptual model, discuss stochastic modelling in porous media, and discuss the case of CO_2 storage, followed by numerical analysis, simulation, and discussion.

7.2. Conceptual model

We consider a two-dimensional system as in (Figure 7-2). During injection, the CO_2 drains and expands pore spaces occupied by reservoir fluid (brine), initially at rest. This causes pressure buildup within the reservoir, the overarching risk concern. The objective, therefore, is to monitor and maintain the pressure buildup below the reservoir fracture pressure. To achieve this objective, experimental and use of accurate data collected under operational conditions of CO_2 injection is needed; however, this data is only available once injection has begun. Therefore, the use of mathematical models and numerical approximation techniques has found great application (Mathias, 2009; Bao et al., 2013; Azizi et al., 2013). When injected through a well open in a saline aquifer, the shape characteristics and evolution of the plume are linked to the intrinsic geological formation conditions and fluid properties of the invading and resident fluids, i.e., CO_2 and brine, respectively. Carbon dioxide ingress happens through the formation's displacement, a process associated with the development of three saturation regions, as depicted in (Figure 7.2). A fractional operator (ABC) is used in stochastic differential and integral equations to capture stochastic processes with memory-dependent behaviours in the current scenario.

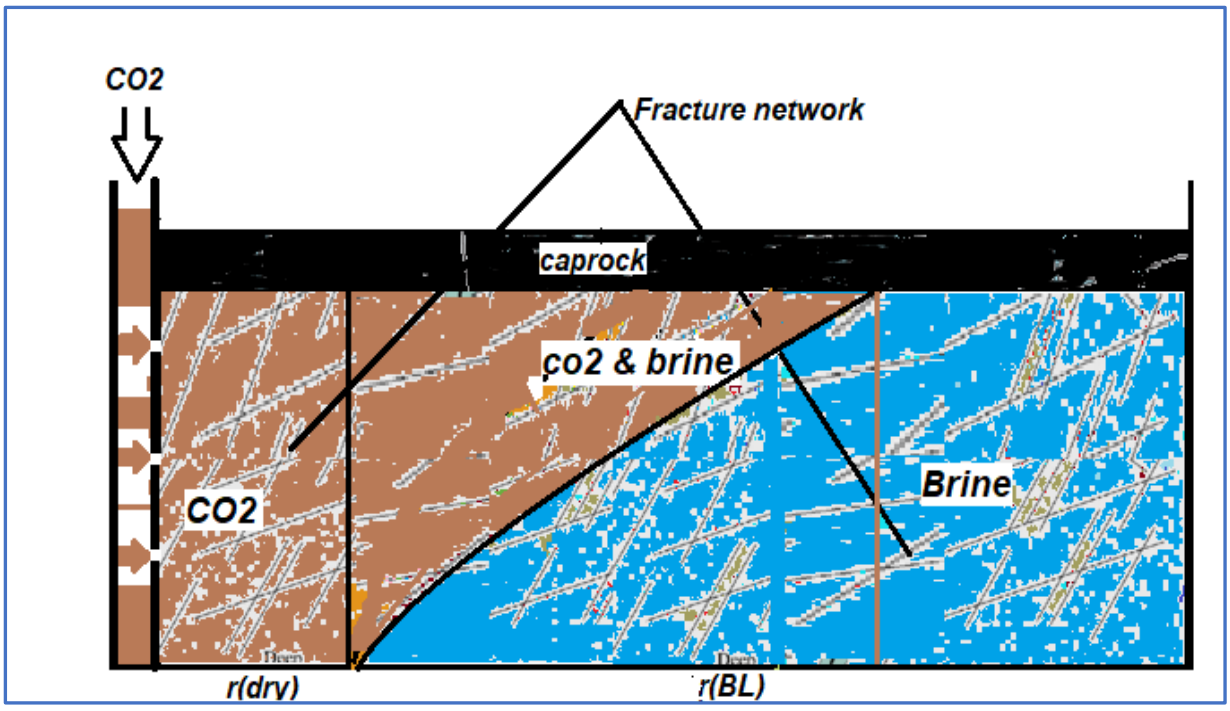

Figure 7-2: Two-dimensional conceptual model showing pressure profiles and structural and reservoir heterogeneity.

7.3. Application of stochastic modelling in pressure buildup due to CO_2 injection in saline reservoirs

One of the challenges encountered in most reservoir simulation studies is quantifying the uncertainties of the subsurface conditions irrespective of the quantity of geological and geophysical data available. That is why a probability approach (stochastic modelling) is essential. The use of stochastic modelling is familiar to reservoir studies. For example (Hewett, 1986) and (Haldorsen, 1987) applied the approach in the petroleum industry to estimate sand drainage between producing wells. In CO_2 storage, stochastic models coupled with fluid flow simulations have been successfully used to update reservoir parameters such as porosity and permeability predictions for uncertainty calculations (Gasda et al., 2012; Liu et al., 2020), while risk assessment and storage capacity estimates have been studied in several other works (Burruss et al., 2009; Jung et al., 2018). However, accurate uncertainty quantification during CO_2 migration remains, and predictions based on this approach are still standard. In other studies, geophysical measurements (seismic, gravity, and electromagnetic data) have been used to perform static reservoir simulation for plume monitoring. Some of these works focused on predicting the extent of the pressure plume front (Nordbotten and Celia, 2011; Gluyas and Mathias, 2013).

Static reservoir models can be updated to render dynamic models more reliable for predictive purposes (Sun et al., 2013). In the petroleum industry, data assimilation for history matching is achieved using a Kalman filter or a smoother ensemble (Emerick, 2013). More recently, the same goal has been achieved with Machine learning techniques (Etienam, 2019, Tahmasebi et al., 2018). The current study is based on the following assumptions:

- Flow is a non-steady state and non-uniform
- The porous system is inhomogenous, non-isotropic and
- There is no mass transfer between the solid and liquid phases.

7.3.1. Stochastic particle tracking

In porous medium flow, a particle is characterized by a unique kind of random walk as it makes its way through the matrix pores. Displacement of the particle happens through a sequence of steps of random lengths with a random waiting time between each step.

7.3.1.1. Waiting time distribution

The waiting time distribution is a fundamental concept in stochastic modelling and has many applications, so probability theory. Defined as the probability distribution of the time duration between successive event steps of a stochastic process. They are used to evaluate the timing and local correlation of events. Additionally, fractional derivatives have been used to model waiting time distribution in diffusion processes. In addition, in non-Markovian processes, waiting time distribution deviates from Exponential distribution, expressing more of a heavy-tailed behavior indicative of the long-range correlation. In continuous systems, waiting time distribution is obtained by discretization, which has an uncertainty implication on the jump measure, is characterized by noise, and might require repeated experimentation. An alternative approach is to apply the Fokker-Plank equation to derive the density function associated with the stochastic process (Barkai et al., 2000).

7.3.1.2. Mean squared displacement.

The mean squared displacement (MSD) describes the random displacement of a stochastic system over time. The mean squared displacement. For a one-dimensional continuous-time stochastic process, for example, Brownian motion or diffusion follows the scaling law

$$(\Delta x)^2 = \langle (x - \langle x \rangle)^2 \rangle = 2Dt^{\alpha} \qquad 7.1.0$$

Where D is the diffusion coefficient, and the equation will describe sub-diffusion $0 < \alpha < 1$, supper-diffusion, with $1 < \alpha < 2$ and ballistic diffusion $= 2$ The MSD is a critical metric used to analyze and characterize stochastic processes, providing a valuable understanding of the underlying behaviours of random particles.

7.4. Types of stochastic processes

Stochastic processes can be considered mathematical models that describe the change of random systems over time or space. Here are descriptions of the main types of random stochastic processes.

7.4.1. Markov process.

A Markov process is a memory-less stochastic process where the future state of the processes is dependent on the current state.

7.4.2. Weiner process

Also called Brownian motion, the Weiner process is a continuous time stochastic process with continuous random fluctuating particle paths. It has stationary and independent increments, meaning that the change in position over time is a function of changes in the other intervals.

7.4.3. Random walk

A random walk models the displacement of a particle as it randomly moves from one position to another. In a one-dimensional random walk, the particle starts at the origin with an equal probability for either direction (left or right). The direction of each step follows the Bernoulli distribution (Keilson and Servi, 1986), with a 50/50 chance for either path. Some essential properties of the random walk include.

- Lack of memory as the direction of the step taken only depends on the current position.
- The random walk shows diffusive behavior with an increasing number of steps. The MSD grows linearly with time in a one-dimensional random walk.
- They are inherently random, leading to diverse trajectories.

7.5. Numerical analysis

The mathematical model includes three systems of three equations as used in the previous chapters. The equations are restated and assume the same initial and boundary conditions as in Chapter 3. We present two models with stochastic properties: the classical delta Dirac and ABC cases. First, we present the stochastic model for the classical solution.

$$H_1\left(t, r_D, p_{D1}(t, r_D)\right) = \frac{\partial^2 p_{D1}}{\partial^2 r_D} + \frac{1}{r}\frac{\partial p_{D1}}{\partial r_D} \tag{7.1.1}$$

$$H_2\left(t, r_D, p_{D2}(t, r_D)\right) = \left(F_{\lambda g}\eta_{D2}\right)\left[\frac{\partial^2 p_{D2}}{\partial^2 r_D} + \frac{1}{r}\frac{\partial p_{D2}}{\partial r_D}\right] \tag{7.1.2}$$

$$H_3\left(t, r_D, p_{D3}(t, r_D)\right) = \left(\eta_{D3}\right)\left[\frac{\partial^2 p_{D3}}{\partial^2 r_D} + \frac{1}{r}\frac{\partial p_{D3}}{\partial r_D}\right] \tag{7.1.3}$$

We consider the following system of equations for the given initial and boundary conditions.

7.5.1. Classical stochastic model for pressure buildup.

We consider the usual Cauchy presentation for initial value problem:

$$\begin{cases} \frac{dp_{D1}(t,r_D)}{dt} = \mathcal{H}_1(t,r_D,p_1(t,r) + \sigma P_{D1}(t,r_D).dB(\tau) \\ \frac{dp_{D2}(t,r_D)}{dt} = \mathcal{H}_2(t,r_D,p_1(t,r) + \sigma P_{D2}(t,r_D).dB(\tau) \\ \frac{dp_{D2}(t,r_D)}{dt} = \mathcal{H}_3(t,r_D,p_1(t,r) + \sigma P_{D3}(t,r_D).dB(\tau) \\ P_{D1},P_{D2},P_{D3}(r,0) = P_0 = 0 \end{cases} \quad 7.1.4$$

We consider a generalized Cauchy problem for the system of equations

$$\frac{dp_{Dn}(t,r_D)}{dt} = \mathcal{H}_n(t,r_D,p_n(t,r) + \sigma P_{Dn}(t,r_D).dB(\tau)$$

$$P_D,(r,0) = P_0 = 0$$

From the fundamental theorem of calculus, we can transform the set of PDE's into an inter-gral differential equation.

$$dp_{Dn}(t,r_D) = \mathcal{H}_n(t,r_D,p_n(t,r) + \sigma P_{Dn}(t,r_D).dB(\tau)$$

Where $\sigma P_{Dn}(t,r_D)$, is the density distribution function and $dB(\tau)$ characterizes the random walk property.

$$p_{Dn}(t,r_D) - p_{Dn}(0,r_D) = \int_0^{t_{k+1}} \mathcal{H}_n(t,r_D,p_n(t,r)dt + \int_0^{t_{k+1}} \sigma P_{Dn}(\tau,r_D)dB(\tau)$$

7.5.2. Approximation with the two-step LaGrange method.

This section completes the numerical solution using the polynomial method to approximate the unknown function as discrete points. This is followed by applying the integral to obtain the summation (Approximation).

Substitute at $t = t_{k+1}$, we have

$$p_{Dn}(t_{k+1},r_{D,i}) = p_{Dn}(0,r_{D,i}) + \int_0^{t_{n+1}} \mathcal{H}_n(\tau,r_{D,i},p_n(\tau,r_{D,i})d\tau + \int_0^{t_{k+1}} \sigma P_{Dn} r_{D,i} dB(\tau)$$

Substituting $t = t_n$ get,

$$p_{Dn}(t_k,r_{D,i}) = p_{Dn}(0,r_{D,i}) + \int_0^{t_k} \mathcal{H}_n(\tau,r_{D,i},p_n(\tau,r_{D,i})d\tau + \int_0^{t_k} \sigma P_{Dn}(\tau,r_{D,i})dB(\tau)$$

Subtracting yields

$$p_{Dn}(t_{k+1},r_D) - p_{Dn}(t_k,r_D) = \int_{t_n}^{t_{n+1}} \mathcal{H}_n(\tau,r_D,p_n(\tau,r)d\tau + \int_{t_n}^{t_{k+1}} \sigma P_{Dn}(\tau,r_D).dB(\tau)$$

7.1.5

Gowning forward, we use the two-step Lagrange to approximate the unknown function given by $\mathcal{H}_n(\tau, r_D, p_n(\tau, r)$.

Approximation with two-step Lagrange

For a function $f(t, y(t)$, the Lagrange two step polynomial is given as

$$f(t, y(t) \approx \mathcal{H}_n(\tau, r_D, p_n(\tau, r) = \frac{\tau - t_k}{t_k - t_{k-`1}} \mathcal{H}_n(t_k, r_D, p_n(t_k, r) - \frac{\tau - t_{k-1}}{t_k - t_{k-`1}} \mathcal{H}_n(t_{k-1}, r_D, p_n(t_{k-1}, r)$$

Substituting, we obtain

$$p_{Dn}(t_{k+1}, r_D) - p_{Dn}(t_k, r_D) = \int_{t_n}^{t_{n+1}} \frac{\tau - t_k}{t_k - t_{k-`1}} \mathcal{H}_n(t_k, r_D, p_n(t_k, r) - \frac{\tau - t_{k-1}}{t_k - t_{k-`1}} \mathcal{H}_n(t_{k-1}, r_D, p_n(t_{k-1}, r) + \int_{t_n}^{t_{k+1}} \sigma P_{Dn}(\tau, r_D). dB(\tau)$$

The next step is to evaluate the definite integrals, for which the solutions are given below as:

$$\int_{t_n}^{t_{n+1}} \mathcal{H}_n(\tau, r_D, p_n(\tau, r) d\tau = \frac{3\Delta t}{2} \mathcal{H}_n(t_k, r_D, p_n(t_k, r) - \frac{\Delta t}{2} \mathcal{H}_n(t_{k-1}, r_D, p_n(t_{k-1}, r)$$

7.1.6a

$$\int_{t_n}^{t_{k+1}} \sigma P_{Dn}(\tau, r_D). dB(\tau) d\tau = \sigma P_{Dn}(C_k). \{B(t_{n+1}) - B(t_n)\}$$

7.1.6b

Where $C_k = [t_k, t_{k+1}]$

Substituting, we obtain

$$p_{Dn}(t_{k+1}, r_D) = p_{Dn}(t_k, r_D) + \frac{3\Delta t}{2} \mathcal{H}_n(t_k, r_D, p_n(t_k, r) - \frac{\Delta t}{2} \mathcal{H}_n(t_{k-1}, r_D, p_n(t_{k-1}, r) + \sigma P_{Dn}(C_k). \{B(t_{n+1}) - B(t_n)\}$$

7.1.7

This equation is the final classical-stochastic numerical solution for the pressure buildup. As demonstrated in the previous chapters, we can obtain the pressure for region 1, region 2, and region three by substituting the discretized scheme of the appropriate pressure diffusivity model to avoid repetition:

where

$$H_1\left(r_{D,i}, t_k, p_{D1}(r_{D,i}, t_k)\right)\Big|_{(r_{Di},\, t_k)} = \left[\frac{1}{r_{D,i}}\left(\frac{p_{D1}(r_{Di+1}, t_k) - p_{D1}(r_{Di-1}, t_k)}{2\Delta r}\right) + \frac{p_{D1}(r_{Di+1}, t_k) - 2p_{D1}(r_{Di}, t_k) + p_{D1}(r_{Di-1}, t_k)}{\Delta r^2}\right]$$

$$H_1(r_{Di}, t_{k-1}, p_{D1}(r_{Di}, t_{k-1}))\Big|_{(r_{Di},\ t_{k-1})} = \left[\left(\frac{p_{D1}(r_{Di+1}, t_{k-1}) - 2p_{D1}(r_{Di}, t_{k-1}) + p_{D1}(r_{Di-1}, t_{k-1})}{\Delta r^2}\right) + \frac{1}{r_{D,i}}\left(\frac{p_{D1}(r_{Di+1}, t_{k-1}) - p_{D1}(r_{Di-1}, t_{k-1})}{2\Delta r}\right)\right]$$

As previously followed, from the fundamental theorem of calculus, we have that.

$$p_n(t, r_D) - p(0, r_D) = (1-\alpha)\left[\mathcal{H}_n\left(t_{k+1}, r_D, p_n(r_{D,i}, t_{k+1})\right) + \sigma P_{Dn}(t, r_D)dB(t)\right] + \frac{\alpha}{\Gamma(\alpha)}\int_0^t \mathcal{H}_n(\tau, r_D, p_1(\tau, r_D)(t-\tau)^{\alpha-1}d\tau + \frac{\alpha}{\Gamma(\alpha)}\sigma\int_0^t P_{Dn}(\tau, r_D)(t-\tau)^{\alpha-1}dB(\tau) \quad 7.1.8$$

Were $n = 1,2,3,\ such\ that\ p_n = p_1, p_2, p_3\ and\ \mathcal{H}_n = \mathcal{H}_1, \mathcal{H}_2, \mathcal{H}_3$

We consider the point $t_{k+1} = (k+1)\Delta t$, and substituting gives.

$$p_n(t_{k+1,} r_{D,i}) = p_n\left(r_{D,i}, 0\right) + (1-\alpha)\left[\mathcal{H}_n\left(t_{k+1}, r_D, p_n(r_{D,i}, t_{k+1})\right) + \frac{B(t_{k+1}) - B(t_k)}{\Delta t}\sigma P_{Dn}(t_{k+1}, r_D)\right] + \frac{\sigma\alpha}{\Gamma(\alpha)}\sum_{j=0}^{k}\int_{t_j}^{t_{j+1}} \mathcal{H}_n(r_{D,i}, \tau, p_n(\tau, r_D)(t_{k+1} - \tau)^{\alpha-1}d\tau + \frac{\sigma\alpha}{\Gamma(\alpha)}\sum_{j=0}^{k}\int_{t_k}^{t_{k+1}} p_n\left(\tau, r_{D,i}\right)(t_{k+1} - \tau)^{\alpha-1}dB(\tau) \quad 7.1.9$$

Where $P_{Dn}(t, r_D)$ is differentiable

$$p_n(t_{k+1,}r_{D,i}) = p_n(r_{D,i},0) + (1-\alpha)\left(\mathcal{H}_n\left(t_{k+1},r_D,p_n(r_{D,i},t_{k+1})\right)\right) + (1-\alpha)\sigma P_{Dn}(t,r_D)\frac{B(t_{k+1})-B(t_k)}{\Delta t} + \frac{\alpha}{\Gamma(\alpha)}\sum_{j=0}^{k}\mathcal{H}_n(r_{Di,k},\tau,p_n(t_k,r_D)\int_{t_j}^{t_{j+1}}(t_{k+1}-\tau)^{\alpha-1}d\tau + \frac{\sigma\alpha}{\Gamma(\alpha)}\sum_{j=0}^{k}\mathcal{H}_n(r_{Di,t_k},\tau,p_n(t_k,r_D)\int_{t_j}^{t_{j+1}}(t_{k+1}-\tau)^{\alpha-1}d\tau \quad 7.2.0$$

$$p_n(t_{k+1,}r_{D,i}) = p_n(0,r_{D,i}) + (1-\alpha)\left(\mathcal{H}_n\left(t_{k+1},r_D,p_n(r_{D,i},t_{k+1})\right)\right) + (1-\alpha)\sigma P_{Dn}(t,r_{Di})\frac{B(t_{k+1})-B(t_k)}{\Delta t} + \frac{\alpha}{\Gamma(\alpha)}\sum_{j=0}^{k}\mathcal{H}_n(r_{Di,t_k},\tau,p_n(t_k,r_{D,i})\left\{\frac{(t_{k+1}-t_j)^{\alpha}}{\alpha} - \frac{(t_{k+1}-t_{j+1})^{\alpha}}{\alpha}\right\} + \frac{\alpha\sigma}{\Gamma(\alpha)}\sum_{j=0}^{k}\int_{t_j}^{t_{j+1}}p_n(\tau,r_{D,i})(t_{k+1}-\tau)^{\alpha-1}d\tau \quad 7.2.1$$

$$p_n(r_{D,i},t_{k+1}) = p_n(r_{D,i},0) + (1-\alpha)\left(\mathcal{H}_n\left(t_{k+1},r_D,p_n(r_{D,i},t_{k+1})\right)\right) + (1-\alpha)\sigma P_{Dn}(t,r_D)\frac{B(t_{k+1})-B(t_k)}{\Delta t} + \frac{(\Delta t)^{\alpha}}{\Gamma(\alpha)}\sum_{j=0}^{k}\mathcal{H}_n(r_{Di,t_k},t_m,p_n(t_m,r_{Di})\delta_{n.k}^{\alpha} + \frac{\sigma(\Delta t)^{\alpha}}{\Gamma(\alpha)}\sum_{j=0}^{k}\frac{B(t_{k+1})-B(t_k)}{\Delta t}\delta_{n.k}^{\alpha} \quad 7.2.2$$

where

$$\delta_{n.k}^{\alpha} = (k-j+1)^{\alpha} - (k-j)^{\alpha}$$

In simplified form, we can have that.

$$p_{n,i}^{k+1} = p_{n,i}^{0} + (1-\alpha)\mathcal{H}_n\left(t_{k+1}, r_{Di}, p_{n,i}^{k+1}\right) + (1-\alpha)\sigma p_{n,i}^{k+1}\frac{B(t_{k+1}) - B(t_k)}{\Delta t} \qquad 7.2.3$$
$$+ \frac{(\Delta t)^{\alpha}}{\Gamma(\alpha)}\sum_{j=0}^{k}\left(\mathcal{H}_n(r_{Di,t_k}, t_m, p_{n,i}^{k}\{\delta_{n.k}^{\alpha}\}\right)$$
$$+ \frac{\sigma(\Delta t)^{\alpha-1}}{\Gamma(\alpha)}\sum_{j=0}^{k}(B(t_{k+1}) - B(t_k)\delta_{n.k}^{\alpha})$$

Where the function in region 1 is finally discretized to obtain the numerical solutions for pressure buildup

$$H_1\left(r_{Di}, t_{k-1}, p_{D1}(r_{Di}, t_{k-1})\right)\Big|_{(r_{Di},\ t_k)}$$
$$= \left[\left(\frac{p_{D1}(r_{Di+1}, t_k) - 2p_{D1}(r_{Di}, t_k) + p_{D1}(r_{Di-1}, t_k)}{\Delta r^2}\right)\right.$$
$$\left. + \frac{1}{r_{D,i}}\left(\frac{p_{D1}(r_{Di+1}, t_k) - p_{D1}(r_{Di-1}, t_k)}{2\Delta r}\right)\right]$$

Region 2

$$H_2\left(r_{D,i}, t_k, p_{D1}(r_{D,i}, t_k)\right)\Big|_{(r_{Di},\ t_k)}$$
$$= \left(F_{\lambda g}\eta_{D2}\right)\left[\left(\frac{p_{D1}(r_{Di+1}, t_k) - 2p_{D1}(r_{Di}, t_k) + p_{D1}(r_{Di-1}, t_k)}{\Delta r^2}\right)\right.$$
$$\left. + \frac{1}{r_{D,i}}\left(\frac{p_{D1}(r_{Di+1}, t_k) - p_{D1}(r_{Di-1}, t_k)}{2\Delta r}\right)\right]$$

Region 3

$$H_3\left(r_{D,i}, t_k, p_{D1}(r_{D,i}, t_k)\right)\Big|_{(r_{Di},\ t_k)}$$
$$= (\eta_{D3})\left[\left(\frac{p_{D1}(r_{Di+1}, t_k) - 2p_{D1}(r_{Di}, t_k) + p_{D1}(r_{Di-1}, t_k)}{\Delta r^2}\right)\right.$$
$$\left. + \frac{1}{r_{D,i}}\left(\frac{p_{D1}(r_{Di+1}, t_k) - p_{D1}(r_{Di-1}, t_k)}{2\Delta r}\right)\right]$$

7.6. Numerical simulation

This section presents the numerical solutions obtained using the fractional-stochastic approach to predict and model pressure buildup due to CO_2 sequestration. Graphs are based on dimensionless pressure, radius, and time.

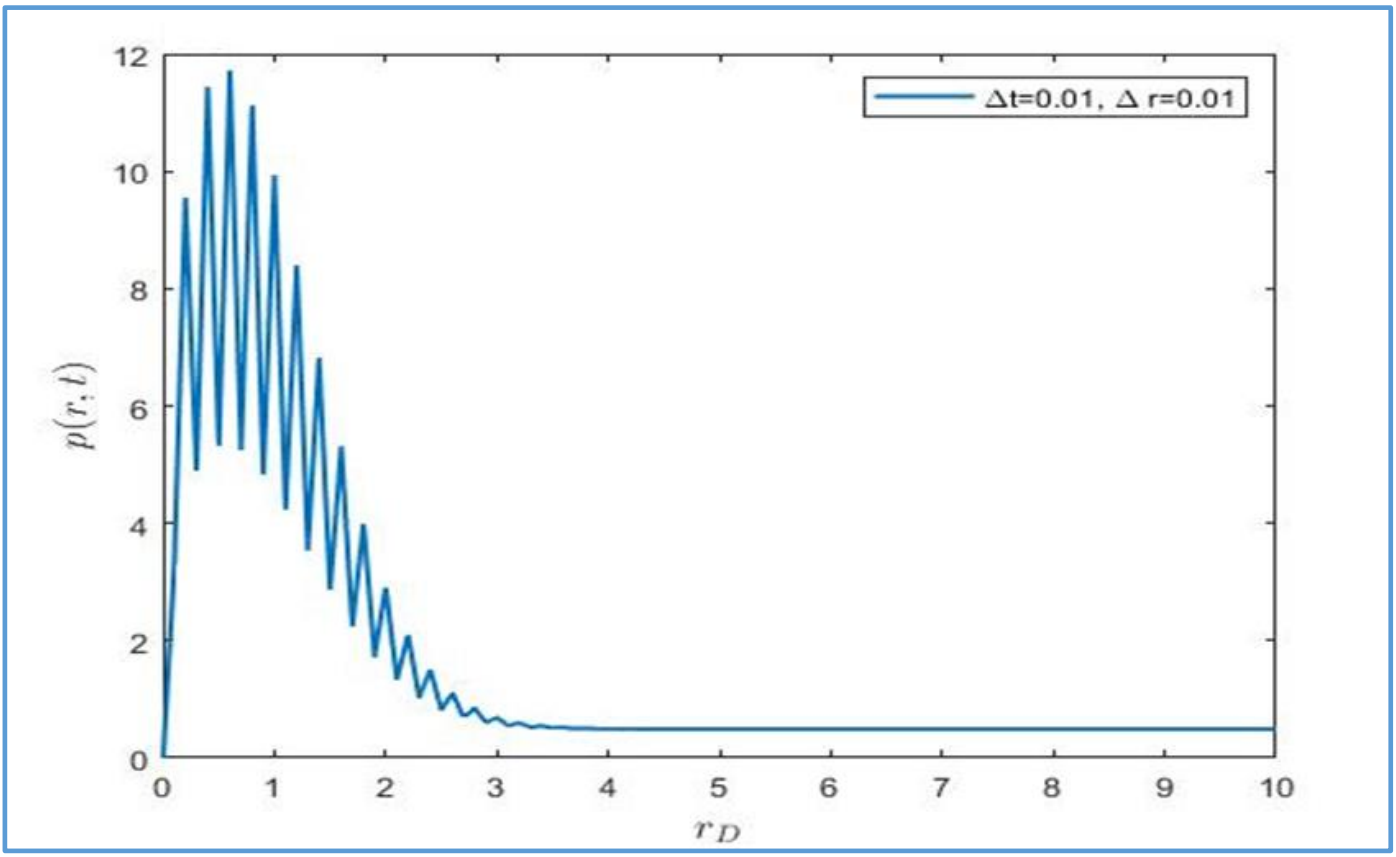

Figure 7-3: Plot P vs r (near well region).

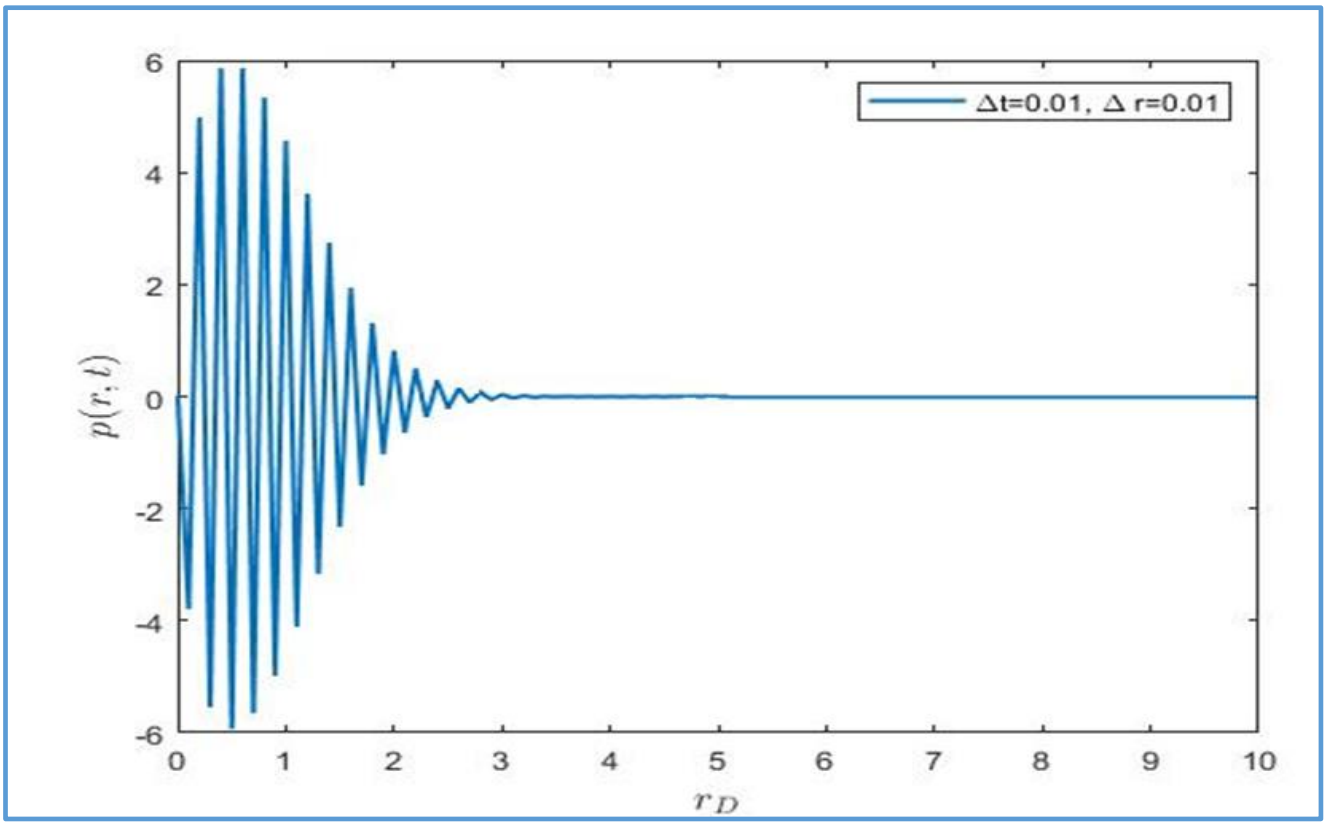

Figure 7-4: Plot P vs r (two-phase flow region).

7.7. Discussion and conclusion

The effect of flow instabilities on trapping mechanisms such as capillarity and dissolution, including and pressure build-up is a notable origin of uncertainty in CO_2 sequestration modelling. The results show that high-energy fluctuations and uncertainty at early times in the near well vicinity as pressure builds up near the well stochastically before stabilising and returning to background values. Carbon dioxide injecting underground is a highly coupled problem with many uncertainties. The stochastic model introduces randomness to the deterministic models, which allows for uncertainty and parameter sensitivity to be studied.

The stochastic models are also relevant for the linear stability analysis of the migrating fluid. Capillarity and dissolution trapping results in viscous and gravity-enhanced fingering as observed through numerical experiments. Stochastic models can be reformulated to capture this process, which is highly characteristic of the CO_2 advancing front.

CHAPTER EIGHT: MODELLING TWO-PHASE IMMISCIBLE FLOW OF CO2-BRINE: IMPLICATIONS FOR GEOLOGICAL CARBON STORAGE.

8.1. Introduction and Background

Carbon Capture and Storage is a pivotal transition technology towards a future NetZero emission target. CCS will buy time to enable carbon-intensive sectors to remain competitive, while oil and coal-dependent nations continue with fossil fuels as part of their energy mix, without causing further global warming. CCS involves the capture, separation, transport, and injection of CO_2 underground, where it is permanently stored and contained for long time lengths. As already observed in the earlier chapters, three saturation fields (Figure 8-1) are created due to CO_2 injection in a saline aquifer: dry out one, two-phase immiscible flow region and a brine region (Birkholzer, 2009). Due to the large difference in fluid densities, the two-face flow region is differentiated into a bottom brine layer and a top CO_2 layer, separated by a transitional region. The flow dynamics in the two-phase region is controlled by the relative permeability's of both phases, saturation, and capillarity. During the vertical ascend of CO_2 towards the cap rock, it maintains contact with the formation brine, increasing the likelihood of mass transfer between the two fluids. A less steep contact transition plane enables more dissolution and capillary trapping. The pressure gradient usually has an impact beyond the mobile plume's physical location, thus modelling pressure buildup requires the plume's advancing front and its position to be known. Once injection stops, the wetting phase (brine) capillarity displaces carbon dioxide (non-wetting phase) as reservoir brines from nearby formations rocks reoccupy pores spaces where carbon dioxide had already occupied, a process called imbibition (Bachu, 2013). Residual trapping happens when the carbon dioxide is held in place by capillary forces due to the interaction of carbon dioxide and reservoir brine. Carbon dioxide sequestration in a saline aquifer is therefore heavily dependent on the role of capillary trapping, where portions of free phase CO_2 are disconnected along pore throats, and immobilized as trapped fractions (Raeini and Bijeljic, 2015) and disolution.

The two-phase flow problem is described by the Buckley Leverette theory (Lake, 1989). The theory allows the calculation of shock fronts in a radial space as brine is being displaced. Many studies have been dedicated to model and describe the fractional flow as it applies to CCS (Scanziani et al., 2020; Juanes et al., 2006). To assess the storage efficiency, (Burton et al., 2009) used a modified version of the Buckley Leverette to solve for the maximum lateral

migration distance of the mobile plume phase. Also, by the method of characteristics (Ghanbarnezhad Moghanloo, 2012) presented a solution for the CO_2 mass conservation equation considering two-phase flow in a 1-D homogenous reservoir. This solution describes the rate of change of saturation, and how fast the compressible plume will migrate from the injection point. Important conclusions derived include: the velocity of the saturation front is constrained by the flux, fractional flow terms (relative permeability and viscosity) and the slope of the fractional flow curve. A semi analytical model solution that solves pressure advancing front was obtained by (Woods, 1962).

Numerical models build on the concept of fractional flow, involving a two-phase immiscible system remain tools for researchers to explore diverse sets of physical problems unique to geological carbon sequestration. For example (Nordbotten, 2005) adopted the concept of energy minimization to develop a space-time solution that predicts plume advancement. Based on the radial Buckley Leverette model, the authors inferred, the relationship of two different time scales in the CO_2 injection problems are proportional to $\sqrt{t}$, i.e., diffusive transient pressure, and secondly, the advective force responsible for the moving CO_2 front. In an independent study, (Mathias et al., 2009) extended (Nordbotten et al., 2005) by considering a sharp interface a similarity solution, based on the method of matched asymptotic expansion was achieved by solving coupled ODEs for continuity to obtain the CO_2-brine interphase column heights as a function of both time and radial distance from the injection position. These solutions assume a sharp interphase and the effect of partial miscibility while ignoring the effect of gravity.

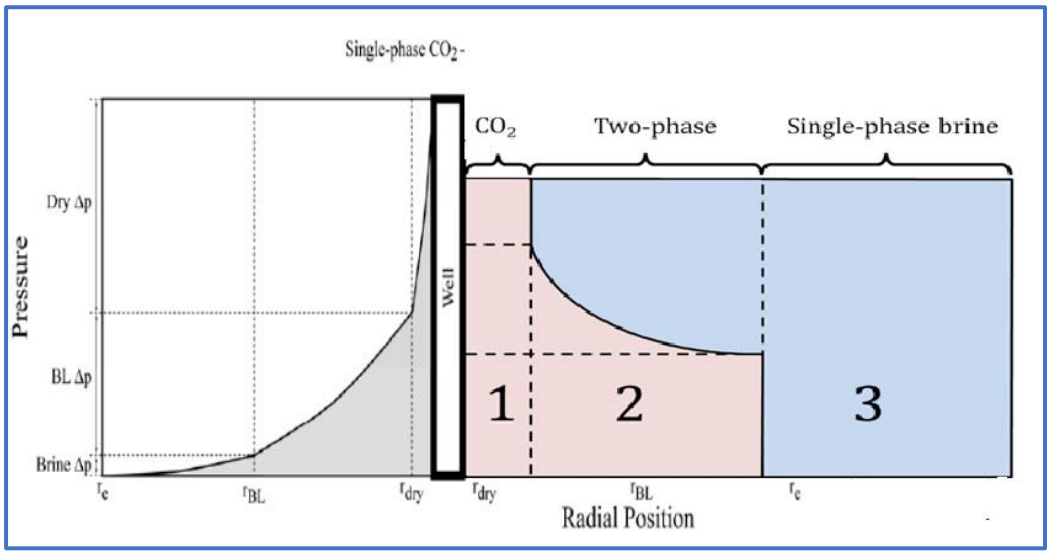

Figure 8-1: Schematic model of the reservoir saturation profile (Adapted from Azizi et al., 2013)

Furthermore, (Sminchak et al., 2012) suggested a model to calculate the effective phase mobility based on the inverse linear relation of mobility with distance, in the two-phase flow region. Their studies concluded that the saturation solutions of (Noh et al., 2007) produced better results while (Burton et al., 2009) under predicted the pressure distribution and buildup, while their prediction of the effective phase mobility's agree with results obtained by using the STOMP- CO_2 simulator.

Based on this short review, the following factors can be considered as process constraints in the two-phase flow:

- Heterogeneity: Heterogeneity affects the movement of and distribution of CO_2 plume and reservoir fluids. For example, capillarity decreases with disorder.
- Gravity: Gravity drives the buoyancy up dip flow of CO_2 in a reservoir due to significant differences in fluid densities. Ignoring the role of gravity can lead to erroneous results.

A comparison of obtain results and field scale observations suggests that instability in fluid flow through porous media greatly reduces the effect of capillarity. This increases with the order of disorder such that quantifying the effect of reservoir heterogeneity becomes important for accurate predictions of two-phase flow and saturation. Current field-scale modelling software packages fail to consider the local variation in reservoir properties and hence can lead to an overestimate of the saturation or underestimate of the pressure buildup within the reservoir. This is due to the inability to capture sub-grid variabilities of gravity, relative permeability's channeling, and viscous forces. Moreover, these models are based on extensions of Darcy's law, which relates flux to the gradient, which lacks the memory necessary to capture local variability in the reservoir and fluid properties. Examples of non-linear behaviours observed with the two-phase flow region include viscous fingering of CO_2 into the brine phase.

To capture the effect of non-locality due to reservoir disorder, fractional derivatives with memory have been used to capture the effects of sub-grid variation which is otherwise blind to the traditional Newtonian differential operators.

In this regard, the chapter's focus is to study two-phase immiscible flow, considering gravity, and heterogeneity effects. The model uses a known phase saturation and a global pressure term as independent variables. A two-phase problem is handled as a single fluid mix, where

individual phases are modelled as sub-fractions of the whole. By coupling the global pressure equation with the saturation (Buckley-Laverette) model, the effect of saturation on the reservoir pressure buildup can be examined. To model saturation in the context of the stated points, the Buckley-Leverette model is extended to the non-local frame of analysis by introducing fractional derivatives to the model the ordinary Differential Equations (ODEs) that calculate saturation.

The chapters structured thus: mathematical formulation, obtention of the steady state solution, background on fractional operators, application of fraction operators (Caputo Fabrizio with a weak cross-over, and ABC with strong cross-over effect. The numerical analysis makes use of the two-step Lagrange method, nouvelle middle point method and Adam Bashford schemes to develop the numerical solutions for pressure buildup.

8.2. Conceptual model and mathematical formulation

As already stated, CO_2 injected geological formation creates three saturation regions, a near-well region, a middle region, and far-field regions. Figure 8-2 illustrates the intermediate regions (two-phase flow region), which we will use in the sections below as the conceptual bases of the modelling problem.

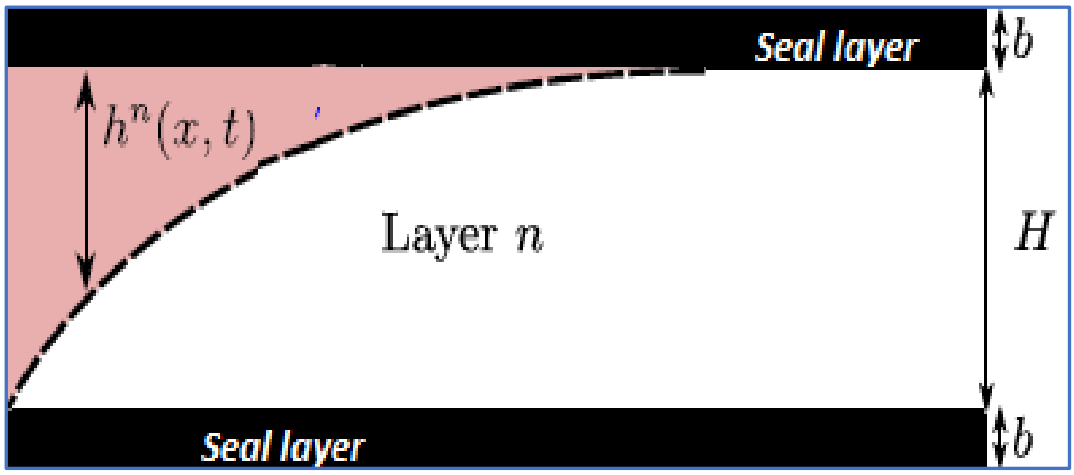

Figure 8-2: Schematic presentation of the two-phase region, saturation profile region. (Buckley-Leverette fractional flow region) for a 1-Dimentional radial system. Adapted from. Adapted from *(Jenkins, 2019)*.

For a two-phase immiscible flow, the following partial differential equation in one-dimension can be written. 8.1

$$\left(\frac{\partial v}{\partial t}\right)_r = -\frac{qt}{\emptyset A}\left(\frac{\partial f_v}{\partial x}\right)_t$$

Where

v = saturation of displacing fluid, t = time, q =total flow rate through section of the reservoir, $\emptyset$ = Porosity, A =Cross-sectional area, f_v= fraction flow stream, comprising displacing fluid (CO2)

8.2.1. Mathematical formulation

We consider the Cauchy problems for fractional flow defined below.

$$\text{BL)} \begin{cases} \frac{\partial v}{\partial t} + \frac{\partial f(v)}{\partial x} = 0 & in \quad Q = \{(x,t): x > 0, t > 0\}, \\ v(x,0) = 0 & x > 0 \\ v(0,t) = k & t > 0 \end{cases} \tag{8.2}$$

We consider the inequality $0 \leq V \leq H$

However, we note that

$$S_w + S_{CO2} = 1 \tag{8.3}$$

Therefore, in our case, for this to be satisfied, we will require that $H_{max} = 1$

And for $k = \frac{v}{\sqrt{H}}$, we define the following non-linear function f: $\mathbf{R}^+ \rightarrow \mathbf{R}^-$ given by

$$f(S) = \frac{v^2}{\frac{v^2}{H} + M\left(1 - \frac{v}{\sqrt{H}}\right)^2} \tag{8.4}$$

Where the function$\big(f(S)\big)$ is the characteristic drainage s-shape.

H is the thickness of the reservoir. At this point, we assume H to be constant, meaning it does not vary as a function of space.

In our context, $S(x,t)$, thus replacing the original equation, we have that

$$\begin{cases} \frac{dS}{dt} + \frac{d}{dx}\left(\frac{S^2}{\frac{S^2}{H} + M\left(1 - \frac{v}{S_H}\right)^2}\right) = 0 \\ S(x,0) = 0 \\ S(0,t) = \frac{S_B}{H} \end{cases} \tag{8.5}$$

Moving forward, we present an analysis of the above formulation, starting with

8.2.2. Steady state analysis

This section presents the condition of the state associated with the above system. To accomplish this objective, we assume that $S(x,t)$, in this case, the saturation of CO_2 is independent of the time parameter, in which case, we have that;

$$\frac{\partial S(x,t)}{\partial t} = 0$$

Which then implies that;

$$\frac{S^2}{\frac{S^2}{H} + M\left(1 - \frac{v}{\sqrt{H}}\right)^2} = a\ constant \tag{8.6}$$

If the constant is zero, then.

$$S^2 = 0 \implies S^* = 0 \tag{8.7}$$

Which defines one of the steady-state solutions. In the case where the constant is different from zero, it is a positive number, say a, then,

$$S^2 = a\left(\frac{S^2}{H} + M\left(1 - \frac{S}{\sqrt{H}}\right)^2\right) \tag{8.8}$$

$$S^2 = a\left(\frac{S^2}{H} + M\left(1 - 2\frac{S}{H} + \frac{S}{H}^2\right)\right) \tag{8.9}$$

We simplify further to obtain.

$$v^2\left(1 - \frac{a}{H} - \frac{aM}{H}\right) + 2a\frac{vM}{H} - aM = 0 \tag{8.1.0}$$

$$\text{If } 1 - \frac{a}{H} - \frac{aM}{H} = 0$$

$$v^* = \frac{aM}{2a\frac{M}{H}} \neq 0, \tag{8.1.1}$$

Then

$$v^* = \frac{\frac{2aM}{H\left(1 - \frac{a}{H} - \frac{Ma}{H}\right)} \pm \sqrt{\left(\frac{2aM}{H\left(1 - \frac{a}{H} - \frac{Ma}{H}\right)}\right)^2 + 4aM}}{2} \tag{8.1.2}$$

Since the function v is positive, we shall only consider the positive steady state, which a given set of parameters can determine. The PDE is a non-linear differential equation since the chosen function, $f(v)$, is highly non-linear; thus, the analysis relevant to the case context is analytically unachievable; hence, for this study, we will proceed by numerically solving the system. We have considered two methods in the following section.

8.3. Numerical analysis

In this section, we shall employ 1) an existing method and 2) a modified scheme to numerically solve the problem under investigation.

To start,

We discretize the time component,

$$0 \le t_1 \le t_2, \dots . t_n \quad \text{And the space component as}$$

$$0 \le x_1 \le x_2, \dots . x_n$$

Then

$$\begin{cases} v(x_i, 0) = 0 \quad \forall\, i \in \{0, \dots n\} \\ v(0, t_j) = \dfrac{v_B}{H} \quad \forall\, i \in \{0, \dots n\} \\ v(x_j, t_{n+1}) = v(x_j, t_n) + \dfrac{\Delta t}{2\Delta x} \left\{ \dfrac{v^2(x_{i+1}, t_n)}{\dfrac{v^2(x_{i+1}, t_n)}{H} + M\left(1 - \dfrac{v(x_{i+1} t_n)}{\sqrt{H}}\right)^2} - \dfrac{v^2(x_{i+1}, t_n)}{\dfrac{v^2(x_{i+1}, t_n)}{H} + M\left(1 - \dfrac{v(x_{i+1} t_n)}{\sqrt{H}}\right)^2} \right\} \end{cases} \tag{8.1.3}$$

For simplicity's sake, we have

Alternatively, we can convert the equation as follows

$$v(x, t) = v(x, 0) + \int_0^t F\big(x, \tau, v(x, \tau)\big)\, d\tau \tag{8.1.4}$$

Where

$$F\big(x, t, v(x, t)\big) = -\frac{\partial}{\partial x}\left(\frac{v^2}{\dfrac{v^2}{H} + M\left(1 - \dfrac{v}{\sqrt{H}}\right)^2}\right) \tag{8.1.5}$$

At $t_{n+1} = t$ and $x = x_i$, we have

$$v(x_i, t_{n+1}) = v(x_i, 0) + \int_0^{t_{n+1}} F\big(x_i, \tau, v(x_i, \tau)\big)\, d\tau$$

$$v(x_i, t_n) = v(x_i, 0) + \int_0^{t_n} F\big(x_i, \tau, v(x_i, \tau)\big)\, d\tau$$

Subtracting yields

$$v(x_i, t_{n+1}) = v(x_i, t_n) + \int_0^{t_{n+1}} F\big(x_i, \tau, v(x_i, \tau)\big)\, d\tau \qquad 8.1.6$$

We then use a polynomial approximation, in this case, ''Lagrange,'' to approximate the function inside the integral sign as follows.

$$v(x_i, t_{n+1}) = v(x_i, t_n) + \frac{\Delta t}{3} F\big(x_i t_n, v(x_i, t_n)\big) - \frac{\Delta t}{2} F\big(x_i, t_{n-1}, v(x_i, t_{n-1})\big) \qquad 8.1.7$$

We note that.

$$F\big(x_i t_n, v(x_i, t_n)\big) \qquad 8.1.8$$

$$= -\frac{1}{2\Delta x}\left\{ \frac{v^2(x_{i+1}, t_n)}{\frac{v^2}{H}(x_{i+1}, t_n) + M\left(1 - \frac{v}{\sqrt{H}}(x_{i+1} t_n)\right)^2} - \frac{v^2(x_{i-1}, t_n)}{\frac{v^2}{H}(x_{i-1}, t_n) + M\left(1 - \frac{v}{\sqrt{H}}(x_{i-1} t_n)\right)^2} \right\}$$

And

$$F\big(x_i, t_{n-1}, v(x_i, t_{n-1})\big) \qquad 8.1.9$$

$$= -\frac{1}{2\Delta x}\left\{ \frac{v^2(x_{i+1}, t_{n-1})}{\frac{v^2}{H}(x_{i+1}, t_{n-1}) + M\left(1 - \frac{v}{\sqrt{H}}(x_{i+1} t_{n-1})\right)^2} - \frac{v^2(x_{i+1}, t_{n-1})}{\frac{v^2}{H}(x_{i+1}, t_{n-1}) + M\left(1 - \frac{v}{\sqrt{H}}(x_{i+1} t_{n-1})\right)^2} \right\}$$

Finally, replacing 8.18 and 8.19 into equation 8.17 yields

$$v_i^{n+1} = v_i^n + \frac{3\Delta}{4\Delta x}\left\{\frac{v^2(x_{i-1},t_n)}{\frac{v^2}{H}(x_{i-1},t_n) + M\left(1-\frac{v}{\sqrt{H}}(x_{i-1}t_n)\right)^2} - \frac{v^2(x_{i+1},t_n)}{\frac{v^2}{H}(x_{i+1},t_n) + M\left(1-\frac{v}{\sqrt{H}}(x_{i+1}t_n)\right)^2}\right\} + \frac{\Delta t}{4\Delta x}\left\{\frac{v^2(x_{i+1},t_{n-1})}{\frac{v^2}{H}(x_{i+1},t_{n-1}) + M\left(1-\frac{v}{\sqrt{H}}(x_{i+1}t_{n-1})\right)^2} - \frac{v^2(x_{i-1},t_{n-1})}{\frac{v^2}{H}(x_{i+1},t_{n-1}) + M\left(1-\frac{v}{\sqrt{H}}(x_{i-1}t_{n-1})\right)^2}\right\} \quad 8.2.0$$

8.4. Analysis of the Buckley-Leveret model with gravitational effect

Equation 8.20 is the numerical solution for the Buckley Leveret two-phase flow model obtained with the classical derivative.

This section will present a new analysis of the same model using a non-local operator. However, we consider accommodating one of the critical assumptions, gravity. This is a crucial geological component that, if ignored, can lead to accurate results and correct predictions. Generally, assumptions used in the mathematical formulation are simply the models considered to render them easily solvable, analytically, or numerically. Gravity, which in this case is interchangeable with density, is the overlooked component. It is important to remember that gravity, which derives from the Latin gravitas weight, is an essential interaction that causes all objects with mass or energy to be attracted to one another. Consequently, we will analyse a mathematical equation containing a density term in this part.

$$\frac{\partial(\emptyset\rho_l S_l)}{\partial t} + \nabla.(V_l) = 0, \quad l = w, nw \quad 8.2.1$$

With the velocity expression given as

$$V_l = -K\frac{k_l}{\mu_l}\nabla(pl + \rho_l gz), \quad l = w, nw \quad 8.2.2$$

Substituting equation 8.22 into equation 8.21, we obtain

$$\frac{\partial(\emptyset\rho_l S_l)}{\partial t} - \nabla^2.\left(\rho_l K \frac{k_l}{\mu_l}(\rho_l l + \rho_l g z)\right) = 0, \quad l = w, nw \qquad 8.2.3$$

We investigate a steady state (equilibrium point) solution for the new equation. This is to assess the system's dependency on space, as we know that relative permeabilities are functions of position and fluid saturation.

8.4.1. Modelling effect of geologic heterogeneity in modelling Two-phase immiscible

Geological formations, especially sedimentary basins, can be notoriously heterogeneous. They are also unique in their historical evolution, depositional mechanisms, and lithological compositions, which result in a diverse set of complex geological architectures at the pore and basin scales (Koltermann and Gorelick, 1996). As a result, engineering endeavours that use flow and transport simulations require maps of heterogeneity that represent features concurrent to the flow and transport processes of interest. This requires basin-specific analysis to obtain comprehensive knowledge and distribution of their heterogeneity patterns. Such characteristics would directly influence the reservoir's ability to constrain fate determinants, e.g., fluid diffusion and dispersion processes. For each sedimentary basin, such parameters as relative and specific permeabilities, capillarity forces, and porosity are of importance in most applications of fluid dynamics in porous media. During CO_2 injection and migration, migration in the subsurface, is important, therefore, no surprise that issues arise in the carbon storage problem. Therefore, formation heterogeneity is variability resulting from inherent formation heterogeneities that are of critical importance for most of the modelling and simulation applications that are commonly encountered.

In a two-phase immiscible flow system, as in the case of geological carbon sequestration, the saturation profile is a vital modelling requirement. It defines the evolution of the plume front used to restrict the plume geometry and extend, a factor extensively used to monitor CO_2 migration at both plume and spore scales (Azizi and Yildan, 2013). The evolution of a saturation front depends predominantly on the relative permeabilities of the two fluids through the porous geological formation and the capillary forces acting on the fluids as they make their way through the pore networks in the geological formation. Formation heterogeneity has been shown to significantly influence this parameter. Different techniques have been used to

capture and describe the effect of geological heterogeneity on fluid saturation and including the use of mathematical formulations that generate fingering results along the advancing fronts, as well as stochastic formulations that use statistical distributions to assign varying parameters to capture some scales of geological heterogeneity. Such analysis has been used to illustrate some characteristic properties that need addressing to describe complexities that arise with fractional flow functions, such as the Buckley-Leverett fractional flow model.

The injection and migration of CO_2 in a porous saline geological formation give rise to an immiscible displacement process. This is because CO_2 (the non-wetting phase) dissolution is limited and has lower mass density than brine (the aqueous or wetting phase), giving rise to gravity override in typical petroleum engineering parlance. The outcome is the vertical partitioning of the two fluids along the advancing front. The amount of CO_2 trapped in pore space is described as the residual saturation and defined as the volume of CO_2 in the pore space constrained by factors such as rock property, fluid viscosity, density, and the velocity of the injected CO_2. Already, studies have confirmed that the amount of residual saturation increases for a high initial saturation. The initial gas saturation is also dependent on pore size distribution. The well-known Buckley Leverett model for which the analysis has been performed in the first part of this work is based on the relative permeabilities of the two fluids. The typical S-shaped drainage curve fits the predicted front shape for assumptions of a homogenous, isotropic, and negligible gravity scenario. The top of the curve close to the sealing layer depicts the drainage process of pores due to intruding CO_2. In contrast, the bottom tail describes the imbibition process responsible for residual trapping. Residual trapping is one of the essential trapping mechanisms, according to experimental investigations and experience from the oil and gas industry.

Geological heterogeneity significantly affects the buoyant forces, relative permeabilities, and capillarity. As a result, poor quantification of their effect can lead to erroneous saturation calculations. If simulation models provide realistic predictions of fluid saturation, they must account for the different scales of heterogeneity.

8.5. Fractional derivatives

Fractional calculus, or generalized or non-integer calculus, is the branch of mathematics investigating derivatives of non-integer order. Its specific applications involve solving differential equations with fractional derivatives of the unknown function, generally denoted as fractional differential equations. Fractional calculus, which originated during the same time

as classical calculus in 1695, was resurrected in the past few decades when it became recognized as a powerful tool to capture non-local behaviours exhibited by most complex phenomena. First hypothesized by Leibniz, who sought to interrogate the geometrical significance of the half derivative$\left(\frac{d^{1/2}y}{dx^{1/2}}\right)$, different mathematicians have worked hard to establish the foundations of such obscure imagination. The chronology of its development is captured in a diverse scope of text (reviews and books) where its applications find solid ground (Loverro, 2004; Machado, 2011; Caputo and Fabrizio, 2015; Atangana and Baleanu, 2016).

Non-local variability is familiar with many natural phenomena, a property observed in most data sets. As a natural outcome, fractional integrals have emerged as a compelling predictive tool to model problems in the areas where heterogeneity constraints the accumulation rates of a quantity. Therefore, extending our fractional flow model, which describes the CO_2 saturation rate in a saline reservoir during carbon dioxide injection for storage purposes, is only sensible. While there exists a multitude of fractional differential derivatives, we will only focus on three most recent formulations: the Caputo derivative with power law kernel formulation, Caputo Fabrizio derivative with exponential decay kernel, and the Atangana-Baleaonu derivative with cross-over behavior, formulated with the generalized Mittag-Leffler kernel.

Firstly, we recall that the definitions of the three mentioned fractional derivatives are convolutions of the unknown function with the associated kernels See$(equation\ 8.2.4)$.

$$\mathcal{V}(x) * \mathcal{U}(x) = \int_0^x \mathcal{V}(x).\mathcal{U}(x-\tau)\,d\tau, \qquad 8.2.4$$

Therefore, for a function$f(x) \in H_2^1\,[0,1]$, the three fractional derivatives and their corresponding integrals are thus defined.

Caputo derivative:

$$ {}_0^C\mathcal{D}_t^\alpha f(x) = \frac{1}{\Gamma(1-\alpha)} \int_0^t \frac{d}{d\tau} f(\tau)(t-\tau)^{-\alpha} d\tau \qquad 8.2.5$$

The integral associated with the Caputo derivative is

As a convolution, we have that,

$$\frac{df(t)}{dt} * \frac{1}{\Gamma} \frac{t^{-\alpha}}{(1-\alpha)} \qquad 8.2.6$$

Where $\frac{1}{\Gamma}\frac{t^{-\alpha}}{(1-\alpha)}$ is the power law operator otherwise known as the Kernel (See figure 8.3).

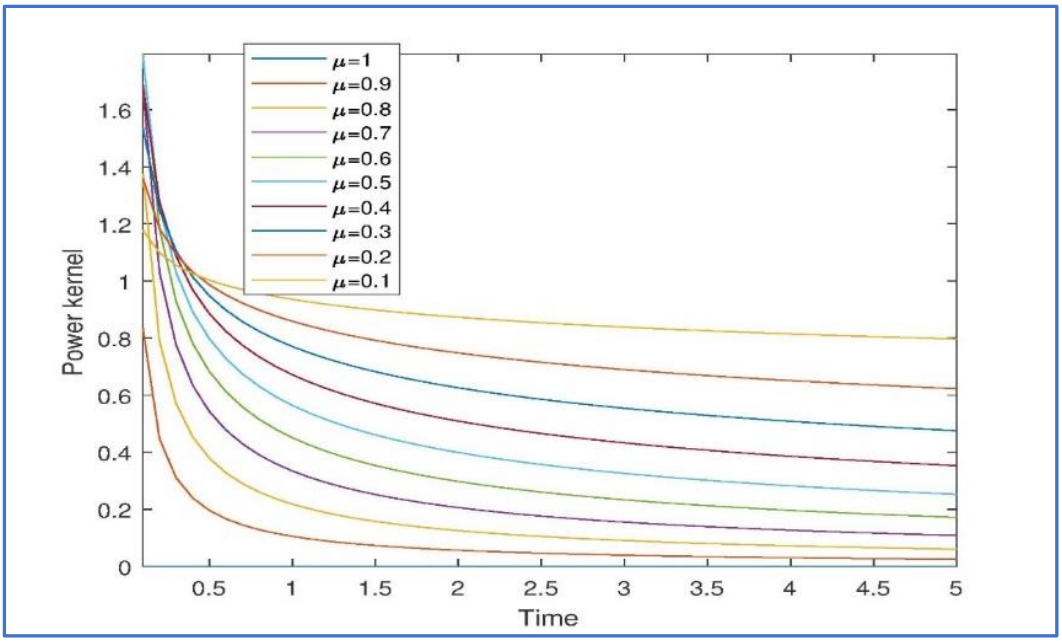

Figure 8-3: Power law graphs for α∈[0.1-1].

The Caputo-Fabrizio derivative

$$ {}^{CF}_{0}\mathcal{D}^{\alpha}_{t} f(x) = \frac{M(\alpha)}{\Gamma(1-\alpha)} \int_{0}^{t} \frac{df(\tau)}{d\tau} Exp\left\{-\frac{\alpha}{1-\alpha}(t-\tau)\right\} d\tau \qquad 8.2.7 $$

Where $M(\alpha) = 1$

As a convolution, we have that,

$$ \frac{df(t)}{dt} * \frac{M(\alpha)}{(1-\alpha)} Exp\left(-\frac{\alpha t}{1-\alpha}\right) \qquad 8.2.8 $$

Where $Exp\left(-\frac{\alpha t}{1-\alpha}\right)$ is the exponential Kernel, otherwise known as the exponential operator (see Figure 8.4)

Caputo-Fabrizio integral

$$ {}^{CF}_{0}I^{\alpha}_{t} f(x) = \frac{(1-\alpha)}{M(\alpha)} f(x) + \frac{\alpha}{M(\alpha)} \int_{0}^{t} \frac{df(\tau)}{d\tau} d\tau \qquad 8.2.9 $$

Figure 8-4: Exponential decay graphs for $\alpha \in [0.1 - 1]$.

Atangana-Baleanu derivative

In the sense of Caputo, it is defined as

$$ {}^{ABC}_{a}D_t^{\alpha}u(t) = \frac{AB(\alpha)}{1-\alpha}\int_a^t \frac{d}{d\tau} f(\tau)E_{\alpha}\left[-\frac{\alpha}{1-\alpha}(t-\tau)^{\alpha}\right]d\tau \quad 8.3.0 $$

As a convolution, $equation\ 29$ is expressed as

$$ \frac{df(t)}{dt} * \frac{AB(\alpha)}{1-\alpha}E_{\alpha}\left[-\frac{\alpha}{1-\alpha}(t)^{\alpha}\right] \quad 8.3.1 $$

Where $E_{\alpha}\left[-\frac{\alpha}{1-\alpha}(t)^{\alpha}\right]$ is the Mittag-Leffler function.

Likewise, the Atangana Baleanu derivation in the Riemann Lowville sense is defined as

$$ {}^{ABC}_{a}D_t^{\alpha}f(t) = \frac{AB(\alpha)}{1-\alpha}\frac{d}{dt}\int_a^t \frac{d}{d\tau} f(\tau)E_{\alpha}\left[-\frac{\alpha}{1-\alpha}(t-\tau)^{\alpha}\right]d\tau \quad 8.3.2 $$

$$ \frac{df(t)}{dt} * \frac{AB(\alpha)}{1-\alpha}E_{\alpha}\left(\left[-\frac{\alpha}{1-\alpha}(t)^{\alpha}\right]\right) \quad 8.3.3 $$

Where equation 30.1 is the Mittag Leffler kernel (Figure 8-5)

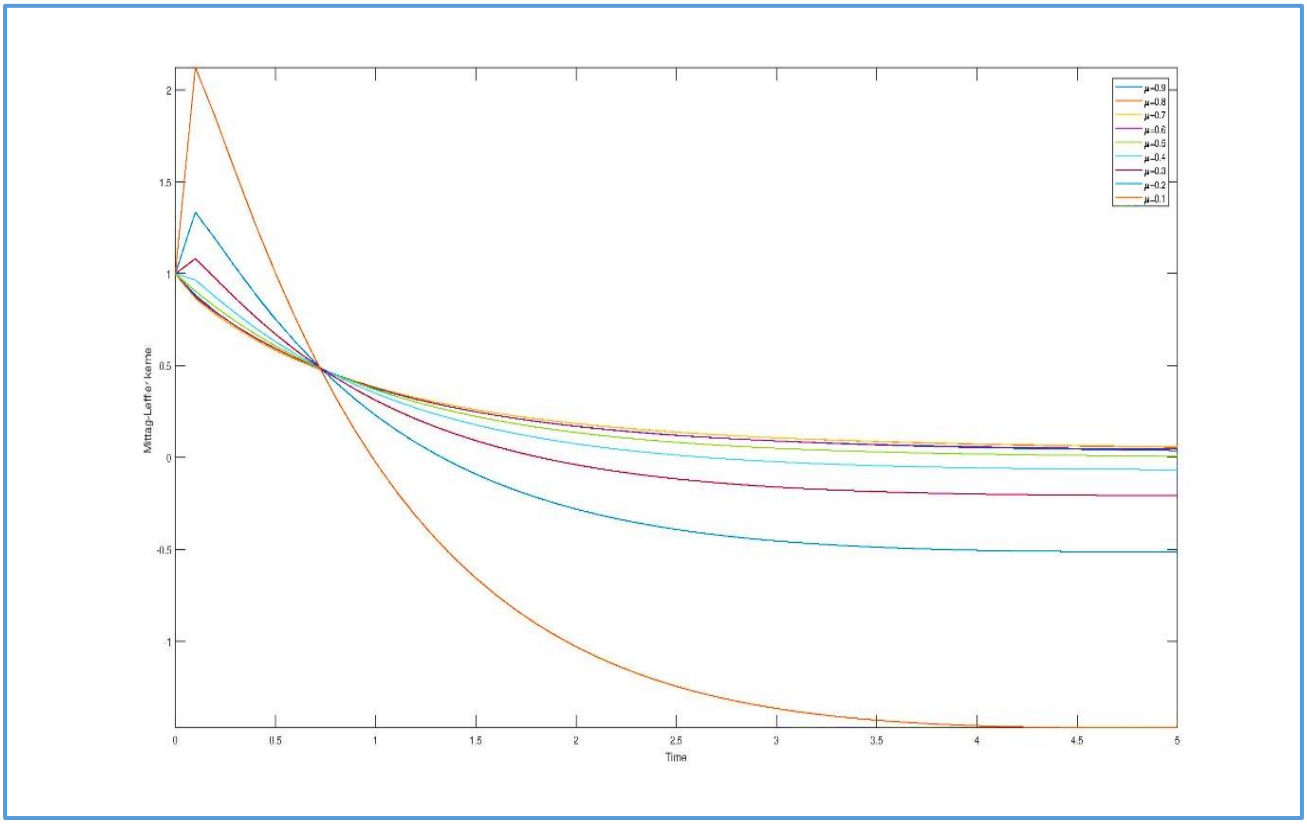

Figure 8-5: Mittag Leffler graphs for α ∈ [0.1-1].

Likewise, we have the integral associated with the ABC derivative given as

$$ {}^{ABC}_{a}I_t^{\alpha}u(t) = \frac{1-\alpha}{AB(\alpha)}u(t) + \frac{\alpha}{AB(\alpha)\Gamma(\alpha)}\int_a^t u(\tau)E_{\alpha}(t-\tau)^{\alpha-1}d\tau \quad 8.3.4 $$

In general, a kernel is a function that define the underlying structure or behaviour of a mathematical operation and, therefore it is used to define fractional operators, especially those exhibiting certain non-localities. This approach was motivated by the results of high-resolution experimental techniques, that reveal novel mass transport behaviours on different time scales. Of course, in their respective capacities, the memory retaining ability which underlie the continuous time differentiability of the function as required in the fractional formalisms (Atangana and Sonal, 2018) is seen as a measure of robustness in modelling complex real world problems. Fractional operators tend to handle with ease the perturbation of boundary conditions and other external forces. This has use in models' problems that involve walks and diffusion with certain anomalous behaviours (Tateishi et al., 2017).

Pore scale processes that govern saline aquifer fluid dynamic include porosity, permeability, and fluid saturation, all of which are controlled by the capillary pressure of the porous media. Their inter- and intra-relations follow different trends, and for many reservoir settings, predicting flow behaviours is usually accomplished through matching different flow curves that describe the fluid propagation phenomena in porous media, such as capillary pressure (P_c)/relative permeability curves or capillary/saturation, e.g., Brookes and Corey (Wang and Tokunaga, 2015). However, understanding the properties and characteristics of each Kernel, i.e., the power law, exponential, and Mittag-Leffler kernels, is essential for the accurate representation and interpretability of a problem context.

The power law Kernel also known as the Pareto kernel, is generally characterized by the high volume of data mobilized for extreme values due to its heavy tail distribution. The power law kernel is limited in that its non-locality cannot be directly inferred and is scale-invariant (Atangana and Sonal, 2018). however, it has found use and success in many traditional and fractional calculus applications, such as network analysis, where affinities are prioritized for a select data grouping at specific times. Fractional calculus has opened many research avenues involving complex systems with non-local and memory-dependent interplays. For example, in geologic reservoirs, capillary pressure controls the saturation distribution of fluids through an inverse proportionality relationship with the pore throat radius. The graph of fluid volumes in pores against pore throat radius exhibits a long tail dependence, indicating less entrapment for large values of pore throat radius.

$$P_c = 2\sigma \cos\theta R \qquad 8.3.5$$

The implications of this dependence are of practical application in hydrocarbon exploitation and carbon dioxide injection problems.

Unlike the power kernel, the exponential decay kernel brings closer data points with higher values while spreading data points of lower values further apart. This property makes it useful for clustering and classification, for example, in studying the activity of radioactive nuclei with multiple long half-lives between parent and daughter nuclei. In fractional calculus, where the order of the derivative is a non-integer, the exponential function has been successfully applied in areas such as image processing to achieve better tuning. For higher-values orders, the response of the Kernel is more sensitive as the curve drops sharply with an almost vertical gradient before levelling out. The higher the ranking of differentiation, the faster the function decays to a zero value. On the other hand, graphs generated with a lower differential order show a flattening gradient. In contrast, differential orders below 0.5 generally cross over at the same position, progressively becoming flat as the order approaches zero.

Even though the Brook and Corey power law model has been widely utilized to model capillary pressure, this has led to some erroneous results since its validity is limited to low wetting phase saturations. However, in a recent study (Afrough et al., 2019) the capillary pressure of Hunt developed for random fractals with lognormal pore size distribution was simplified to an exponential function via Taylor series expansion. The results showed that exponential capillary pressure functions will simplify oil recovery factors for gravity drainage in fractured reservoirs. The deviations observed were attributed to the effect of structural pores and film flow at high and low wetting phase saturations, respectively.

Finally, the Mittag-Leffler kernel is a function with unique properties, as defined in $equation\ 8.3.2$. The first future note is the unique cross-over position, a path travelled by all graphs generated for differential order of alpha between $[0: 1]$. All the graphs show a characteristic change in trend from an exponential decay law type distribution to the long-range dependence, typical of a power law, with the change seemingly perturbed at the cross-over position. Secondly, a sharp short-lived trend shift observed for all graphs is more prominent, with a positive gradient for fractional order <0.5 and less for fractional order >0.5. In the first case, the graphs are widely spaced, as opposed to the later cases, where all graphs almost converge along the heavy tail-dependent distribution. The Mittag-Leffler function can

capture a wide range of phenomena that does the power or exponential Kernel independently, owing mainly to its cross-over behaviour. Since its first formulation and use in the generalization of fractional calculus (Atangana and Baleaunu, 2016), it has found widespread application in many fields of science, achieving great success in modelling many real-world problems that are problematic for the power law and exponential functions. In reservoir geologic reservoirs, heterogeneity of varying scales affects transport and migration processes significantly. Thanks to this Kernel, the ABC derivative can capture and consider a wide range of non-localities in various modelling setups, such as flow fracture to matrix flows, flows from confined to unconfined aquifers, flow from leaky to non-leaky aquifers, etc.

8.5.1. Application

In this section, to include in the mathematical formulation of non-local behaviours, we shall replace the classical differential operator concerning time with fractional differential operators based on the power law, exponential decay, and the generalized Mittag-Leffler function. We start first with the Caputo fractional derivative.

Numerical solution with Caputo derivation

$$\text{BL)}\begin{cases}\frac{\partial v(z,t)}{\partial t} = F\big((x,t,v(x,t)\big) & in \quad Q=\{(z,t): x>0, t>0\},\\ v(x,0)=0 & x>0\\ v(0,t)=\frac{v_B}{H} & t>0\end{cases} \qquad 8.3.5$$

In fractional Caputo notation, we rewrite.

$$\text{BL)}\begin{cases}{}_0^C\mathcal{D}_t^{\alpha} v(z,t) = F\big((z,t,v(z,t)\big) & in \quad Q=\{(z,t): x>0, t>0\},\\ v(z,0)=0 & x>0\\ v(0,t)=\frac{v_B}{H} & t>0\end{cases} \qquad 8.3.6$$

Where v is the saturation and f is the fractional flow.

Let

$$F\big((z,\tau,v(z,t)\big)=\frac{v^2}{\frac{v^2}{H}+M\left(1-\frac{v}{S_H}\right)^2} \tag{8.3.7}$$

From the fundamental theorem of calculus, we have that,

$$v(z,t)-v(z,0)=\frac{1}{\Gamma(\alpha)}\int_0^t F\big((z,\tau,v(z,\tau)\big)(t-\tau)^{\alpha-1}d\tau \tag{8.3.8}$$

At the point

$t=t_{k+1}=(k+1)\Delta\text{t}$ and $x_i,$ we can write the scheme

$$v(z_i,t_{k+1})-v(x_i,0)=\frac{1}{\Gamma(\alpha)}\int_0^{t_{k+1}} F\big((z_i,\tau,v(z_i,\tau)\big)(t_{k+1}-\tau)^{\alpha-1}d\tau \tag{8.3.9}$$

And at the point

$t=t_k=k\Delta\text{t}$ and $x_i,$ we can write the scheme.

$$v(z_i,t_k)-v(x_i,0)=\frac{1}{\Gamma(\alpha)}\int_0^{t_k} F\big((z_i,\tau,v(z_i,\tau)\big)(t_k-\tau)^{\alpha-1}d\tau \tag{8.4.0}$$

Subtracting the two, we get

$$v(z_i,t_{k+1})-v(x_i,0)=\frac{1}{\Gamma(\alpha)}\int_{t_k}^{t_{k+1}} F\big((z_i,\tau,v(z_i,\tau)\big)(t_{k+1}-\tau)^{\alpha-1}d\tau \tag{8.4.1}$$

To simplify the resulting numerical scheme, we replace the above integral with its Lagrange polynomial $P_j(\tau)$ at $t_k\ and\ t_{k-1}$

Or better written as

$$P_j(\tau)=\frac{\tau-t_{j-1}}{\Delta t}F\left((z_i,t_j,v\big(x_i,t_j\big)\right)-\frac{\tau-t_j}{\Delta t}F\left((\text{z},t_{j-1},v\big(z_i,t_{j-1}\big)\right) \tag{8.4.2}$$

$$\begin{aligned} v(z_i,t_{k+1}) &= v(x_i,0) \\ &+\frac{1}{\Gamma(\alpha)}\sum_{j=1}^{k}\int_{t_j}^{t_{j+1}}\left\{\frac{\tau-t_{j-1}}{\Delta t}F\left((z_j,t_j,v\big(z_j,t_j\big)\right)\right. \\ &\left.-\frac{\tau-t_j}{\Delta t}F\left((z_j,t_{j-1},v\big(z_j,t_{j-1}\big)\right)\right\}(t_{k+1}-\tau)^{\alpha-1}d\tau \end{aligned} \tag{8.4.3}$$

For simplicity, the equation can be reorganized in the following steps,

$$\begin{aligned} v(x_i,t_{k+1}) &= v(x_i,0) \\ &+\frac{1}{\Gamma(\alpha)}\sum_{j=0}^{k}\int_{t_j}^{t_{j+1}}\frac{\tau-t_{j-1}}{\Delta t}F\left((z_i,t_j,v\big(z_i,t_j\big)\right)(t_{k+1}-\tau)^{\alpha-1}d\tau \\ &-\int_{t_j}^{t_{j+1}}\frac{\tau-t_j}{\Delta t}F\left((z_i,t_{j-1},v\big(z_i,t_{j-1}\big)\right)(t_{k+1}-\tau)^{\alpha-1}d\tau \end{aligned} \tag{4.4.4}$$

$$v(x_i, t_{k+1}) = v(x_i, 0) \qquad 8.4.5$$
$$+\frac{1}{\Gamma(\alpha)}\sum_{j=0}^{k}\frac{F\left((z_i, t_j, v(x_i, t_j)\right)}{\Delta t}\int_{t_j}^{t_{j+1}}(\tau - t_{j-1})(t_{k+1}-\tau)^{\alpha-1}d\tau$$
$$-\frac{1}{\Gamma(\alpha)}\sum_{j=0}^{k}\frac{F\left((\mathrm{z}, t_{j-1}, v(z_i, t_{j-1})\right)}{\Delta t}\int_{t_j}^{t_{j+1}}(\tau - t_j)(t_{k+1}-\tau)^{\alpha-1}d\tau$$

The following solutions are separately obtained computationally for the right-hand side integrals.

$$\int_{t_k}^{t_{k+1}}(\tau - t_{k-1})(t_{k+1}-\tau)^{\alpha-1}d\tau \qquad 8.4.6a$$
$$= \frac{(\Delta t)^{\alpha+1}}{\alpha(\alpha+1)}[(k-j+1)^{\alpha}(k-j+2-\alpha)$$
$$-(k-j)^{\alpha}(k-j+2-\alpha)]$$

$$\int_{t_k}^{t_{k+1}}(\tau - t_k)\,(t_{k+1}-\tau)^{\alpha-1}d\tau \qquad 8.4.6b$$
$$= \frac{(\Delta t)^{\alpha+1}}{\alpha(\alpha+1)}[(k-j+1)^{\alpha+1} - (k-j)^{\alpha}(k-j+1+\alpha)]$$

However, they can also be calculated and obtained through the following steps,

$$\int_{t_j}^{t_{j+1}}(\tau - t_{j-1})(t_{k+1}-\tau)^{\alpha-1}d\tau = \int_{t_j}^{t_{j+1}}\tau(t_{k+1}-\tau)^{\alpha-1}d\tau - t_{j-1}\int_{t_j}^{t_{j+1}}(t_{k+1}-\tau)^{\alpha-1}\,d\tau$$

For the first part, we can obtain the integral as a set: The complete beta and the incomplete beta solutions, given below as

$$\int_{t_j}^{t_{j+1}}\tau(t_{k+1}-\tau)^{\alpha-1}d\tau = t_{j-1}^{\alpha+1}\left\{B(2,\alpha) - B\left(\frac{t_j}{t_{j+1}}, 2, \alpha\right)\right\}$$

Where the solution set is defined for

$$(Complete\ Beta) \qquad B(a,b) = \int_0^1 z^{a-1}\,(1-z)^{b-1}dz$$

and

$$(Incomplete\ Beta) \quad B(z,a,b) = \int_0^z u^{a-1}\,(1-u)^{b-1}du$$

On the other hand, a solution by the method of change of variable can be obtained such that

$$t_{j-1}\int_{t_j}^{t_{j+1}}(t_{k+1}-\tau)^{\alpha-1}\,d\tau = \frac{t_{j-1}}{\alpha}(t_{j+1}-t_j)^{\alpha} = -\frac{h(j-1)}{\alpha}\{h(j+1)-hj\}^{\alpha}$$
$$= \frac{h^{\alpha+1}}{\alpha}(j-1)$$

In the following steps, we replace re-substitute the computed integral and simplify to arrive the final numerical scheme.

$$v(x_i, t_{k+1}) = v(x_i, 0) \tag{8.5.7}$$
$$+ \frac{(\Delta t)^\alpha}{\Gamma(\alpha+2)} \sum_{j=0}^{k} F\left(x_i, t_j, v(x_i, t_j)\right) \int_{t_j}^{t_{j+1}} (\tau - t_{j-1})(t_{k+1} - \tau)^{\alpha-1} d\tau$$
$$- \frac{(\Delta t)^\alpha}{\Gamma(\alpha+2)} \sum_{j=0}^{k} F\left(x_i, t_{j-1}, v(x_i, t_{j-1})\right) \int_{t_j}^{t_{j+1}} (\tau - t_j)(t_{k+1} - \tau)^{\alpha-1} d\tau$$

$$v(x_i, t_{k+1}) = v(x_i, 0) \tag{8.5.8}$$
$$+ \frac{(\Delta t)^\alpha}{\Gamma(\alpha+2)} \sum_{j=0}^{k} F\left(x_k, t_j, v(x_k, t_j)\right) \frac{(\Delta t)^{\alpha+1}}{\alpha(\alpha+1)} [(k-j+1)^\alpha (k-j+2-\alpha)$$
$$- (k-j)^\alpha (k-j+2-\alpha)]$$
$$- \frac{(\Delta t)^\alpha}{\Gamma(\alpha+2)} \sum_{j=0}^{k} F\left(x_k, t_{j-1}, v(x_k, t_{j-1})\right) \frac{(\Delta t)^{\alpha+1}}{\alpha(\alpha+1)} [(k-j+1)^{\alpha+1}$$
$$- (k-j)^\alpha (k-j+1+\alpha)]$$

Recalling $F\big(x, \tau, v(x,\tau)\big) = -\frac{\partial}{\partial x}\left(\frac{v^2}{\frac{v^2}{H} + M\left(1 - \frac{v}{\sqrt{H}}\right)^2}\right)$, which can be discretized using the method of central difference, we obtain the following expressions.

$$F\big((x_{i+1}, t_k, v(x_{i+1}, t_k)\big) \tag{8.5.9}$$
$$= -\left[\frac{1}{2\Delta x}\left(\frac{\left(v_{i+1}^k\right)^2}{\frac{\left(v_{i+1}^k\right)^2}{H} + M\left(1 - \frac{v_{i+1}^k}{\sqrt{H}}\right)^2} - \frac{\left(v_{i-1}^k\right)^2}{\frac{\left(v_{i-1}^k\right)^2}{H} + M\left(1 - \frac{v_{i-1}^k}{\sqrt{H}}\right)^2}\right)\right]$$

$$F\big(x_i, t_{k-1}, v(x_i, t_{k-1})\big) \tag{8.6.0}$$
$$= -\left[\frac{1}{2\Delta x}\left(\frac{\left(v_{i+1}^{k-1}\right)^2}{\frac{\left(v_{i+1}^{k-1}\right)^2}{H} + M\left(1 - \frac{v_{i+1}^{k-1}}{\sqrt{H}}\right)^2} - \frac{\left(v_{i-1}^k\right)^2}{\frac{\left(v_{i-1}^{k-1}\right)^2}{H} + M\left(1 - \frac{v_{i-1}^{k-1}}{\sqrt{H}}\right)^2}\right)\right]$$

Upon substitution, we obtain the following final expression.

$$v(x_i, t_{k+1}) = v(x_i, 0) \qquad 8.7.1$$

$$+\frac{(\Delta t)^{\alpha}}{\Gamma(\alpha+2)}\sum_{j=0}^{k}\left[\frac{1}{2\Delta x}\left(\frac{\left(v_{i+1}^{k-1}\right)^2}{\frac{\left(v_{i+1}^{k-1}\right)^2}{H}+M\left(1-\frac{v_{i+1}^{k-1}}{\sqrt{H}}\right)^2}\right.\right.$$

$$\left.\left.-\frac{\left(v_{i-1}^{k}\right)^2}{\frac{\left(v_{i-1}^{k-1}\right)^2}{H}+M\left(1-\frac{v_{i-1}^{k-1}}{\sqrt{H}}\right)^2}\right)\right]\frac{(\Delta t)^{\alpha+1}}{\alpha(\alpha+1)}[(k-j+1)^{\alpha}(k-j+2-\alpha)$$

$$-(k-j)^{\alpha}(k-j+2-\alpha)]$$

$$-\frac{(\Delta t)^{\alpha}}{\Gamma(\alpha+2)}\sum_{j=0}^{k}\left[\frac{1}{2\Delta x}\left(\frac{\left(v_{i+1}^{k-1}\right)^2}{\frac{\left(v_{i+1}^{k-1}\right)^2}{H}+M\left(1-\frac{v_{i+1}^{k-1}}{\sqrt{H}}\right)^2}\right.\right.$$

$$\left.\left.-\frac{\left(v_{i-1}^{k}\right)^2}{\frac{\left(v_{i-1}^{k-1}\right)^2}{H}+M\left(1-\frac{v_{i-1}^{k-1}}{\sqrt{H}}\right)^2}\right)\right]\frac{(\Delta t)^{\alpha+1}}{\alpha(\alpha+1)}[(k-j+1)^{\alpha+1}$$

$$-(k-j)^{\alpha}(k-j+1+\alpha)]$$

8.5.2. Numerical solution of immiscible two-phase flow with gravity

In this section, $equation\ 8.2.2\ and\ 8.2.3$ are recalled for a system of two immiscible fluids: A wetting and non-wetting phase. In a porous media, we assume the flow of these phases to be adequately described by Darcy's law for the specific discharge. In this context, the numerical solution to this 1-dimensional fractional flow equation is considered in the presence of gravity. As earlier defined, we assume an impermeable interphase at $Z = 0\ and\ Z = H$.

$$\frac{\partial(\emptyset\rho_l v_l)}{\partial t} + \nabla.(u_l) = 0, \quad l = wetting, non-wetting \qquad 8.7.2$$

Where the velocity, u_l, is expressed as

$$V_l = -\mathrm{K}\frac{k_l}{\mu_l}\nabla(p_l + \rho_l g e_z), \quad l = wetting, non-wetting \qquad 8.7.3$$

Equation 8.2.2 is a mass conservation expression, where $\emptyset$, is the formation porosity while $\rho_l\,[Kg\,m^{-3}]$, v_l, and $u_l[m\,s^{-1}]$, respectively, represent density, saturation, and specific discharge (velocity). In the discharge equation $(8.2.3)$, $p_l\,[Pa]$, $u_l\,[Pa\,s]$, $k_l\,[-]$, and $g[\,m\,s^{-2}]$ represent the fluid pressure, viscosity, the fluid relative permeability of each phase, and the gravitational acceleration constant and $K\,[m^2]$ is the absolute permeability tensor. For simplicity, the formulation assumes a rigid (incompressible) isotropic domain in

which the porosity, relative, and absolute permeabilities are time-independent, such that the tensor K reduces to a scale K. The effect of capillarity forces is also neglected such that the $p_{nw} = p_w = p$, where p is the fluid pressure related to the injection pressure.

Under these assumptions, $equations$ 8.2.2 and 8.2.3 reduce to

$$\emptyset \frac{\partial(v_l)}{\partial t} + \nabla.(u_l) = 0, \quad l = wetting, non - wetting \tag{8.7.4}$$

$$u_l = -\frac{Kk_l}{\mu_l}(\nabla p_l + \rho_l g e_z), \quad l = wetting, non - wetting \tag{8.7.5}$$

Substituting

$$\emptyset \frac{\partial(v_l)}{\partial t} + \nabla.\left(-\frac{Kk_l}{\mu_l}(\nabla p_l + \rho_l g e_z)\right) = 0 \tag{8.7.6}$$

Where the relative permeability is a function of saturation v_l, i.e.

$$k_l = k_l(v_l)$$

$$\emptyset \frac{\partial(v_l)}{\partial t} + \nabla.\left(-\frac{Kk_l(v_l)}{\mu_l}\nabla p_l - \frac{Kk_l(v_l)}{\mu_l}\rho_l g e_z\right) = 0 \tag{8.7.7}$$

Expanding the expression, we obtain

$$\emptyset \frac{\partial(v_l)}{\partial t} - \frac{K}{\mu_l}\nabla(k_l(v_l)\nabla p_l) - \frac{K\rho_l g e_z}{\mu_l}\nabla k_l(v_l) = 0 \tag{8.7.8}$$

$$\emptyset \frac{\partial(v_l)}{\partial t} = \frac{K}{\mu_l}\nabla(k_l(v_l)\nabla p_l) + \frac{K\rho_l g e_z}{\mu_l}\nabla k_l(v_l) \tag{8.7.9}$$

Following the product rule, $(k_l(v_l).\nabla p_l)$ can be expressed as

$$\frac{K}{\mu_l}\frac{\partial}{\partial z}\left(k_l(v_l)\frac{\partial p_l}{\partial z}\right) = \frac{K}{\mu_l}\left\{\frac{\partial k_l(v_l)}{\partial z}\frac{\partial p_l}{\partial z} + \frac{\partial^2 p_l}{\partial z^2}k_l(v_l)\right\} \tag{8.8.0}$$

Substituting further we arrive

$$\emptyset \frac{\partial(v_l)}{\partial t} = \frac{K}{\mu_l}\left\{\frac{\partial k_l(v_l)}{\partial z}\frac{\partial p_l}{\partial z} + \frac{\partial^2 p_l}{\partial z^2}k_l(v_l)\right\} + \frac{K\rho_l g e_z}{\mu_l}\frac{\partial k_l(v_l)}{\partial z} \tag{8.8.1}$$

$$\emptyset \frac{\partial(v_l)}{\partial t} = \frac{K}{\mu_l}\left\{\frac{\partial k_l(v_l)}{\partial z}\frac{\partial p_l}{\partial z} + \frac{\partial^2 p_l}{\partial z^2}k_l(v_l) + \rho_l g e_z \frac{\partial k_l(v_l)}{\partial z}\right\} \quad 8.8.2$$

$$\frac{\partial(v_l)}{\partial t} = \frac{K}{\emptyset\mu_l}\left\{k_l(v_l)\frac{\partial^2 p_l}{\partial z^2} + \left(\frac{\partial p_l}{\partial z} + \rho_l g e_z\right)\frac{\partial k_l(v_l)}{\partial z}\right\} \quad 8.8.3$$

Numerical analysis for two-phase immiscible flow with gravity formulation.

This section presents a detailed numerical analysis of the new gravity-formulated two-phase immiscible flow differential equation. The numerical solvers are obtained via functional approximations using the new middle point and the two-step Lagrange approximation schemes. For this analysis, we will consider the case of classical derivative, power law, and Mittag-Leffler (cross-over) kernels. In the following steps, the numerical solution with middle point approximation is ensued using the classical derivative.

Solution with the classical derivative

Recalling equation 52, we let

$$\frac{K}{\emptyset\mu_l}\left\{k_l(v_l)\frac{\partial^2 p_l}{\partial z^2} + \left(\frac{\partial p_l}{\partial z} + \rho_l g e_z\right)\frac{\partial k_l(v_l)}{\partial z}\right\} = F(t,p,z,v(t,p,z)) \quad 8.8.4$$

So that we consider the following fractional Cauchy problem:

$$\begin{cases} v'(z,p,t) = F\big(\tau,z,p,v(\tau,z,p)\big) \\ v(0,z) = v_0\,, \qquad for\ \ t = 0 \end{cases} \quad 8.8.5$$

Assuming that $F\big(\tau,z,p,v(\tau,z,p)\big)$ is twice differentiable and that $v(\tau,z,p)$ is classically differentiable, from the fundamental theorem of calculus, we can convert 8.8.5 to an integral equation, as

$$v(z,t) = v(\mathrm{z},0) + \int_0^t F\big(\tau,z,P_l,v_l(\tau,z,p)\big)d\tau$$

To obtain a general numerical scheme for the model,

we consider the point.

$t = t_{k+1} = (k+1)\Delta t \qquad \forall\, k \in [0,1,2\ldots]$

$$v_l(t_{k+1},z_i) = v_l(z_i,0) + \int_0^{t_{k+1}} F\left(\tau,z_i,P_{l,i},v_l(\tau,z_i,p_i)\right)d\tau \quad 8.8.6$$

And the point $t = t_k = (k)\Delta t$

$$v_l(z_i, t_k) = v_l(z_i, 0) + \int_0^{t_k} F\left(\tau, z_i, P_{l,i}, v_l\left(\tau, z_i, P_{l,i}\right)\right) d\tau \quad 8.8.7$$

Combining both equations by taking their difference, we have that

$$v_l(z_i, t_{k+1}) = v_l(z_i, t_k) + \int_{t_k}^{t_{k+1}} F\left(\tau, z_i, P_{l,i}, v_l\left(\tau, z_i, P_{l,i}\right)\right) d\tau \quad 8.8.8$$

Next, we obtain an approximation for $F\left(\tau, z_i, P_{l,i}, v_l\left(\tau, z_i, P_{l,i}\right)\right)$ between the points$[t_{k+1} - t_k]$ by utilizing the middle point method, which is stated in simple terms as

$$F\left(\tau, v_l(\tau,)\right) = F\left(\frac{t_{k+1} + t_n}{2}, \frac{v_{k+1} + v_k}{2}\right)$$

Applying the scheme, we have

$$v_{l,k+1} = v_{l,k} + \int_{t_k}^{t_{k+1}} F\left(z_i, P_{l,i}\frac{t_{k+1} + t_k}{2}, \frac{v_{l,k+1} + v_k}{2}\left(z_i, P_{l,i}\right)\right) d\tau \quad 8.8.9$$

$$v_{l,k+1} = v_{l,k} + F\left(z_i, P_{l,i}\frac{t_{k+1} + t_n}{2}, \frac{v_{l,k+1} + v_{l,k}}{2}\left(z_i, P_{l,i}\right)\right)\int_{t_k}^{t_{k+1}} d\tau \quad 8.9.0$$

$$v_{l,k+1} = v_{l,k} + F\left(z_i, P_{l,i}\frac{t_{k+1} + t_k}{2}, \frac{v_{l,k+1} + v_{l,k}}{2}\left(z_i, P_{l,i}\right)\right)[t_{k+1} - t_k] \quad 8.9.1$$

$$v_{l,k+1} = v_{l,k} + hF\left(z_i, P_{l,i}\frac{t_{k+1} + t_k}{2}, \frac{v_{l,k+1} + v_{l,k}}{2}\left(z_i, P_{l,i}\right)\right) \quad 8.9.2$$

From $t_{k+1} - t_k = h, \Rightarrow t_{n+1} = t_n + h$, we can rewrite 60.1 as

$$v_{l,k+1} = v_{l,k} + hF\left(z_i, P_{l,i}\frac{h + 2t_k}{2}, \frac{v_{l,k+1} + v_{l,k}}{2}\left(z_i, P_{l,i}\right)\right) \quad 8.9.3$$

$$v_{l,k+1} = v_{l,k} + hF\left(z_i, P_{l,i}\left(\frac{h}{2} + t_k\right), \frac{v_{l,k+1} + v_{l,k}}{2}\left(z_i, P_{l,i}\right)\right)$$

By observing, we can identify the implicit form of Equation 8.9.3, which is a computation challenge. To deal with the issue, we use the Heunz method, as demonstrated below.

$$v_{l,k+1} = v_{l,k} + hF\left(z_i, P_{l,i}\left(\frac{h}{2} + t_k\right), \frac{\bar{v}_{l,k+1} + v_{l,k}}{2}, z_i, P_{l,i}\right) \quad 8.9.4$$

Were,

$$\bar{v}_{l,k+1} = v_l(t_k) + \int_{t_k}^{t_{k+1}} F\left(\tau, z_i, P_{l,i}, v_l\left(\tau, z_i, P_{l,i}\right)\right) d\tau$$

$$\bar{v}_{l,k+1} = v_l(t_k) + \int_{t_k}^{t_{k+1}} F\left(t_k, z_i, P_{l,i}, v_{l,k}\left(z_i, P_{l,i}\right)\right) d\tau \quad 8.9.5$$

$$\bar{v}_{l,k+1} = v_l(t_k) + hF\left(t_k, z_i, P_{l,i}, v_{l,k}\left(z_i, P_{l,i}\right)\right)$$

Substitute we get

$$v_{l,k+1} = v_{l,k} + hF\left((b\ + t_k), v_{l,k}(z_i, P_{l,i}) + \frac{h}{2}F\left(t_k, v_{l,k}, \left(z_i, P_{l,i}\right)\right)\right) \quad 8.9.6$$

Equation 64 is the numerical approximation for the two-phase immiscible flow with the classical derivative.

Numerical scheme with Mittag-Leffler kernel (ABC derivative)

This section presents a detailed numerical analysis of the new gravity-formulated two-phase immiscible flow model. The numerical solvers are obtained via functional approximations using the unique middle point and the two-step Lagrange approximation schemes. For this analysis, we will consider the case of classical derivative, power law, and Mittag-Leffler (cross-over) kernels.

In the first analysis, we transformed $equation\ 5.3$ into a fractional saturation model using the Mittag-Leffler kernel formulated by the ABC derivative. We formulate and present the complete numerical scheme using the middle point approximation method.

Firstly, we consider the Cauchy problem.

$$\begin{cases} {}^{ABC}_{t_0}D_t^{\alpha} v(z,t) = F\left(\tau, z, p, v(\tau, z, p)\right) \\ v(z, t_0) = v_0(z).\ for\ \ t = 0 \end{cases} \quad 8.9.7$$

$$v(z,t) = v(z,t_0) + (1-\alpha)F\left(\tau, z, v(\tau, z)\right) + \frac{\alpha}{\Gamma(\alpha)}\int_{t_0}^{t} (t-\tau)^{\alpha-1} F\left(\tau, z, v(\tau, z)\right) d\tau \quad 8.9.8$$

At (z_i, t_{n+1}), we have that.

$$v(z_i, t_{n+1}) = v(z_i, t_0) + (1-\alpha)F\big(t_{n+1}, z_i, v(t_{n+1}, z_i)\big) + \frac{\alpha}{\Gamma(\alpha)}\sum_{j=0}^{n}\int_{t_j}^{t_{j+1}}(t_{n+1}-\tau)^{\alpha-1}F\big(t_{n+1}, z_i, v(t_{n+1}, z_i)\big)d\tau \quad 8.9.9$$

Next, we will use the middle point method to approximate $F\left(\tau, z_i, P_{l,i}, v_l\big(\tau, z_i, P_{l,i}\big)\right)$ within $\big[t_{j+1}, t_j\big]$.

$$F\big(\tau, z_i, , v_l(\tau, z_i,)\big) = F\left(z_i, \frac{t_j + t_{j+1}}{2}, \frac{v(z_i, t_j) + v(z_i, t_{j+1})}{2}\right) \simeq F\left(z_i, \frac{t_j + t_{j+1}}{2}, \frac{v_i^{j+1} + v_i^j}{2}\right) \quad 8.10.1$$

Replacing equation 8.10.1 in 8.9.9 8.10.2

$$v_i^{n+1} = v_i^0 + (1-\alpha)F\big(t_{n+1}, z_i, \bar{V}(t_{n+1}, z_i)\big) + \frac{\alpha}{\Gamma(\alpha)}\sum_{j=0}^{n}F\left(z_i, \frac{t_j + t_{j+1}}{2}, \frac{v_i^{j+1} + v_i^j}{2}\right)\left\{\frac{(t_{n+1}-t_j)^\alpha}{\alpha} - \frac{(t_{n+1}-t_{j+1})^\alpha}{\alpha}\right\}$$

Where the integral is calculated as

$$\int_{t_j}^{t_{j+1}}(t_{n+1}-\tau)^{\alpha-1}d\tau = \quad 8.10.3$$

$$v_i^{n+1} = v_i^0 + (1-\alpha)F\big(t_{n+1}, z_i, \bar{V}(t_{n+1}, z_i)\big) + \frac{\alpha}{\Gamma(\alpha)}\sum_{j=0}^{n-1}F\left(z_i, \frac{t_j + t_{j+1}}{2}, \frac{v_i^{j+1} + v_i^j}{2}\right)\frac{h^\alpha}{\alpha}\{(n-j+1)^\alpha - (n-j)^\alpha\} + \frac{h^\alpha}{\Gamma(\alpha)}F\left(z_i, t_n + \frac{h}{2}, \bar{V}_i^{n+1}\right) \quad 8.10.4$$

Where

$$\bar{V}_i^{n+1} = v_i^0 + (1-\alpha)F(t_n, z_i, V_i^n) + \frac{h^\alpha}{\Gamma(\alpha)}\sum_{j=0}^{n}F\big(z_i, t_j, v_i^j\big)\{(n-j+1)^\alpha - (n-1)^\alpha\} \quad 8.10.5$$

Going forward, we discretize the function F given as recall the function

$$\frac{K}{\emptyset\mu_l}\left\{k_l(v_l)\frac{\partial^2 p_l}{\partial z^2} + \left(\frac{\partial p_l}{\partial z} + \rho_l g e_z\right)\frac{\partial k_l(v_l)}{\partial z}\right\} = F(t, p, z, v(t, p, z)) \quad 8.10.6$$

For $F\left(t, z_i, P_{l,i}, v\left(z_i, P_{l,i}, t_j\right)\right)$

$$v_i^{n+1} = v_i^0 + (1-\alpha)F\left(t_{n+1}, z_i, \bar{V}(t_{n+1}, z_i)\right) + \frac{\alpha}{\Gamma(\alpha)}\sum_{j=0}^{n-1} F\left(z_i, \frac{t_j + t_{j+1}}{2}, \frac{v_i^{j+1} + v_i^j}{2}\right)\frac{h^\alpha}{\alpha}\{(n-j+1)^\alpha - (n-j)^\alpha\} + \frac{h^\alpha}{\Gamma(\alpha)}F\left(z_i, t_n + \frac{h}{2}, \bar{V}_i^{n+1}\right) \quad 8.10.7$$

$$\frac{\partial F\left(t, z_i, P_{l,i}, v\left(z_i, P_{l,i}, t_j\right)\right)}{\partial z} = \frac{K}{\emptyset\mu}.\left\{k_l(v_l).\frac{1}{2(\Delta z)^2}\left(P_l(t_j, z_{i+1}) - 2P_l\left(t_j, z_i\right) + P_l(t_j, z_{i-1})\right) + \left[\frac{1}{2\Delta z}\left(p(t_j, z_{i+1}) - p(t_j, z_{i-1})\right) + \rho_l g e_z\right]\frac{1}{2\Delta z}\left(v_l(t_j, z_{i+1}) - v_l(t_j, z_{i-1})\right)\right\}$$

$$\frac{\partial^2 p_l}{\partial z^2} = \frac{1}{2(\Delta z)^2}\left(P_l(t_j, z_{i+1}) - 2P_l\left(t_j, z_i\right) + P_l(t_j, z_{i-1})\right) \quad 8.10.8$$

$$\frac{\partial p_l}{\partial z} = \frac{1}{2\Delta z}\left(p(t_j, z_{i+1}) - p(t_j, z_{i-1})\right)$$

$$\frac{\partial k_l(v_l)}{\partial z} = \frac{1}{2\Delta z}\left(v_l(t_j, z_{i+1}) - v_l(t_j, z_{i-1})\right)$$

$$v_i^{n+1} = v_i^0 + (1-\alpha)F\left(t_{n+1}, z_i, \bar{V}(t_{n+1}, z_i)\right) + \frac{\alpha}{\Gamma(\alpha)}\sum_{j=0}^{n-1} F\left(\frac{K}{\emptyset\mu}.\left\{k_l(v_l).\frac{1}{2(\Delta z)^2}\left(P_l(t_j, z_{i+1}) - 2P_l\left(t_j, z_i\right) + P_l(t_j, z_{i-1})\right) + \left[\frac{1}{2\Delta z}\left(p(t_j, z_{i+1}) - p(t_j, z_{i-1})\right) + \rho_l g e_z\right]\frac{1}{2\Delta z}\left(v_l(t_j, z_{i+1}) - v_l(t_j, z_{i-1})\right)\right\}, \frac{t_j + t_{j+1}}{2}, \frac{v_i^{j+1} + v_i^j}{2}\right)\frac{h^\alpha}{\alpha}\{(n-j+1)^\alpha - (n-j)^\alpha\} + \frac{h^\alpha}{\Gamma(\alpha)}F\left(\frac{K}{\emptyset\mu}.\left\{k_l(v_l).\frac{1}{2(\Delta z)^2}\left(P_l(t_j, z_{i+1}) - 2P_l\left(t_j, z_i\right) + P_l(t_j, z_{i-1})\right) + \left[\frac{1}{2\Delta z}\left(p(t_j, z_{i+1}) - p(t_j, z_{i-1})\right) + \rho_l g e_z\right]\frac{1}{2\Delta z}\left(v_l(t_j, z_{i+1}) - v_l(t_j, z_{i-1})\right)\right\}, t_n + \frac{h}{2}, \bar{V}_i^{n+1}\right) \quad 8.10.9$$

Where

$$\bar{V}_i^{n+1} = v_i^0 + (1-\alpha)F(t_n, z_i, V_i^n) + \frac{h^\alpha}{\Gamma(\alpha)}\sum_{j=0}^{n} F\left(z_i, t_j, v_i^j\right)\{(n-j+1)^\alpha - (n-1)^\alpha\}$$

$$\frac{K}{\emptyset\mu}.\left\{k_l(v_l).\frac{1}{2(\Delta z)^2}\left(P_l(t_j, z_{i+1}) - 2P_l\left(t_j, z_i\right) + P_l(t_j, z_{i-1})\right) + \left[\frac{1}{2\Delta z}\left(p(t_j, z_{i+1}) - p(t_j, z_{i-1})\right) + \rho_l g e_z\right]\frac{1}{2\Delta z}\left(v_l(t_j, z_{i+1}) - v_l(t_j, z_{i-1})\right)\right\}$$

8.5.2.1. Numerical approximation with the Caputo derivative

Cognizance of our model, we let

$$\frac{K}{\emptyset\mu_l}\left\{k_l(v_l)\frac{\partial^2 p_l}{\partial z^2} + \left(\frac{\partial p_l}{\partial z} + \rho_l g e_z\right)\frac{\partial k_l(v_l)}{\partial z}\right\} = F(t, p, z, v(t, p, z)) \quad 8.11.0$$

The Cauchy problem system can be obtained

$$\begin{cases} {}_0^C\mathcal{D}_t^\alpha v(z, p, t) = F\left(\tau, z, p, v(\tau, z, p)\right) \\ v(z, 0) = 0 \end{cases} \quad 8.11.1$$

Recalling the Caputo derivative and associated integral, we have from the fundamental theorem of calculus that

$$v(z, t) - v(\mathrm{z}, 0) = \frac{1}{\Gamma(\alpha)}\int_0^t F\left(\tau, z, P_l, v_l(\tau, z, p)\right)(t-\tau)^{\alpha-1}d\tau \quad 8.11.2$$

Again, we consider the point.

$t = t_{k+1} = (k+1)\Delta t \qquad \forall\, k \in [0,1,2\ldots]$

$$v_l(t_{k+1}, z_i) - v(z_i, 0) = \frac{1}{\Gamma(\alpha)}\int_0^{t_{k+1}} F\left(\tau, z_i, P_{l,i}, v_l(\tau, z_i, p_i)\right)(t_{k+1} - \tau)^{\alpha-1}d\tau \quad 8.11.3$$

And at the point $t = t_k = (k)\Delta t$

$$v_l(z_i, t_k) - v_l(z_i, 0) = \frac{1}{\Gamma(\alpha)}\int_0^{t_k} F\left(\tau, z_i, P_{l,i}, v_l\left(\tau, z_i, P_{l,i}\right)\right)(t_k - \tau)^{\alpha-1}d\tau \quad 8.11.4$$

Combining both equations by taking their difference, we have that

$$v_l(z_i, t_{k+1}) = v_l(z_i, 0) + \frac{1}{\Gamma(\alpha)}\sum_{j=0}^{k}\int_{t_k}^{t_{k+1}} F\left(\tau, z_i, P_{l,i}, v_l\left(\tau, z_i, P_{l,i}\right)\right)(t_{k+1} - \tau)^{\alpha-1}d\tau \quad 8.11.5$$

To proceed, we will make use of Lagrange polynomial, $P_j(\tau)$ to approximate the non-linear function$F\left(\tau, z, p, v(\tau, z, p)\right)$ at $\left(t_j\ and\ t_{j-1}\right)$.

$$P_j(\tau) = \frac{\tau - t_{j-1}}{t_{j+1} - t_{j-1}} F\left(t_j, z_i, P_{l,i}, v_l\left(z_i, p_i t_j\right)\right) - \frac{\tau - t_j}{t_{j+1} - t_{j-1}} F\left(t_{j-1}, z_i, P_{l,i}, v_l\left(z_i, P_{l,i}, t_{j-1}\right)\right)$$

$$v(z_i, t_{k+1}) = v(z_i, 0) + \frac{1}{\Gamma(\alpha)} \sum_{j=1}^{k} \int_{t_j}^{t_{j+1}} \left[\frac{\tau - t_{j-1}}{t_{j+1} - t_{j-1}} F\left(t, z_i, p_i, v_l\left(z_i, p_i t_j\right)\right) - \frac{\tau - t_j}{t_{j+1} - t_{j-1}} F\left(t_{j-1}, z_i, p_i, v_l\left(z_i, p_i(t_{j-1})\right)\right) \right] (t_{k+1} - \tau)^{\alpha-1} d\tau \quad 8.11.6$$

$$v(z_i, t_{k+1}) = v(z_i, 0) + \frac{1}{\Gamma(\alpha)} \sum_{j=0}^{k} \int_{t_j}^{t_{j+1}} \left[\frac{\tau - t_{j-1}}{t_{j+1} - t_{j-1}} F\left(t_j, z_i, p_i, v_l\left(z_i, p_i(t_j)\right)\right) - \frac{\tau - t_j}{t_{j+1} - t_{j-1}} F\left(t_{j-1}, z_i, p_i, v_l\left(z_i, p_i(t_{j-1})\right)\right) \right] (t_{k+1} - \tau)^{\alpha-1} d\tau \quad 8.11.7$$

$$v(z_i, t_{k+1}) = v(z_i, 0) + \frac{1}{\Gamma(\alpha)} \sum_{j=1}^{k} \frac{F\left(t_j, z_i, P_{l,i}, v_l\left(z_i, P_{l,i}, t_j\right)\right)}{\Delta t} \int_{t_j}^{t_{j+1}} (\tau - t_{j-1})(t_{k+1} - \tau)^{\alpha-1} d\tau - \frac{1}{\Gamma(\alpha)} \sum_{j=1}^{k} \frac{F\left(t_{j-1}, z_i, P_{l,i}, v_l\left(z_i, P_{l,i}, t_{j-1}\right)\right)}{\Delta t} \int_{t_j}^{t_{j+1}} (\tau - t_j)(t_{k+1} - \tau)^{\alpha-1} d\tau \quad 8.11.8$$

Substituting the computed integrals and discretizing, we obtain the numerical solver.

$$\int_{t_k}^{t_{k+1}} (\tau - t_{k-1})(t_{k+1} - \tau)^{\alpha-1} d\tau = \frac{(\Delta t)^{\alpha+1}}{\alpha(\alpha+1)} [(k-j+1)^{\alpha}(k-j+2-\alpha) - (k-j)^{\alpha}(k-j+2-\alpha)] \quad 8.11.9$$

$$\int_{t_k}^{t_{k+1}} (\tau - t_k)\,(t_{k+1} - \tau)^{\alpha-1} d\tau = \frac{(\Delta t)^{\alpha+1}}{\alpha(\alpha+1)} [(k-j+1)^{\alpha+1} - (k-j)^{\alpha}(k-j+1+\alpha)] \quad 8.12.0$$

However,

$$F(t, p, z, v(t, p, z)) = \frac{K}{\emptyset \mu_l} \left\{ k_l(v_l) \frac{\partial^2 P_l}{\partial z^2} + \left(\frac{\partial P_l}{\partial z} + \rho_l g e_z \right) \frac{\partial k_l(v_l)}{\partial z} \right\} \quad 8.12.1$$

Such that

For $F\big(t,p,z,v(t,p,z)\big) = F\left(t,z_i,P_{l,i},v\big(z_i,P_{l,i},t_j\big)\right)$

$$\frac{\partial F\left(t_j,z_i,P_{l,i},v\big(z_i,P_{l,i},t_j\big)\right)}{\partial z} = \frac{K}{\emptyset\mu}.\Big\{k_l(v_l).\frac{1}{2(\Delta z)^2}\big(P_l(t_j,z_{i+1}) - 2P_l\big(t_j,z_i\big) + P_l(t_j,z_{i-1})\big) + \left[\frac{1}{2\Delta z}\big(p(t_j,z_{i+1}) - p(t_j,z_{i-1})\big) + \rho_l g e_z\right]\frac{1}{2\Delta z}\big(v_l(t_j,z_{i+1}) - v_l(t_j,z_{i-1})\big)\Big\} \quad 8.12.2$$

$$\frac{\partial^2 p_l}{\partial z^2} = \frac{1}{2(\Delta z)^2}\big(P_l(t_j,z_{i+1}) - 2P_l\big(t_j,z_i\big) + P_l(t_j,z_{i-1})\big) \quad 8.12.3$$

$$\frac{\partial p_l}{\partial z} = \frac{1}{2\Delta z}\big(p(t_j,z_{i+1}) - p(t_j,z_{i-1})\big)$$

$$\frac{\partial k_l(v_l)}{\partial z} = \frac{1}{2\Delta z}\big(v_l(t_j,z_{i+1}) - v_l(t_j,z_{i-1})\big)$$

For $F\big(t,p,z,v(t,p,z)\big) = F\left(t_{j-1},z_i,P_{l,i},v\big(z_i,P_{l,i},t_{j-1}\big)\right)$

$$\frac{\partial F\left(t_{j-1},z_i,P_{l,i},v\big(z_i,P_{l,i},t_{j-1}\big)\right)}{\partial z} = \frac{K}{\emptyset\mu}.\Big\{k_{l,i}\big(v_{l,i}\big).\frac{1}{2(\Delta z)^2}\big(P_l(t_{j-1},z_{i+1}) - 2P_l\big(t_{j-1},z_i\big) + P_l(t_{j-1},z_{i-1})\big) + \left[\frac{1}{2\Delta z}\big(p(t_{j-1},z_{i+1}) - p(t_{j-1},z_{i-1})\big) + \rho_l g e_z\right]\frac{1}{2\Delta z}\big(v_l(t_{j-1},z_{i+1}) - v_l(t_{j-1},z_{i-1})\big)\Big\} \quad 8.12.4$$

Substituting we get

$$v(z_i, t_{k+1}) = v(z_i, 0) \qquad 8.12.5$$
$$+ \frac{1}{\Gamma(\alpha)} \sum_{j=0}^{k} \frac{1}{\Delta t} \frac{K}{\emptyset \mu} . \Big\{ k_l(v_l) . \frac{1}{2(\Delta z)^2} \big(P_l(t_j, z_{i+1}) - 2P_l\big(t_j, z_i\big)$$
$$+ P_l(t_j, z_{i-1}) \big)$$
$$+ \left[\frac{1}{2\Delta z} \big(p(t_j, z_{i+1}) - p(t_j, z_{i-1}) \big) + \rho_l g e_z \right] \frac{1}{2\Delta z} \big(v_l(t_j, z_{i+1})$$
$$- v_l(t_j, z_{i-1}) \big) \Big\} \int_{t_k}^{t_{k+1}} (\tau - t_{j-1})(t_{k+1} - \tau)^{\alpha-1} d\tau$$
$$- \frac{1}{\Gamma(\alpha)} \sum_{j=0}^{k} \frac{1}{\Delta t} \frac{K}{\emptyset \mu} . \Big\{ k_{l,i}\big(v_{l,i}\big) . \frac{1}{2(\Delta z)^2} \big(P_l(t_{j-1}, z_{i+1}) - 2P_l\big(t_{j-1}, z_i\big)$$
$$+ P_l(t_{j-1}, z_{i-1}) \big)$$
$$+ \left[\frac{1}{2\Delta z} \big(p(t_{j-1}, z_{i+1}) - p(t_{j-1}, z_{i-1}) \big) + \rho_l g e_z \right] \frac{1}{2\Delta z} \big(v_l(t_{j-1}, z_{i+1})$$
$$- v_l(t_{j-1}, z_{i-1}) \big) \Big\} \int_{t_k}^{t_{k+1}} (\tau - t_j)(t_{k+1} - \tau)^{\alpha-1} \, d\tau$$

Substituting the calculated integrals equations:

$$\int_{t_k}^{t_{k+1}} (\tau - t_{k-1})(t_{k+1} - \tau)^{\alpha-1} d\tau \qquad 8.12.6$$
$$= \frac{(\Delta t)^{\alpha+1}}{\alpha(\alpha+1)} [(k-j+1)^{\alpha}(k-j+2-\alpha)$$
$$- (k-j)^{\alpha}(k-j+2-\alpha)]$$

$$\int_{t_k}^{t_{k+1}} (\tau - t_k) \, (t_{k+1} - \tau)^{\alpha-1} d\tau \qquad 8.12.7$$
$$= \frac{(\Delta t)^{\alpha+1}}{\alpha(\alpha+1)} [(k-j+1)^{\alpha+1} - (k-j)^{\alpha}(k-j+1+\alpha)]$$

$$v(z_i, t_{k+1}) = v(z_i, 0) \qquad 8.12.8$$
$$+ \frac{1}{\Gamma(\alpha)} \sum_{j=1}^{k} \frac{1}{\Delta t} \frac{K}{\emptyset \mu} . \Big\{ k_l(v_l) . \frac{1}{2(\Delta z)^2} \big(P_l(t_j, z_{i+1}) - 2P_l\big(t_j, z_i\big)$$
$$+ P_l(t_j, z_{i-1}) \big)$$
$$+ \Big[\frac{1}{2\Delta z} \big(p(t_j, z_{i+1}) - p(t_j, z_{i-1}) \big) + \rho_l g e_z \Big] \frac{1}{2\Delta z} \big(v_l(t_j, z_{i+1})$$
$$- v_l(t_j, z_{i-1}) \big) \Big\} \frac{(\Delta t)^{\alpha+1}}{\alpha(\alpha+1)} [(k-j+1)^{\alpha}(k-j+2-\alpha)$$
$$- (k-j)^{\alpha}(k-j+2-\alpha)]$$
$$- \frac{1}{\Gamma(\alpha)} \sum_{j=1}^{k} \frac{1}{\Delta t} \frac{K}{\emptyset \mu} . \Big\{ k_{l,i}\big(v_{l,i}\big) . \frac{1}{2(\Delta z)^2} \big(P_l(t_{j-1}, z_{i+1}) - 2P_l\big(t_{j-1}, z_i\big)$$
$$+ P_l(t_{j-1}, z_{i-1}) \big)$$
$$+ \Big[\frac{1}{2\Delta z} \big(p(t_{j-1}, z_{i+1}) - p(t_{j-1}, z_{i-1}) \big) + \rho_l g e_z \Big] \frac{1}{2\Delta z} \big(v_l(t_{j-1}, z_{i+1})$$
$$- v_l(t_{j-1}, z_{i-1}) \big) \Big\} \frac{(\Delta t)^{\alpha+1}}{\alpha(\alpha+1)} [(k-j+1)^{\alpha+1}$$
$$- (k-j)^{\alpha}(k-j+1+\alpha)]$$

$$v(z_i, t_{k+1}) = v(z_i, 0) \qquad 8.12.9$$
$$+ \frac{1}{\Gamma(\alpha)} \sum_{j=0}^{k} \frac{1}{\Delta t} \frac{K}{\emptyset \mu} . \Big\{ k_{l,i}\big(v_{l,i}\big) . \frac{1}{2(\Delta z)^2} \big(P_l(t_j, z_{i+1}) - 2P_l\big(t_j, z_i\big)$$
$$+ P_l(t_j, z_{i-1}) \big)$$
$$+ \Big[\frac{1}{2\Delta z} \big(p(t_j, z_{i+1}) - p(t_j, z_{i-1}) \big) + \rho_l g e_z \Big] \frac{1}{2\Delta z} \big(v_l(t_j, z_{i+1})$$
$$- v_l(t_j, z_{i-1}) \big) \Big\} \frac{(\Delta t)^{\alpha+1}}{\alpha(\alpha+1)} [(k-j+1)^{\alpha}(k-j+2-\alpha)$$
$$- (k-j)^{\alpha}(k-j+2-\alpha)]$$
$$- \frac{1}{\Gamma(\alpha)} \sum_{j=0}^{k} \frac{1}{\Delta t} \frac{K}{\emptyset \mu} . \Big\{ k_{l,i}\big(v_{l,i}\big) . \frac{1}{2(\Delta z)^2} \big(P_l(t_{j-1}, z_{i+1}) - 2P_l\big(t_{j-1}, z_i\big)$$
$$+ P_l(t_{j-1}, z_{i-1}) \big)$$
$$+ \Big[\frac{1}{2\Delta z} \big(P_l(t_{j-1}, z_{i+1}) - P_l(t_{j-1}, z_{i-1}) \big)$$
$$+ \rho_l g e_z \Big] \frac{1}{2\Delta z} \big(v_l(t_{j-1}, z_{i+1}) - v_l(t_{j-1}, z_{i-1}) \big) \Big\} \frac{(\Delta t)^{\alpha+1}}{\alpha(\alpha+1)} [(k-j$$
$$+ 1)^{\alpha+1} - (k-j)^{\alpha}(k-j+1+\alpha)]$$

8.6. Numerical simulation

This section presents numerical simulations that describe the saturation evolution due to fractional flow at the two-phase (CO_2-water) flow region. The scheme is a high-resolution scheme for numerically solving non-linear conservation law problems. The numerical scheme is stable and prevents the development of spurious near edge oscillations by use of numerical viscosity terms. The order of convergence for all models are computed using the Harten-Lax-van Leer (HLL) flux. The numerical results are presented in figure [8.6-8.8].

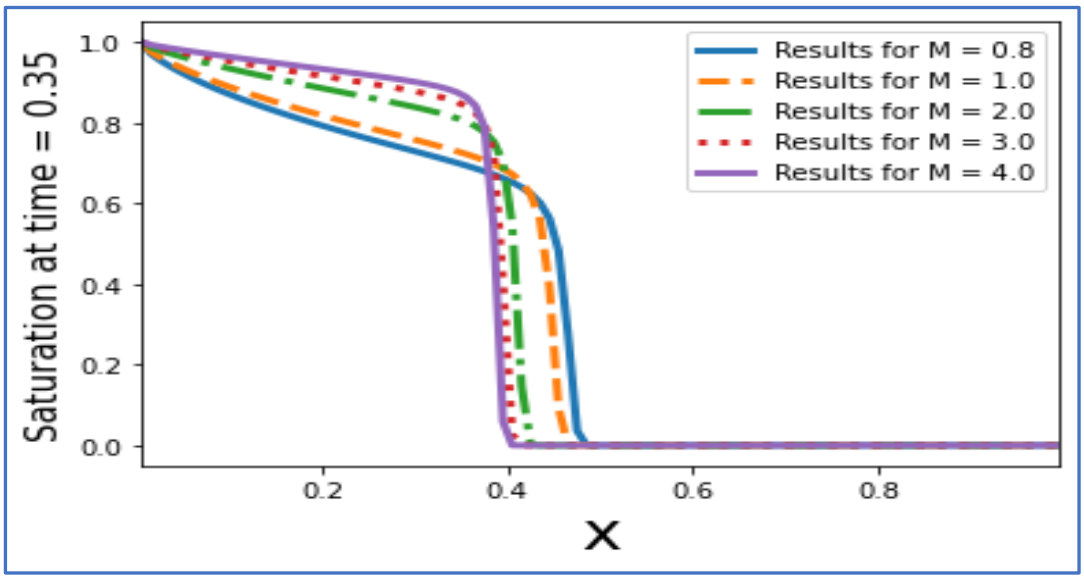

Figure 8-6: Plot of CO2 Saturation vs distance (t=0.35).

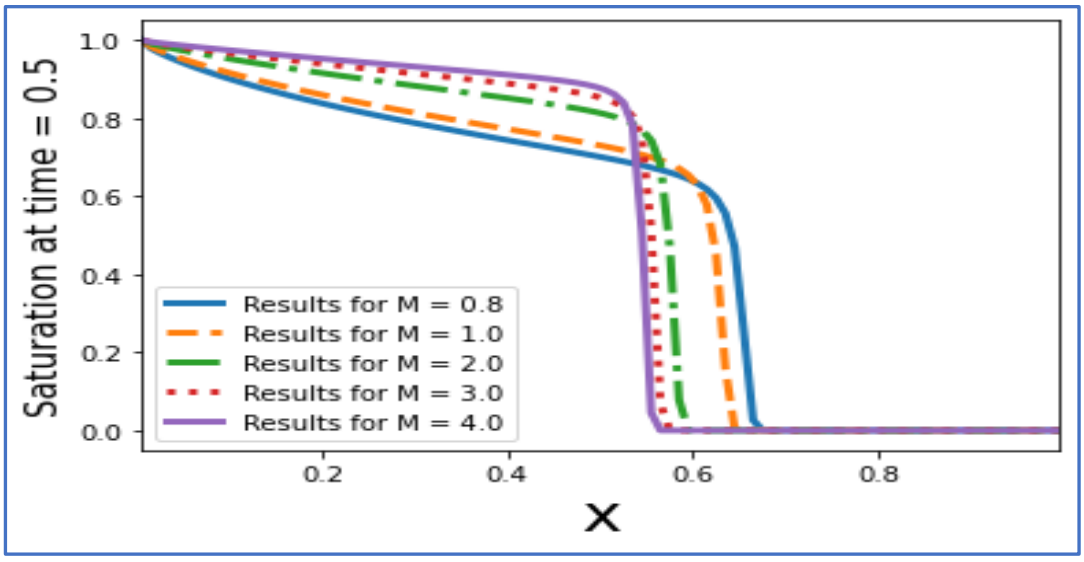

Figure 8-7: Plot of Saturation vs distance (t=0.5).

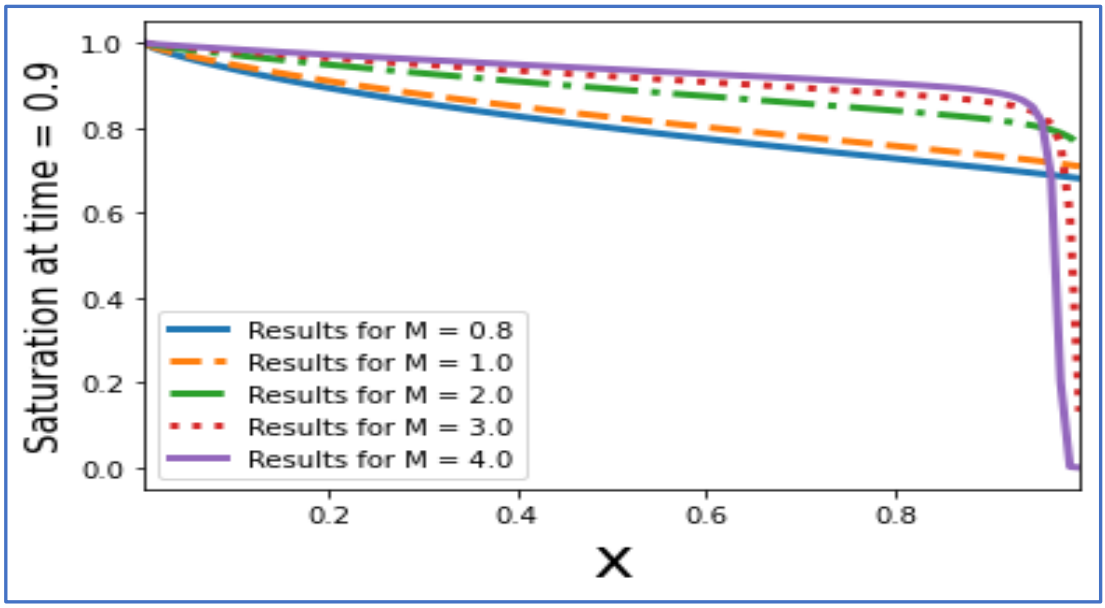

Figure 8-8: Plot of CO2 Saturation vs distance from well (t=0.9).

8.7. Discussion and conclusion

This chapter has presented numerical solutions that model the evolution of saturation, as invoked in geological sequestration of supper critical CO_2. The numerical methods discussed are considered for their physically correct and scientifically sound properties like boundary conditions, drainage response, and invariant domain. The results obtain for different run times $t = 0.35,\ t = 0.5\ and\ t = 0.9$ are outputted and shown above. The graphs for different values of $\boldsymbol{M}$ versus runtime time, to predict the rate of decrease in CO_2 saturation with distance from the injection well (the start point) are presented. Carbon dioxide saturation is maximum at the start of the model run, and gradually decrease over time and space. M is inversely related to the degree of saturation. This means for low values of M, the S-shape profile is steep with a high angle. On the other hand, low M values represent a more horizontal profile where saturation and diffusion are enhanced by both the gravity and the injection flux.

Fractional flow predicts the shock fronts of mobile phase CO_2 plume and can be used to assess the CO_2 storage capacity. The primary outcome of the numerical study is to present a new numerical model to predict the saturation gradient for any given radial distance (X) from the injection well. As expected, pressure increases close to the injection well due to high CO_2 gas saturation. Of course, the significance of inertial loss is more pronounced in the near well region.

CHAPTER NINE: CONCLUSION AND RECOMMENDATIONS

9.1. Conclusions

The systems that maintain the current global ecological balance, necessary for survival and adaptation on Earth are under increasing stress due to climate change. This is predominantly associated to the increase in the production of anthropogenic CO_2, a chemical product of fossil fuel combustion for power generation. This trend is likely to carry on if business continues as usual, with the likelihood of irreversible changes (Knorr and Blodau, 2009). CCS can offer a window of transition while consumption of fossil fuels peaks before gradual decline towards NetZero targets, without further contributing to global warming.

Geological Carbon Sequestration is possible through the displacement of the formation brine in a process called imbibition. Carbon dioxide migration and fluid displacement is associated with pore expansion and the buildup of reservoir pressure over time. Pressure buildup enhances diffuse leakage through the cap rock, or along reactivated faults regions, which is a primary safety concern for the quality of shallow fresh groundwater capture regions. The numerical solutions developed in this thesis provide an overview of the transient pressure behavior, under far field and near field conditions. They are useful tools for risk assessments of geo-sequestration, in basins with shallow freshwater capture regions.

The work in this research reflects the application of local and non-local differential operators to approximate the 1-dimensional diffusivity pressure buildup model in radial space. Geological reservoirs are notoriously heterogeneous at varying scales and dimensions, implying a diverse set of operator capabilities is needed to constrain the efforts of reservoir characterization. The research in this thesis makes use of fractional derivatives to develop numerical models that predict the buildup of pressure during CO_2 injection. Even though the new model solutions are obtained with the fractional and the classical formalism, the contention of this thesis is to capture non-local behavior with fractional derivatives. These include the effect of effect long tail power law process, fading memory with weak crossover exponential law processes Strong crossover from stretched exponential to power-law with Mittag-Leffler kernel and the random walk process with fractional stochastic formulation.

In addition, CCS is a new technology with some uncertainties. Geological heterogeneity is a big source of deviation from the presumed classical formalisms, which in turn affects cost, and capacity estimates. In addition, only a handful of CCS projects exist at various stages of development, making the available limited data a subject of intense scrutiny, achieved through uncertainty studies. Chapter 9 presents a fractional stochastic model for pressure buildup due to CO_2 injection. The results agree with the overall risks profile for a CO_2 injection scheme. The near well region has a unique pressure profile that sharply peaks, before leveling further away from the well. This observation is also consistent with the stochastic model results in chapter 7 (Figure 7-3 and 7-4). High variation in the near well transient pressure response alludes to the degree of uncertainty. In a real-life reservoir, the near well conditions are characterized by high energy, viscous flows, coupled with permeability's changes and porosity reduction due to salt precipitation. These processes take place at varying spatio-temporal scales and highlight a source of great uncertainty for predictive modelling. The data set (table 2) used for simulation reflect real world parameters readings.

Table 2: Data used for Pressure build-up simulation analysis.

Parameter	Value
Formation thickness	40 m
Formation depth	1000 m
Formation permeability	55 m^2
Formation Porosity	0.14
Injection rate	1,000,000 m^3
Rock compressibility	5x10-5 Pa^{-1}
Brine compressibility	4.5x10-5 Pa^{-1}
Gas relative permeability	0.6 m^2
Gas viscosity	0.066 $N\ s\ m^{-2}$
Brine viscosity	0.47 $N\ s\ m^{-20'}$
Time	Dimensionless.

In Chapter 3, Numerical models based on the classical derivative to estimate pressure buildup in each of the three saturation regions (A, B, and C) are presented. The models are based on the traditional Darcy formulation, which assumes a homogenous and isotropic reservoir with uniform thickness. Two models are presented: A two-step LaGrange polynomial and middle point approximation method. The mathematical formulation considers relative permeability, the effect of two-phase immiscible flow, and slight fluid and matrix compressibility to

compute pressure buildup predictions. Experiments of parameter sensitivity suggest that the relative CO_2 permeability and compressibility affect the pressure results, but not significantly. While this solution fairly replicates the pressure buildup signature due to CO_2 injection, it is classically defined and has no memory. The model could not accurately differentiate between the near Well and fractional flow regions.

Chapters 4 and 5 present new numerical solutions to calculate pressure buildup using the Caputo and the Caputo Fabrizio derivatives, respectively. From the results, the new models reveal complex processes that were invisible to the classical derivative in Chapter 3. Both solutions depict a heavy-tailed dependence with an exponential early time pressure response, with the Caputo and Caputo-Fabrizio fractional derivatives, respectively. The accurately approximated pressure buildup, while the study suggests some inaccuracies of the classical model to resolve shock fronts as pressure buildup is over-estimated in the classical model, compared to the Caputo and Caputo Fabrizio cases. The model could accurately distinguish the piecewise description of the initial problem. At early injection time, the pressure peaks at the bottom of the hole before dropping to the correct equilibrium when the mobile phase plume forms the drying-out region. This is because earlier intruded pockets of variable CO_2 saturation result in the peaking of the pressure buildup. The pressure eventually drops to an equilibrium point, and if the injection was seized before this time, the maximum pressure would be missed, and the pressure would decrease much faster (figure 5.3). The drop is much faster in the Caputo Fabrizio case than in the Caputo case.

Chapter 6 and 7 present new numerical models based on ABC derivative and fractional differential model with a stochastic property based on the generalized Mittag-Leffler function. The model theoretical matched the results obtained with field data for the near well region (Azizi, 2013). Figure 6-1 shows crossover behavior, starting with slow dissipation pressure before returning to a steep drop. The presence of a fracture decompresses the fluid pressure creating a change in the advancing pressure front.

On the other hand, the stochastic model accurately captures the deterministic response as already described. However, high-frequency variation is observed at early times. The variation talks to high uncertainty with the pressure evolution. It should be noted that the

near-well region is a high-energy region dominated by viscous and frictional forces. Stochastic noise is observed in all three two-face flow fractional flow modelling of CO_2 injection.

Regions: however, it is much lower in the distal brine region. The stochastic model introduces randomness into a given deterministic model, transforming it into a powerful mathematical approach to capture complex real-world problems (Atangana & Koca, 2019). These results are consistent with the CO_2 injection risk profile depicted in (figure 2-7). The risk is maximum during ongoing injection due to high-pressure buildup during the early injection times. The risk and uncertainty decrease over time when the pressure starts to recover, and secondary trapping mechanisms activate. Parameter sensitivity studies in both models suggest that the relative permeability of CO_2 significantly affects the pressure buildup. The closer the relative permeability is to one, the lower the pressure buildup rate, the lower the relative permeability, the greater the calculated pressure buildup.

Lastly, Chapter 8 presents a new model to approximate the saturation for the two-phase immiscible flow region (region two). The Buckley-leveret saturation model describes the two-phase immiscible flow. So far, the discussed numerical models are based on finite difference schemes. In this chapter, the presented numerical solutions that predict the fractional flow are based on the finite volume method. The finite volume method calculates the parameters at discrete nodes within a finite volume problem domain. To obtain a numerical model, the mass balance equations are coupled with the saturation function to accurately describe the CO_2 saturation profile in the fractional flow region. According to the simulation results, saturation decreases with time and space and away from the injection well point. Carbon dioxide saturation in the fractional flow region is controlled by capillarity and rate of dissolution. The forces are a function of fractional flow decreases with CO_2 saturation. Saturation decreases with an increase in the dissolution rate so that the saturation builds up gradually. This results in a variably saturated front, which fringes on CO_2 ingress, causing pressure to peak.

Overall, the modelling results fit with observed data on CO_2 saturation in space, as CO_2 migrates away from the injection. The saturation generally decreases with time and distance, X.

9.2. Recommendations

1. All the models presented in this thesis assume a reservoir of uniform thickness, which is originally horizontal. In practice, reservoirs are non-uniform and tend to extend up-dip, at distant boundaries, due to topologic variation in the lower boundary. Recently the concept of the global derivative that considers the rate of change concerning a function instead of a constant step has been suggested to handle problems of this nature. Therefore, it is suggested to use global derivatives to study the effect of dipping reservoirs and varying topography on the pressure buildup approximations.
2. The proposed numerical models assume a negligible gravity effect on the pressure buildup. As indicated in the literature section, CO_2 injection and migration are buoyancy driven due to the density difference between CO_2 and reservoir brine. Neglecting gravity leads to pressure overestimates. Further studies recommend incorporating gravity into the pressure diffusivity model in this context.
3. All the presented models assumed that the CO_2 stream is uniform and homogenous. However, many studies relating to wastewater injection have recognized the role of fluid quality (impurities) in pressure buildup. Extending the current models by including the effect of CO_2 impurities on pressure build is recommended.
4. Limits of capillary forces control pressure buildup in the near Well region. However, the capillarity effect needs to be addressed in their models. Including the effect of capillarity in further studies of this nature is recommended.
5. The models presented in this thesis all represented injection through a single vertical Well. A study on the effect of horizontal Well injection on transient pressure behavior is recommended.
6. Finally, it is recognized that the future of CCS will involve multiple injection points for a single reservoir. Since the current models only consider a single well injection scenario, modelling the effect of multiple wells and the interaction between different plumes is recommended to further our understanding of the pressure buildup and how it can be managed.

Bibliography

Afrough, Armin and Moghaddam, Mehdi Bahari and Romero-Zeron, Laura and Balcom, Bruce J. 2019. "Exponential Capillary Pressure Functions in Sedimentary Rocks." *E3S Web of Conferences* (EDP Sciences) 89: 02005.

Agarwal, Ritu and Yadav, Mahaveer Prasad and Baleanu, Dumitru and Purohit, SD4141899. 2020. "Existence and uniqueness of miscible flow equation through porous media with a non singular fractional derivative."

Ahmed, Barzan I and Al-Jawad, Mohammed S. 2020. "Geomechanical modelling and two-way coupling simulation for carbonate gas reservoir." *Journal of Petroleum Exploration and Production Technology* 10 (8): 3619-3648.

Ahmed, Barzan I and Al-Jawad, Mohammed S. 2020. "Geomechanical modelling and two-way coupling simulation for carbonate gas reservoir." *Journal of Petroleum Exploration and Production Technology* (Springer) 10: 3619-3648.

Al Hameli, Fatima and Belhaj, Hadi and Al Dhuhoori, Mohammed. 2022. "CO2 sequestration overview in geological formations: Trapping mechanisms matrix assessment." *Energies* (MDPI) 15 (20): 7805.

Alan Buis. 2019. "Global Climate Change." *nasa.gov.* October 9. Accessed January 17, 2023. https://climate.nasa.gov.

Alcalde, Juan and Flude, Stephanie and Wilkinson, Mark and Johnson, Gareth and Edlmann, Katriona and Bond, Clare E and Scott, Vivian and Gilfillan, Stuart MV and Ogaya, Xenia and Haszeldine, R Stuart. 2018. "Estimating geological CO2 storage security to deliver on climate mitigation." *Nature communications* (Nature Publishing Group UK London) 9 (1): 2201.

Al-Khdheeawi, Emad A and Vialle, Stephanie and Barifcani, Ahmed and Sarmadivaleh, Mohammad and Zhang, Yihuai and Iglauer, Stefan. 2018. "Impact of salinity on CO2 containment security in highly heterogeneous reservoirs." *Greenhouse Gases: Science and Technology* (Wiley Online Library) 8 (1): 93-105.

Almeida, Ricardo and Malinowska, Agnieszka B and Monteiro, M Teresa T. 2018. "Fractional differential equations with a Caputo derivative with respect to a kernel function and their applications." *Mathematical Methods in the Applied Sciences* (Wiley Online Library) 41 (1): 336-352.

Arif, Muhammad and Kumam, Poom and Kumam, Wiyada and Akgul, Ali and Sutthibutpong, Thana. 2021. "medium, Analysis of newly developed fractal-fractional derivative with power law kernel for MHD couple stress fluid in channel embedded in a porous." *Scientific Reports* (Nature Publishing Group UK London) 11 (1): 20858.

Atangana, Abdon and Baleanu, Dumitru. 2016. "New fractional derivatives with nonlocal and non-singular kernel: theory and application to heat transfer model."

Atangana, Abdon and Gomez-Aguilar, Jose Francisco. 2018. "Decolonisation of fractional calculus rules: breaking commutativity and associativity to capture more natural phenomena." *The European Physical Journal Plus* (Springer) 133: 1-22.

Atangana, Abdon and Goufo, Emile Franc Doungmo. 2020. "Some misinterpretations and lack of understanding in differential operators with no singular kernels." *Open Physics* (De Gruyter) 18 (1): 594-612.

Atangana, Abdon and Hammouch, Zakia. 2019. "Fractional calculus with power law: The cradle of our ancestors." *The European Physical Journal Plus* (Springer Berlin Heidelberg) 134 (9): 429.

Atangana, Abdon and Hammouch, Zakia. 2019. "Fractional calculus with power law: The cradle of our ancestors." *The European Physical Journal Plus* 134 (9): 429.

Atangana, Abdon and Hammouch, Zakia. 2019. "Fractional calculus with power law: The cradle of our ancestors." *The European Physical Journal Plus* (Springer Berlin Heidelberg) 134 (9): 429.

Atangana, Abdon and Jain, Sonal. 2018. "The role of power decay, exponential decay and Mittag-Leffler function's waiting time distribution: application of cancer spread." *Physica A: Statistical Mechanics and its Applications* (Elsevier) 512: 330-351.

Atangana, Abdon. 2017. "Fractal-fractional differentiation and integration: connecting fractal calculus and fractional calculus to predict complex system." *Chaos, solitons & fractals* (Elsevier) 102: 396-406.

Aydin, Gokhan and Karakurt, Izzet and Aydiner, Kerim. 2010. "Evaluation of geologic storage options of CO2: Applicability, cost, storage capacity and safety." *Energy Policy* (Elsevier) 38 (9): 5072-5080.

Aydin, Gokhan and Karakurt, Izzet and Aydiner, Kerim. 2010. "Evaluation of geologic storage options of CO2: Applicability, cost, storage capacity and safety." *Energy Policy* 38 (9): 5072-5080.

Azizi, Ehsan and Cinar, Yildiray. 2013. "A new mathematical model for predicting CO2 injectivity." *Energy Procedia* (Elsevier) 3250-3258.

Azizi, Ehsan and Cinar, Yildiray. 2013. "A new mathematical model for predicting CO2 injectivity." *Energy Procedia* (Elsevier) 37: 3250-3258.

Bachu, Stefan and Bonijoly, Didier and Bradshaw, John and Burruss, Robert and Holloway, Sam and Christensen, Niels Peter and Mathiassen, Odd Magne. 2007. "CO2 storage capacity estimation: Methodology and gaps." *International journal of greenhouse gas control* (Elsevier) 1 (4): 430-443.

Bachu, Stefan and Gunter, WD and Perkins, EH. 1994. "Aquifer disposal of CO2: hydrodynamic and mineral trapping." *Energy Conversion and management* (Elsevier) 35 (4): 269-279.

Bachu, Stefan and Gunter, William D. 2004. "Acid-gas injection in the Alberta basin, Canada: a CO2-storage experience." *Geological Society, London, Special Publications* (The Geological Society of London) 233 (1): 225-234.

Bachu, Stefan. 2013. "Drainage and imbibition CO2/brine relative permeability curves at in situ conditions for sandstone formations in western Canada." *Energy Procedia* (Elsevier) 4428-4436.

Bachu, Stefan. 2013. "Drainage and imbibition CO2/brine relative permeability curves at in situ conditions for sandstone formations in western Canada." *Energy Procedia* (Elsevier) 37: 4428-4436.

Bachu, Stefan. 2003. "Screening and ranking of sedimentary basins for sequestration of CO2 in geological media in response to climate change." *Environmental Geology* (Springer) 44 (3): 277-289.
Bachu, Stefan. 2003. "Screening and ranking of sedimentary basins for sequestration of CO2 in geological media in response to climate change." *Environmental Geology* (Springer) 44 (3): 277-289.
Bao, Ting and Burghardt, Jeff and Gupta, Varun and Edelman, Eric and McPherson, Brian and White, Mark. n.d. "Experimental workflow to estimate model parameters for evaluating long term viscoelastic response of CO2 storage caprocks." *International Journal of Rock Mechanics and Mining Sciences* (Elsevier) 146: 104796.

Barkai, Eli and Metzler, Ralf and Klafter, Joseph. 2000. "From continuous time random walks to the fractional Fokker-Planck equation." *Physical review E* (APS) 61 (1): 132.

Bar-Yam, Yaneer. 2011. "Concepts: Power Law." *New England Complex Systems Institute.* 07 16. Accessed 07 16, 2023. https://necsi.edu/power-law.

Bauke, Heiko. 2007. "Parameter estimation for power-law distributions by maximum likelihood methods." *The European Physical Journal B* (Springer) 58: 167-173.

Bielinski, Andreas. 2007. *Numerical simulation of CO2 sequestration in geological formations.*

Birkholzer, Jens T and Oldenburg, Curtis M and Zhou, Quanlin. 2015. "CO2 migration and pressure evolution in deep saline aquifers." *International Journal of Greenhouse Gas Control* (Elsevier) 40: 203-220.

Birkholzer, Jens T and Zhou, Quanlin. 2009. "Basin-scale hydrogeologic impacts of CO2 storage: Capacity and regulatory implications." *International Journal of Greenhouse Gas Control* (Elsevier) 6 (3): 745-756.

Bogdanov, II and Mourzenko, VV and Thovert, J-F and Adler, PM. 2007. "Effective permeability of fractured porous media with power-law distribution of fracture sizes." *Physical Review E* (APS) 76 (3): 036309.

Bohling, Geoff. 2005. "Stochastic simulation and reservoir modeling workflow." *Kansas Geological Survey.*

Bounaceur, Roda and Lape, Nancy and Roizard, Denis and Vallieres, Cecile and Favre, Eric. 2006. "Membrane processes for post-combustion carbon dioxide capture: a parametric study." *Energy* (Elsevier) 31 (14): 2556--2570.

Bradshaw, John and Bachu, Stefan and Bonijoly, Didier and Burruss, Robert and Holloway, Sam and Christensen, Niels Peter and Mathiassen, Odd Magne. {2007. "CO2 storage capacity estimation: issues and development of standards." *International journal of greenhouse gas control* (Elsevier) 1 (1): 62-68.

Burruss, Robert C and Brennan, Sean T and Freeman, Philip A and Merrill, Matthew D and Ruppert, Leslie F and Becker, Mark F and Herkelrath, William N and Kharaka, Yousif K and Neuzil, Christopher E and Swanson, Sharon M and others. 2009. "storage, Development of a probabilistic assessment methodology for evaluation of carbon dioxide." *US Geological Survey Open-File Report* 1035 (2009): 81.

Burton, McMillan and Kumar, Navanit and Bryant, Steven L. 2009. "CO2 injectivity into brine aquifers: Why relative permeability matters as much as absolute permeability." *Energy Procedia* (Elsevier) 1 (1): 3091-3098.

Caputo, Michele and Plastino, Wolfango. 2004. "Diffusion in porous layers with memory." *Geophysical Journal International* (Blackwell Publishing Ltd Oxford, UK) 158 (1): 385-396.

Cihan, Abdullah and Birkholzer, Jens T and Zhou, Quanlin. 2013}. "Pressure buildup and brine migration during CO2 storage in multilayered aquifers." *Groundwater* (Wiley Online Library) 51 (2): 252-267.

Cook, Peter J and Benson, Sally M. 2005. "Overview and current issues in geological storage of carbon dioxide." *Greenhouse Gas Control Technologies 7* (Elsevier) 15-20.

Cotel, Aline. 1999. "A trigger mechanism for the Lake Nyos disaster." *Journal of Volcanology and Geothermal Research* 88 (4): 343-347. Accessed 5 1, 2023. https://sciencedirect.com/science/article/pii/s0377027399000177.

CQUESTRA, a risk and performance assessment code for geological sequestration of carbon dioxide. 2008. "LeNeveu, DM." *Energy Conversion and Management* 49 (1): 32-46.

de Coninck, Heleen and Benson, Sally M. 2014. "Carbon dioxide capture and storage: issues and prospects." *Annual review of environment and resources* (Annual Reviews) 39: 243-270.

Dentz, Marco and Tartakovsky, Daniel M. 2009. "Abrupt-interface solution for carbon dioxide injection into porous media." *Transport in Porous Media* (Springer) 79: 15-27.

Di Giuseppe, Erika and Moroni, Monica and Caputo, Michele. 2010. "Flux in porous media with memory: models and experiments." *Transport in Porous Media* (Springer) 83: 479--500.

Dowd, Anne-Maree and Itaoka, Kenshi and Ashworth, Peta and Saito, Aya and de Best-Waldhober, Marjolein. 2014. "Investigating the link between knowledge and perception of CO2 and CCS: An international study." *International Journal of Greenhouse Gas Control* (Elsevier) 28: 79-87.

Eiken, Ola and Ringrose, Philip and Hermanrud, Christian and Nazarian, Bamshad and Torp, Tore A and Hoier, Lars. 2011. "Lessons learned from 14 years of CCS operations: Sleipner, In Salah and Snohvit." *Energy procedia* (Elsevier) 4: 5541-5548.

Emerick, Alexandre A and Reynolds, Albert C. 2013. "Ensemble smoother with multiple data assimilation." *Computers& Geosciences* (Elsevier) 55: 3-15.

Etienam, Clement. 2019. "4D seismic history matching incorporating unsupervised learning." In *SPE Europec featured at EAGE Conference and Exhibition?* SPE.

2023. "Experimental and theoretical investigation of the mechanisms of drying during CO2 injection into saline reservoirs." *Sokama-Neuyam, Yen Adams and Yusof, Muhammad Aslam Md and Owusu, Shadrack Kofi and Darkwah-Owusu, Victor and Turkson, Joshua Nsiah and Otchere, Adwoa Sampongmaa and Ursin, Jann Rune* (Nature Publishing Group UK London) 13 (1): 9155.

Falcon-Suarez, Ismael Himar and Livo, Kurt and Callow, Ben and Marin-Moreno, Hector and Prasad, Manika and Best, Angus Ian},. 2020. "Geophysical early warning of salt precipitation during geological carbon sequestration." *Scientific Reports* (Nature Publishing Group UK London) 10 (1): 16472.

Ganjdanesh, Reza and Pope, Gary A and Sepehrnoori, Kamy. 2015. "Production of energy from saline aquifers: a method to offset the energy cost of carbon capture and storage." *International Journal of Greenhouse Gas Control* (Elsevier) 34: 97-105.

Gasda, Sarah E and Nordbotten, Jan M and Celia, Michael A. 2009. "Vertical equilibrium with sub-scale analytical methods for geological CO 2 sequestration." *Computational Geosciences* (Springer) 13: 469-481.

Gasda, Sarah E and Wangen, Magnus and Bjornaraa, Tore I and Elenius, Maria T. 2017. "Investigation of caprock integrity due to pressure build-up during high-volume injection into the Utsira formation." *Energy Procedia* (Elsevier) 114: 3157-3166.

Ghanbarnezhad Moghanloo, Rouzbeh. 2012. "Applying method of characteristics to model the flow of compressible CO2 in aquifers." *SPE Western Regional Meeting.*

Gluyas, Jon and Mathias, Simon. 2013. *Geological storage of carbon dioxide (CO2): geoscience, technologies, environmental aspects and legal frameworks.* Elsevier.

Goodarzi, Somayeh and Settari, Antonin and Zoback, M and Keith, DW. 2010. "Thermal aspects of geomechanics and induced fracturing in CO2 injection with application to CO2 sequestration in Ohio River Valley." In *SPE International Conference on CO2 Capture, Storage, and Utilization*. OnePetro.

Han, Hongxue and Khan, Safdar and Ansari, Sajjad Ahmed and Khosravi, Nader and others. 2012. "Prediction of injection induced formation shear." *SPE International Symposium and Exhibition on Formation Damage Control.* Society of Petroleum Engineers.

Hendriks, CA and Blok, K. 1993. "Underground storage of carbon dioxide." *Energy Conversion and Management* (Elsevier) 34 (9-11): 949-957.

Hesse, MA and Woods, AW. 2010. "Buoyant dispersal of CO2 during geological storage." *Geophysical Research Letters* (Wiley Online Library) 37 (1).

Hesse, Marc Andre. 2008. *Mathematical modeling and multiscale simulation of carbon dioxide storage in saline aquifers.* Stanford University.

Hestres, Luis E and Nisbet, Matthew C. 2018. "Environmental advocacy at the dawn of the Trump era." *Environmental policy: New directions for the 21st century* 66-86.

Hildebrand, Ashleigh N and Herzog, Howard J. 2009. "Optimization of carbon capture percentage for technical and economic impact of near-term CCS implementation at coal-fired power plants." *Energy Procedia* (Elsevier) 1 (1): 4135-4142.

Holloway, Sam and van der Straaten, Ricks. 1995. "The Joule II project the underground disposal of carbon dioxide." *Energy Conversion and Management* (Elsevier) 36 (6-9): 519--522.

Horner, DR. 1951. "Pressure build-up in wells." *World Petroleum Congress.* WPC. WPC--4135.

Hosseini, Amir Hossein and Ghadery-Fahliyany, Hossein and Wood, David and Choubineh, Abouzar. 2020. "Artificial intelligence-based modeling of interfacial tension for carbon dioxide storage." *Gas Processing Journal* (University of Isfahan) 8 (1): 83-92.

Hoteit, Hussein and Firoozabadi, Abbas. 2008. "An efficient numerical model for incompressible two-phase flow in fractured media." *Advances in Water Resources* (Elsevier) 31 (6): 891-905.

Huaman, Ruth Nataly Echevarria and Jun, Tian Xiu. 2014. "Energy related CO2 emissions and the progress on CCS projects: a review." *Renewable and Sustainable Energy Reviews* (Elsevier) 31: 368-385.

Hulme, Michael. 2002. *Climate change scenarios for the United Kingdom: the UKCIP02 scientific report.* Tyndall Centre for Climate Mental Sciences University.

Iglauer, Stefan and Rahman, Taufiq and Sarmadivaleh, Mohammad and Al-Hinai, Adnan and Fern{\o}, Martin A and Lebedev, Maxim. 2016. "Influence of wettability on residual gas trapping and enhanced oil recovery in three-phase flow: A pore-scale analysis by use of microcomputed tomography." *SPE Journal* (SPE) 21 (06): 1916-1929.

IPCC. 2005. Cambridge: Cambridge University Press.

Isah, Abubakar and Arif, Muhammad and Hassan, Amjed and Mahmoud, Mohamed and Iglauer, Stefan. 2022. "A systematic review of Anhydrite-Bearing Reservoirs: EOR Perspective, CO2-Geo-storage and future research." *Fuel* (Elsevier) 320: 123942.

Jenkins, Luke. 2019. *Fluid injection and migration in layered aquifers.* University of Oxford.

Jiang, Peixue and Li, Xiaolu and Xu, Ruina and Wang, Yongsheng and Chen, Maoshan and Wang, Heming and Ruan, Binglu. 2014. "Thermal modeling of CO2 in the injection well and reservoir at the Ordos CCS demonstration project, China." *International journal of greenhouse gas control* (Elsevier) 23: 135-146.

Jiang, Xi. 2011. "A review of physical modelling and numerical simulation of long-term geological storage of CO2." *Applied energy* (Elsevier) 88 (11): 3557-3566.

Jin, Lu and Pekot, Lawrence J and Smith, Steven A and Salako, Olarinre and Peterson, Kyle J and Bosshart, Nicholas W and Hamling, John A and Mibeck, Blaise AF and Hurley, John P and Beddoe, Christopher J. 2018. "Effects of gas relative permeability hysteresis and solubility on associated CO2 storage performance." *International Journal of Greenhouse Gas Control* (Elsevier) 75: 140-150.

Johnson, James W and Nitao, John J and Knauss, Kevin G. 2004. "Reactive transport modelling of CO2 storage in saline aquifers to elucidate fundamental processes, trapping mechanisms and sequestration partitioning." *Geological Society, London, Special Publications* (Geological Society of London) 233: 107-128.

Juanes, Ruben and Spiteri, EJ and Orr Jr, FM and Blunt, MJ. 2006. "Impact of relative permeability hysteresis on geological CO2 storage." *Wiley Online Library* (Water resources research) 42 (12): 55467.

Jung, Hojung and Singh, Gurpreet and Espinoza, D Nicolas and Wheeler, Mary F. 2018. "Quantification of a maximum injection volume of CO2 to avert geomechanical perturbations using a compositional fluid flow reservoir simulator." *Advances in water resources* (Elsevier) 112: 160-169.

Kearns, David and Liu, Harry and Consoli, Chris. 2021. "Technology readiness and cost of CCS." *Glocal CCS Institute* 3.

Keilson, J and Servi, LD. 1986. "Oscillating random walk models for GI/G/1 vacation systems with Bernoulli schedules." *Journal of applied Probability* (ambridge University Press) 23 (3): 790-802.

Keogh, Kevin Joseph and Martinius, Allard Willem and Osland, Rune. 2007. "The development of fluvial stochastic modelling in the Norwegian oil industry: A historical review, subsurface implementation and future directions." *Sedimentary Geology* (Elsevier) 202 (1-2): 249-268.

Khan, Sikandar and Khulief, Yehia and Al-Shuhail, Abdullatif and Bashmal, Salem and Iqbal, Naveed. 2020. "The geomechanical and fault activation modeling during CO2 injection into deep Minjur reservoir, eastern Saudi Arabia." *Sustainability* (MDPI) 12 (23): 9800.

Kim, Jin-Seop and Kwon, Sang-Ki and Sanchez, Marcelo and Cho, Gye-Chun. 2011. "Geological storage of high level nuclear waste." *KSCE Journal of Civil Engineering* (Springer) 15: 721-737.

Kim, Myeongsub and Sell, Andrew and Sinton, David. 2013. "Aquifer-on-a-Chip: understanding pore-scale salt precipitation dynamics during CO 2 sequestration." (Royal Society of Chemistry) 13 (13): 2508--2518.

Kivi, IR and Makhnenko, RY and Vilarrasa, Victor. 2022. "Two-phase flow mechanisms controlling CO2 intrusion into shaly caprock." *Transport in Porous Media* (Springer) 141 (3): 771-798.

Kling, George W and Clark, Michael A and Wagner, Glen N and Compton, Harry R and Humphrey, Alan M and Devine, Joseph D and Evans, William C and Lockwood, John P and Tuttle, Michele L and Koenigsberg, Edward J. 1987. "The 1986 lake nyos gas disaster in cameroon, west Africa." *Science* (American Association for the Advancement of Science) 236 (4798): 169-175.

Knorr, Klaus-Holger and Blodau, Christian. 2009. "Impact of experimental drought and rewetting on redox transformations and methanogenesis in mesocosms of a northern fen soil." *Soil Biology and Biochemistry* (Elsevier) 41 (6): 1187-1198.

Koltermann, Christine E and Gorelick, Steven M. 1996. "Heterogeneity in sedimentary deposits: A review of structure-imitating, process-imitating, and descriptive approaches." *Water Resources Research* (Wiley Online Library) 32 (9): 2617-2658.

Kopp, A and Class, H and Helmig, R. 2009. "Investigations on CO2 storage capacity in saline aquifers—Part 2: Estimation of storage capacity coefficients." *International Journal of Greenhouse Gas Control* (Elsevier) 3 (3): 277-287.

Lake, Larry W. n.d. *Enhanced oil recovery.* 1989: Old Tappan, NJ; Prentice Hall Inc.

Langhi, L and Ricard, L and Strand, J and Dewhurst, D. 2019. "Numerical Simulation of Fault Compartmentalisation in CCS Reservoir." *European Association of Geoscientists \& Engineers.* European Association of Geoscientists \& Engineers. 1-5.

Lawandy, Nabil M. 1980. "Optoacoustic measurement of vibrational-translational (VT) rates using a short pulse CO 2 laser." *Infrared Physics* 20 (2): 131-132.

Li, Shengyue and Wang, Shuxiao and Wu, Qingru and Zhang, Yanning and Ouyang, Daiwei and Zheng, Haotian and Han, Licong and Qiu, Xionghui and Wen, Yifan and Liu, Min and others. 2023. "Emission trends of air pollutants and CO 2 in China from 2005 to 2021." *Earth System Science Data* (Copernicus Publications Gottingen, Germany) 15 (6): 2279-2294.

Li, Xiaochun and Fang, Zhi-ming. 2014. "Current status and technical challenges of CO 2 storage in coal seams and enhanced coalbed methane recovery: an overview." *International Journal of Coal Science \& Technology* (Springer) 1: 93-102.

Li, Xiaojiang and Li, Gensheng and Wang, Haizhu and Tian, Shouceng and Song, Xianzhi and Lu, Peiqing and Wang, Meng. 2017. "A unified model for wellbore flow and heat transfer in pure CO2 injection for geological sequestration, EOR and fracturing operations." *International Journal of Greenhouse Gas Control* (Elsevier) 57: 102-115.

Lindeberg, Erik and Wessel-Berg, Dag. 1997. "Vertical convection in an aquifer column under a gas cap of CO2." *Energy Conversion and management* (Elsevier) 38: S229-S234.

Lipponen, Juho and McCulloch, Samantha and Keeling, Simon and Stanley, Tristan and Berghout, Niels and Berly, Thomas. 2017. "The politics of large-scale CCS deployment." *Energy Procedia* (Elsevier) 114: 7581-7595.

Liu, Hejuan and Hou, Zhengmeng and Were, Patrick and Gou, Yang and Sun, Xiaoling},. 2014. "Simulation of CO 2 plume movement in multilayered saline formations through multilayer injection technology in the Ordos Basin, China." *Environmental earth sciences* (Springer) 71: 4447-4462.

Liu, Mingliang and Grana, Dario. 2020. "Petrophysical characterization of deep saline aquifers for CO2 storage using ensemble smoother and deep convolutional autoencoder." *Advances in Water Resources* (Elsevier) 142: 103634.

Liu, Yongge and Hou, Jian and Zhao, Haifeng and Liu, Xiaoyu and Xia, Zhizeng. 2019. "Numerical simulation of simultaneous exploitation of geothermal energy and natural gas hydrates by water injection into a geothermal heat exchange well." *Renewable and Sustainable Energy Reviews* (Elsevier) 109: 467-481.

Loverro, Adam and others. 2004. "Fractional calculus: history, definitions and applications for the engineer." *Rapport technique, Univeristy of Notre Dame: Department of Aerospace and Mechanical Engineering* 1-28.

—. 2004. *Fractional calculus: history, definitions and applications for the engineer.*

Lu, Meng and Connell, Luke D. 2008. "Non-isothermal flow of carbon dioxide in injection wells during geological storage." *International journal of greenhouse gas control* (Elsevier) 2 (2): 248-258.

Lucier, Amie and Zoback, Mark and Gupta, Neeraj and Ramakrishnan, TS. 2006. "Geomechanical aspects of CO2 sequestration in a deep saline reservoir in the Ohio River Valley region." *Environmental Geosciences* (American Association of Petroleum Geologists (AAPG)) 13 (2): 85-103.

Machado, J Tenreiro and Kiryakova, Virginia and Mainardi, Francesco. 2011. "Recent history of fractional calculus." *Communications in nonlinear science and numerical simulation* (Elsevier) 16 (3): 1140-1153.

Marland, GTABRJA and Andres, RJ and Boden, TA and others. 1994. "Global, regional, and national CO2 emissions." *Trends 93: A Compendium of Data on Global Change* (Oak Ridge National Laboratory, ORNL/CDIAC-65, Oak Ridge, Tenn., USA) 505-584.

Mathias, Simon A and Gonzalez Martinez de Miguel, Gerardo J and Thatcher, Kate E and Zimmerman, Robert W. 2011. "Pressure buildup during CO 2 injection into a closed brine aquifer." *Transport in porous media* (Springer) 89: 383-397.

Mathias, Simon A and Gonzalez Martinez de Miguel, Gerardo J and Thatcher, Kate E and Zimmerman, Robert W. 2011. "Pressure buildup during CO 2 injection into a closed brine aquifer." *Transport in porous media* (Springer) 383--397.

Mathias, Simon A and Hardisty, Paul E and Trudell, Mark R and Zimmerman, Robert W}. 2009. "Approximate solutions for pressure buildup during CO 2 injection in brine aquifers." *Transport in Porous Media* (Springer) 79: 265-284.

Mathieson, Allan and Wright, Iain and Roberts, David and Ringrose, Philip. 2009. "Satellite imaging to monitor CO2 movement at Krechba, Algeria." *Energy Procedia* (Elsevier) 1 (1): 2201-2209.

McCoy, Sean T and Rubin, Edward S. 2005. "Models of CO2 transport and storage costs and their importance in CCS cost estimates."

Meite, Daouda and Rafini, Silvain and Chesnaux, Romain and Ferroud, Anouck. 2022. "eview of petroleum and hydrogeology equations for characterizing the pressure front diffusion during pumping tests." *Geosciences* (MDPI) 12 (5): 201.

Metz, Bert and Davidson, Ogunlade and De Coninck, HC and Loos, Manuela and Meyer, Leo. 2005. *IPCC special report on carbon dioxide capture and storage.* Cambridge: Cambridge University Press.

Michael, K and Allinson, G and Golab, A and Sharma, S and Shulakova, Valeriya. 2009. "CO2 storage in saline aquifers II--experience from existing storage operations." *Energy Procedia* (Elsevier) 1 (1): 1973-1980.

Middleton, Richard S and Ogland-Hand, Jonathan D and Chen, Bailian and Bielicki, Jeffrey M and Ellett, Kevin M and Harp, Dylan R and Kammer, Ryan M. 2020. "Identifying geologic characteristics and operational decisions to meet global carbon sequestration goals." *Energy & Environmental Science* (Royal Society of Chemistry) 13 (12): 5000-5016.

Mijic, Ana and LaForce, Tara C and Muggeridge, Ann H. 2014. "CO2 injectivity in saline aquifers: The impact of non-Darcy flow, phase miscibility, and gas compressibility." *Water Resources Research* (Wiley Online Library) 50 (5): 4163-4185.

Mohebbi, Rasul and Delouei, Amin Amiri and Jamali, Amin and Izadi, Mohsen and Mohamad, Abdulmajeed A. 2019. "Pore-scale simulation of non-Newtonian power-law fluid flow and forced convection in partially porous media: thermal lattice Boltzmann method." *Physica A: Statistical Mechanics and Its Applications* (Elsevier) 525: 642-656.

Morakaladi, Makosha Ishmaeline Charlotte and Atangana, Abdon. 2023. "Mathematical model for conversion of groundwater flow from confined to unconfined aquifers with power law processes." *Open Geosciences* (De Gruyter) 15 (1): 20220446.

Mosaheb, Mojtaba and Zeidouni, Mehdi. 2017. "Above-zone pressure response to distinguish between fault and caprock leakage." *SPE Western Regional Meeting*, D041S013R009.

Mudakkar, Syeda Rabab and Zaman, Khalid and Khan, Muhammad Mushtaq and Ahmad, Mehboob. 2013. "Energy for economic growth, industrialization, environment and natural resources: living with just enough." *Renewable and Sustainable Energy Reviews* (Elsevier) 580-595.

Neufeld, Jerome A and Hesse, Marc A and Riaz, Amir and Hallworth, Mark A and Tchelepi, Hamdi A and Huppert, Herbert E. 2010. "Convective dissolution of carbon dioxide in saline aquifers." *Geophysical research letters* (Wiley Online Library) 37 (22).

Nicot, Jean-Philippe and Solano, Silvia and Lu, Jiemin and Mickler, Patrick and Romanak, Katherine and Yang, Changbing and Zhang, Xiaodong. 2013. "Potential subsurface impacts of CO2 stream impurities on geologic carbon storage." *Energy Procedia* (Elsevier) 37: 4552-4559.

Nicot, Jean-Philippe. 2008. "Evaluation of large-scale CO2 storage on fresh-water sections of aquifers: An example from the Texas Gulf Coast Basin." *International Journal of Greenhouse Gas Control* (Elsevier) 2 (4): 582-593.

Niu, Ben and Krevor, Samuel. 2020. "The impact of mineral dissolution on drainage relative permeability and residual trapping in two carbonate rocks." *Transport in Porous Media* (Springer) 131 (2): 363-380.

Noh, Myeong and Lake, Larry Wayne and Bryant, Steven Lawrence and Araque-Martinez, A. 2007. "Implications of coupling fractional flow and geochemistry for CO2 injection in aquifers." *SPE Reservoir Evaluation \& Engineering* (OnePetro) 10 (04): 406-414.

Nooner, Scott L and Eiken, Ola and Hermanrud, Christian and Sasagawa, Glenn S and Stenvold, Torkjell and Zumberge, Mark A. 2007. "Constraints on the in situ density of CO2 within the Utsira formation from time-lapse seafloor gravity measurements." *international journal of greenhouse gas control* (Elsevier) 1 (2): 198-214.

Nordbotten, Jan M and Dahle, Helge K. 2011. "Impact of the capillary fringe in vertically integrated models for CO2 storage." *Water Resources Research* (Wiley Online Library) 47 (2).

Nordbotten, Jan Martin and Celia, Michael A and Bachu, Stefan. 2004. "Analytical solutions for leakage rates through abandoned wells." *Water Resources Research* (Wiley Online Library) 40 (4).

Nordbotten, Jan Martin and Celia, Michael A and Bachu, Stefan. 2005. "Injection and storage of CO 2 in deep saline aquifers: analytical solution for CO 2 plume evolution during injection." *Transport in Porous media* (Springer) 58: 339-360.

Nordbotten, Jan Martin and Celia, Michael A. 2011. *Geological Storage of CO2: Modeling Approaches for Large-scale Simulation.* John Wiley & Sons.

Obdam, A and Van Der Meer, L and May, F and Kervevan, C and Bech, N and Wildenborg, A. 2003. *Effective CO2 storage capacity in aquifers, gas fields, oil fields and coal fields.* Elsevier.

Oberdorfer, June A and Peterson, Frank L. 1985. "Waste-water injection: Geochemical and biogeochemical clogging processes." *Groundwater* (Wiley Online Library) 23 (6): 753-761.

Oruganti, YagnaDeepika and Bryant, Steven L. 2009. "Pressure build-up during CO2 storage in partially confined aquifers." *Energy procedia* (Elsevier) 1 (1): 3315-3322.

Pacala, Stephen and Socolow, Robert. 2004. "Stabilization wedges: solving the climate problem for the next 50 years with current technologies." *science* (American Association for the Advancement of Science) 305 (5686): 968-972.

Palmer, MD and Domingues, CM and Slangen, ABA and Dias, F Boeira. 2021. "An ensemble approach to quantify global mean sea-level rise over the 20th century from tide gauge reconstructions." *Environmental Research Letters* (IOP Publishing) 16 (4): 044043.

Pan, Lehua and Oldenburg, Curtis M and Pruess, Karsten and Wu, Yu-Shu. 2011. "Transient CO2 leakage and injection in wellbore-reservoir systems for geologic carbon sequestration." *Greenhouse Gases: Science and Technology* (Wiley Online Library) 1 (4): 335-350.

Peters, Glen and Sognnaes, Ida. 2019. "The role of carbon capture and storage in the mitigation of climate change." *CICERO Report* (CICERO Center for International Climate and Environmental Research-Oslo).

Postma, Tom and Bandilla, Karl W and Celia, Michael. 2021. "A Computationally Efficient Method for Field-Scale Reservoir Simulation of CCS in Basalt Formations." *Proceedings of the 15th Greenhouse Gas Control Technologies Conference.* 15-18.

Pruess, Karsten and Garcia, Julio. 2002. "Multiphase flow dynamics during CO 2 disposal into saline aquifers." *Environmental Geology* 42: 282-295.

Pruess, Karsten and Spycher, Nicolas. 2007. "ECO2N--A fluid property module for the TOUGH2 code for studies of CO2 storage in saline aquifers." *Energy conversion and management* (Elsevier) 48 (6): 1761-1767.

Raeini, Ali Q and Bijeljic, Branko and Blunt, Martin J. 2015. "Modelling capillary trapping using finite-volume simulation of two-phase flow directly on micro-CT images." *Advances in Water Resources* (Elsevier) 83: 102-110.

Raeini, Ali Q and Bijeljic, Branko and Blunt, Martin J. 2015. "Modelling capillary trapping using finite-volume simulation of two-phase flow directly on micro-CT images." *Advances in Water Resources* (Elsevier) 83: 102-110.

Raistrick, Mark and Mayer, Bernhard and Shevalier, Maurice and Perez, Renee J and Hutcheon, Ian and Perkins, Ernie and Gunter, Bill. 2006. "Using chemical and isotopic data to quantify ionic trapping of injected carbon dioxide in oil field brines." *Environmental science technology* (ACS Publications) 40 (21): 6744-6749.

Ramsay, John G and Lisle, Richard John. 2000. *Applications of continuum mechanics in structural geology (Techniques of modern structural geology. Vol. 3.* Vol. 3. Academic Press.

Raza, Arshad and Gholami, Raoof and Rezaee, Reza and Bing, Chua Han and Nagarajan, Ramasamy and Hamid, Mohamed Ali. 2018. "CO2 storage in depleted gas reservoirs: A study on the effect of residual gas saturation." *Petroleum* (Elsevier) 4 (1): 95-107.

Ren, Bo. 2018. "Local capillary trapping in carbon sequestration: Parametric study and implications for leakage assessment." *{International Journal of Greenhouse Gas Control* (Elsevier) 78: 135-147.

Rinaldi, Antonio P and Rutqvist, Jonny and Finsterle, Stefan and Liu, Hui-Hai. 2017. "Inverse modeling of ground surface uplift and pressure with iTOUGH-PEST and TOUGH-FLAC: The case of CO2 injection at In Salah, Algeria." *Computers \& Geosciences* (Elsevier) 108: 98-109.

Ringrose, Philip. 2020. "How to store CO2 underground: Insights from early-mover CCS projects." (Springer).

Roeloffs, Evelyn A. 1988. "Fault stability changes induced beneath a reservoir with cyclic variations in water level." *Journal of Geophysical Research: Solid Earth* 93 (B2): 2107-2124.

Rother, Gernot and Ilton, Eugene S and Wallacher, Dirk and Hauβ, Thomas and Schaef, Herbert T and Qafoku, Odeta and Rosso, Kevin M and Felmy, Andrew R and Krukowski, Elizabeth G and Stack, Andrew G and others. 2013. "CO2 sorption to subsingle hydration layer montmorillonite clay studied by excess sorption and neutron diffraction measurements." *Environmental science & technology* (ACS Publications) 47 (1): 205-211.

Roussanaly, Simon and Ouassou, Jabir A and Anantharaman, Rahul and Haaf, Martin. 2020. "Impact of uncertainties on the design and cost of CCS from a waste-to-energy plant." *Frontiers in Energy Research* (Frontiers Media SA) 8 (17).

Roy, Pratanu and Morris, Joseph P and Walsh, Stuart DC and Iyer, Jaisree and Carroll, Susan. 2018. "Effect of thermal stress on wellbore integrity during CO2 injection." *International Journal of Greenhouse Gas Control* (Elsevier) 77: 14-26.

Rubin, E and De Coninck, H. 2005. "IPCC special report on carbon dioxide capture and storage." *UK: Cambridge University Press. TNO (2004): Cost Curves for CO2 Storage, Part* 2 (14).

Rutqvist, Jonny and Vasco, Donald W and Myer, Larry. 1020. "Coupled reservoir-geomechanical analysis of CO2 injection and ground deformations at In Salah, Algeria." *International Journal of Greenhouse Gas Control* (Elsevier) 4 (2): 225-230.

Saadatpoor, Ehsan and Bryant, Steven L and Sepehrnoori, Kamy. 2010. "ew trapping mechanism in carbon sequestration." *Transport in porous media* (Springer) 82 (1): 3-17.

Saadatpoor, Ehsan and Bryant, Steven L and Sepehrnoori, Kamy. 2010. "New trapping mechanism in carbon sequestration." *Transport in porous media* (Springer) 82: 3-7.

Saadatpoor, Ehsan and Bryant, Steven L and Sepehrnoori, Kamy. 2010. "New trapping mechanism in carbon sequestration." *Transport in porous media* (Springer) 82: 3-17.

Saqib, Muhammad and Khan, Ilyas and Shafie, Sharidan. 2018. "Application of Atangana--Baleanu fractional derivative to MHD channel flow of CMC-based-CNT's nanofluid through a porous medium." *Chaos, Solitons \& Fractals* (Elsevier) 116: 79-85.

Scanziani, Alessio and Singh, Kamaljit and Menke, Hannah and Bijeljic, Branko and Blunt, Martin J. 2020. "Dynamics of enhanced gas trapping applied to CO2 storage in the presence of oil using synchrotron X-ray micro tomography." *Applied Energy* (Elsevier) 259: 114136.

Serra De Souza, Antonio Luiz and Meurer, Gustavo Bechara and Pastor, Jorge Aurelio and Naveira, Vanessa Palma and Souza, Jorge and Frydman, Marcelo and Chaves, Ricardo AP and Chaves, Michelle and others. 2012. "Reservoir geomechanics study for deepwater field identifies ways to maximize reservoir performance while reducing geomechanics risks." *SPE Asia Pacific Oil and Gas Conference and Exhibition.* Society of Petroleum Engineers.

Shao, Qi and Boon, Maartje and Youssef, AbdAllah and Kurtev, Kuncho and Benson, Sally M and Matthai, Stephan K. 2022. "Modelling CO2 plume spreading in highly heterogeneous rocks with anisotropic, rate-dependent saturation functions: A field-data based numeric simulation study of Otway." *International Journal of Greenhouse Gas Control* (Elsevier) 119: 103699.

Shepherd, John G. 2009. *Geoengineering the climate: science, governance and uncertainty.* Royal Society.

Singh, AK and Goerke, U-J and Kolditz, O. 2011. "Numerical simulation of non-isothermal compositional gas flow: application to carbon dioxide injection into gas reservoirs." *Energy* (Elsevier) 36 (5): 3446-3458.

Singh, M and Chaudhuri, A. 2023. "Evaluation of low-to moderate-enthalpy shallow sedimentary reservoirs for CCS-CPG systems." *Enhanced Geothermal Systems (EGS)* 1-16.

Sminchak, Joel and Majors, Shawn and Mishra, Srikanta and Oruganti, Yagnadeepika. 2012. *Infrastructure analysis for geologic CO2 storage applications in the Arches Province of the midwest United States.* CMTC.

Soltanian, Mohamad Reza and Amooie, Mohammad Amin and Gershenzon, Naum and Dai, Zhenxue and Ritzi, Robert and Xiong, Fengyang and Cole, David and Moortgat, Joachim. 2017. "Dissolution trapping of carbon dioxide in heterogeneous aquifers." *Environmental Science & Technology* (ACS Publications) 51 (13): 7732-7741.

Song, ZhiYong and Song, Hongqing and Cao, Yang and Killough, John and Leung, Juliana and Huang, Gang and Gao, Sunhua. 2015. "Numerical research on CO2 storage efficiency in saline aquifer with low-velocity non-Darcy flow." *Journal of Natural Gas Science and Engineering* (Elsevier) 23: 338-345.

Sousa, J Vanterler da C and Frederico, Gastao SF and De Oliveira, E Capelas. 2020. psi-Hilfer pseudo-fractional operator: new results about fractional calculus." *Computational and Applied Mathematics* (Springer) 39 (4): 254.

Spanos, TJT and De La Cruz, V and Hube, J and Sharma, RC. 1986. "An analysis of Buckley-Leverett theory." *Journal of Canadian Petroleum Technology* (PETSOC) 25 (1).

Sun, HongGuang and Zhang, Yong and Baleanu, Dumitru and Chen, Wen and Chen, YangQuan. 2018. "A new collection of real world applications of fractional calculus in science and engineering." *Communications in Nonlinear Science and Numerical Simulation* (Elsevier) 64: 213-231.

Sun, Y and Tong, C and Trainor-Guitton, WJ and Lu, C and Mansoor, K and Carroll, SA. 2013. "Global sampling for integrating physics-specific subsystems and quantifying uncertainties of CO2 geological sequestration." *International Journal of Greenhouse Gas Control* (Elsevier) 108-123.

Swartzendruber, Dale. 1962. "Modification of Darcy's law for the flow of water in soils." *Soil Science* (LWW) 93 (1): 22-29.

Tahmasebi, Pejman and Sahimi, Muhammad and Shirangi, Mehrdad G. 2018. "Rapid learning-based and geologically consistent history matching." *Transport in Porous Media* (Springer) 122: 279-304.

Talapatra, Akash. 2020. "A study on the carbon dioxide injection into coal seam aiming at enhancing coal bed methane (ECBM) recover." *Journal of Petroleum Exploration and Production Technology* (Springer) 10 (5): 1965-1981.

Tateishi, Angel A and Ribeiro, Haroldo V and Lenzi, Ervin K. 2017. "The role of fractional time-derivative operators on anomalous diffusion." *Frontiers in Physics* (Frontiers Media SA) 5: 52.

Thuiller, Wilfried. 2007. "Climate change and the ecologist." *Nature* (Nature Publishing Group UK London) 448 (7153): 550-552.

Trevisan, Luca and Pini, Ronny and Cihan, Abdullah and Birkholzer, Jens T and Zhou, Quanlin and Illangasekare, Tissa H. 2015. "Experimental analysis of spatial correlation effects on capillary trapping of supercritical CO 2 at the intermediate laboratory scale in heterogeneous porous media." *Water Resources Research* (Wiley Online Library) 51 (11): 8791-8805.

Tyndall, John. 1881. *Heat: a mode of motion.* D. Appleton.

Vacek, Zdenek and Vacek, Stanislav and Cukor, Jan. 2023. "European forests under global climate change: Review of tree growth processes, crises and management strategies." *Journal of Environmental Management* (Elsevier) 332: 117353.

van der Meer, LGH Bert and Yavuz, Ferhat. 2009. "CO2 storage capacity calculations for the Dutch subsurface." *Energy Procedia* (Elsevier) 1 (1): 2615-2622.

Vasco, DW and Ferretti, Alessandro and Novali, Fabrizio. 2008. "Reservoir monitoring and characterization using satellite geodetic data: Interferometric synthetic aperture radar observations from the Krechba field, Algeria." *Geophysics* (Society of Exploration Geophysicists) 73 (6): WA113-WA122.

Vialle, Stephanie and Druhan, Jennifer L and Maher, Katharine. 2016. "Multi-phase flow simulation of CO2 leakage through a fractured caprock in response to mitigation strategies." *International Journal of Greenhouse Gas Control* (Elsevier) 44: 11-25.

Vilarrasa, Victor and Bolster, Diogo and Olivella, Sebastia and Carrera, Jesus. 2010. "Coupled hydromechanical modeling of CO2 sequestration in deep saline aquifers." *International Journal of Greenhouse Gas Control* (Elsevier) 4 (6): 910-919.

Wang, Rui and Yue, Xiang'an and Zhao, Renbao and Yan, Pingxiang and Freeman, Dave. 2009. "Effect of stress sensitivity on displacement efficiency in CO 2 flooding for fractured low permeability reservoirs." *Petroleum Science* (Springer) 6: 277-283.

Wang, Shibo and Tokunaga, Tetsu K. 2015. "Capillary pressure--saturation relations for supercritical CO2 and brine in limestone/dolomite sands: Implications for geologic carbon sequestration in carbonate reservoirs." *Environmental science \& technology* (ACS Publications) 49 (12): 7208-7217.

Wang, Yuhang and Vuik, Cornelis and Hajibeygi, Hadi. 2022. "CO2 Storage in deep saline aquifers: Impacts of fractures on hydrodynamic trapping." *{International Journal of Greenhouse Gas Control* (Elsevier) 113: 103552.

Wei, Lingli and Saaf, Fredrik. 2009. "Estimate CO 2 storage capacity of the Johansen formation: numerical investigations beyond the benchmarking exercise." *Computational Geosciences* (Springer) 13: 451-467.

Wendt, Anna and Sheriff, Alana and Shih, Chung Yan and Vikara, Derek and Grant, Tim. 2022. "A multi-criteria CCUS screening evaluation of the Gulf of Mexico, USA." *International Journal of Greenhouse Gas Control* 118: 103688.

White, Joshua A and Chiaramonte, Laura and Ezzedine, Souheil and Foxall, William and Hao, Yue and Ramirez, Abelardo and McNab, Walt. 2014. "Geomechanical behavior of the reservoir and caprock system at the In Salah CO2 storage project." *Proceedings of the National Academy of Sciences* (National Acad Sciences) 111 (24): 8747-8752.

White, Mark D and McPherson, Brian J and Grigg, Reid B and Ampomah, William and Appold, Martin S. 2014. "Numerical simulation of carbon dioxide injection in the western section of the Farnsworth Unit." *Energy Procedia* (Elsevier) 63: 7891-7912.

Woods, EG and Comer, AG. 1962. "Saturation distribution and injection pressure for a radial gas-storage reservoir." *Journal of Petroleum Technology* (SPE) 14 (12): 1389-1393.

Yang, Changbing and Trevino, Ramon H and Zhang, Tongwei and Romanak, Katherine D and Wallace, Kerstan and Lu, Jiemin and Mickler, Patrick J and Hovorka, Susan D. 2014. "Regional assessment of CO2-solubility trapping potential: A case study of the coastal and offshore Texas Miocene Interval." *Environmental science \& technology* (ACS Publishings) 48 (14): 8275-8282.

Zahasky, Christopher and Krevor, Samuel. 2020. "Global geologic carbon storage requirements of climate change mitigation scenarios." *Energy \& Environmental Science* (Royal Society of Chemistry) 13 (6): 1561-1567.

Zakrisson, Johan and Edman, Ingrid and Cinar, Yildiray. 2008. "Multiwell injectivity for CO2 storage." One Petro.

Zeighami, Farhad and Lenci, Alessandro and Di Federico, Vittorio. 2022. "Drainage of power-law fluids from fractured or porous finite domains." *Journal of Non-Newtonian Fluid Mechanics* (Elsevier) 305: 104832.

Zheng, Liange and Spycher, Nicolas and Varadharajan, Charuleka and Tinnacher, Ruth M and Pugh, John D and Bianchi, Marco and Birkholzer, Jens and Nico, Peter S and Trautz, Robert C. 2015. "On the mobilization of metals by CO2 leakage into shallow aquifers: exploring release mechanisms by modeling field and laboratory experiments." *Greenhouse Gases: Science and Technology* (Wiley Online Library) 5 (4): 403-418.

Zheng, Ligang. 2011. *Oxy-fuel combustion for power generation and carbon dioxide (CO2) capture.* Elsevier.

Zheng, Yangfeng and Zhai, Cheng and Sun, Yong and Xu, Jizhao and Cong, Yuzhou and Tang, Wei and Chen, Aikun. 2021. "Experimental study on the effect of coal particle size on the mechanics, pore structure, and permeability of coal-like materials for low-rank coalbed methane reservoir simulation." *Energy & Fuels* (ACS Publications) 35 (21): 17566-17579.

Zhou, Quanlin and Birkholzer, Jens T and Mehnert, Edward and Lin, Yu-Feng and Zhang, Keni. 2010. "Modeling basin-and plume-scale processes of CO2 storage for full-scale deployment." *Groundwater* (Wiley Online Library) 48 (4): 494-514.

Zimmerman, Robert W and Somerton, Wilbur H and King, Michael S. 1986. "Compressibility of porous rocks." *Journal of Geophysical Research: Solid Earth* (Wiley Online Library) 91 (B12): 12765-12777.